Quantitative Investigation into the Relationship Between Substrate Strain and Phenotypic Modulation

Thesis Submitted for the Degree of PhD

Jaspal Puri

Principle Supervisor: Dr. Richard Day.
Subsidiary Supervisor: Prof. Quentin Pankhurst.

2018

Declaration

I, Jaspal Puri, confirm that the work presented in this thesis is my own. Where information has been derived from other sources, I confirm that this has been indicated in the thesis.

Abstract

When cells are stretched through substrate strain they respond with changes to their phenotypic behaviour. Given the highly dynamic and mechanically active environment of the human body, this makes sense. *In vitro* experimentation has demonstrated both this relationship together with the ability to control phenotype using mechanical stimulus alone. Harnessing mechanical stimulus to engineer tissue is thus highly desirable to create new and advance old therapeutics.

This thesis questions whether the relationships, as we understand them, between substrate strain and phenotypic modulation are optimal. To build anything new, arguably is it better to know more than you use than to use only what you know. To employ mechanical stimulus as a tool to either create or repair tissue, understanding relationships *in general* is therefore better.

General strain-phenotype relationships, however, are not reported in the literature; dose response type curves do not exists. Arguably this is because current commercial available systems are not designed to do so and to do so would be inhibited by excessive costs.

This thesis details the development of a new apparatus conceived to increase the volume of information generated about strain-phenotype relationships with minimal experimentation and costs. The apparatus is based on the principle that the mechanical stimulus delivered to a monolayor of cells, contrary to the majority of apparatus previously developed, is highly heterogeneous. Together with non-destructive assays, image analysis and physical and theoretical modelling, a novel framework to understand these general relationships is sought.

To this end, a bespoke 3D printed apparatus is developed which actuates augmented BioFlex® plates with small magnets using secondary rotating magnets. The method of actuation is such that it delivers a heterogeneous strain regime across the surface of a BioFlex® well. The apparatus is accompanied both by hardware and software to control the periodicity of actuation.

Both physical measurement and finite element modelling were utilised to characterise the heterogeneous strain regime across the BioFlex® well. Physical measurements were made using digital image correlation techniques offered by Dantec Dynamics GmbH. The technique developed to measure strain deformation on BioFlex® plates provides results which concur with intuition and offers a novel alternative to similar strain measurements used on the FlexCell® actuation system. Results related to the system developed here

highlighted that the variance of strain was not wide enough to suit the ends of the thesis. Finite element modelling was employed to provide a way for the system to achieve the goals of this work as part of future development.

The extraction of general strain-phenotype relationships is based upon recording the behaviour of all cells on the BioFlex® membrane together with their position on the membrane. A bespoke image acquisition and automated image analysis pipeline is developed which translates cell behaviour across the whole BioFlex® membrane into numerical maps for the purpose of statistical correlation studies comparing the equivalent strain stimulus map.

Research was also conducted into finding a suitable cell biology paradigm in which the proof of concept apparatus and methodology could be tested within. Experimentation was based upon proliferation studies from the literature however results here are often at odds. Alternative paradigms in the form of plasmid transfection are found to be an avenue for future development.

Approaching the need for high-throughput in strain biology experiments through utilising a heterogeneous strain regime as opposed to homogeneous is novel and the development of the bespoke apparatus allows for this idea to be tested further. Characterisation of strain across BioFlex® plates utilising digital image correlation has not been done before and appears to be a good high resolution method for physical measurements applicable to other strain inducing modalities, in particular the FlexCell® system. The development of a bespoke image analysis methodology allows for tailoring the full pipeline to suit experimental needs and offers an effective way of recording and analysing all cells on a 35 mm BioFlex® membrane. Taken together, although the proof of concept is left incomplete, this thesis still makes important contributions to the field.

Acknowledgements

First and foremost, thanks and appreciation is owed to Dr. Richard Day, my principal supervisor, for having the faith that a mathematician by training could succeed academically in a biological world. The ethos of the PhD program I entered UCL through – that of bridging the gap between disciplines – has been tested over the years I spent in the Day Lab. Although not always an easy endeavour, I would not have anywhere near the level of biological and experimental knowledge had Dr. Day not been patience, supportive, and understanding of this interdisciplinary ethos. It will never be forgotten – thank you, Richard.

Thanks is also due to those who got me to the point of even thinking I could do a PhD. In the face of early failures, rebuilding my confidence through love and support means this submission is as much theirs as it is mine. In particular my parents, Sheila and Satpal Puri, my sister, Priya Puri and my old friend, Jennifer Petrie.

Throughout my PhD years I am indebted to the support shown to me by others within UCL. Thank you to my friends, Niamh and Eseelle for drinks throughout the day and at all possible altitudes. To Nina and Yani, who in the face of me repeatedly breaking sterility, kept calm and continued to welcome me to the lab. To Paul Frankel and his lab for fostering me and providing guidance and support. To CoMPLEX for giving me the chance in the first place and to my CoMPLEX cohort for simply being a bizarre but truly wonderful collection of imaginations.

To the van Dorps, thank you for sheltering me, feeding me, and ironing my shirts even when I insisted on doing them myself.

Reserved for last a special thanks to (Dr.) Lucy van Dorp who has, despite singularly enduring a most turbulent version of myself, without wavering has supported me through the highs and lows of PhD life. Her discipline in maintaining this state is perplexing and this is as much hers as it is mine.

Thanks is given necessarily together with apologies. For missing events, for damaging relationships, and for putting upon you a misery entirely unwarranted and unnecessarily grand – to you all, I sincerely apologise.

Contents

List of Figures

List of Tables

List of Protocols

List of Algorithms

Preface

This PhD project was conducted through the four year interdisciplinary PhD program created by CoMPLEX, University College London (UCL)[1]. The program seeks to bring together life and medical scientists with mathematicians, physicists and engineers to bridge the gap across disciplines and better equip researchers tackling complexity in the life sciences and medicine.

My background before UCL was that of applied mathematics. For my PhD years I was based in the Applied Biomedical Engineering Group (ABEG) in UCL's Division of Medicine. ABEG is part of the division's Centre for Cardiovascular Biology and Medicine and is led by Dr. Richard Day. The focus of the group is in experimental biology and engineering medical therapeutics. For a mathematician, working in an purely biological environment was entirely keeping with the ethos of CoMPLEX and the interdisciplinary nature of this thesis is entirely reflective of this.

Together with CoMPLEX, this thesis was also supported by funding from the British Heart Foundation.

Thesis Formatting

Throughout this thesis units are expressed in plain text whereas unit prefixes are expressed in italicised text. Software names are printed in bold text. Protocols, algorithms, figures, tables, chapters, sections and footnotes have unique numerical identifiers and in the .pdf version of this thesis are all hyper-linked to the original source. This is known from the labels printed in red font. Citations in the literature are printed in blue font and in the .pdf version are hyper-linked to the source in the bibliography. Where references are given to parts of this thesis from different chapters, page numbers are also printed with the numerical identifier.

[1] The UCL Centre for Computation, Mathematics and Physics in the Life Sciences and Experimental Biology (CoMPLEX).

Chapter 1

Introduction

As it is on the outside, the world inside our bodies is dominated by physical forces. The contracting force of our hearts, for example, continuously pumping fluid around a complex network of vessels. The vessels themselves, soft and deformable, forcefully acting against the pulsating pressure generated as a result. Our bones maintain the rigidity of our bodies against the external load our skeletal muscles purposely contract to hold.

The cellular building blocks of our bodies not only actively generate or passively resist these forces, but also, for better or worse, actively respond to as well (Orr et al., 2006). The ability of our brain to maintain total pressure yet still increase oxygen supplies through vasodilation is an example of such a biological response to a mechanical message (Goriely et al., 2015). Forces have the power, as in nature, not only to form but also to disrupt and destroy a biological system (Miller and Davidson, 2013; Peiffer et al., 2013).

Although the relationship between mechanical force and biological response has been studied for decades, arguably the full potential of force as a therapeutic *drug* has not been realised. The advancement of technology generates opportunity for exploitation of force in medical therapeutics. An area from which the concept underlying this thesis initially grew is the idea that cyclic stretch can modulate the rate at which cells synthesise DNA and therefore proliferate (Sumpio and Banes, 1988). Although this can also be controlled with delivery of molecular, exogenous, soluble agents – such as serum and various growth factors (Lee et al., 2011) – the ability to control this without the use of exogenous stimuli has obvious benefits. As magnetic technologies and therapeutics advance (as demonstrated, for example, by the rise of magnetic nano particle technology (Pankhurst et al., 2009)), it is not outside the realms of possibility that such forces can be directly applied, within the body from outside, to stimulate the proliferation of cells following damage in an effort to enhance repair. Compared to a systemic delivery of a molecule, the local delivery of force potentially has far fewer peripheral effects.

Another area from which the ideas in this thesis has grown from is the ability to control the alignment of cells using external forces. Particularly with muscle, engineering functional tissue requires distinct alignment of cells relative to each other in order for

successful contraction to occur. The therapeutic delivery of muscle cells to a region of damage *in vivo* requires successful engraftment to native tissue. Currently there is no robust guarantee that cells will en-graft with this required alignment. Exploiting the behaviour of cells responding to controlled forces could offer potential to enhance the efficacy of cell therapies if a method could be found to do this *in vivo*.

Much of the application of proliferative and alignment control has been in *ex vivo* tissue engineering. In many cases engineered tissue, to function as close as possible to its *in vivo* analogue, is now supplied with appropriate forces during development to enhance growth and its biomimetic properties (Martin et al., 2004). The idea behind this being that once implanted into the body the engineered tissue will en-graft and function better with host tissue.

With regards to cyclic stretch, the work in this thesis is primarily less concerned with its application as a therapeutic tool, and more so with the fundamental question of how we discover what the relationship is between cyclic strain and cellular modulation. This thesis is both a critique of current methods which investigate cyclic strain and cellular behaviour and a multi-disciplinary development of a new system which, at its core, is designed to substantially increase the volume of information currently available. This is done with the ethos that to use cyclic strain as a tool in any form of tissue engineering or therapeutics, it is advantageous to have a broad spectrum understanding of cellular response to strain rather than understanding only a handful of strain parameters and corresponding effects. The argument for doing this is that if a full, general relationship between strain and cellular effects is not known, then the information available to researchers to engineer tissues and therapeutics, and hypothesise further, is narrow, and as a result anything developed further is potentially sub-optimal. This is an observation shared by others (Balestrini and Hinz, 2014).

In this thesis I develop a new method and pipeline for the study of cellular modification as the result of cyclic stretch. The aim of this method is to improve quantification, increase the experimental throughput and allow for the generation of better data upon which therapeutic engineering and testable hypotheses can be constructed. This introduction provides both the context of this work as well as the arguments for why this work is needed. Through a review of key literature and as well a novel theoretical analysis, this chapter will argue that current popular apparatus is not sufficient in terms of throughput and that current methodologies generate an error which cannot be ignored. Both are enough to justify the investigation of something new.

1.1 Cyclic Strain and Cellular Modulation

A reason for the lack of throughput in this field is due to a lack of appropriate technology. This section provides context for the work developed in this thesis by way of describing existing methods of experimentally stretching cells.

1.1.1 Methods of Experimental Stretch

Stretch is the elongation of one or many axes of a material body beyond its natural resting state caused by either internal or external forces. Compression is the counterpart term for shortening of one or many axes. Strain, a term which encompasses both stretch and compression, is a measurement of deformation of the body which describes the displacement of particles within the body relative to a reference point.

Strains are experienced by cells throughout the human body. Engineering systems to deliver strains to cultured cells for investigating cellular response is an endeavour that has been conducted for decades. An early example is found by Arem and Madden (1976) who investigated the effect of strain on tendon scar formation. They implanted permanent magnets to the tendons of live rats. By applying a periodic external magnetic field to generate strain upon the tendon they demonstrated a difference in tendon scar formation relative to an unstrained control.

The engineering of apparatus to deliver strain to biological tissue has evolved over recent decades and continues to do so. This is perhaps in accordance with the evolution of available technology and their accessibility in experimental labs. Systematic reviews can be found in Davis et al. (2015); Riehl et al. (2012); Brown (2000). In particular, the review by Davis et al. provides a detailed evolution of custom and commercial apparatus. Here, a brief description of the variety of apparatus engineered for *in vitro* delivery of strain is given for context.

For completeness, the nomenclature for strain modalities used here are in line with the definitions found in Davis et al. (2015). *Uniaxial* strain is defined as stretch along a single axes. Usually, a device stretches a deformable, rectangular cell substrate at opposite ends but in the same direction. With this type of strain materials undergoing deformation are also subject to the Poisson effect; stretching in one direction is accompanied by a compression in the perpendicular or transverse axis. *Biaxial* strain is where a deformable membrane is stretched in two perpendicular axes. When the stretch is equal in all in plane directions, this is referred to as *equibiaxial* strain.

In general, the apparatus discussed here deforms a cell substrate to which cells are attached. Deformation of the substrate is translated to the cell via integrin components and focal adhesion points. Therefore, the mechanical signals cells receive are greatly dependent on anything which effects the cell-substrate junction, for example, surface coating proteins and coating protocols. Friedrich et al. (2017) argues that because of this, much more importance should be given to calibrating the cell-substrate junction in cell stretching experiments. Consideration of this goes beyond the scope of this thesis but is acknowledged as being a vital point to address for the advancement of the field.

The methods detailed below consider only methods which deliver strain to cells via interaction with the cell substrate. Methods exist for single cell delivery of mechanical force but are beyond the context of this thesis – a review and description of these can be found in Friedrich et al. (2017) and a good example of magnetic nano particle induced strain is found in Cartmell et al. (2005). Following on from the classifications given by

Brown (2000), methods to deliver strain are stratified according to the mechanics used.

1.1.1.1 Clamp Based

Clamp based methods consist of fixing the ends of a deformable substrate to a controllable fixture. Through a linear actuation of the clamps, the membrane stretches. An early example of this is found in Leung et al. (1977). They used purified elastin membranes from bovine aortas on which to grow cells. The membranes were then stretched using a motor which was coupled to a support frame holding the membrane in place. They used their system to show an increase in DNA synthesis in rabbit aortic smooth muscle cells as a result of 48 hours of cyclic stretching.

There have been many clamp based methods for stretching membranes and some of which are described in detail in the reviews mentioned above. There is still continual developments of new apparatus to stretch membranes using clamp based methods. Arguably, for 3D cell cultures and tissue constructs, clamp methods are better suited than the methods detailed below.

For example, Seriani et al. (2016) build a system where Polydimethylsiloxane (PDMS) substrates are stretched by fixed clamps. The system was such that substrates can be inserted into Petri dishes containing cell medium. The machine, however, is large in comparison to the Petri dish. King et al. (2016) similarly constructed a platform which delivered uniaxial stretch for PDMS substrates but only operated on a single substrate at a time. Subramanian et al. (2017) constructed a uniaxial tensile machine which stretched silicone loading chambers. The system allows for four chambers to be stretched at any given time but also allows for stretching 3D collagen structures.

Common to almost all fixed clamp systems is a lack of throughput. Although they are capable of generating uniaxial and biaxial strain, and despite being better suited and easier to design for live cell microscopy, it is often only one substrate which can be stretched at a time. A central pillar of this thesis is addressing and arguing for the need of high throughput in mechanostimulation experiments in cell biology. Therefore, no further attention is given here to clamp based methods.

1.1.1.2 Vacuum Driven

Vacuum driven strain is associated with those devices which use vacuum pressure underneath a sealed deformable substrate to, usually, generate downward force. The vacuum pressure is such that the deformable substrate stretches against the pressure and translates this as strain to the cells adhered on the top side.

This form of delivery is the basis of the most popular system, FlexCell® , first conceived by Sumpio et al. (1987). The work in this thesis is steeped upon an analysis of this apparatus and is therefore reserved for a fuller description and deeper discussion in Section 1.1.2. Contrarily, and around the same time, Winston et al. (1989) used positive pressure underneath a deformable substrate to bulge the substrate upwards.

Vacuum pressure driven strain is more amenable to throughput. The FlexCell® system utilises both 6 and 12 well culture plates with deformable substrates. As discussed later, although this makes experiments easier, it does not necessary help to increase throughput.

1.1.1.3 Platen Driven

Where vacuum driven strain in the form of FlexCell® is the most popular commercial tool, bespoke, in-house apparatus tend to favour the platen method. Platen driven strain is the category given to those devices which use a mechanical force to push a platen against a deformable substrate. The translation of the substrate strain is therefore translated to cells adhered to the top side of the substrate.

Rosenblatt et al. (2004) created a system where a rotating piston actuates a hollow cylindrical platen pushing down upon a soft membrane. They report membrane stretch reaching up to 60% in their elastomer membranes of 76 μm thickness. The platen in this system, uncharacteristically, pushes down onto the culture side of the membrane. A recent platen based apparatus was constructed with a view to create arbitrary oscillations (Lau et al., 2014). They argue that the BioFlex® system does not provide sufficient control over the rates at which cells go from unstretched to stretched. The group 3D printed bespoke apparatus where six platens push up against the commercial 6-well BioFlex® culture plate. The upward push is generated from a magnetically controlled see-saw type arm. Because the magnetic actuation is controlled with a pulse width modulator (PWM), the waveform of the actuation can be arbitrarily set. On the theme of augmenting existing products, recently Toume et al. (2016) 3D printed bespoke apparatus which, through motorised screws, lowered BioFlex® plates over an array of hollowed platens.

In a move to address the lack of throughput in cell stretching experiments, Moraes et al. (2010) constructed a micro fabricated array based on the work of Schaffer et al. (1994). They constructed 9 by 12 micro platen arrays made from Polydimethylsiloxane (PDMS). The platens are driven upwards against a single membrane by positive pressure. Platens can be calibrated to deliver different strain regimes. Therefore the single cell layer on top of the membrane will have multiple variations of strain delivered depending where they are in the array and so offers a higher throughput in the experimental process. Although each platen can be calibrated to deliver a different stretch regime, and as the authors note, because cells are cultured across a single membrane, paracrine communication between cells over different platens may confound results.

A criticism of any platen driven device is the existence of contact between the stretching mechanism and the membrane to be stretched. Despite using lubricants, the contact will never be frictionless and any alterations in the lubrication process will necessarily change the friction dynamics between substrates. If there are deviations, then the strain profile generated by platens will not be consistent and will confound experimental results.

A benefit of platen based methods is a greater ability to deform 3D constructs.

Elsaadany et al. (2017), for example, constructed a system where cells embedded in collagen constructs are deformed between controllable silicone posts. In this way there were able to cyclically strain cells in 3D cultures.

1.1.1.4 Magnetically Driven

Magnetic driven substrate strain is of considerable interest to this thesis. This is the category given to deformation of a substrate by way of magnetic force. Although magnetic forces have been used in biological testing for many decades (Arem and Madden, 1976), it has only been recently where its use as the generator of force has been used in construction for substrate strain delivery.

Fuhrer et al. (2013), for example, created a substrate made of a combination of hydrogel and inert carbon coated metal nano magnets. The nano-magnets are bound to the polymer strands of the hydrogel. Similar to the BioFlex® plates, the membranes are clamped above and below to form a circular well. An electromagnet underneath creates the force to deform the membrane downwards. Strains have not been characterised in this study but the authors claim that force is applied at each polymer strand in the membrane such that all polymer strands will displace in a similar way. Using their apparatus they showed that mesenchymal stem cells were shifted towards a chondrogenic state in cyclicly strained cultures compared to static controls.

The use of magnetic forces by Khademolhosseini et al. (2016) is one which, independently, resembles methodologies developed in oncoming chapters. The authors augmented a BioFlex® plate so that two neodymium disc magnets were placed in the middle of a well, one above the membrane and the other underneath, and held in place by the magnetic attraction between the two. Upon a bespoke electro magnet base, the system, which was named **MACSAT**[1], deforms the membrane through interaction with the electro magnet and the embedded magnets. Quantification using finite element modelling (FEM) analysis suggested the distribution of strain across the membrane was non-homogeneous with a strain range of -4 to 7%. They used their system to show a strain dependent alignment in human umbilical vein endothelial cells as a result of cyclic strain.

The apparatus constructed by Khademolhosseini et al., however, is lacking in throughput. The depiction of their system shows only one of the wells in the 6-well BioFlex® plate being used. It is likely that this is because multiple electromagnets acting on the same 6-well plate would have undesirable interactions both with each other and consequently with magnets in the BioFlex® plate.

In a recent study, Harshad et al. (2016) constructed a device where magnets are used to stretch a membrane along a single axes and in plane. The permanent magnet is embedded in a PDMS device constrained at one end. Theoretical analysis in a separate study (Kamble et al., 2016) show the distribution of strain to be non-homogeneous.

[1] As well as methodologies resembling those developed in this thesis, the name given to their system also resembles the name given to the one here. This is entirely coincidental.

Like the apparatus constructed by Khademolhosseini et al. there are similarities in the methodology Harshad et al. (2016) use for experimental quantification to the methodology proposed in this thesis. The authors exploit this heterogeneity by sampling images from defined points across the membrane. For each image they associate the theoretically calculated strain value at the image position and therefore capture a greater variety of experimental conditions within the same experiment. This is a similar strategy as employed in this thesis.

1.1.2 The FlexCell® System

The apparatus discussed in the previous section is only a subset of those developed over the last 40 years. Focus is instead diverted to the most popular of those used for cell stretching experimentation.

The FlexCell® system has cornered the market. This is perhaps attributable by the commercialisation and manufacturing of multi well culture plates with deformable substrates which come with a variety of pre-coated surface proteins. Publications which utilise this system are tallied at more than a thousand. The system, however, is not without criticism. This section describes the evolution of the system in preparation for analysis in Section 1.4. This analysis, in part, underpins the justification for the aims of this thesis.

One of the first methodologies to investigate cyclic forces using vacuum driven strain is found in the work of Banes et al. (1985). They used vacuum pressure to deform 60 mm and 100 mm plastic Petri dishes. The pressure deformed the base of the dish by a 1.5 mm deflection generating an average maximum compressive strain of 0.13%. As a general methodology this is an inconsequential amount, however, this is likely the work which spawned the beginning of what is now the industry standard method for conducting mechanical experiments on cells.

A move to culture cells on a deformable membranes with the use of a vacuum was made by Sumpio et al. (1987). Sumpio et al. created 6-well type tissue culture with deformable membrane, where each well is deformed by the vacuum acting on the wells in parallel. This was named the Flex I plate and is schematised in Figure 1.1. In the absence of the vacuum the membrane is in the undeformed state (Figure 1.1(a)). As the vacuum is slowly increased, so that the underside of the membrane is in negative pressure, the membrane deforms downwards as depicted in Figure 1.1(b).

Gilbert et al. (1994) first conducted finite element modelling (FEM) on this initial, 2.1 mm thick membrane to understand the distribution of strain caused by the vacuum. They modelled the membrane as a incompressible, neo-hookean material with a Mooney-Rivlin strain energy function, and an elastic modulus of around 600 kilo Pascals (kPa). They don't, however, provide justification for why this value was chosen. Their results indicate that for the thick membrane schematised in Figure 1.1, the distribution of radial strain is non-homogeneous for a negative pressure of 22 kPa. They show the presence of a gradient of strain (itself non-uniform) ranging from 0% at the center of the membrane

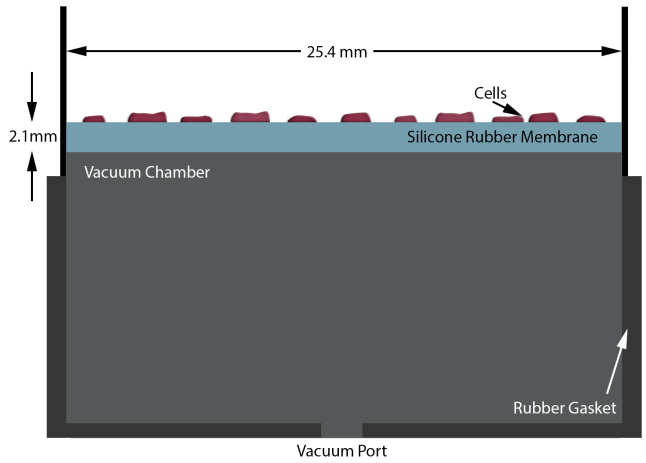

(a) Undeformed

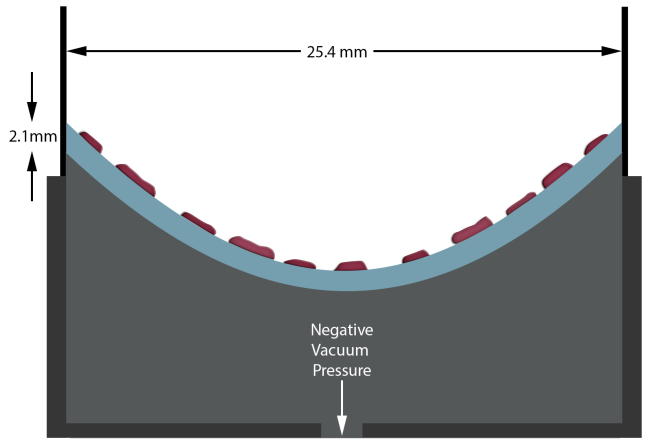

(b) Deformed

Figure 1.1
Schematic of Flex I Stress Unit using Flex I plates adapted from Sumpio et al. (1987) and Gilbert et al. (1994). Within a vacuum chamber sealed with a rubber gasket, negative vacuum pressure (the removal of air) deforms a flexible membrane. The stretch caused by the deformation is translated to cells cultured and adhered on-top of the membrane.

to a strain of 25% at a radial distance of 10 mm from the center.

Tools available at the time for cellular quantification generally relied upon population averaging techniques. For example, in early experiments much focus was given to the effect of cyclic strain upon proliferation of cells. Typically to assess proliferation researchers would either count the cells or use a ^{3}H-thymidine incorporation assay to measure DNA synthesis. Both of these methods however ignore the position of the cell on the membrane. Since strain analysis had shown that not every cell can be said to have experienced the same stimulus on the Flex I plate, quantification using popula-

tion averaging methods cannot be robust. Because of this, a heterogeneous strain is, understandably, far from ideal.

Despite the confirmed strain heterogeneity of the Flex 1 plates, a number of papers in the 1990's instead found a way to exploit it. In a Flex I study of the effect of stretch upon the proliferation of Bovine Aortic Endothelial Cells (BAEC), Li et al. (1994) selectively seeded cells either in the central region of a Flex I well or in the peripheral region. In this way they exploited the heterogeneous delivery of strain across the membrane by discretising it into Two distinct regions: the central region where strain ranges from 0-7%, and the peripheral where the range is 7-25%. Through performing binary experiments with cells either in the center or periphery, they showed the BAEC's proliferated at a greater rate in the central region than cells in the periphery. This 'fencing' method is also seen in the subsequent studies of Basson et al. (1996), Mills et al. (1997) and Sumpio et al. (1998).

Although the utilisation of heterogeneity is arguably more sensible than ignoring it, the range of strain included on each side of the fence is high. Considering that in Rat Aortic Smooth Muscle Cells (RASMC) a 5% stretch is considered 'normal' whereas 15% is 'pathological' (Qi et al., 2010), as a method, the large strain ranges in the fencing method could obscure any meaningful biology.

As well as analysing the Flex I system, Gilbert et al. (1994) also conducted analysis for a thinner membrane with a thickness of 0.5 mm. The results of the thinner plate indicated a much more homogeneous distribution of strain when compared to the thicker plate.

It is unsurprising that the Flex I system evolved towards a more homogeneous system. With patents filed under the assignee *FlexCell International Corporation*, the company marketed the BioFlex® culture plate together with a vacuum system designed to produce homogeneous, in plane-strain. Quite cleverly, they combined the vacuum driven strain method with a platen design. A solid post was placed under each membrane for the membranes to deform over. The addition of this post was to address a need for in plane, homogeneous strain. This is schematised in Figure 1.2. The deformable membrane of the BioFlex® culture plate is 35 mm in diameter with a thickness of 0.5 mm - both thinner and larger in area than its Flex I counterpart. Given this is now a contact strain system, as with all platen systems, a layer of lubricant is required between the post and the membrane. The vacuum deforms the membrane around the post to, in theory, stretch the membrane equibiaxially to generate a radially symmetric, homogeneous in-plane stretch over the surface of the post. Like the Flex I plates, each BioFlex® is in 6-well tissue culture format and the FlexCell® system is capable of deforming four BioFlex® plates at a time. Each well, however, can only be prescribed the same strain regimen as the other wells. In recent years the company also released a 24-well format of the BioFlex® plates, however, like the 6-well counterparts, and what is here considered a great limitation, each well will only deliver the same strain parameters across all the plates.

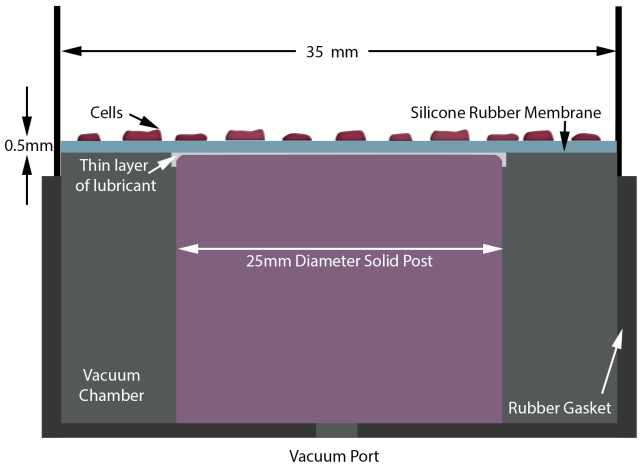

(a) Undeformed

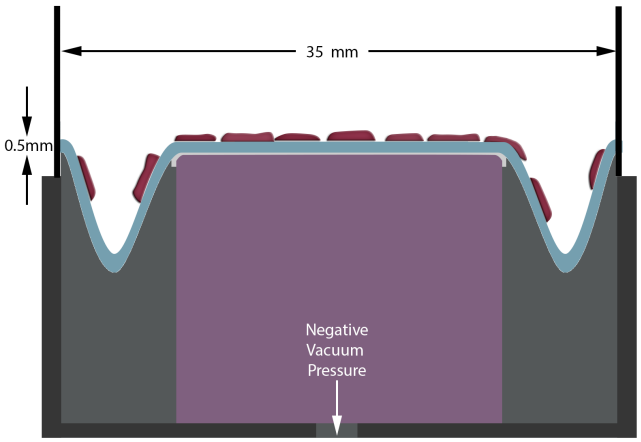

(b) Deformed

Figure 1.2
Schematic of FlexCell® Stress Unit using BioFlex® plates. Within a vacuum chamber sealed with a rubber gasket, negative vacuum pressure (the removal of air) deforms a flexible membrane over a solid post (platen). The stretch caused by the deformation is translated to cells cultured and adhered on top of the membrane such that the region above the post stretches in plane with biaxial strain.

The system can be purchased with different sized loading posts - 25, 28 or 31 mm diameters. The minimum and maximum strains achievable are dependent upon the post diameter. According to the FlexCell® user manual the minimum and maximums are 0.08-21.8%, 1-15.9% and 0.8-6% for the 25, 28 and 31 mm posts, respectively.

The FlexCell FX-5000 Tension System – the latest in a long line of products – is quoted for just over €40,000. The 6 well BioFlex® plates are sold separately and retail for around €30 per plate depending on surface protein pre-treatment. The coatings

available are amino, collagen type 1, collagen type 4, elastin, ProNectin and laminin. Untreated BioFlex® plates are also available for €26 per plate.

FlexCell® has for over a decade dominated the field in terms of mechanical loading of cells. This is demonstrated by the 1000 plus publications returned using Google Scholar with the search terms '*BioFlex FX Tension*'[2]. Given this, a deeper analysis and critique of the FlexCell system is discussed later in Section 1.3.

1.1.3 Heterogeneous Strain

The transition made by the company behind FlexCell® from a heterogeneous strain delivery to something which they claim is in general homogeneous is important to this thesis. Despite this move allowing for easier and more robust experimental protocols, there are instances in the literature where a heterogeneous strain delivery is instead sought.

Acknowledging that *in vivo* tissues are exposed to a wide range of non-uniform mechanical loads, Balestrini et al. (2010) investigated the effect of strain gradients across a substrate cultured with dermal fibroblasts. The group augmented the FlexCell® system in two ways. Firstly, they affixed a rigid glass coverslip onto the middle of the cell culture side in BioFlex® wells. When the membrane deforms over the post in the FlexCell® system, the central fixture causes a non uniform distribution of strain across the membrane. Despite the FlexCell® system only being capable of delivering the same strain to each well, based on theoretical modeling conducted by Mori et al. (2005), Balestrini et al. included a retrofitted device to adjust the strain in each well regardless of the vacuum pressure being the same for each well. An annular insert was placed around the loading post of the FlexCell® system. This insert limits the distension of the membrane caused by the vacuum. The height of this insert therefore directly affects the levels of strain on the membrane above. This allows for parallel strain experiments within the same BioFlex® plate and greatly enhances the throughput of the FlexCell® system. Using microscopy images taken at defined regions along the radius of the membrane, they showed a preferential alignment of dermal fibroblasts where prevalence was seen in certain regions of the membrane.

The retrofit used to increase throughput is not itself without issues. As the authors themselves note, annular inserts change the waveform of the oscillation period. Cyclic strain which was programmed to be sinusoidal becomes more square as the height of the inserts increases. As has been alluded to by Lau et al. (2014) and Leung et al. (1977), the waveform should be a tunable experimental parameter in and of itself. Therefore the insert method of increasing throughput results in diminished control of another parameter: strain period waveform.

Richardson et al. (2011) was similarly interested in the effect of a strain gradient rather than uniform strain. They constructed a motorised platen based system to push down upon a circular membrane. Based on either creating a circular hole in the center of

[2]Conducted in December 2016

the membrane or, similar to Balestrini et al. (2010), a central fixture, they were able to generate a non-uniform, radially dependent strain distribution across a membrane. Dependent on the geometry of the fixture or hole, a variety of strain patterns and variations were achievable.

The studies mentioned here are interesting for two reasons. Firstly, they purposely generated a non-uniform strain distribution in their experiments and secondly, this was done by augmenting BioFlex® plates. The methods employed in this thesis follow a similar suit.

1.2 FlexCell® Usage in Literature

This section reviews some of the literature surrounding FlexCell®. Two biological phenomena which this thesis utilises as 'testing paradigms' are described. The literature itself is vast, and so the first part of this section presents a meta analysis of the literature.

1.2.1 Meta Analysis

When querying Google scholar for literature relating to FlexCell® the volume of results is such that a full analysis is beyond the scope of this project. However, a meta analysis is performed on publication titles to illuminate the size of the field.

The open source software *Publish or Perish*[3] was used to extract the meta data of all publications available by Google Scholar where titles and abstracts include the words 'flexcell' and 'strain'. This generated 3646 entries spanning back to 1990. This list was further filtered to include only the publication titles which included any of the keywords 'mechanotransduction', 'strain' or 'stretch'. This filtered list included 1176 entries.

Figure 1.3(a) shows these publications stratified by year beginning 1990 – the year in which FlexCell® became a commercial product – to February, 2017 – the date the meta analysis was conducted. There is a linear increase in publications from 1990 with a peak in 2014 where nearly 100 publications were released. This steady gradient demonstrates the increasing popularity of FlexCell®. If the trend continues then the expectation is another large release of publications by the end of 2017. This plot suggests that although the technology is dated, it is incumbent. Therefore, discussion and critique of the system is still justified.

To explore the span of biological topics which are associated with FlexCell®, the title of each publication was analysed and visualised as a word cloud plot using **Wolfram Mathematica**. The titles were split by word into a single list. From this list specific key words were removed – for example, prepositions and erroneously printed words. A full list of the removed keywords is presented in Appendix B.1. Figure 1.3(b) shows the 100 most common words from this list where word size is proportional to frequency. This

[3] Ann-Will Harzing: https://www.harzing.com/resources/publish-or-perish

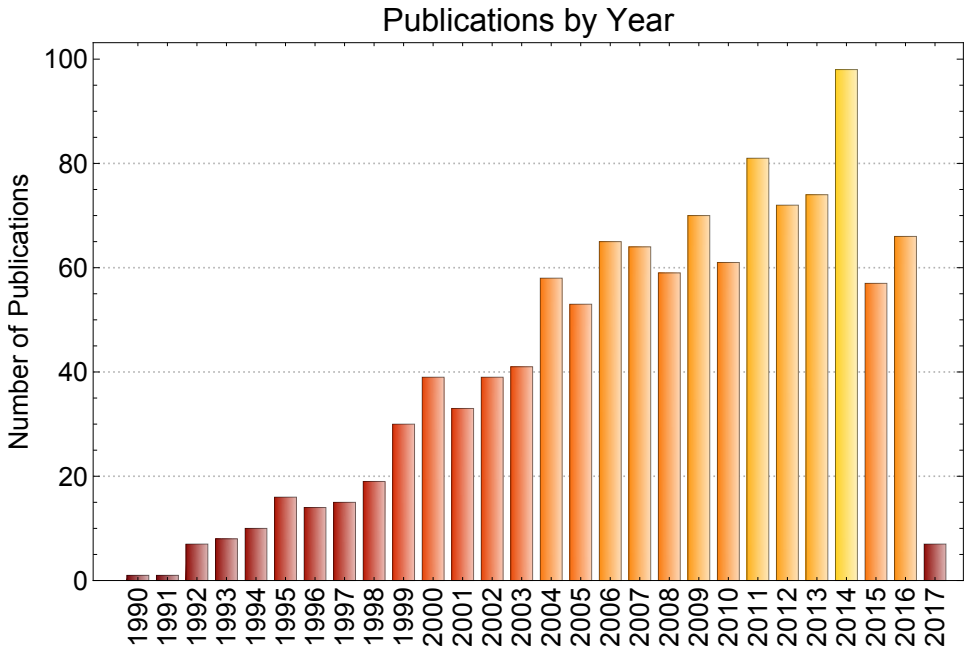

(a)

(b)

Figure 1.3

High Level Literature Review of FlexCell® extracted from *Publish or Perish* and further filtered using *Wolfram Mathematica*. (a) shows the number of publications released each year where either the title or abstract contain the words 'flexcell' and 'strain'. (b) shows a word cloud analysis of the words used in these titles to illuminate the biological fields investigated using FlexCell®.

analysis provides an informal guide to the biological areas that FlexCell® has been most used in investigation of.

As would be expected by a stretch inducing apparatus, biological focus has been predominantly in human smooth muscle and endothelial tissue with protein and gene expression being a strong area of study. A further predominant area of study is both the differentiation and proliferation of cells. The latter of these is a topic of interest for this thesis.

Figure 1.3(b) shows more than just the main areas of study using FlexCell®, but also describes the variety of biological phenomena which are being elucidated by FlexCell®. When coupled with the increasing number of publications each year using this system, a discussion of the validity, and operational use of FlexCell® is both warranted and needed; when much of the biological information is derived using this system, we should be asking whether the information is valid. Importantly, given the cost of the system, we should be asking whether it could be made better.

1.2.2 Phenotypic Modulation

Section 1.2.1 clearly indicates the vast biological space that FlexCell® is used within. For this thesis, there are two biological areas of interest: modulation of proliferative phenotypes and plasmid transfection efficacy. These two areas are reviewed below.

1.2.2.1 Inhibition/Stimulation of Proliferation

The proliferative response of cells by cyclic strain is an important foundational layer to this thesis and a niche in which the ideas of this thesis grew. This section discusses the literature within this subject employing the FlexCell® system as an investigative tool. The inhibition and stimulation of proliferation in a variety of cell types has been demonstrated using the FlexCell® systems (with both the Flex I and BioFlex® plates) over the last 2 decades.

The first study which investigated a connection between cyclic strain and the growth rate of cells is found in Sumpio et al. (1987). Using the newly developed Flex I system the group subjected BAEC cultured on collagen 1 coated plates to 10% stretch at a frequency of 0.05 Hz. Over a period of 7 days, and against a static control, they showed a comparative increase in cell number and concluded the induction of a proliferative phenotype as a result of cyclic stretch. This was shown again several years later by Li et al. (1994). However, the cell seeding density, strain frequency and duration of the experiment differed.

Woodell et al. (2003), using the then recently released BioFlex® system, also investigated the proliferative response of BAEC. Contrary to the studies of Sumpio et al. the authors instead showed an inhibition of proliferation in response to cyclic stretch. Again, however, the experimental parameters involved greatly differ: a strain frequency of 0.1 Hz or 0 Hz (indicating static stretch), 4% stretch and an experiment duration of 4 hours. Cell density was calculated through trypsination and counting and DNA synthesis was

measured through protocols utilising ^{3}H-thymidine incorporation. Both measurements indicated inhibition of proliferation both in the 4% static and dynamic stretch regimes.

Because the Woodell et al. (2003) experiment was a question of cell number and proliferation, the group performed a series of optimisations so that both experimental and control plates would have the same number of cells at the final time point. Therefore, initial cell seeding was different for the control case. In light of this, it is difficult to compare this result to other studies. For comparison of experimental parameters for the above studies these experiments are stratified in the first four rows in Table 1.1.

The aforementioned studies were conducted on aortic endothelial cells. In the aorta, the inner layer (the intima) is formed of endothelial cells and is the surface in direct contact with the pulsatile flow of blood. The middle layer (the media), contains a network of smooth muscle cells which provide contractile strength to resist the pressure pulses against the intima. The intima is also the layer which vasoconstricts to maintain physiological homoeostasis. Many subsequent studies were conducted on aortic smooth muscle cells. However, just as with the studies using endothelial cells, studies using aortic smooth muscle cells also at times conflict.

Sumpio and Banes (1988), alongside their study of BAEC also studied Porcine Aortic Smooth Muscle Cells (PASMC). Using the Flex I system and over 7 days they subjected these cells to 24% stretch at a frequency of 0.05 Hz. Through cell counting and ^{3}H-thymidine incorporation they showed an inhibition of proliferation over the duration of the experiment. Using the same apparatus, Mills et al. (1997) instead showed a stimulation of proliferation in Bovine Aortic Smooth Muscle Cells (BASMC) and Li et al. (1997) demonstrated a stimulation of proliferation in Rabbit Aortic Smooth Muscle Cells (RbASMC). Experimental parameters, however, differ between studies as displayed in Table 1.1.

At the turn of the century, the BioFlex® system replaced the Flex I system. With this system Chapman et al. (2000) and Hipper and Isenberg (2000) demonstrated an inhibition of proliferation in both Rat Aortic Smooth Muscle Cells (RASMC). These studies were conducted with different experimental parameters: different cell seeding densities, strain frequencies, strain magnitudes and experiment duration. Schad et al. (2011) demonstrated a similar result in RASMC using the BioFlex® system in the absence of the loading post (see Section 1.1.1).

Using RASMC and with a similar set up as the studies above, Qi et al. (2010) discovered two values of stretch within the same study where inhibition and stimulation of proliferation were observed, respectively. They exposed cells which had been serum starved for 24 hours to 5 and 15% stretch at a frequency of 1.25 Hz. These stretch values were chosen as the former is understood to be physiologically relevant (Asanuma et al., 2003) and the latter pathologically relevant (Morrow et al., 2005). Using the BrdU Proliferation ELISA, they showed, compared to a static control, an inhibition of proliferation when stretched at 5% and a stimulation of proliferation when 15%.

That there must be a value in between 5 and 15% stretch where the proliferative

phenotype of the cells switches from inhibitory to stimulatory is an important result for the arguments of this thesis. All of the studies cited here tend not to titrate the stretch regime but instead choose one or two values to test. To mitigate the potential for a switching point in phenotype behaviour many more stretch values should be evaluated. The high cost of consumables in FlexCell® may be a reason for the absence of this.

Many other studies using the Flex I stress system have also investigated proliferative effects of cyclic strain in a variety of cell types. Predel et al. (1992) showed a stimulation of proliferation in Human Saphenous Vein Smooth Muscle Cells (HSVSMC); Yang et al. (1993): stimulation in Human Coronary Artery Smooth Muscle Cells (HCASMC); Wilson et al. (1993): stimulation in Rat Vascular Smooth Muscle Cells (RVSMC); Smith et al. (1994): stimulation in Canine Tracheal Smooth Muscle Cells (CTSMC), and Basson et al. (1996): stimulation in CACO-2 cells.

All of the studies mentioned above are stratified by experimental parameters in Table 1.1. From doing so, it is clear that the differences in experimental parameters (cell type, frequency, percentage strain) make it nearly impossible to combine information from the literature. This is characteristic of many studies involving FlexCell®. Arguably, what little throughput there is in FlexCell® experiments is hindered further by a lack of consistent experimental protocol.

1.2.2.2 Plasmid Transfection

Alongside proliferation, another biological area this thesis has interest in is stretch associated increases in plasmid transfection efficacies.

Taylor et al. (2003) investigated whether cyclic stretch had an effect on the transfection efficiency of A549 cells (a cell line derived from a human lung epithelial carcinoma). They used FlexCell® to subject A549 cells to 10% stretch at 1 Hz on laminin coated BioFlex® plates and subsequently transfected the cells with a luciferase expressing plasmid using lipolex. They discovered that with as a little as 30 minutes of stretch immediately after transfection there was a significantly greater expression of luciferase 24 hours post transfection than in unstretched controls. A luciferase expression increase of 10 times compared to unstretched controls was observed.

The same group have conducted several studies exploring the mechanisms behind this. Geiger et al. (2006) suggested that this increased efficacy is in part caused by cytoskeletal reorganisation of both the microtubule and microfilament network as a direct consequence of cyclic strain. Lam and Dean (2008) used *in situ* hybridisation methods to examine the location of plasmids as well as multiple transcription factors associated with plasmid nuclear entry. They found a non-uniform distribution of plasmid focussed around the nucleus as well as increased levels of transcription factors. Comparatively, in non stretched controls the distribution of plasmids throughout the cytoskeleton was relatively uniform. Later, Eldib and Dean (2011) suggest that an additional reason for the enhanced gene transfer could be both increased levels of acetylated microtubles responsible for directed active transport as well as a reduction in cytoplasmic stiffness

Cell Type	Quie.L.	ρ ($x10^3$)	Hz	%	Time	Method	Fence	Surf.	Phenotypic Output	Reference
BAEC	0	96	1.6	0-7/7-25	5	Flex I	Yes	collagen 1	(Strain Dependent) Stimulation of Proliferation	Li et al. (1994)
BAEC	0	10	0.05	10	7 days	Flex I	No	N/A	Inhibition of Proliferation	Sumpio et al. (1987)
BAEC	0	⋆	0	4	4 hours	BioFlex® . w. Post	Yes	type 1 collagen	Inhibition of Proliferation	Woodell et al. (2003)
BAEC	0	⋆	0.1	4	4 hours	BioFlex® . w. Post	Yes	type 1 collagen	Inhibition of Proliferation	Woodell et al. (2003)
BASMC	0	96	1	0-7/7-25	3-5 days	Flex I	Yes	type 1 collagen	(Strain Dependent) Stimulation of Proliferation	Mills et al. (1997)
PASMC	N/A	20	0.05	24	7 days	Flex I			Inhibition of Proliferation	Sumpio and Banes (1988)
RbASMC	24	1 - 5	0.5	5	1	Flex I	No	collagen 1	Stimulation of Proliferation	Li et al. (1997)
RbASMC	24	10 - 50	0.5	10	1	Flex I	No	collagen 1	Stimulation of Proliferation	Li et al. (1997)
RbASMC	24	10 - 50	0.5	20	1	Flex I	No	collagen 1	Stimulation of Proliferation	Li et al. (1997)
RbASMC	24	19 - 77	0.5 0.5/1.5s	15		Flex I	No	type 1 or type 4 collagen	Stimulation of Proliferation (detected sooner in high serum than low serum).	Birukov et al. (1995)
RASMC	48	50	1	10	Up to 5 days	BioFlex® . w. Post	No	type 1 collagen	Inhibition of Proliferation	Chapman et al. (2000)
RASMC	72	100	0.5	5	2 days	BioFlex® . w. Post	No	Coating Independent	Inhibition of Proliferation	Hipper and Isenberg (2000)
RASMC	24	300	1.25	5	1	BioFlex® . w. Post		N/A	Inhibition of Proliferation	Qi et al. (2010)
RASMC	24	300	1.25	15	1	BioFlex® . w. Post		N/A	Stimulation of Proliferation	Qi et al. (2010)
RASMC	24	65	1	‡	2	BioFlex® w/o. Post	No	type 1 collagen	Inhibition of Proliferation	Schad et al. (2011)
CACO-2	0	18	0.05	0-7/7-25	24	Flex I	Yes	type 1 collagen	(Strain Dependent) Stimulation of Proliferation	Basson et al. (1996)
CTSMC	N/A		0.5	27-30	5 days	Flex 1	No	type 1 collagen	Stimulation of Proliferation	Smith et al. (1994)
HiMSMC	48	100	1	25	1	Flex I	No	type 1 collagen	No Significant Change	Predel et al. (1992)
HCASMC	48	100	1	25	1	Flex I	No	type 1 collagen	Stimulation of Proliferation (Compounded by PDGF)	Yang et al. (1993)
HSVSMC	48	100	1	25	1	Flex I	No	type 1 collagen	Stimulation of Proliferation	Predel et al. (1992)
RVSMC	0	Until Confluency	1	†	2	Flex I	No	type 1 collagen	Induction of Proliferation (inhibited by PDGF Antibodies)	Wilson et al. (1993)
HADSC	N/A	Confluency	0.5 for 12 hours/day	5	6	BioFlex® w. Post	No	N/A	Stimulation of Proliferation	Paul et al. (2017)

Table 1.1

Comparison of Parameters in Proliferation Experiments. Column titles provide information on experimental design and results. **Quie.L.** is the length of time cells were serum starved before experimentation. ρ ($x10^3$) is the cell seeding density. **Hz** and **%** are the strain parameters frequency and stretch percentage. **Time** is the time spend in actuation. **Fence** indicates whether the fencing method was used. **Surf** is the membrane surface coating.

which results in increased diffusion.

These studies use the lung epithelial carcinoma cell line, A549. In a separate study Bryer and Koh (2007) examined the same principles in the skeletal muscle myotube cell line, C2C12; a particular cell line of choice when investigating muscle. On collagen 1 coated BioFlex® plates they subjected cells to 20% strain at a frequency of 1 Hz for 1 hour before transfecting the cells with a luciferase plasmid. They showed a 2.5 fold increase in the expression of luciferase in cells which had been cyclicly strained compared to static controls. Not only this, they show also showed a dependence on this fold increase by strain frequency, magnitude, and time which suggests that a set (or sets) of parameters exist which generate an optimal response.

Regardless of the mechanisms or cell lines, an increase in plasmid transfection efficacy due to mechanical stimuli is a promising development in gene therapy where arguably the safety of viral transfection methods is still of substantial concern. Coupled with potential technologies for *in vivo* delivery of mechanical force, there may be therapeutic potential for spatially targeted gene therapy modalities.

1.2.2.3 Examples of Other Cell Types and Phenotypes

Predominance is here given to examples of stretch related proliferation in smooth muscle and endothelial cells. However, as highlighted by Figure 1.3(b), the study of stretch and cellular behaviour is not limited to these examples.

For example, cyclic strain is implicated in increased expression of collagen synthesis and degradation compounds (Liu et al., 2015), secretion of growth factors (Sumpio et al., 1998; Schad et al., 2011), gene expression (Birukov et al., 1995; Riha et al., 2007), and cellular morphology (Standley et al., 2002; Cha et al., 2006; Liu et al., 2008).

In cardiac biology, the FlexCell® system has also been used to explore stretch related effects. For example, in cardiac myocytes, stretch is associated with hypertrophic and apoptotic responses (Ruwhof et al., 2000; Pimentel et al., 2001), vascular endothelial growth factor release (Seko et al., 1999) and gene expression (Van Wamel et al., 2000) to name but a few. Myocytes derived from human-induced pluripotent stem cells in co-culture with human embrionic stem cell have been shown to proliferate at a significantly higher rate when exposed to cyclic strain compared to without (Tulloch et al., 2011). In efforts to engineer cardiovascular tissue, cyclic strain has been implicated in beneficially enhancing mechanical properties of tissue constructs (Boerboom et al., 2008; Syedain and Tranquillo, 2009).

The mechanobiology field is large and the cell types known to be implicated as influenced by mechanical stretch are far greater in number than mentioned here. The promising results of mechanically conditioning tissue for, in particular, cardiac related purposes is further indicative of the potential gains to be made by having a good general understanding of the relationship between strain and phenotype, with the assumption that more information better informs future studies.

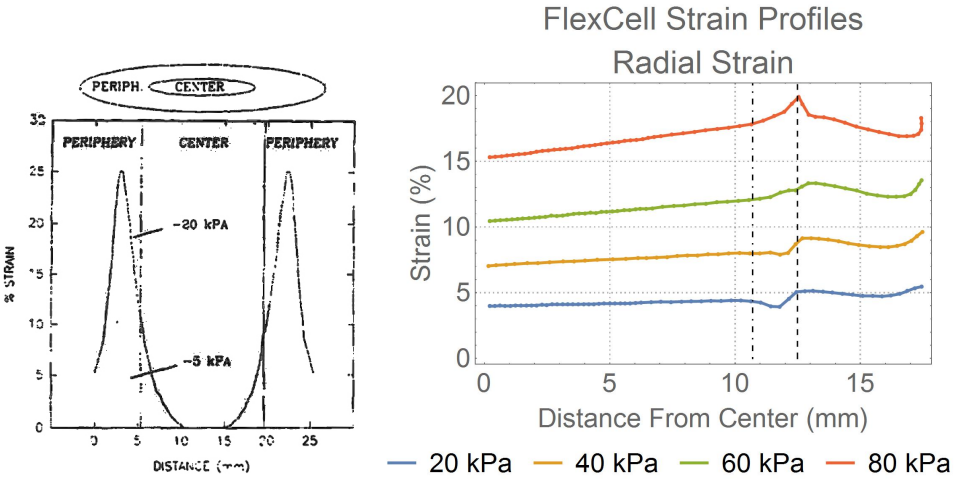

(a) (b)

Figure 1.4

Adapted results of Li et al. (1994) and Vande Geest et al. (2004) giving the inferred relationship between distance from the center and percentage strain. (a) is taken directly from Li et al. (1994) of FEM for the Flex I system. Strain is radially dependent and symmetric. (b) results have been extracted from the original plot of Vande Geest et al. (2004) using the open source software 'Plot Digitizer'. It shows FEM results for four pressures in the BioFlex® system with a 25 mm post. The region to the left of the first dashed line is the membrane which is above the post. The period in between the two dashed lines is the region of the membrane over the fillet region of the post. The region to the right of the second dashed line is the region of the membrane beyond the post.

1.3 Strain Analysis of The FlexCell® System

Given the vast volume of literature on the FlexCell® system, a deeper discussion of the distribution of strain delivered by the system is warranted. Theoretical work presented in Section 1.4 argues that there are inherent problems with the system based on standard experimental use. Here, the history and methodology of analysis of strain distributions is presented for context.

The work of Gilbert et al. (1990) and Gilbert et al. (1994) is the first study of the distribution of strain across the Flex I membranes. In the earlier of the two, Gilbert et al. imprinted, using toner ink, a series of concentric circles onto the underside of a Flex I membrane whilst it was partially cured. They filmed the membrane deforming under vacuum pressure and, with a suitable reference image and armed with a protractor, manually measured quantities from hard copies of the images. This allowed for calculation of strain for each circle. Their results indicated a heterogeneous distribution of strain. Although this method of calculation may now be considered primitive, their result was subsequently backed by the finite element analysis (FEA) in Gilbert et al. (1994).

As previously discussed, Gilbert et al. treated the Flex I membrane as an incompress-

ible, hyperelastic material with a neo-Hookean strain energy function. They assigned the value of $C_{10} = 100$ kPa which corresponds to an equivalent elastic modulus of around 600 kPa. No justification, however, was given for why this value was chosen. The geometry of the Flex I membrane is defined as 25.4 mm in diameter and 2.1 mm thick. Their results, directly reproduced from Li et al. (1994) in Figure 1.4(a) suggest with 20 kPa of negative pressure generating a radial strain ranging between 5% to 25% dependent on radial location on the membrane.

As discussed in Section 1.1, a homogeneous distribution of strain is desired for quantification methods of cell experiments. With this understanding Gilbert et al. also conducted FEA of a measuring 34.5 mm in diameter and 0.5 mm thick. With 46 kPa of negative pressure the membrane produces a relatively homogeneous strain of around 10% but with a sharp increase to around 27% strain a few millimetres from the membrane edge. This theoretical work is likely the foundation for the BioFlex® system.

For the system with the addition of the fixed platen (referred to as the 'post system'), there has been only two FEA studies since the device was patented in 2000. The first and most cited comes from Vande Geest et al. (2004).

In the FlexCell® user manuals only a single strain value per vacuum pressure is given. How these have been calculated is not disclosed. Vande Geest et al. realised that a significant portion of the membrane would be deforming 'off-post' (see Figure 1.2) where the strain is unlikely to be homogeneous. They provided the first theoretical investigation on the spatial distribution across the entire membrane in the post system.

Like Gilbert et al. (1994), Vande Geest et al. treated the (now thinner) membrane as an incompressible, hyperelastic material using the neo-Hookean strain energy function to characterise the material. They conducted uniaxial tensile tests of the membrane together with non-linear least-squares methods to deduce the value of the parameter C_{10}. They determine the value of C_{10} to be 282 kPa for the BioFlex® membrane. This corresponds to an equivalent elastic strain modulus of around 1638 kPa.

Vande Geest et al. (2004) constructed their FEM model as follows. The 17.49 mm radius (0.5 mm thick) membrane sits over a rigid post with a radius of 12.70 mm. The top edge of the post is given a fillet with a radius of 1.778 mm – a value provided by FlexCell®. The lubrication layer between the membrane and the post is represented in the model as a contact friction coefficient equal to 0.03. Membrane edges were prescribed a zero displacement boundary condition to represent the edge of the well. Pressure is applied directly to the underside of the membrane between the membrane edge and the edge of the loading post.

Their results indicate a heterogeneous distribution of radial and circumferential strain across the membrane. An increase in variation of this distribution is seen as negative pressure increases. They demonstrate a notable difference in membrane behaviour between the regions over the post and the regions off the post. Specifically, differences between radial and circumferential strain which suggest the absence of true biaxial strain as claimed by BioFlex® . Their results have been adapted for this thesis in Figure 1.4(b).

For pressure of -80 kPa, the theoretical strain at the center of the membrane is calculated to be 15% and increases to 20% at the edge of the post region before decreasing in the off post region and increasing near the boundaries of the membrane. Compared to the results for -20 kPa of pressure, strain distributions become increasingly heterogeneous when greater strains are programmed.

This analysis provides a major criticism of the FlexCell® system. If strain distributions over the membrane are neither homogeneous or even consistently heterogeneous, then not only is the information generated using this system inaccurate, but also the comparison of results from different programmed strain regimes may not be sound. For example, an experiment comparing the response of cells when stretched at 5% and 20% will actually compare cells stretched roughly at 5% with cells stretched anywhere in a range between 15% and 20%. Not only is this not desirable as a method in cell biology, but any statistical test which doesn't take this into account will produce false p-values and hence generate unsound scientific conclusions.

Chiang et al. (2010) present the second FEM analysis which has been conducted of the BioFlex® system. The group identify a flaw in the method of Vande Geest et al. and attempt to improve the model. They noted that the negative pressure in the FE model was only applied to the portion of the membrane initially exposed outside the post region. In reality, the area which the pressure is applied to would increase as a greater proportion of the membrane stretches over the post. To address this, Chiang et al. developed what they termed an 'adaptive loading algorithm'. This ramps the pressure from 0 to a desired amount in small increments where after each increment the newly exposed membrane is subject to the pressure in the next increment. The group did uniaxial stress-strain measurements, similar to Vande Geest et al. to deduce an elastic strain modulus of 1750 kPa.

Critically, there is no discussion of heterogeneous strain in their FEM results. There is also no indication of how they associate a strain value to a specific pressure load. For example, for 20 kPa of pressure, their model suggests a strain on the membrane of 3%; given that the distribution of strain is heterogeneous, how this value is calculated is not disclosed. The aim of their work seems to be to generate a pressure-strain formula which is dependent on the radius of the membrane and post, membrane thickness, and elastic strain modulus with free parameters fit by regression analysis of multiple FEMs. Such may be a useful tool if the distribution of strain is homogeneous. However, under the assumption the Vande Geest et al. data (herin referred to as 'VG Data') is true, the theoretical analysis presented in the next section arguably negates the value of deducing a formula of this kind.

Discrepancies between theoretically measured strains and what the FlexCell® software programs have been well established. Colombo et al. (2008), in particular, using empirical strain measurements, showed significant differences from the FlexCell® user programmed strain, the strain reported back by the software, and empirically measured strain when frequency is varied. Woodell et al. (2003) showed changes in measured strain over time,

initially lower than the software predicted but eventually exceeding predicted values over 5 days. Colombo et al. argue that user calibration to set the pressure-deformation equation (the central component of the programming for the FlexCell® vacuum) is needed for each experiment in order to improve comparability of studies.

The FlexCell® system is still used by many and as discussed is the backbone for at least 1000 publications. Given 1) strain distributions are not as homogeneous as initially thought, and 2) programming the system to deliver a strain regime may not do so without further calibration, it is reasonable to be asking whether the methodology is valid.

1.4 A Theoretical Exploration on the Validity of FlexCell®

Section 1.3 discussed efforts to understand the distribution of strain across BioFlex® membranes. This information has only ever been used in the literature as a description of the FlexCell® system. Given a heterogeneous strain distribution, the question of the validity of using population averaging quantification (for example, ^{3}H-thymidine incorporation, BrdU ELISA's, trypsination and cell counting) has never been asked. In this section, using data extracted from Vande Geest et al. (2004), a small, but novel, analysis is conducted to assess the FlexCell® system. This analysis is based on two assumptions:

1. The strain profiles across BioFlex® membranes generated by Vande Geest et al. (2004) are true.

2. Arbitrary strain-phenotype (S-P) relationships of a fictional cell type can be adequately defined.

The strategy is to use pre-defined S-P relationships together with the VG data to build *in silico* experiments which are analogous to the current usage of FlexCell® where cell population are averaged for behaviour. Because the S-P relationships are pre defined, we can quantitatively evaluate the degree to which the *in silico* experiments are able return the original S-P relationship. This analysis is designed to illuminate the validity of experiments in literature.

1.4.1 Methods

An interpolating function is used in *Wolfram Mathematica* to construct functions for each of the Vande Geest et al. strain curves in Figure 1.4(b) where for any radial distance from the center of the membrane the strain is given. This information is used to construct 2-dimensional distribution maps of strain across the membrane for each pressure value. The interpolated mean values are calculated as being the spatial mean value of these maps. That is, if the maps were broken into equal 1 mm square segments, the value of strain in each is totalled and averaged across all square segments.

Two types of hypothetical S-P relationship are defined. The first assumes a continuous relationship between strain and phenotype where transitions between inhibition to stimulation are possible. Such a model may be justified based on the work of Qi et al. (2010) who used FlexCell® to show a switching of inhibition to stimulation of proliferation in smooth muscle cells when stretched at 5% and 15% respectively. In this case a function is prescribed of the form:

$$r_1(s) = \frac{s}{10} \times \sin\left(\frac{\alpha s}{\beta}\right), \tag{1.4.1}$$

where the dependent variable, s, is strain, $\alpha \in \{-1, 1\}$, $\beta \in [3, 10]$ and $\{\alpha, \beta\} \in \mathbb{R}$. Figure 1.5(a) displays this function for various choices of α and β. The y-axis value represents an arbitrary metric describing phenotype activity relative to an unstretched control. For example, if the phenotype of interest was proliferation, then $r = 1$ would represent a 1 fold increase in proliferation. Equally, an $r = -1$ represents a 1 fold decrease. The function imposes that at $s = 0$ there is no change in phenotype compared to control.

The second type of S-P relationship we consider is one which is discontinuous. This type of relationship assumes the requirement for specific strains to be reached in order for a change in the phenotypic response to occur. It is defined through the piecewise function $r_2(s)$:

$$r_2(s) = \begin{cases} 0, & 0 \leq s < x_1, \\ \dfrac{y_2(x_1 - s)}{x_1 - x_2}, & x_2 \leq s \leq x_2, \\ y_2, & x_2 < s < x_3, \\ \dfrac{s(y_2 - y_4) - x_4 y_2 + x_3 y_4}{x_3 - x_4}, & x_3 \leq s \leq x_4, \\ y4, & s > x_4, \end{cases} \tag{1.4.2}$$

where $x_1 \in [0.5, 10]$, $x_2 \in [x_1 + 1, x_1 + 10]$, $x_3 \in [x_2 + 1, x_2 + 7]$, $x_4 \in [x_3 + 1, x_3 + 10]$, $y_2 \in [-1, 1]$, $y_4 \in [-1, 1]$ and $\{x_1, x_2, x_3, x_4, y_2, y_4\} \in \mathbb{R}$. Figure 1.5(b) shows function $r_2(s)$ plotted for random parameters choices and is interpreted as above. Parameter ranges in Equation 1.4.1 and 1.4.2 were chosen through trial and error.

In silico experiments are conducted by assuming a homogeneous distribution of cells across the membrane. With this, the S-P functions are used to map the behaviour of the cells according to the strain at each particular location in space. The function mapping generates 'phenotype maps' (shown in the first row of Figure 1.6(a) for an example $r_1(s)$). As would be conducted in real experiments, this phenotype map is spatially averaged where this averaged value is associated with the strain regime originally delivered.

The decision of which strain is associated with this averaged response will have an effect on the validity of the result. Three methods of defining this strain value is conducted

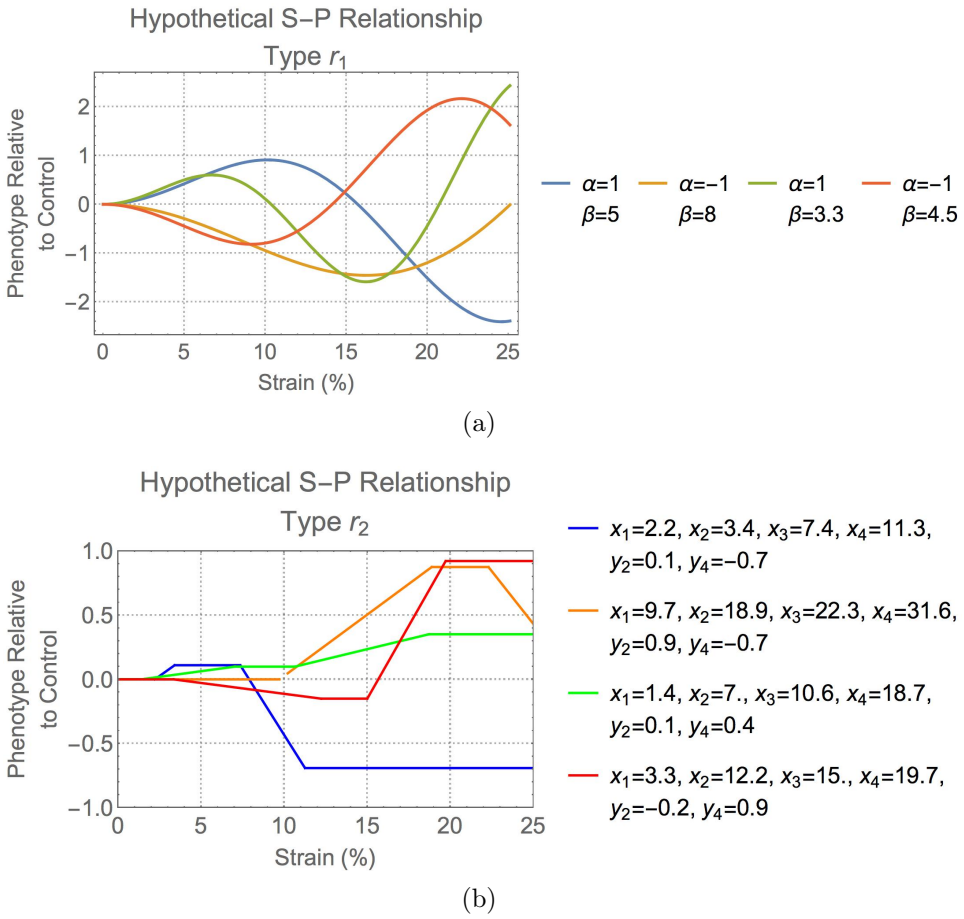

Figure 1.5

Four examples for each hypothetical strain-phenotype (S-P) relationship. (a) Type r_1 relationships are continuous functions which are always 0 for strain values of 0. (b) Type r_2 relationships are piecewise and account for the possibility that strain thresholds must be reached for particular changes in phenotype activity. By randomizing the parameters in each model, different hypothetical $S-P$ relationships can be generated.

as follows: (i) 'FlexCell® ': using the value of strain that the FlexCell® documentation associates with each pressure value, (ii) 'Center': using the value of strain at the center of the membrane – as in Vande Geest et al. (2004), and (iii) 'Interpolated Mean': using the mean value of the strain distributions from Figure 1.4(b) after interpolation. These values are detailed in Table 1.2.

Given the strain phenotype relationship is pre-defined, the error returned in the *in silico* experiments can be assessed by mean square error (MSE). If $s_i = [s_1, s_2, s_3, s_4]$ are the proscribed strain values for each applied pressures 20, 40, 60, 80 kPa, respectively, and $\bar{p}_i = (\bar{p}_1, \bar{p}_2, \bar{p}_3, \bar{p}_4)$ are the averaged responses from each phenotype map, then, for each experiment, the MSE is defined as

$$MSE = \frac{1}{4}\sum_{i=1}^{4}(\bar{p}_i - r(s_i))^2. \tag{1.4.3}$$

Table 1.2
FlexCell® Strain Regime Values Depending on Method. Values of strains are associated with the averaged response for each pressure value depending on method of calculation.

Pressure (kPa)	Strain (%)		
	(i) FlexCell®	(ii) Center	(iii) Interpolated Mean
20	3.7	4	4.4
40	9.2	7	8
60	15.6	10.5	11.7
80	20.2	15.2	17

To generate distributions of MSE, stochastic re-sampling is run 10,000 times for both $r(s)$ functions and for each associated value of strain. This involves for each step:

1. Random assignment of the parameters detailed for each of the equations 1.4.1 and 1.4.2 based on their defined constraints.

2. Calculating the resultant phenotype mean after applying the randomly generated $r(s)$ to each of the four strain distributions.

3. Calculation of the MSE for each strain value in Table 1.2.

4. Repeat.

Accuracy of the FlexCell® system and methodology is therefore based on comparisons of MSE distributions.

1.4.2 Results and Discussion

Figure 1.6 illustrates a single step in the stochastic resampling process for the r_1 type relationship with $\alpha = 1$ and $\beta = 5$ (Figure 1.6(d)). The mapping of strain distribution to phenotype distribution using the S-P function is displayed by density maps in the second row of Figure 1.6(a). The greater the heterogeneity in strain distribution the greater it is in the phenotype. This is shown more formally in the distributions in Figures 1.6(b) and 1.6(c). Here, the spatial maps are discretised into 1 mm squares and the phenotype values in each square obtained from the distribution. The phenotype distribution for -80 kPa ranges from 0 to -1.5 but with a mean located around -0.5. Figure 1.6(d) displays the results of associating each set of applied strain values (FlexCell®, Center Strain, Interpolated Mean) with the mean phenotype distribution overlaid on the true relationship. It is immediately clear that, if the results of Vande Geest et al. are held to be true, the values of applied strain that the FlexCell® system proscribes for 20, 40, 60 and 80 kPa of pressure do not represent the true relationship when the cellular phenotype response is averaged. For higher levels of pressure the predicted relationship is skewed to the right. Similarly, when the central value of strain is associated with the mean phenotype (values used by Vande Geest et al. (2004)), for higher levels of

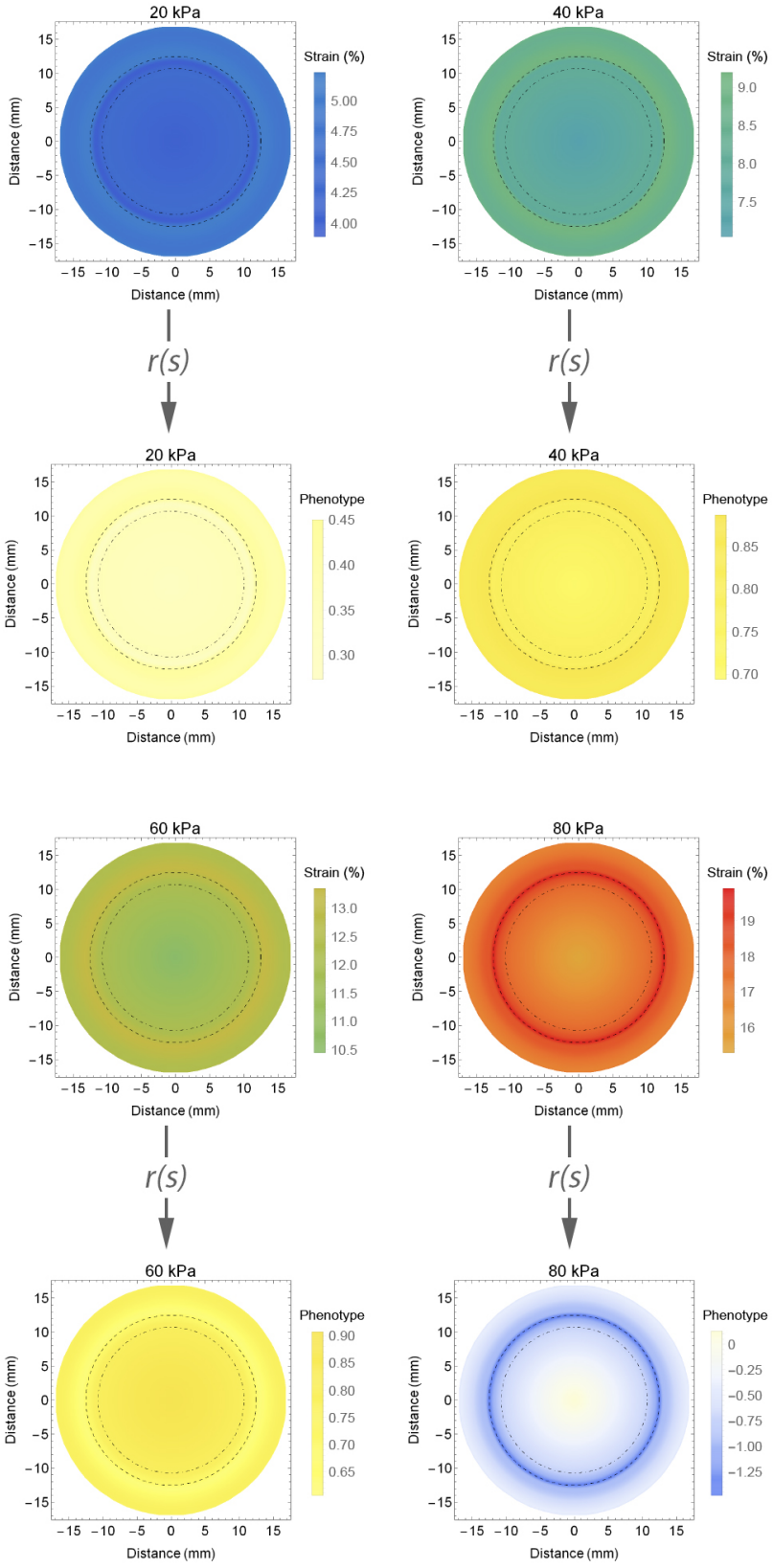

(a) Figure continued overleaf.

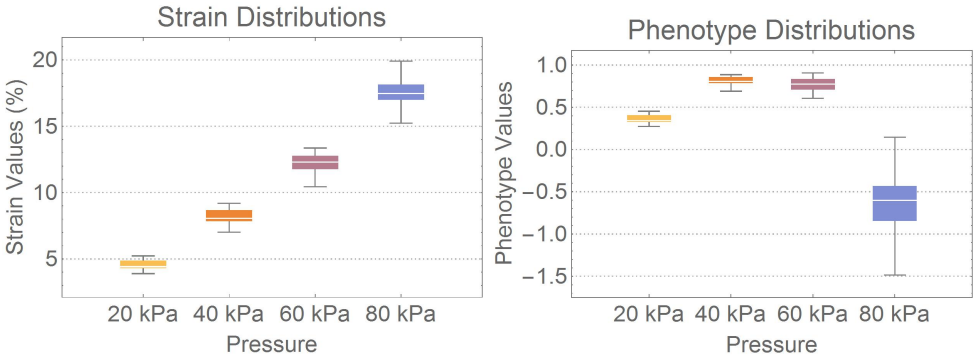

(b)

(c)

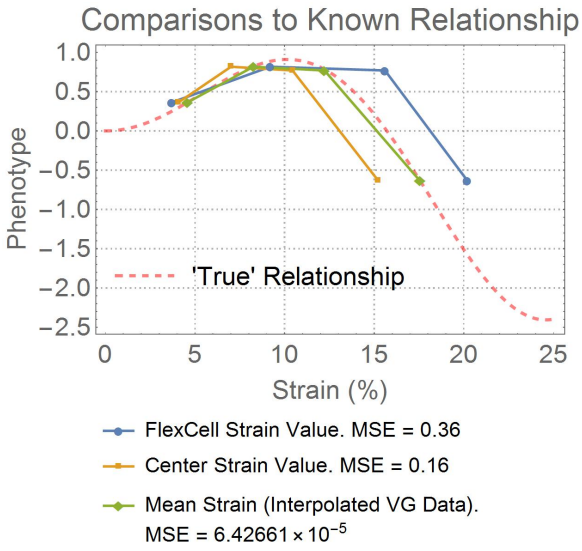

(d)

Figure 1.6

Example of the analysis flow using an S-P relationship governed by $r(s) = s \times \frac{\sin[\frac{s}{5}]}{10}$. (a) shows graphically, the $r(s)$ function being applied to the strain map to generate the resulting phenotype map. (b)-(c) provide the distributions from (a) showing that in this case the spread of phenotype values for 80 kPa is wide. (d) shows the effect of associated different strain values to the mean of the phenotype. MSE values suggest the best association is one which uses the interpolated mean of the strain map.

pressure, the relationship is skewed to the left. However, this discrepancy is overcome when the interpolated mean of the strain is associated with mean phenotype. Use of this strain value results in a strong correlation even at higher pressures. The visual interpretation is corroborated by the MSE values being 0.36, 0.16 and 6.4×10^{-5} for the FlexCell®, Center, and Interpolated Mean values of strain, respectively.

This result is analytically trivial. The region over which the strain is most heterogeneous (80 kPa, 15 - 20% strain) coincides with the S-P relationship being approximately linear. Given the distribution of strain for 80 kPa is roughly normal (Figure 1.6(c)), the mean of the strain will correctly associate with the mean of the phenotype.

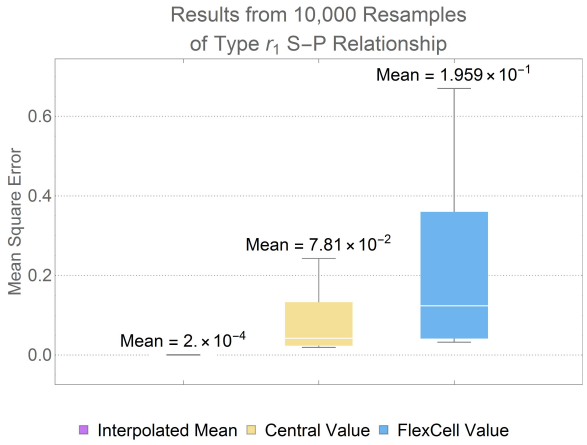

(a)

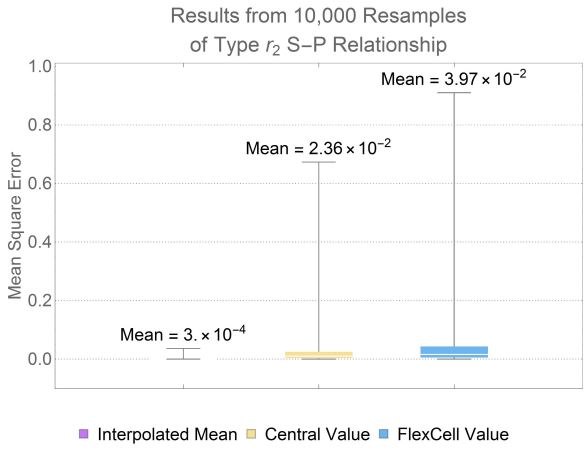

(b)

Figure 1.7
The results from 10,000 re-sampling steps for both r_1 type (a) and r_2 type (b) functions. In both cases, when the interpolated mean strain is associated with the mean phenotype, the MSE is significantly lower than when using the central strain value and the value FlexCell® gives.

There is no reason, however, to assume that the true relationship will be linear over this region. Therefore 10,000 random samples of the S-P functions were generated and each *in silico* experiment quantified using the mean square error function (Equation 1.4.3). The results of this are shown in Figure 1.7. For the continuous r_1 type relationships the mean MSE incurred by using the FlexCell® strain values is an order of magnitude greater than using the central strain value, and four orders greater than when the interpolated mean is used (Figure 1.7(a)). A similar result is seen for the piecewise r_2 type relationships (Figure 1.7(b)).

The standard biological usage of the FlexCell® Tension System involves delivering a strain regime to a monolayer of cells set by a computer – for example 20% stretch which corresponds to 80 kPa of negative pressure – and then assessing the cells for a phenotype of interest through a population averaging method. Although the finite element analysis

of Vande Geest et al. is often cited in the literature for a standard description of the FlexCell® system, there doesn't appear to be a discussion of the implications of this work, and in particular the validity of population averaging given the strain stimulus heterogeneity.

The pressure-strain relationship of the FlexCell® system is in conflict with the values Vande Geest et al. use to describe the relationship (Table 1.2). Using the analysis described here, these values were tested in the *in silico* experiments together with an interpolated mean of the VG data.

The results here suggest the need for caution when performing FlexCell® experiments and interpretation of previous results. Under the assumption that the VG data is true, if using the strain values that FlexCell® assigns to applied pressure then the probability of uncovering a false or partially false S-P relationship is, compared to when using the central strain value of the VG data, high. However, even in the central value case there is still a chance of error that when compared to the results of using the interpolated mean, is unsatisfactory.

Under the assumption that the VG data is inaccurate in describing the values of strain but correct in the distribution, the results here suggest that population averaging is, based on the $r(s)$ functions chosen here, an acceptable method despite the heterogeneity. This however comes with the caveat that the strain value associated with the averaged phenotype response must be the mean across the entire membrane. If the values given in the FlexCell® manual are not representative of this, then there is an inherent and unknown error in the FlexCell® method. Arguably, this can be rectified if further investigation and scientific agreement can be reached about what this mean value is.

Although not examined as part of this analysis, an interesting continuation of this work is asking the question of whether by considering only on-post regions of the BioFlex® membrane, together with the VG data and this analysis method, does exclusion of the outer annulus improve the MSE scores. In part this mimics the methodology employed by Li et al. (1994) but would serve as an interesting addition to this work.

1.5 Limitations of FlexCell®

Although widely popular and an industry standard technology, there are still limitations of the FlexCell® system.

Aside from not allowing for economical study of general strain-phenotype relationships – a lack of throughput – there are unanswered questions of intra-experimental strain variance caused by the manual lubrication of the loading post. There exists no studies which examine the effect of lubrication volume and dispersion across the loading post and any changes to the resultant distribution of strain in the FlexCell® system. It stands to reason that the consistency of this lubrication process will not be constant. Without an analysis of the effects of this, arguably confidence in the repeatability of the system is hindered.

Another limitation of the system arises from personal experience of its use. Throughout this thesis the FlexCell® FX 3000 has been utilised for experimentation. The loading plate, however, shows signs of warping and preliminary biological experimentation (not here presented) alludes to a wide intra-well strain variance within each experiment. The suggestion being that warping of the loading plate results in the delivery of differing strain regimes to each well in a BioFlex® plate. Although not a limitation of how the system theoretically works, it calls into question the validity of results based on the shelf life of the apparatus.

1.6 Advantages/Disadvantages of Utilising Heterogeneous Strain

The FlexCell® system delivers a relatively homogenous distribution of strain to a monolayer of cells. To address the problem with a lack of high throughput in strain-phenotype experiments this thesis proposes utilising a heterogeneous strain stimulus as a method of capturing as wide as possible population of strain-phenotype cell behaviour. However, this itself is open to critique.

In particular this idea necessarily assumes that the response of a cell to a particular magnitude of stretch does not influence its neighbouring cells. With strain induced proliferation, at the very least, this assumption is not true. Wilson et al. (1993) showed that neonatal rat vascular smooth muscle cells, when stretched using the Flex I system, are induced to proliferate through an autocrine secretion of Platelet Derived Growth Factor (PDGF). Therefore, in a heterogeneous strain regime it is entirely possible that the PDGF released by a population of cells triggered by an unknown strain magnitude would diffuse through media and similarly stimulate other cells experiencing a different strain magnitude to proliferate. In this case, without advanced statistical methodology, it would be impossible to decouple the general relationship between strain magnitude upon cellular proliferation.

This highlights a limitation of utilising heterogeneous strain and demonstrates the need for care taken over which phenotypes are investigated and how they are investigated. As explored more in Chapter 5, the mechanisms for strain induced plasmid transfection is likely to be due to cytoskeletal rearrangement and therefore purely intracellular (Geiger et al., 2006). Because of this, although not certain, the triggering of rearrangement of a cell caused by a specific strain magnitude is unlikely to influence neighbouring cells. Therefore this serves as a better candidate for general exploration utilising heterogeneous strain.

It is important to note, however, that the methodology developed here which is based upon delivering heterogeneous strain is not designed to be a replacement for conventional apparatus like the FlexCell® system or a methodology for conditioning tissue for engineering therapeutics, but instead a strategy for uncovering relationships on a deeper level. The primary purpose is to rapidly elucidate strain parameters required for a de-

sired phenotype to better inform either further experimentation, using for example the FlexCell® system, or the engineering of novel mechanical bioreactors for conditioning or building biological tissue.

The problem of exploiting heterogeneous strain regimes and communication between cells is a problem for those phenotypes where signalling molecules or cell junction communication is implicated. However, this problem is theoretically mitigated by the assays used to assess cell behaviour. For example, in the work carried out in this thesis and as well as much in the literature, BrdU ELISA and EdU imaging assays are used to assess proliferation after cells have been exposed to stretch. As discussed above, the implication of PDGF as an autocrine/endocrine factor means that assessment using EdU imaging assays will not allow correlation between the heterogeneous stimulus and the cellular response. However, if instead of measuring for proliferation, the production of PDGF could be appropriately recorded and associated with strain then perhaps general correlations could still be uncovered utilising heterogeneous strain and still inform a general relationship between strain and phenotype.

Using a heterogeneous strain stimulus for uncovering general strain-phenotype relationships has disadvantages, but the absence of a high throughput system using a homogeneous strain delivery (for example, a 48 well type BioFlex® plate where each well could be exposed to a different but homogeneous strain magnitude) justifies exploration of unconventional methods.

There are, however, advantages of developing a system using heterogeneous strain. It is conceivable that force as a therapeutic could be harnessed using magnetic pressure delivered within the body powered from outside, for example with the rise of magnetic nanotechnology. The strain delivered would most likely rarely be homogeneous and mechanisms to be able to understand the response of tissue to inhomogeneous strains is useful in this respect. Therefore, caution is required in deriving general strain-phenotype results when utilising heterogeneous strain, but the potential benefits currently outweigh the disadvantages.

1.7 Thesis Aims and Objectives

This final section of the introduction synthesises the discussion up to this point. With this, an argument for the need of improvement is made and a potential avenue for doing so proposed.

1.7.1 Motivation for Generalisation

From the perspective of engineering an object from constituent components, regardless of what this object is, arguably the best strategy is to have a solid, foundational understanding of each component which is to make up this object.

Prior to this thesis we were exploring tissue engineering strategies which utilised cyclic mechanical strain as a therapeutic tool to condition tissue, both *ex* and *in vivo*.

Although *ex vivo* tissue engineering was already utilising mechanical stimulus in bespoke bioreactors, we saw potential for similar strategies *in vivo* using magnetic material as the delivery vehicle of force to generate strains within the body.

The review in Section 1.2 highlights the lack of studies which quantitatively examine the general relationships between a single cell type and strain parameters. Despite there being evidence that different strain values can switch cell behaviour from an inhibitive to proliferative phenotype (Qi et al., 2010), there is no effort to understand a single cell type across a spectrum of strain values. Considering many *ex vivo* tissue engineering strategies utilising mechanical stimulus would be anchored some extent upon FlexCell® studies, it should be legitimate to ask whether these efforts are fully optimal.

As a point of argument, it is optimal to know as much as possible about a 'thing' before adding and manipulating 'things' to engineer something new; that as a maxim it is better to know more than you use than to use only what you know. To this end, general strain-phenotype relationships should be sought. Currently however, this is both time consuming and expensive and perhaps explains why this is never done. The studies we presently have which use FlexCell®, as a point of contention, tell us only that there *is* a relationship between cyclic stretch and cellular phenotype modulation but not, crucially for engineering, *what* this relationship is in general.

Because of this, the primary aim of this thesis is to develop a new method for conducting experiments between strain and cellular behaviour which increases the volume of data to allow for rapid and generalised characterisation of cellular behaviour.

1.7.2 Thesis Hypothesis: Exploiting Spatial Heterogeneity

The small theoretical work conducted in Section 1.4 grew from the discussion in Section 1.3. Given the FlexCell® system exhibits heterogeneity in the distribution of strain across the membrane, by beginning with the supposition that the relationship between strain and cellular phenotype is known, the theoretical analysis demonstrates instances where the system completely fails to capture 'truth'.

Although this work is purely theoretical it points to a possibility of experimental failure. This failure is entirely due to a fundamental experimental mismatching which applies a heterogeneous stimulus but quantifies with a homogeneous, population averaging methodology.

The FlexCell® system was a redevelopment of the Flex I system in order to decrease the variation of strain across the membrane. The Flex I system on the other hand had a well known heterogeneous distribution. As discussed in Section 1.2, this was such that researchers physically fenced the membrane into two annular regions and assigned different strain values to the regions despite being from the same membrane. Where Li et al. (1994) used a single physical fence to divide areas, the proposition of this thesis is to deliver a strain regime which is highly heterogeneous and use many hundreds of *virtual fences* to divide the area whilst at the same time attempt to substantially increase the variation of strain across the membrane. This strategy is schematised in Figure 1.8 with

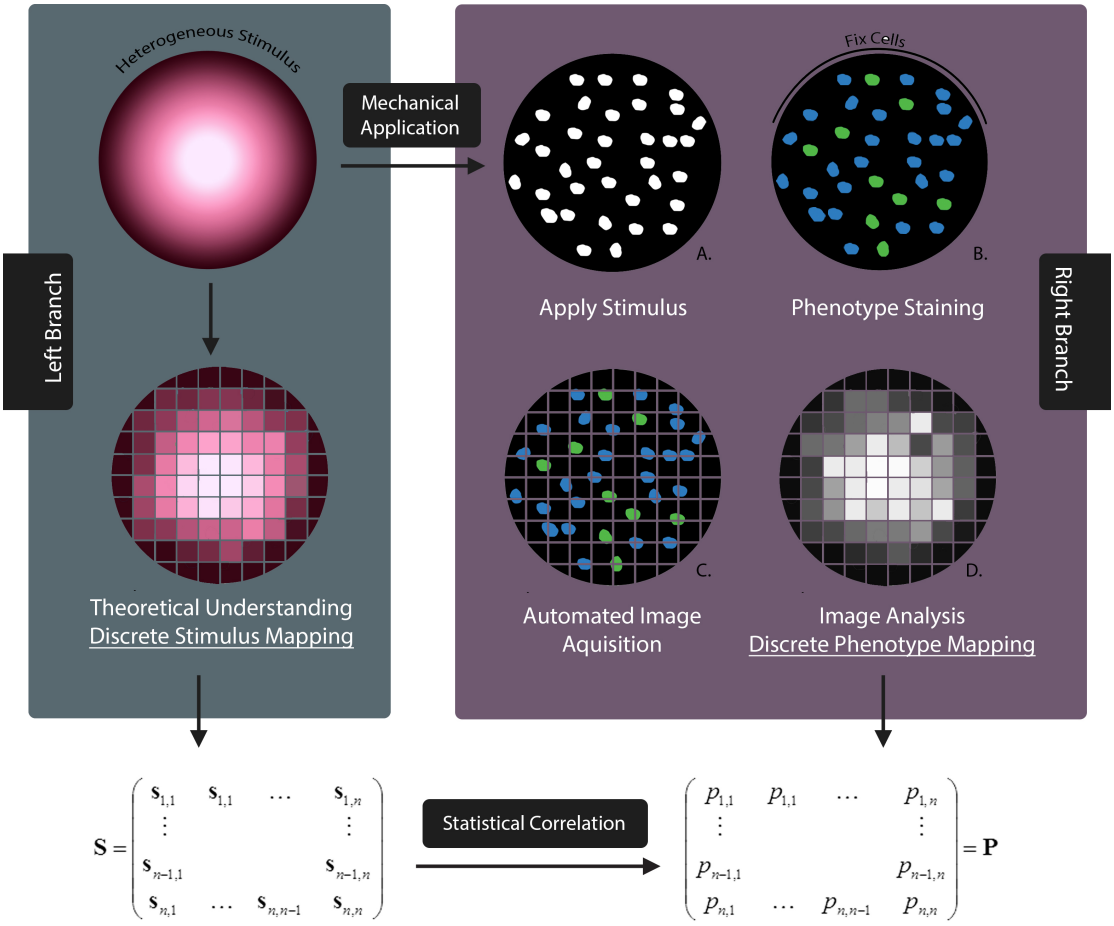

Figure 1.8

Thesis Hypothesis Schematic. A well defined heterogeneous distribution of strain is delivered to a monolayer of cells. Phenotype staining using fluorescent techniques and automated image acquisition will capture the behaviour of all cells. Image analysis to extract the behaviour of every cell in small *voxels* generates a 'phenotype map'. Correspondingly, the heterogeneous stimulus is understood on the same voxel resolution in the 'stimulus map'. Appropriate statistical correlation could then uncover the relationship between stimulus and phenotype for a range of strain parameters from within the same experiment.

the detail as follows:

Right Branch 1: A highly heterogeneous strain stimulus is applied to a cell monolayer of interest.

Right Branch 2: Rather than using a population averaging assay or method, the cells are fixed and fluorescently stained to highlight a particular phenotype of interest. For example, using a life technologies 'Click-it' imaging kit to quantify the proliferative state of each cell. This step is shown by 'B' in Figure 1.8.

Right Branch 3: The fluorescently labelled sample is imaged at high resolution in its entirety using many hundred or possibly thousands of images. Each image serves to discretise the substrate into small 'chunks'. The border of each image is a *virtual fence* analogous to the physical fences in Li et al. (1994). This is 'C' in Figure 1.8.

Right Branch 4: Using bespoke image analysis algorithms, the behaviour of each cell is extracted using fluorescent information to create a *discrete phenotype map*. This is 'D' in Figure 1.8.

Right Branch 5: The discrete phenotype map is considered as a matrix, $\mathbf{P}$, where each value represents the averaged cellular behaviour inside each image.

Left Branch 1: A highly heterogeneous strain stimulus is applied to a cell monolayer of interest.

Left Branch 2: This strain stimulus, either through theoretical or physical measurements, is understood and well defined on the same resolution and with the same dimensions as the virtual fencing. This information is used to create a *discrete stimulus map*.

Left Branch 3: The discrete stimulus map is considered as a matrix, $\mathbf{S}$, where each value represents the averaged strain stimulus for each of the corresponding discrete stimulus entries in $\mathbf{P}$.

LR Correlation 1: Because the entries of S_{ij} are generated from the same area of space that the entries P_{ij} are generated from, statistical correlation between the two matrices may uncover the relationship between strain and phenotype for a range governed by the variance in strain distribution across a membrane.

Creating virtual fences using imaging allows for averages to be taken over a much smaller area where the variance of the stimulus is negligible and therefore each image, or *voxel*, is considered as a single experimental data point. In this way, from one experiment many dozens of strain stimulus values can be simultaneously assessed, whereas many methodologies only allow for one.

Coincidently, this idea has similarities with Khademolhosseini et al. (2016) who sampled images from defined locations across a membrane having been exposed to a heterogeneous stimulus. This is also seen in the work of Harshad et al. (2016) (see Section 1.1.1.4). The key difference between these studies and this thesis is the emphasis on discovering relationships in general. Where they sampled few images from designated locations here the aim is to sample everything without bias which, together with computational methods, utilises all the information to provide relationships as general as possible.

Based on the strategy outlined above, the hypothesis, or more accurately, the aim, of this thesis is that an apparatus can be designed which follows the architecture of Figure 1.8 and does generate an increase in the volume of information available to researchers relating cyclic strain to phenotypic modulation. If this approach is shown to work, consideration of the results of Qi et al. (2010) alludes to potential benefits. Their results indicate the existence of a strain value which switches phenotypic behaviour from a inhibitory proliferative state to a stimulatory. To uncover these values many experiments would need to be conducted on the FlexCell® system together with regression analysis of the results to predict the switching value. Subsequent experiments would then be needed to validate this prediction. The benefit of the heterogeneous strain method proposed here is that, theoretically, this switching value should be uncovered from initial experiments together with the results Qi et al. deduced. Under this approach, assumptions are not required before experimentation and therefore experimentation does not need to be tailored based on a best guess. Therefore, the approach explored here arguably enhances cell stretching experiments and increases the volume of biological information substantially.

This thesis is initially presented in discrete chapters addressing each of the 'Left Branch'/'Right Branch' requirements of the strategy.

Chapter 2 describes the development of a novel apparatus which address the criteria: Right Branch 1 and Left Branch 1.

Chapter 3 describes the development of the protocol of acquiring images as well as the development of bespoke algorithms to generate the discrete phenotype map. This addresses the criteria Right Branch 3 - 5.

Chapter 4 describes efforts to both empirically and theoretically understand the bespoke apparatus described in Chapter 2 in order to construct the discrete stimulus map. This addresses the criteria Left Branch 2 - 3.

Throughout this research project efforts have always been directed towards a completed biological proof of principle. The testing paradigms and biological exemplars are found within Chapters 5. Biological protocols used throughout this thesis are standard methods. These are detailed in Appendix A and are referred to by hyper-linked Protocol reference numbers. The goals of this thesis, however, are never fully realised. In part this is due to time constraints and in part due to the complexity of integrating all components into a working prototype. This is discussed in more detail in the concluding chapter of this thesis, where foundations for continuing research are laid.

Chapter 2

Novel Apparatus: Cyclic Strain by Magnetic Actuation

As discussed in Chapter 1.1.1; page 23 the FlexCell® tension system evolved to deliver strain to BioFlex® membranes which is as homogeneous as possible. Thus, to characterize cellular responses to cyclic strain as proposed in this thesis – by exploiting a heterogeneous stimulus – the FlexCell® system is insufficient. Together with other limiting factors; that (i) the contact between manifold and membrane may not always be constant, (ii) predicted strain regimens are often inconsistent with true strain, and (iii) the analysis conducted in Section 1.4; page 42, which, under the assumption that Vande Geest et al. (2004) is true, shows theoretical inconsistencies with the traditional, population averaging, usage of FlexCell®, a new system to impart strain to cells is needed.

Prior to the work conducted in this this thesis a new system to deform the membrane of BioFlex® plates was conceived, for purposes other than the research here, by Dr. Richard Day. It was realised early that this system may be suitable for providing the heterogeneous strain distribution required for the virtual fencing method proposed here. This chapter details a body of work focussed on engineering developments and refinements to this initial system. The basis of the refinement is drawn from analysis of Dr. Day's original prototype. The refinement itself makes heavy use of computer assisted design (CAD) modelling and Nylon selective laser sintering (SLS) 3D Printing. The outcome of this work is the production of a novel, low cost, portable kit capable of delivering heterogeneous strain to cell cultures in BioFlex® plates.

This work is delivered here in two distinct sections: (i) a description of the initial prototype together with an analysis and critique, and (ii) the steps taken to refine this into a low cost, engineered apparatus. Dr. Day's original apparatus is herein referred to as the 'original prototype'.

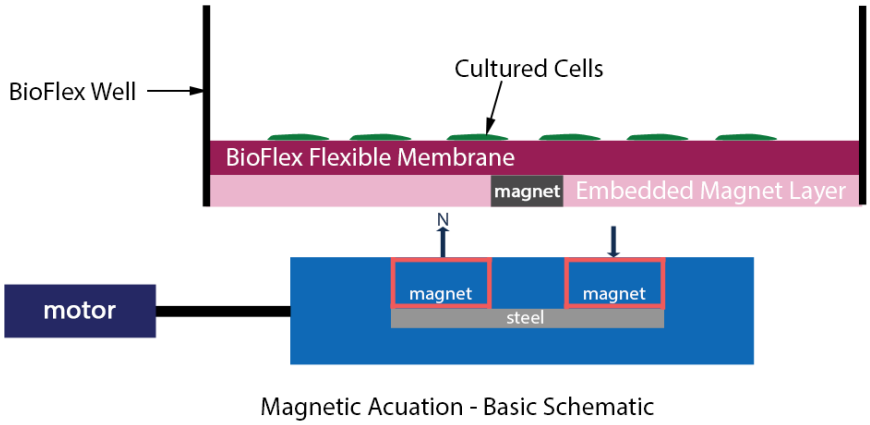

Figure 2.1
Schematic of Basic Principle of Magnetic Actuation. Each membrane in a BioFlex® plate is augmented to include a small permanent magnet. In this way, a second set of magnets underneath each well if rotated would dynamically interact with the embedded magnet in such a way that, given the magnet is fixed in place, it would periodically deform the flexible membrane. Theoretically, if the deformation is sufficient, cultured cells on top of the membrane would be stretched as in the case of the BioFlex® system, but with a distinctly different strain profile.

2.1 Chapter Aims and Requirements

In accordance with the thesis aims detailed in 1.7.2; page 52 the aim of this chapter is to construct apparatus capable of actuating a BioFlex® plate such that it fulfils the following requirements:

1. A heterogeneous strain distribution is generated on each BioFlex® membrane with a variance reaching up to 25% stretch (matching the capability of FlexCell® and containing experimental stretch parameters from studies in literature as detailed in Table 1.1; page 37).
2. The oscillation period of zero to maximum stretch is controllable for each well.
3. The apparatus is designed with consistency and repeatability in mind to be used for experimental purposes.

2.2 Basic Principle

Where the FlexCell® system deforms a flexible membrane using vacuum pressure, the basic principle in the original prototype is instead deformation using magnetism. By embedding small permanent magnet to the underside of the membranes of BioFlex® plates, the rotation of a secondary set of permanent magnets will create interacting magnetic forces. The embedded magnet (EM), schematised in Figure 2.1, is attracted/repulsed as a result of the rotating magnets. The magnetic pressure on the EM causes a deformation

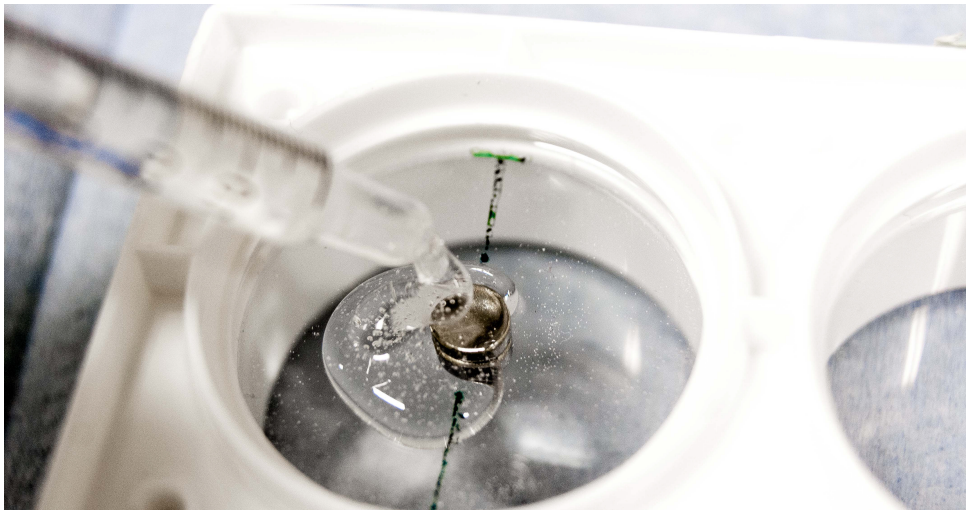

Figure 2.2
BioFlex® plate augmentation according to Protocol C.1. A Magnet is placed in the middle of the underside of a well (by eye) before a 1ml preparation of silicone elastomer is syringed over the top of the magnet and left to cure for 3 days. The magnet is then sandwiched between the 2 flexible layers acting as a transducer of magnetic force to deform the dual elastomer membrane.

of the membrane. If the deformation is sufficient then the flexible membrane stretches and this will be translated to a monolayer of cultured cells on the membrane as cellular strain. Thus, cells can be periodically stretched with a frequency governed by the rotational speed of the motors.

The repeatability of the FlexCell® system is arguably hindered by the membrane having to be in contact with the manifold post. An immediate benefit over the FlexCell® system with a magnetic delivery of strain is the absence of membrane contact.

As will be discussed in the next section which details the initial prototype, the nature of the deformation is one which is spatially heterogeneous across the membrane; cells will experience different magnitudes of strain dependent on their spatial positioning on the membrane. Together with the aims of this thesis, it is with this reason that analysis and development of the initial prototype is sought.

2.3 Initial Prototype and Proof of Concept

The initial prototype and protocols were conceived and constructed prior to this thesis by Dr. Richard Day. Where appropriate, all protocols developed by Dr. Day will be clearly indicated and are detailed here in explicit form only for context. All work attributed to Dr. Day is described here with permission.

2.3.1 BioFlex® Plate Augmentation 1

Magnet augmentation of the BioFlex® plates was initially conducted by sandwiching a 6(d)x2 mm plastic bonded neodymium iron bonded magnet (Magnet sales UK, PNDC00123)

between the underside of each BioFlex® membrane and a 1 mL layer of Sylgard® 184 Elastomer (VWR, 634165S). The procedure for this can be seen in Figure 2.2. In sterile conditions a magnet is placed on the underside of a BioFlex® well before 1 mL of Sylgard® elastomer is syringed on-top. Once cured, the magnet is sandwiched between two layers of silicone. The full protocol for this is detailed in Appendix C.1; page 233.

2.3.2 Prototype Actuator Device

A prototype magnetic actuator according to the basic principle outlined in Figure 2.1 had been constructed by Dr. Richard Day primarily using LEGO components and building blocks. LEGO had been chosen due to ease its of construction, cost effectiveness and durability.

The prototype includes the use of LEGO Power Functions XL Motors (LEGO 8882), LEGO Power Functions IR Speed Remote Controller (LEGO 8879), LEGO Power Functions IR Receiver (LEGO 884), an assortment of LEGO building blocks together with custom made Delrin® components. The material Delrin® was chosen due its low friction coefficients and dimensional stability. The Delrin® components consist of the Delrin® Magnet Holder (DMH) and the Delrin® Magnetic Chassis (DMC) and were commissioned by Dr. Richard Day according to the schematics reproduced in Figure 2.3.

The DMH is designed to hold a pair of magnets (12x8x6 mm) opposing in pole against a sheet of steel (30x8x3 mm). The DMH is connected to the LEGO Power Functions Motor by a steel rod and rotates inside the cylindrical cavity of the DMC; Figure 2.4(a). The motors are powered by LEGO battery packs which hold six rechargeable AA batteries. LEGO Power Functions IR Receivers control the speed of the motors through an LEGO IR Speed Remote Controller. The controller's dial turns in discrete steps from 0 through to 6 and each step increases the motor speed but give no indication of this speed. LEGO blocks were used to build a platform upon which the augmented BioFlex® plate sits. Figure 2.4(b) visually describes the construction of the apparatus. In total there are three rotating DMH actuating three augmented BioFlex® wells and the remaining three wells are used as controls for experimental purposes.

Cross-hairs had been measured and marked out on the DMC to indicate the center point between the rotating magnets. By eye, the augmented BioFlex® plate is aligned with these cross hairs, as seen in Figure 2.4(d).

When the motors are on, the EM attached to the BioFlex® wells undergoes a periodic rocking of the the EM. This rocking behaviour occurs as the DMH rotates to face the EM. The EM is forced to align with the magnetic field of the magnet pair, schematised in Figure 2.5. As the EM is fixed to the membrane, the passive resistance of the silastic membrane results in the EM, and so the membrane, exhibits a periodic rocking movement.

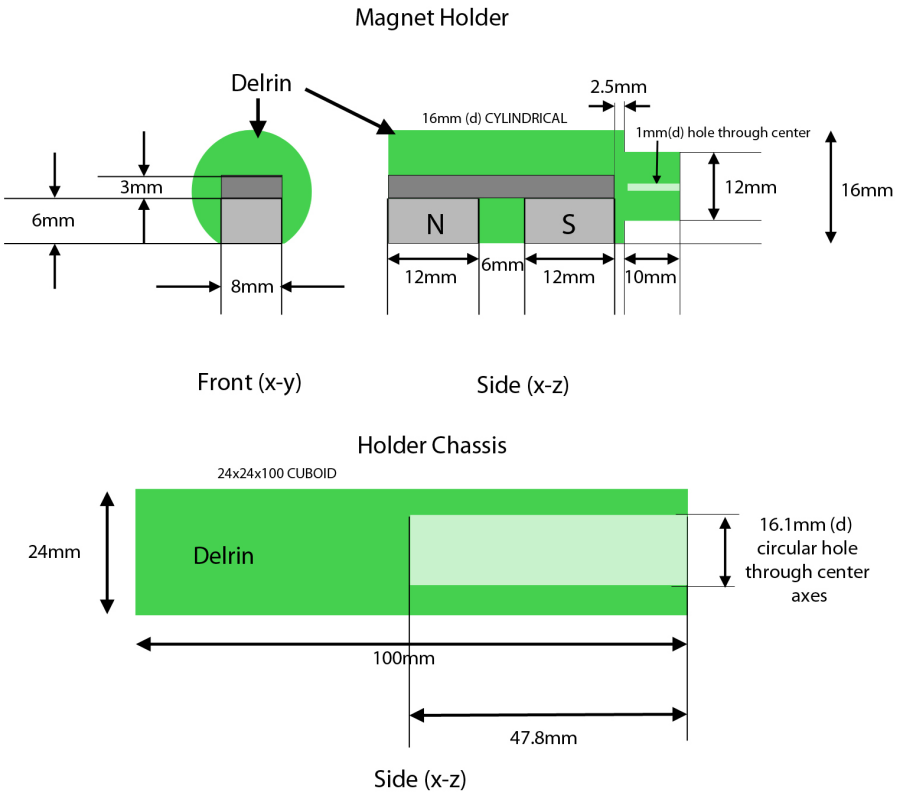

Figure 2.3
Reproduced schematics for the Delrin® Magnet Holder (DMH) and the Delrin® Magnetic Chassis (DMC). The DMH is designed to hold a pair of magnets opposing in pole against a sheet of steel. The DMH slots into the DMC and enables a chassis in which the DMH can rotate.

2.3.3 Proof of Concept 1

A proof of concept experiment was conducted by Dr. Richard Day prior to this thesis. The prototype was used to stretch Human Rectal Smooth Muscle Cells (HRSMC) to study the affect upon proliferation caused by strain. Along with this, Dr. Day, in collaboration with Dr. Gaetano Buriesci, used finite element modelling to describe the distribution of strain across these membranes as they were actuated. Full details of experimental protocols are detailed in Appendix C.2; page 234. In brief, HRSMC were actuated using the prototype device for one hour per day for five days. Following this, the wells were analysed using the BrdU ELISA for a measure of proliferation.

The results of this work are displayed in Figure 2.6 and provided by Dr. Day. Figure 2.6(a) suggests through the use of the BrdU ELISA, HRMSC which have undergone actuation exhibit a greater proliferative phenotype than unstretched controls. Figure 2.6(b) displays the strain distribution as calculated and provided by Dr. Buriesci. The strain distribution is heterogeneous. Regions of higher strain, found in locations around the EM as well as the peripheries of the membrane, are contrasted with regions of lower to zero strain in the middle annular region.

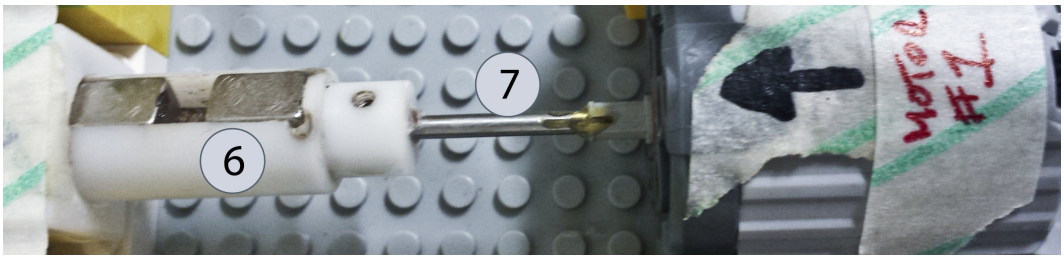

(a) DMH/Motor Interface

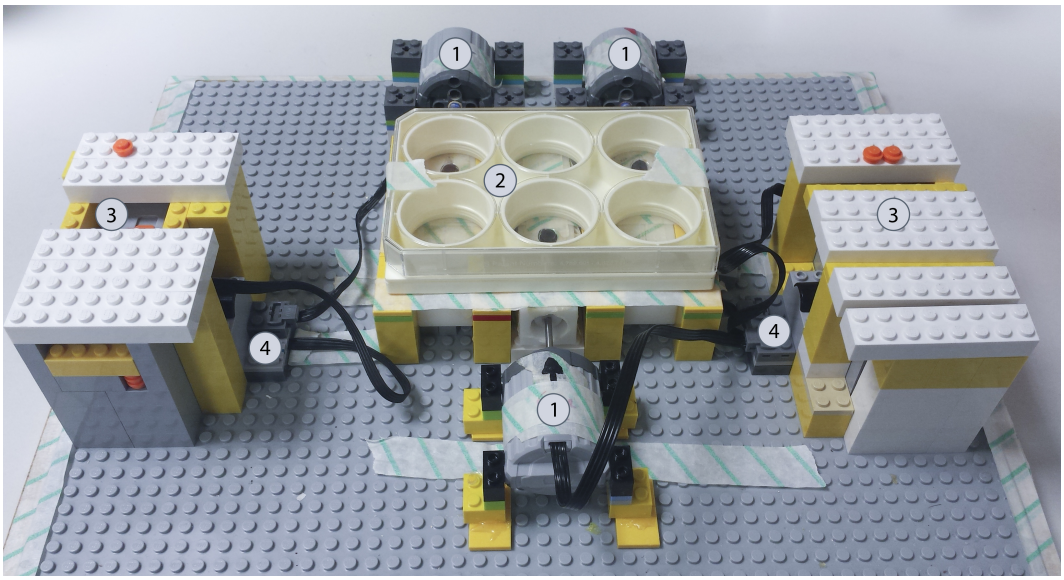

(b) LEGO Magnetic Actuator Device

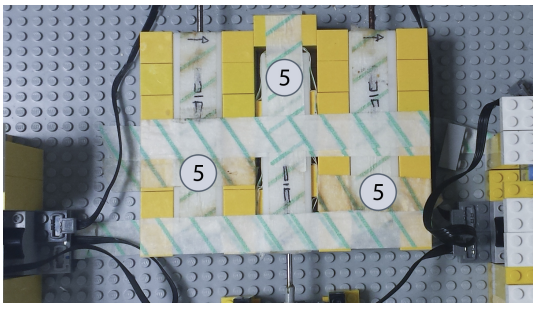

(c) DMC and DMH Placement

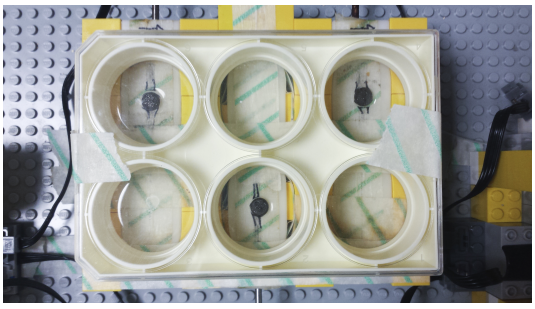

(d) BioFlex® Placement on Device

Figure 2.4
Initial Magnetic Actuator.
1: LEGO Power Functions XL Motors. 2: Customized BioFlex® plate. 3: LEGO battery pack - houses 6x 1.2V AA rechargeable batteries. 4: LEGO Power Functions IR Receiver. 5: DMC housing the DMH with magnets. 6: The DMH containing two magnets opposing in poll. 7: Steel rod which connects the DMH connected to the motor.

This initial work suggests that both that the prototype is able to induce phenotypic responses as a result of substrate strain and that, although the precise distribution of strain isn't known, the strain is likely heterogeneous in distribution.

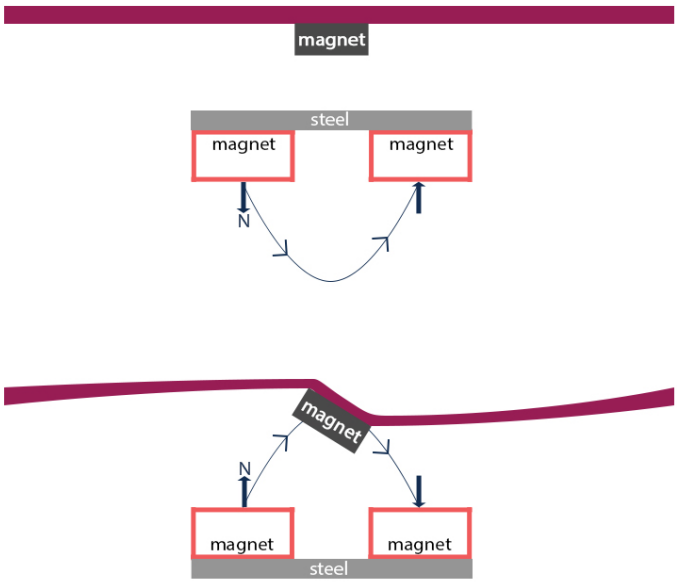

Figure 2.5
Illustration of Membrane Deformation due to Magnetic Actuation.
The magnet is fixed to the membrane. In the top image the magnets are facing away from the EM. As the magnets rotate towards the EM, the EM acts to align itself with the magnetic field lines of the rotating magnets. The passive resistance of the silastic membrane causes the EM to exhibit a rocking behaviour.

2.4 Analysis of Prototype Apparatus

The preliminary experiments in Section 2.3.3 were the initial seed for work in this thesis. Since this apparatus is capable of generating a heterogeneous strain distribution as well as generating phenotypic modulation in smooth muscle cells, the principle of actuation using magnetism in this way is a platform suitable for the virtual fencing method proposed in Section 1.7; page 51. However, the nature of this method is such that the level of precision required is high. For example, if phenotype and stimulus maps are to be correlated then a confidence is needed that the stimulus is the same in every well, every time. With this in mind, the most immediate criticism of the original prototype is that, in all likelihood, this will not be the case. EM's are placed in the center of wells by eye before being embedded by elastomer. Therefore there is no assurance that they are positioned in the center nor positioned in the same location for the next well. BioFlex® plates are placed onto the LEGO platform and aligned by eye over pre drawn cross-hairs. Therefore there is no assurance that they are positioned over the center point between the rotating magnets. The original prototype thus does not facilitate the required experimental condition of repetition.

Alongside repeatability, a major drawback of the prototype is the lack of control of the motor speed. Given the dependence of strain frequency on cellular phenotype (Liu

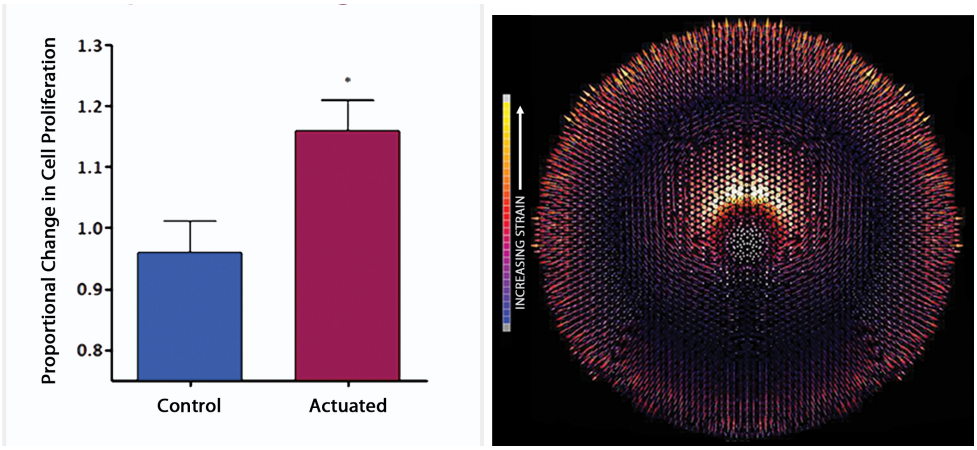

(a) BrdU ELISA Results (b) FEM Strain Distribution

Figure 2.6
Dr. Day's Original Prototype Proof of Concept Results.
(a) Shows the results for BrdU ELISA following 1 hour/day 5 day actuation. The result indicates an increase in the number of HRSMC's in a proliferative state in the actuated wells compared to control. (b) Shows results from FEM mapping the distribution of strain. It indicates a heterogeneous distribution with distinct regions of high and low strain coloured as per the legend at left.

et al., 2008), the original prototype is insufficient due to the lack of control.

2.5 Motor Rotation Speed and Rotation Profile

As part of efforts to understand the motor speeds of the original prototype and as well to facilitate a functional redesign of the prototype, a method suitable for capturing the motor speed was investigated.

2.5.1 Evaluating Motor Rotation Speed

The LEGO IR Remote Control Unit sets the speed of each motor from 1 of 6 discrete speed settings. The precise rotation speed is not here known. Since the rotating DMH is hidden within the DMC, direct measurements to calculate rotation speed are near impossible. However, because the motor is rotating magnets, it stands to reason that the periodic change of magnetic field caused by the rotating magnets can be used as a surrogate for the motor speed. Thus, a strategy was devised upon reading the magnetic field at a particular point in space. Through analysis of this signal, the motor speed can be indirectly known.

Recording the magnetic field can be done using magnetometers. Magnetometers are instruments which measure both the magnetisation of a material and as well the strength of a magnetic field at a point in space. Due to advancement in magnetometer design and incorporation into small circuits the majority of smart phones contain magnetometer microchips. By accessing this sensor signal the magnetic fields of the rotating magnets

can be recorded. With this recording, basic signal analysis can extract the motor speed.

Attempts had been made to develop an Android 'app' to record the magnetic field data but the complexity of this task required seeking simpler methods. For recording magnetic fields, the smart phone application, *Physics Toolbox Magnetometer* was downloaded onto a Samsung Galaxy S4® smart phone[1]. The application records magnetic field strengths of the three principle axes (x, y, and z) in micro Tesla and in discrete time intervals. The data, along with the corresponding time points recorded, are exported to **.csv** file format with the following matrix structure:

$$\begin{pmatrix} \text{COL 1} & \text{COL 2} & \text{COL 3} & \text{COL 4} \\ \text{Time (s)} & x\text{-axis } \mu\text{T} & y\text{-axis } \mu\text{T} & z\text{-axis } \mu\text{T} \\ \vdots & \vdots & \vdots & \vdots \end{pmatrix}. \tag{2.5.1}$$

Algorithm 1 was constructed to process this data to extract average rotational speeds of the motors.

Algorithm 2.1. Processing of Magnetic Field Data

Step 1: From the raw data, apply a low pass filter to the z-axis field readings (COL4) with a cut-off frequency 0.05. This acts to smooth the waveform and therefore minimizes the effect of noise.

Step 2: Compute an interpolating function between the time points (COL1) and the filtered z-axis field recordings.

Step 3: Numerically differentiate the interpolating function. The peaks in the original waveform become zeroes in the differentiated signal.

Step 4: Extract the positions of the zeroes through the time series of the interpolated signal and calculate the average time between each zero based on the discrete time intervals in COL1.

Step 5: Since there are two peaks in one complete rotation of the motor, twice the value given in Step 4 gives the period of rotation and the inverse of the period gives the frequency of rotation. Formally, if t is the average time between zeroes in the interpolated signal then the period, P, and frequency, F, of the motors is:

$$P = 2t, \tag{2.5.2}$$

$$F = \frac{1}{P}. \tag{2.5.3}$$

End of Algorithm 2.1.

[1]Copyright August 2015. Vieyra Software. Chrystian Vieyra and Rebecca Vieyra

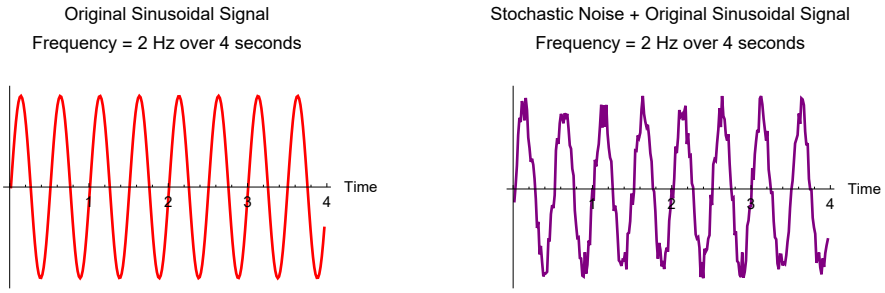

(a) *In Silico* Generated Waveform

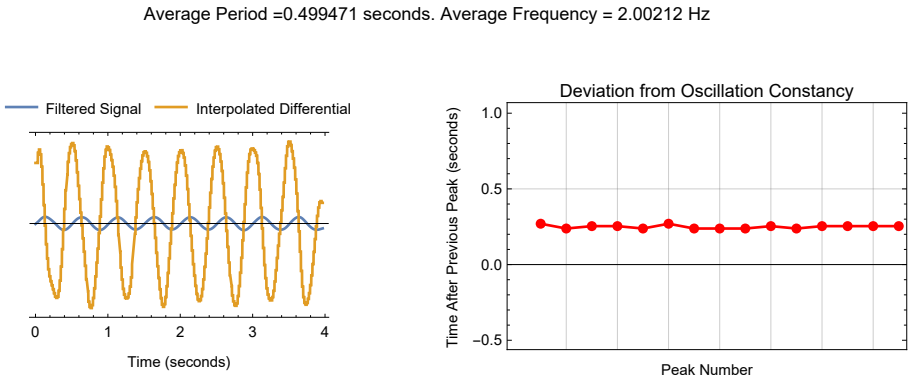

(b) Processed Output Using Algorithm 1

Figure 2.7

In Silico testing of Algorithm 1. (a): Left: A sinusoidal waveform was generated in Wolfram Mathematica with a frequency of 2 Hz over 4 seconds. Right: Stochastic noise was generated by adding a pseudo random value from the range $|x| \leq 0.2$ to each artificial data point. (b) The results from the implementation of Algorithm 1. The algorithm correctly identifies, to within some error, the average frequency of the signal. Right: A secondary infographic displaying how constant the time interval between each peak is. If the periodicity of the waveform is perfectly constant then then a straight line is expected. If the line is not straight then the periodicity of the waveform is not constant. In the context of the motors, this would indicate a 'non-smooth' rotation.

To demonstrate this principle and Algorithm 1, *in silico* testing was performed by artificially creating a sinusoidal waveform in **Wolfram Mathematica**. The waveform was created as a sine wave with a frequency of 2 Hz (hertz) over 4 seconds, Figure 2.7(a) left. Stochastic noise was generated by adding a pseudo random number, α, in the region $|\alpha| \leq 0.2$, or $\pm 20\%$, to each artificial data point, Figure 2.7(a) right. Algorithm 1 was implemented in a small **Mathematica** script and performed on the artificial data. The results are shown in Figure 2.7(b). Given the noise, the script returns the average frequency of the waveform as being 2.00212 Hz.

A supplementary plot is shown in Figure 2.7(b) right. It plots the time between each peak and trough of the artificial waveform as calculated by Step 4: in Algorithm

1. This graphic is indicative of how constant the periodicity of the wave is; a straight line indicates that the periodicity, or rotation, is smooth and constant whereas a jagged line would indicate a non constant rotation. In the context of the rotating motors in the apparatus, a jagged line would indicate that the motors are stuttering at certain points in the rotation.

2.5.1.1 Testing the Speed of the Motors: Method and Results

The method outlined above was used to calculate motor speeds of the LEGO motors when controlled by the LEGO controller. This was done to analyse the performance of the motors in the original prototype.

On multiple time points, separated by at least three days the motors from the prototype apparatus were switched on in turn. A Samsung S4® smart phone running the *Physics Toolbox Magnetometer* application was placed on top of the DMC containing the rotating motor and the magnetic field was recorded. The motors were recorded at various remote control speed settings and the resultant **.csv** for each recording was exported to a desktop computer and was processed in **Wolfram Mathematica** using a custom written script implementing Algorithm 1. Recordings were made for 10-20 seconds for each motor[2].

The results of the analysis are indicative of substantial inadequacies in the original prototype and are summarised as:

Result 1 : Motors do not turn with the same speed between different time points and the change in frequency is not consistent between motors; Figure 2.8(a).

Result 2 : Motor speeds decline after 24 hours inside a humidified CO_2 incubator; Figure 2.8(b).

Result 3 : The smoothness of rotation is not consistent between time points; Figure 2.8(c).

An explanation for these undesirable results are likely found from the fact that (1) the prototype draws its power from a battery pack which decreases unpredictably over time; (2) the axle connecting the motor to the DMH sitting inside the DHC may not be aligned to the axes of rotation. This is further complicated by the observation that LEGO is limited in precision by the dimensions of the LEGO blocks and the grid in which they are secured. If there are discrepancies in alignment, it is possible that a fully charged battery may provide the motors with sufficient torque to overcome any misalignment to exhibit a constant rotation. Conversely, however, and explaining the behaviour in Figure 2.8(c), if the power is depleting then the torque generated may be insufficient.

[2]Wolfram Research, Inc., Mathematica, Version 11.1, Champaign, IL (2017).

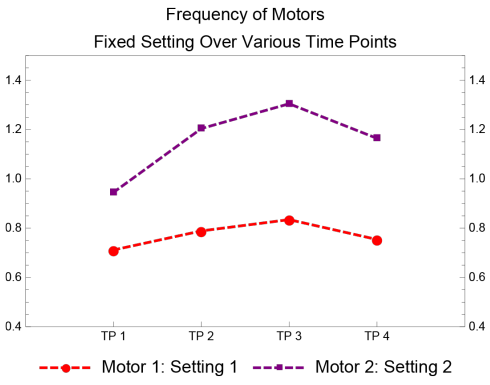

(a) Multiple Time Points

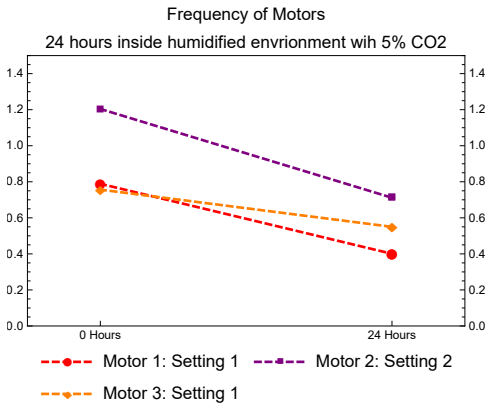

(b) 24 Hours, Incubated

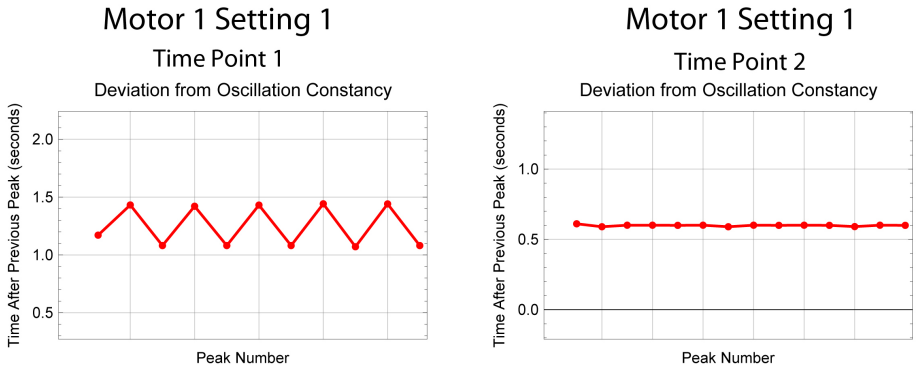

(c) Profile of Rotation over 2 Time Points

Figure 2.8

Analysis of Original Prototype Apparatus: Motor Frequency Results. Settings are the discrete steps on the LEGO controller. (a) Motor frequency calculations taken for motor 1 setting 1 and motor 2 setting 2 over 4 time points separated by at least three days. The results indicate that individual motors do not keep to the same frequency between time points. As well as this, the system does not preserve the difference in frequency between motors through the various time points. (b) Frequency of three motors before and after 24 hours inside a tissue culture incubator. Results indicate that the speed of motors is not fixed after initial setting. (c) Peak to peak analysis indicates that the rotation of motors is not always constant between time points.

Figure 2.9
Membrane Curvature: Protocol C.1; page 233.
The membrane deforms under the weight of the silicone elastomer causing an unequal distribution weighted towards the center of the membrane. Therefore the finite element analysis conducted in Section 2.3.3 cannot represent this system.

2.5.2 Membrane Characteristics and FEM

From conversations with Dr. Buriseci, the finite element analysis conducted for the initial prototype in Section 2.3.3 modelled the membrane as a hyper-elastic cylindrical material. The material parameters were estimated but not made available. The magnet was a rigid body attached to the membrane and the membrane edge was given fixed displacement boundary conditions. The interaction between the magnets was not modelled but instead a displacement was given to the magnet based on an estimate of the system. The analysis represent a large approximation to the system and so any results generated here cannot be used as a 'stimulus map' for the purposes of this thesis.

Further to this, through inspection of excised membranes prepared according to Protocol C.1, the membrane is not uniform in thickness throughout. Intuitively this makes sense. The layer of silicone elastomer applied to the membrane pushes the membrane down under its weight creating a silicone well. As schematised in Figure 2.9, this causes an uneven distribution of elastomer on the membrane.

Taken together, an FEM approach which models the membrane as a cylindrical body does not represent the membrane characteristics from the initial prototype.

2.5.3 Analysis Summary

The analysis of the original prototype uncovers some issues but as well it provides a platform for prototype refinement. In particular, and together with the specific aims of this thesis, redesign had to address the following points:

1. Membrane magnets are not necessarily placed in the center of each BioFlex® well. If a system is to be successful in correlating heterogeneous strain stimulus and phenotype, then this has to be rectified. If the EM is not positioned precisely in the center then experiments are not repeatable.

2. BioFlex® plates are not necessarily positioned over the rotating magnets so that the centroid of the rotating magnets is directly underneath the center of the membrane magnet. Again, this will prevent repeatability.

3. Using battery packs does not provide assurances that motor rotation frequencies are constant or smooth. This assurance is required. Therefore the apparatus is not reliable.

4. Positioning of the motors is limited by the modular spacings of LEGO. Therefore LEGO is not suitable as the building block for re-engineered apparatus in this thesis.

2.6 Prototype Refinement and Redesign

Given the analysis of the original prototype in Section 2.4, the need to re-engineer the apparatus was evident. This section details the iterations of design to increase precision of the prototype. The work culminates with working prototype termed *MagAct*. The work is presented in two sections:

1. Refining the augmentation of BioFlex® plates for consistent EM placement.

2. Re-engineering the original prototype.

The following sections tackle improvements in BioFlex® plate augmentation, the operation and control of the motors and apparatus housing redesign and construction. 3D printing using Nylon SLS printers has been heavily utilised for this purpose.

2.6.1 BioFlex® Augmentation 2.1, 2.2, & 3.1

Refining the augmentation of the membrane to include the EM has been a difficult process. This is primarily because refinements have been constructed and reconstructed based on work described in both Chapters 3 and 4. As work in these chapters has similarly been refined by exploration of BioFlex® augmentations, the list of BioFlex® augmentations to include the EM are detailed here, chronologically, only for reference in future chapters.

Augmentation 2.1

In an initial step to increase the precision of the EM augmentation of the BioFlex® magnets a system was conceived whereby magnets are placed precisely in the center on the underside of the membrane and held fixed during silicone elastomer curing. Holding the magnet fixed in place can be done using a secondary magnet on the other side of the membrane. After the added layer of silicone elastomer cures, the magnet on the cell culture side can be removed knowing the underside magnet is cured in place precisely in the center. In comparison to the photograph in Figure 2.2, this principle is shown schematised in Figure 2.10.

To facilitate precision placement of the embedding of the disc magnet under the BioFlex® membrane, *Magnet Spacers* were constructed in Rhino 3D and printed using Nylon SLS printing. The magnet spacers are discs with an outer diameter of 34 mm with

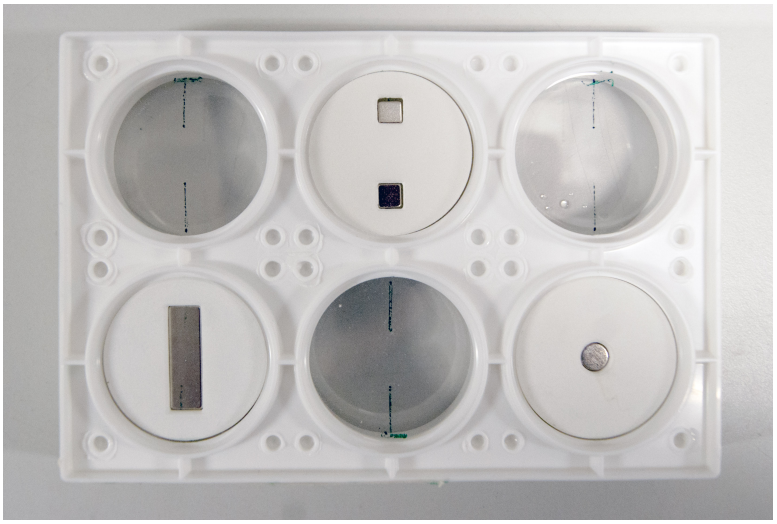

(a) Magnet Spacers on Underside of BioFlex® Wells

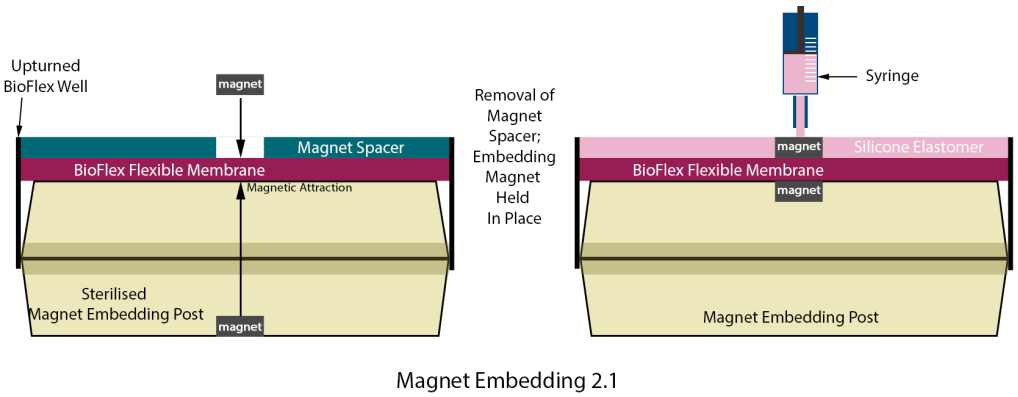

(b) Embedding Schematic

Figure 2.10
BioFlex® augmentation 2.1.
(a) Photograph of magnet spacers on the underside of a BioFlex® plate. Using CAD modelling and 3D printing, the spacers are constructed to position the magnets precisely in the center of each well. (b) Schematic of Protocol C.2. A loading post consisting of 2x35 mm culture dish lids containing a magnet is used to hold the EM in place during curing. This also prevent sagging of the BioFlex® membrane during curing.

central holes and a height of 3 mm . Sat on the underside of a BioFlex® membrane, the spacers sit snugly within the underside of the well allowing the placement of the 6 mm diameter magnet precisely in the center. This is shown photographed in Figure 2.10(a), bottom right corner well. Other spacers for various magnet geometries were also printed and are shown in the same Figure.

The lids of 35 mm culture dishes were used to create a hollow magnetic posts which included a 6(d)x1 mm magnet. Lids were joined together using autoclave tape. This is depicted in Figure 2.10(b). These are referred to herein as 'loading posts'. Through appropriate alcohol sterilisation, BioFlex® plates sit on-top of loading posts. The magnet

contained in the post is attracted to the EM in the spacer. With the spacer removed the EM is then held in place in the center whilst the silicone elastomer cured. This is schematised in Figure 2.10(b).

This refinement attempted to address two criticisms of augmentation used in the original prototype (Protocol C.1; page 233). First, that there is no guarantee that EM are sat precisely in the center of the membrane, and secondly, the addition of the 1 mL elastomer solution causes the membrane to deform under its weight. With the flat surface of the loading post supporting the membrane, it is anticipated that the membrane now cures flat.

With both the new apparatus – magnet spacers and magnetic loading posts – a refinement of Protocol C.1; page 233 was developed. An immediate outcome of augmentation 2.1, however, was that the distribution of silicone elastomer is more evenly distributed over the BioFlex® membrane – images not here presented. This is as a direct result of having a flat surface under the membrane to hold the weight of the elastomer. Although an even distribution of elastomer was sought in this method, it was discovered that is also created an overall stiffer membrane. A downstream implication of this is uncovered in Chapter 4 through measuring strain distributions; such a thick membrane results in very little stretch during magnetic actuation. Ultimately this EM augmentation method proved to be insufficient for delivering heterogeneous strain. The full protocol for conducting augmentation 2.1 is found in Protocol C.2; page 233 but ultimately the method was refined again.

Augmentation 2.2

The stiffer membrane as a result of augmentation 2.1 was detrimental to delivering heterogeneous strain (discussed later in Chapter 4). Because of this, methods of augmenting the membranes to include the EM were sought that did not involve adding a thick layer of silicone elastomer.

To this end, the method described in Figure 2.11(a) was developed. The EM is precoated with a silicone based glue. In the same way as augmentation 2.1, the magnet is then allowed to attract the magnet contained in the embedding post and therefore cure fixed to the center of the membrane.

Similar to the developments in Section 2.6.1, implications of this method were problematic in downstream work conducted in Chapter 3. It was discovered that the embedding post described above (using lids of 35 mm culture dishes), although providing a flat surface, did not sit directly underneath the membrane. Similar to the criticism of the original prototype, this resulted in the membrane curing in a partially deformed status; schematised in Figure 2.11(b). For development of imaging methods in Chapter 3, the membrane is required to be as flat as possible. Therefore this augmentation protocol was once again refined.

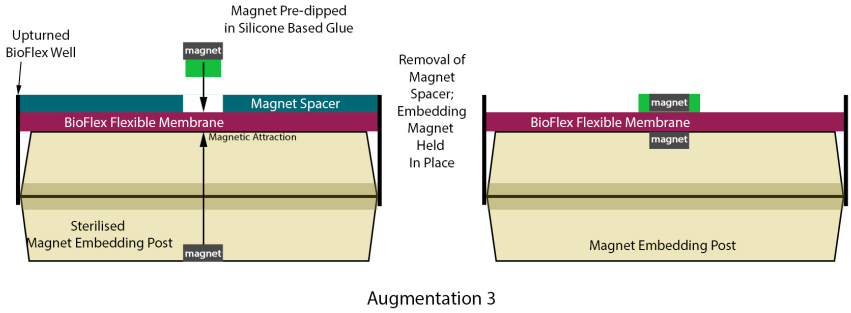

(a)

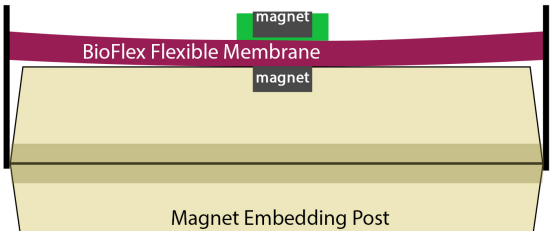

(b)

Figure 2.11
Membrane Augmentation 2.2.
(a) Building upon augmentation 2.1, instead of using a layer of silicone elastomer to fix the EM in place, here the EM is pre-coated with silicone based glue. This was introduced to reduce the stiffness of the membrane. (b) Schematises the core problem with this method, that the embedding post does not reach the membrane. This results in a deformation fixed because of the glue and causes problems for downstream work involving imaging.

Augmentation 3.1

To address the issue of partially deformed membranes after augmentation 2.2 – an issue vital for imaging purposes discussed further in Chapter 3 – 3D printing was employed to re-engineer the embedding post. An embedding post was designed to fit perfectly inside the wells of BioFlex® plate such that there is no gap between the top of the post and the membrane. This is schematised in Figure 2.12. These embedding posts resulted in a flat membrane, and as discussed in later chapters, allowed for efficient fluorescent imaging of the membrane as a whole.

The exploration of imaging methods in Chapter 3 together with strain mapping across the membrane in Chapters 4 have substantially influenced the final BioFlex® EM augmentation protocol. Although having undergone several iterations, the method to augment BioFlex® plates under augmentation 3.1 is defined fully in Protocol 2.1. The loadings posts are shown photographed in Figure 2.13.

Protocol 2.1. BioFlex® EM Augmentation 3.1

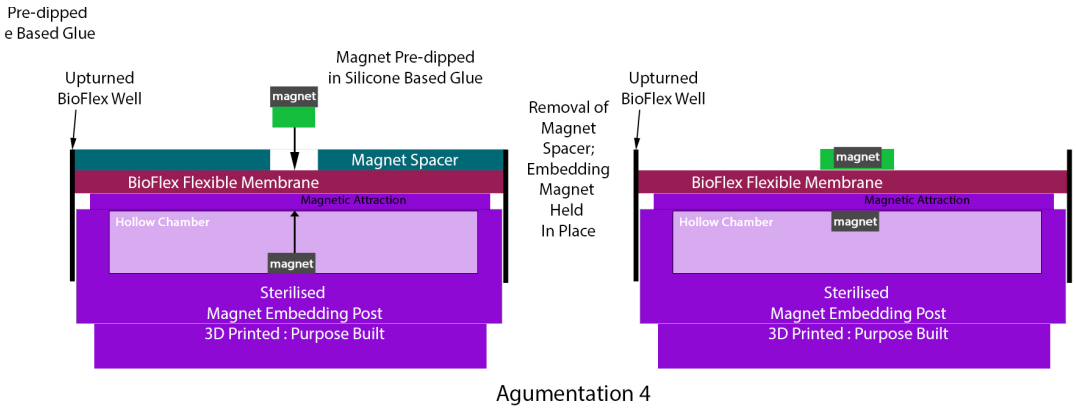

Figure 2.12
Membrane Augmentation 3.1.
Building upon Augmentations 2 and 3, 3D printing was utilised to reconstruct the embedding post. This was done to ensure the membrane is cured flat – a step vital for imaging purposes discussed further in Chapter 3.

Figure 2.13
3D Printed Loading Posts for BioFlex® Augmentation 3.1. 3 loading posts per BioFlex® plate are placed under a sheet of cling film before being thoroughly doused with 70% IMS.

1. For each BioFlex® plate prepare six 3D printed loading posts, each containing a single 6(d)x1 mm magnet. Place the loading posts in a class 2 safety biocabinet in an arrangement that approximates a 6 well plate. Place a large sheet of cling film on top of the six loading posts approximately 300 x 200 mm in size. Douse the the cling film with 70% IMS and allow to air dry completely. This step ensures that the sterility of the membrane is preserved.

2. Open an individually sealed BioFlex® plate inside the safety cabinet.

3. Remove the lid of the plate and hold upside down over the cling film covered loading posts. Push the plate down onto the loading posts, allowing the cling film to move

freely, until the top of the loading posts are touching the ridge of the well. The top face of the loading post will be in direct contact with the membrane.

4. Place the magnet spacer on the membrane. Using a magnetic rod – such as a flat headed screwdriver – attach an EM such that the magnetic poles are consistent with a reference magnet. Squeeze a tube of silicone glue so that the glue protrudes from the nozzle by around 5 mm . With the EM attached to the rod, push the EM into the protruding glue so that the glue reaches, but doesn't cover, the rod side face of the magnet.

5. Separate the magnet from the tube of glue and slowly lower into the magnet spacer. The magnet in the loading post will be attracted and a 'click' will be heard as the magnet reaches the top of the loading post. Carefully separate the EM from the rod and allow around 5 seconds for the EM to settle against the membrane with the loading post magnet holding it in situ. Remove the magnet spacer.

6. Repeat for all wells and allow the glue to cure in the class 2 safety biocabinet for 48 hours.

End of Protocol 2.1.

2.6.2 Motor Housing

The rotation of the DMH was in the original prototype via a steel rod glued to the motor; photographed in Figure 2.4(a). If this rod is misaligned to the axis of rotation then the DMH will wobble. This may be the reason for the stuttering motion deduced in Figure 2.8(c). This section of work is concerned with reverse engineering the LEGO motor housing used in the prototype and retrofitting parts to facilitate a smoother interface between the motor and the DMH. Again, CAD modelling and 3D printing was utilised.

Based on the geometry of the DMH, an interfacing object was conceived using CAD modelling in **Rhino** to sleeve over the 10 mm protrusion (detailed in Figure 2.3) as shown in in Figure 2.14(a)[3]. A suitable design to connect the other end of the interface to the motor was then sought to bridge the DMH. From herein this interfacing bridge will be referred to as the Motor-Delrin Interface (MDI).

To drive design of the MDI, the LEGO motors were de-constructed. Removal of the outer shell of the LEGO motor revealed a double system of planetary gears, photographed and annotated in Figure 2.14(b). The planetary gears serve to slow the natural speed of the motors whilst at the same time maintaining torque.

Initial design of the motor side interface of the MDI was based on re-engineering the entire planetary gear system using 3D printing. This design is shown in Figure 2.15(a). The two attempts to make this design work, and the time spent in doing so, were not

[3]**Rhino** : https://www.rhino3d.com

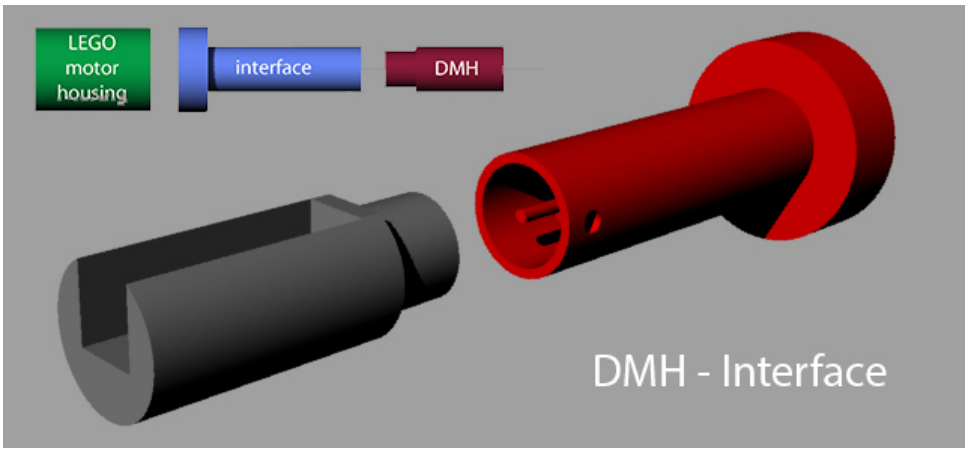

(a) Interface → DMH

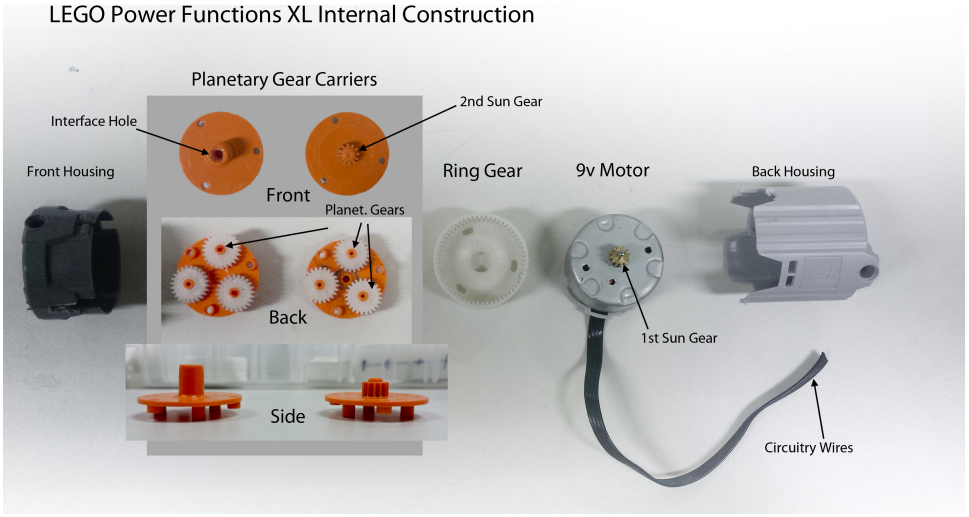

(b) Internal Construction of LEGO Motors

Figure 2.14
Motor Housing Deconstruction and Interface Principle. (a) CAD Model of the DMH side of the interface. The interface is designed to slot snugly over the already constructed DMH. (b) The LEGO motors are geared using a planetary gear system. The interface hole gear carrier is the outermost point of the LEGO motor where previously the steel rod was glued in place. The DMI is iteratively designed together with custom motor housing to integrate with the LEGO motor.

enough to meet the high precision required for the gearing system. This, coupled with frictional problems with the Nylon material used in the printing, halted this approach in pursuit of different solutions and a better use of time.

In moving forward, the second design iteration was centred around keeping all of the LEGO internal components but replacing only the Interface Hole Gear Carrier (IHGC). The pegs in which the gears would have sat in this component were designed to be part of the DMI as in Figure 2.15(b). Similar to the first iteration, the precision required was not achieved. The design was based on vernier calliper measurements of the IHGC.

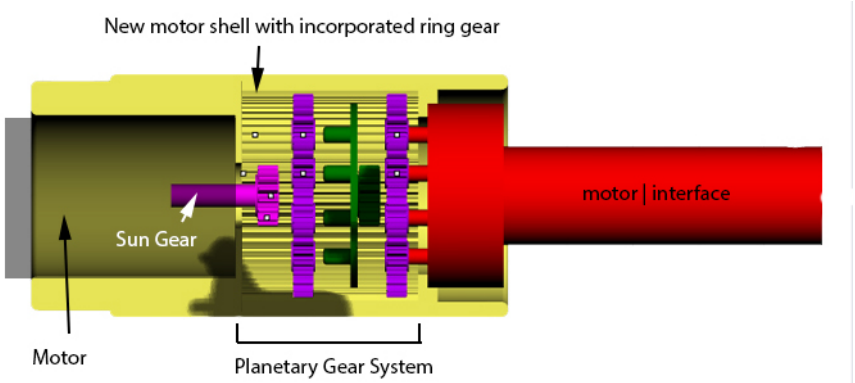

(a) Iteration 1: Printing the Entire Network of Planetary Gears and Housing. Cut-away Schematic

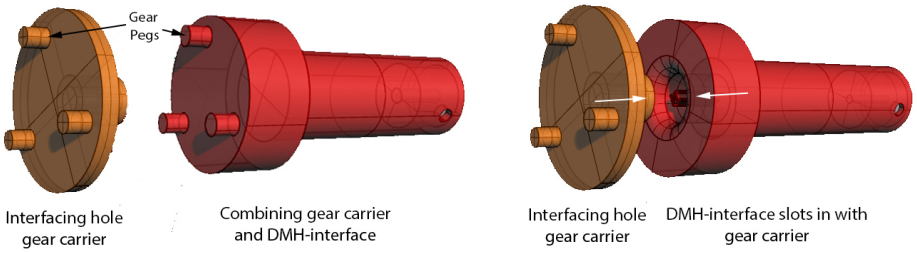

(b) Iteration 2: Replacing only the *interface hole gear carrier*

(c) Iteration 3: Joining only with the *interface hole gear carrier*

Figure 2.15

Motor - Interface Design Iterations. (a) CAD Model replacing all components of the planetary gear system with a 3D printed system similar in principle but the motor interface is rotated directly from the gear cogs. (b) CAD Model where the pegs of the interfacing hole gear carrier were replicated on the motor interface. Again, the precision required to replicate the the triangular position of the pegs using only vernier callipers was not enough to seamlessly integrate the interface with the gears. (c) CAD Model of the interface which accommodates the interface hole gear carrier by slotting into place. This design was implemented for its simplicity.

Calculating the coordinates of each gear post, however, was consistently steeped with error. This error was enough so that the gears were not symmetrically positioned within the ring gear.

After several attempts at designing and printing the two initial iterations enough experience was gained to realise that interfacing directly with the gearing system was not achievable in realistic time scales and with available equipment. Thus, the third iteration was simpler in design and consisted of keeping the entirety of the planetary gear system. A 'docking port' was designed in the DMI which would integrate with the IHGC. This design is shown in Figure 2.15(c). Trials of this design proved were successful in providing a smooth rotation of the DMI and so this design was fixed.

The addition of the DMI requires a new fabrication of the LEGO motor housing. A new design to include the LEGO gearing system, the motor and the newly constructed

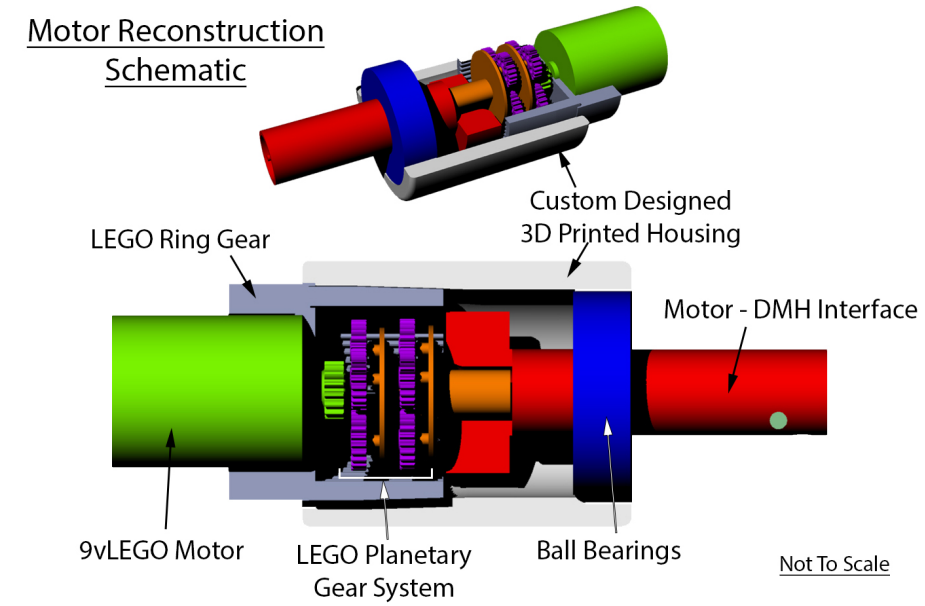

(a) New Apparatus Motor Schematics

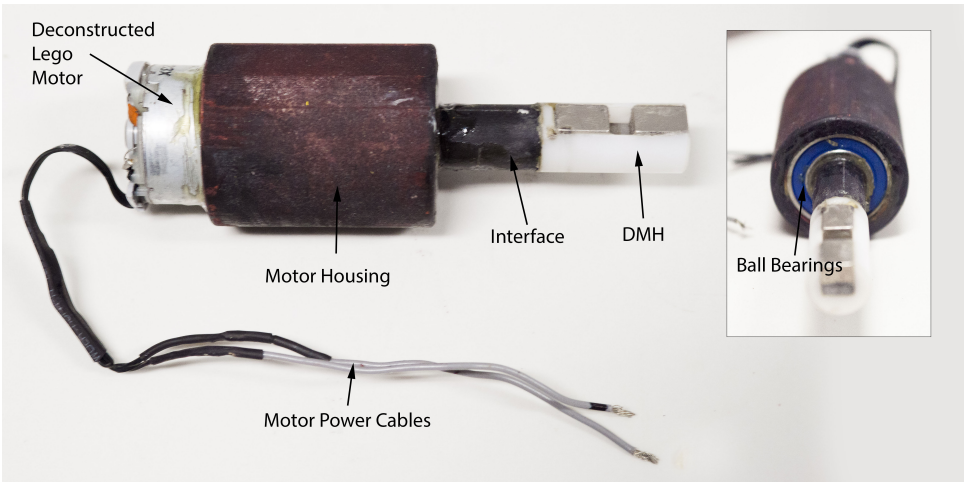

(b) Photographed Final Motor Construct

Figure 2.16

New Apparatus Motor Schematics. (a) Planes cut through cylindrical housing, ring gear and motor-DMH interface to observe internal structure. Housing was designed to accommodate the planetary gear system and to also hold ball bearings to facilitate a smooth rotation of the motor-DMH interface. (b) Image of final motor construct post 3D printing and assembly. 3D printed parts have been given a coating of coloured primer to seal loose residual printing powder. Once in place, the MDI was glued to the internal ball bearing to maintain position.

DMI was designed in **Rhino** based on vernier calliper measurements of key components. With the ability to construct objects freely, an additional cavity to include a 15x32x9 mm ball bearing system was built in. The ball bearing systems were purchased from

amazon.co.uk[4]. This was build in to keep the DMI rotating on the axis of rotation as well as keeping it fixed in place.

The design of this new housing and as well the entire redesign of the motor system are shown in the cut away diagrams in Figure 2.16(a). Figure 2.16(b) shows the design after printing, construction and integration with the DMH. A spray coating of coloured primer has been applied in order to seal any loose powder as a result of the 3D printing process. A two-part epoxy resin has been used to secure components.

2.6.3 Circuitry and Control

Due to the the limitations of the LEGO speed controller, the control and circuity of the original prototype was overhauled. Basic circuitry was conceived so that the refined prototype contained the following:

- A mains supplied power source provided in parallel to the motors.
- Continuous potentiometer dials to finely control the speed of each of the motors.
- On/off switches for each of the motors.

Generic 6V - 28V 3A pulse width modulator (PWM) DC Motor Speed Controller boards were purchased from ebay.co.uk[5]. Pulse width modulators pulse a signal at a high frequency. In the case of motors, pulsing the supply voltage between fully on and fully off at varying frequencies results in changes to the speed of the motors whilst keeping power dissipation to a minimum. Because the amplitude of the voltage supplied to the motor is always constant, the motor is always at full strength. This allows the motor to turn at slower speeds whilst still delivering a constant torque. Generic AC 6A Toggle Switches, power plug connector adapters, and cabling were purchased from Amazon.co.uk[6]. An AC/DC plug adapter was purchased from Maplin. Circuitry was assembled according the the diagram in Figure 2.17 using a 60W Soldering Station (Maplin, A5KJ). Shrink wrap tubing, purchased from amazon.co.uk[7]was used to protect soldered joints. Completed circuitry is shown photographed in later sections.

2.6.4 Motor Rotation Feedback Mechanism

The magnetic field analysis of Section 2.5 was a valuable tool to evaluate motor rotation speeds in the initial prototype. Having a motor rotation feedback mechanism built into the refined prototype is crucial when controlling the motors using potentiometers. Efforts were spent investigating how this could be achieved using the same principles of magnetic field analysis used in Section 2.5.

Initial investigation explored the use of magnetometers in smart phones together with a custom written application to perform the magnetic field analysis (using the

[4]Amazon Marketplace. Supplier: Bearing ShopUK.
[5]Ebay Marketplace. Seller: Comyur.
[6]Amazon Marketplace. Supplier: Sourcingmap.
[7]Amazon Marketplace: Supplier: Rolson.

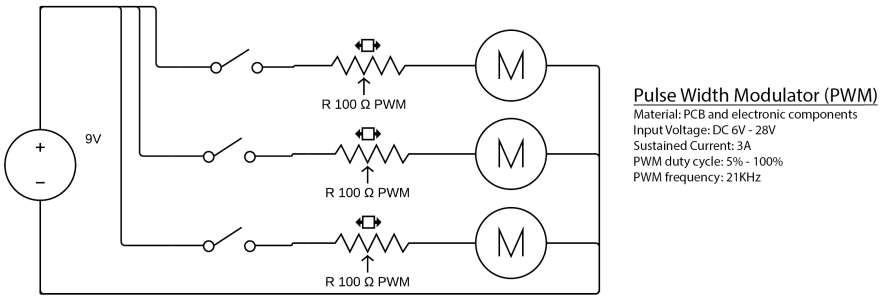

Figure 2.17
Circuit Diagram for Prototype Refinement. The motor constructs are wired after an on/off toggle switch with a pulse width modulator in between which effectively controls motor rotation speed. Each of the 3 motor networks is connected in parallel to a 9V AC/DC power supply.

phone's processor) rather than having to export data to a desktop for processing. The major limitation of this, however, is that motor speeds can only be analysed outside of experimental conditions and only using a smart phone. This was quickly dismissed in favour of a permanent system built into the refined prototype capable of continuous magnetic field analysis. This would therefore provide near real-time motor speed analysis throughout experimentation.

To this end, the use of the open-source microelectronic controller, Arduino, was utilised[8]. Arduino is an inexpensive unit which can be programmed to control a variety of peripheral components – including small sensors and actuators. Included in the wide list of sensors available are magnetometers of the kind found in smart phones. The sensors can be connected to an Arduino UNO through RJ11 cables. The Arduino can be programmed to stream the raw sensor reading to a computer where bespoke software interprets the data stream. Plans were drawn to have three magnetometer sensors built into the refined prototype precisely underneath the centroid of each newly constructed motor.

2.6.4.1 Arduino Feedback: Materials and Assembly

Materials

An Arduino UNO, with Data-Logging Electronics Kit, was purchased from '4tronix' through www.amazon.co.uk[9]. An Arduino Box (housing for Arduino UNO) was purchased from Trinity ICT through Amazon. Generic triple axis compass magnetometer sensor modules (HMC5883L, GY-271) were purchased from www.ebay.co.uk[10]. 4P4C RJ11 female ports were purchased from RS-online (388-2659). Three-meter male to male RJ11 to RJ11 cables were purchased frm RS-online (446-658).

[8] Arduino: https://www.arduino.cc. Last accessed 28th Aug, 2017.
[9] Amazon Marketplace. Supplier: 4Tronix.
[10] Ebay Marketplace. Seller: electro_tv_partss.

Table 2.1
Magnetometer to Arduino Wiring Connections

Sensor Pin	→	**Arduino Pin**
VCC	→	5v
GND	→	GND
SCL	→	A5
SDA	→	A4

Assembly

The basic network for assembling the Arduino circuitry is broken down by the following:

1. Each magnetometer sensor is wired to a 4-pin female RJ11 port.
2. The Arduino UNO is wired to a female 4-pin RJ11 port.
3. The Arduino UNO is connected to a desktop computer via its USB port and cable.
4. Connecting the Arduino RJ11 to the magnetometer RJ11 through a 4-pin male to male RJ11 cable allows selective connecting to each of the magnetometers, and thus each of the motors.

Each magnetometer sensor module was soldered to a five-breakout pad header strip[11]. RJ11 ports are the same as found on telephone lines, and they were chosen here for connection due to thin cabling. In terms of experimentation, this allows connection to the prototype even when inside a tissue culture incubator. The female ports used here have four input ports (4P4C). Although the magnetometer sensor has 5 breakout pads, only four are needed for purposes here.

Arduino cables were soldered from the breakout pad pins on the magnetometer to a RJ11 female port. Similarly, cabling was soldered from the Arduino UNO to its own RJ11 female port so that the connections detailed in Table 2.1 are made when joined by a male-to-male RJ11 cable.

The Arduino UNO, cabling and RJ11 port are held in the Arduino Case. A removable window on the case was utilised to fit a bespoke 3D printed RJ11 port holder for secure and simple connection. These are shown fully assembled in Figure 2.18. The apparatus in Figure 2.18 is herein referred to as the *MagSensor*.

The MagSensor is controlled from scripts flashed to the unit from the desktop **Arduino IDE** software[12]. With the assistance of various guides and forums for programming the Arduino, a small script, based on the Java language, was written and flashed to the MagSensor. When the MagSensor is connected to the magnetometers as well as to a desktop computer through a USB cable, the script commands the MagSensor to read

[11] Prepared according to instructions found here: https://learn.adafruit.com/adafruit-hmc5883l-breakout-triple-axis-magnetometer-compass-sensor/assembly. Last accessed 28th Aug, 2017.

[12] Arduino 1.6.5 can be downloaded from here: https://www.arduino.cc/en/Main/Software

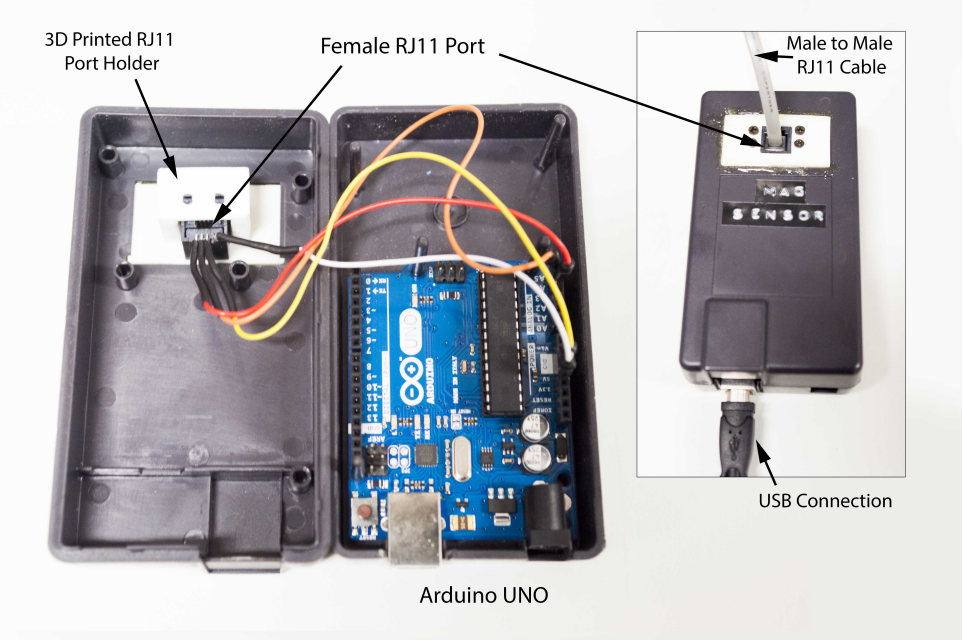

Figure 2.18
Photograph of MagSensor. Arduino UNO connected to RJ11 female port. Connections are made according to Table 2.1. The Arduino is held in a purpose casing. A window in which was utilised to hold the RJ11 port for outer access.

the z-axis magnetic sensor value and transmit it through the desktop COM port at a frequency of 10 milliseconds. This script can be found in Appendix C.3; page 236. Since the data is streamed in near real time, a bespoke program on the desktop can listen to the COM port and process the data according to Algorithm 1.

2.6.4.2 MagSensor Software and Guide

Software to read and analyse the data stream provided by the Arduino sensors was written in **MATLAB** 2015a. It exists as a single page graphical user interface to provide near immediate feedback on the rotation frequency of individual motors.

The processing algorithm embedded in the software is the same as in Section 2.4. In brief, the magnetic field of the rotating magnets is read every 10 milliseconds. These data points are interpolated and differentiated. The distance between the zeros of the differential signal represents the time between each half rotation of the motor. Thus, the averaged rotational frequency can be extracted as well as the standard deviation of half period intervals.

Software Guide

The software has been compiled into a standalone executable program for both Windows and Mac operating systems. Notes on the uncompiled program are given in Appendix C.4; page 237.

When the program has been installed and opened, the opening window is displayed as shown in Figure 2.19(a). The procedure to use the software is given by the following:

1. Ensure that the Arduino UNO is connected both to the sensors as well the computer. For Windows based systems, to connect to the Arduino stream, select the COM port the devices is connected to as well as the BAUD rate the device streams data with. To discover the correct COM port search and open **Device Manager** in Windows and expand the triangle next to '*Ports (COM & LPT)*'. If Arduino is connected it will detail which COM port it is connected to here. In a Mac OS environment this process is different in that the software automatically detects the appropriate COM port.

2. The BAUD rate should be set to 115200.

3. Once the choices have been made, pressing the button '**Test Connection**' will test the connection. If there are connection problems, the error is highlighted by the button colour changing to red, as in Figure 2.19(b). A successful connection with the Arduino will result in the button colour changing to green and the '**Record and Calculate**' button becoming available for use, Figure 2.19(c).

4. The next selection box is to instruct the software over which period to observe the rotation and perform the analysis. The general rule should be that the faster the rotation the less time required to capture the frequency. For a rotation roughly around 1 Hz, 4 seconds of recording is sufficient. Once pressed, the '**Record & Calculate**' button will become unavailable until the action is complete and the graphs and results are displayed, as in Figure 2.19(d).

5. Based on the results, the motors can be adjusted using the potentiometers of the PWM and the '**Record & Calculate**' can be pressed again to refresh the results. This is repeated until the desired speed is set.

2.6.5 Apparatus Housing

Although the design of the prototype refinements have been presented here sequentially, in reality they were investigated simultaneously. Included within this is the design of new housing to accommodate the list of additions and changes described in the previous sections. The motor reconstruction, circuitry and feedback mechanism was, in reality, investigated with a view to be contained as a single unit within bespoke apparatus housing.

Again, CAD modelling and Nylon printing was utilised. Given the precision offered by this modality, DMC's and BioFlex® plates can be positioned exactly so that the center point between rotating magnets sits underneath the center point of each actuating well.

The structure of the printed housing is a cuboidal box with panelled walls. Supporting posts were designed to accommodate M6 square headed bolts running from the top panel

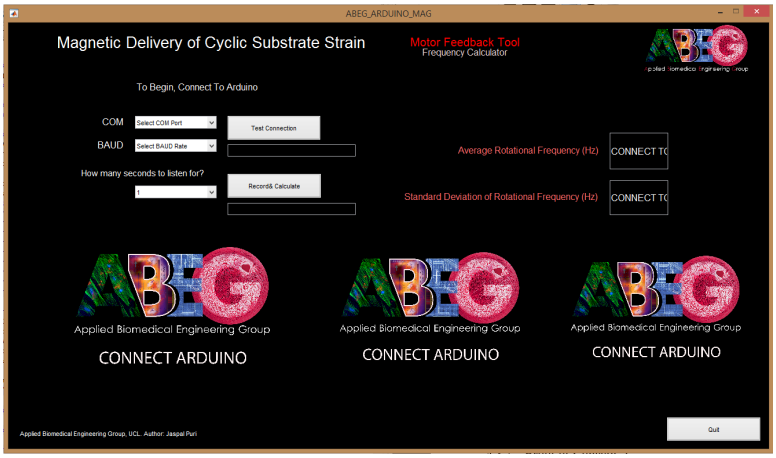

(a) Opening Screen

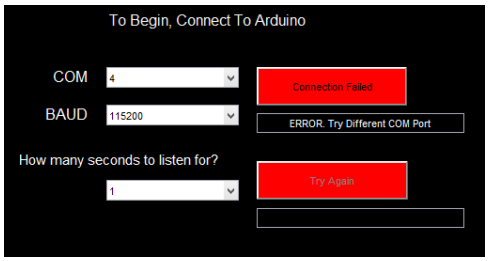

(b) Connection Error

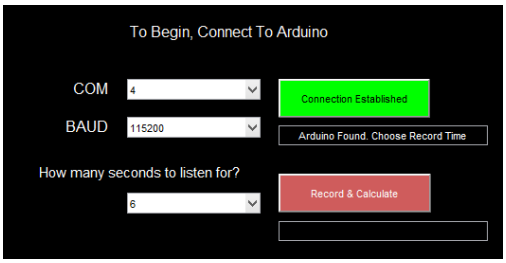

(c) Connection Success

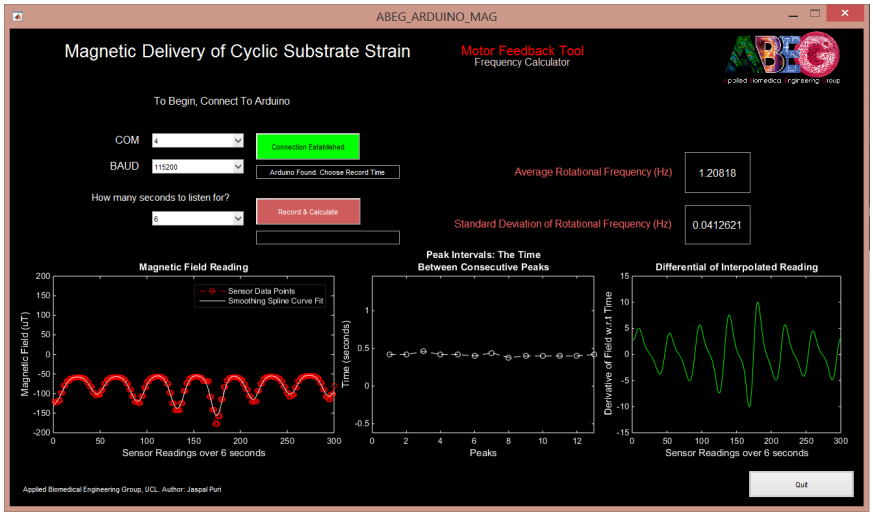

(d) Analysed Data Stream

Figure 2.19
Compendium Images to the MagSensor Software Guide: Section 2.6.4.2 for Windows operating systems.

and fastened underneath the bottom panel using a corresponding nut and washer. For rigidity, the panelled walls have purposely designed indentations for accommodating supporting posts as well as square countersinks on the top panel to hold the bolts flush. Screw holes have been positioned in both the panelling as well the supporting posts for intended use with 3 mm screws. Supporting posts are featured at corners and break

points in the panelling in order to connect together with rigidity and structural support. Indentations are also made to the inner part of the top and bottom panels to hold the DMC precisely in place. To hold the BioFlex® plate in place, an indentation was built into the upper part of the top panel. These designs are annotated in the CAD model in Figure 2.20. The resulting apparatus is herein referred to as *MagAct*.

The cost of 3D printing is decided by the volume of the bounding box of the object to be constructed. Thus, to minimize volume and costs, the housing was designed to be flat-packed requiring self assembly. To minimize costs, the height of the cuboidal box is less than the diameter of the motor construct. Using the precision of CAD modelling, excavations in the top and bottom panel of a cylinder the size of the motor construct allows this; Figure 2.20.

Holes and additional panelling were constructed to accommodate the toggle switches, potentiometers, power supply and RJ11 ports involved in the circuitry of both the motors and magnetometer sensors. Figure 2.21(a) shows the 3D printed apparatus assembled with all components in situ, but without the top panelling. The on/off toggle switch for each motor is situated next to the corresponding PWM potentiometer; Figure 2.21(b). The 9 volt power supply input, PWMs and RJ11 ports are annotated in situ in Figures 2.21(c)(d)(e).

The magnetometer sensors are slotted into three of the seven apparatus legs which hold them precisely underneath the centroid of the rotating magnets. The three legs were designed to hold the sensors on a shelf at a pre-defined distance from the magnets. Cabling for the sensors feeds through purposely placed access ports in the bottom panelling.

Because the system is to be used in cell culture environments, i.e. humid and warm atmospheres, a conformal coating was sprayed on all internal components (rs-online, 497-714). This coating protects electrical components to high temperatures, water, mould growth and oxygen permeability.

2.7 MagAct Summary and Costing

Figure 2.22 shows MagAct fully assembled with a BioFlex® plate held in position over the motors. When comparing this to the FlexCell® system the difference in cost is stark. A quote from the European supplier for the latest FlexCell® Tension System was just under £40,000, a breakdown of this quote is summarised in Table 2.2. This starkly contrasts with the cost of the raw components of MagAct being under £300 and demonstrates the financial benefit of designing and constructing apparatus system in house as well as Nylon SLS printing for experimental and prototyping purposes.

However, cost is not the only difference between the systems. Table 2.3 highlights some key features and differences between FlexCell® and MagAct. Aside from the purposely built in heterogeneous strain distribution, the method of actuation is non-contact. This minimizes any error and inconsistencies which are otherwise involved in applying

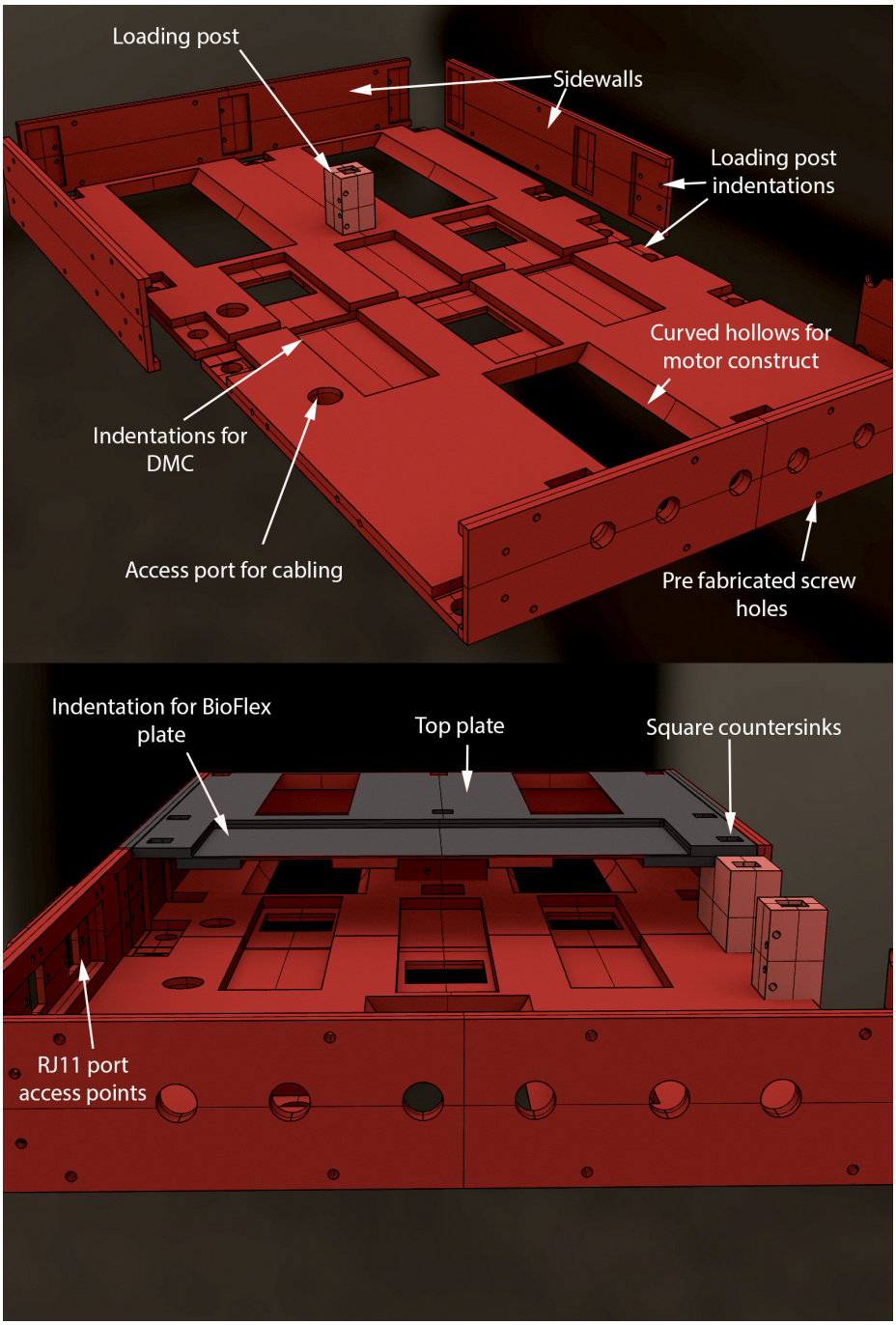

Figure 2.20

CAD Model of MagAct. The body is designed as a panelled box printed flat packed and requiring self assembly. Due to the nature of CAD modelling and Nylon SLS printing, grooves, indentations and screw holes are built into the design and allow for precision construction and ease in terms of assembly. Panelling is held together by loading posts which anchor walls through screws and M6 bolts. Indentations for the BioFlex® plates have been precisely made so that actuated wells will sit precisely over the center points between rotating magnets.

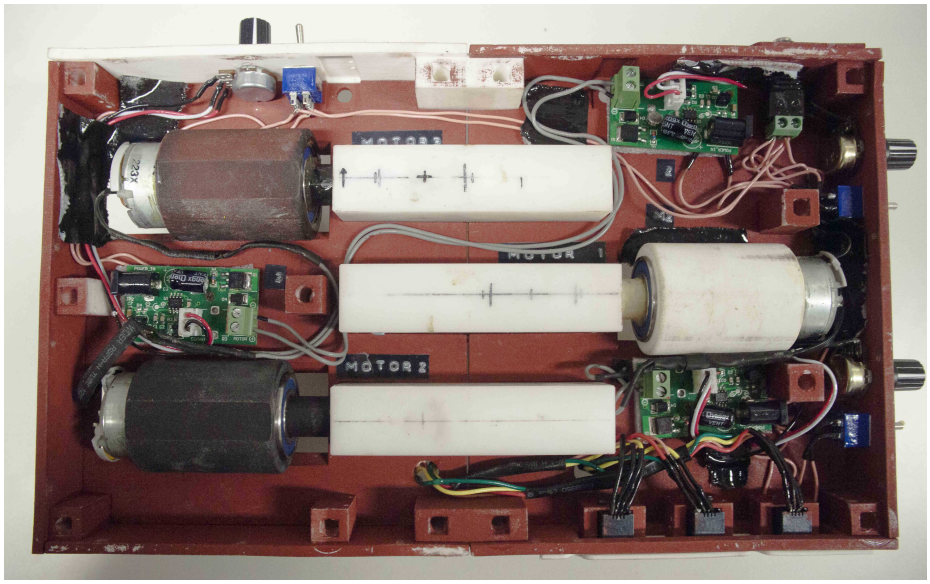

(a) Top Down. Lid removed

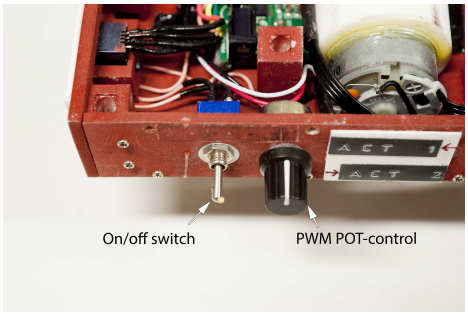

(b) On/off Toggle Switch and Motor Control POT

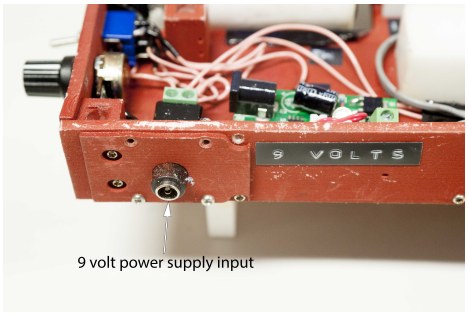

(c) Power Supply

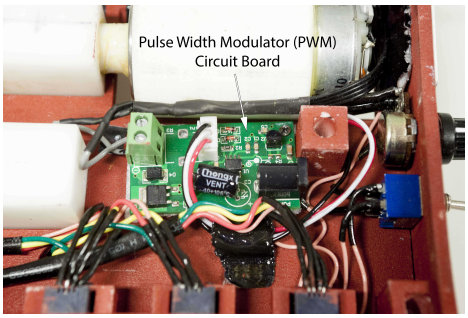

(d) Pulse Width Modulator Board

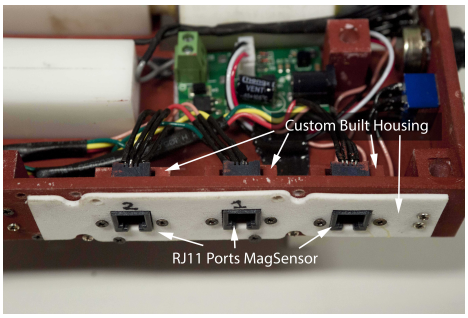

(e) RJ11 Ports for MagSensor

Figure 2.21

Photographs of Internal Structure of MagAct. (a) Displays the completed assembly of MagAct viewed top down without the top panels. Motor constructs and support posts are positioned in pre-fabricated indentations. (b) Displays the on/of toggle switch and PWM POT controls. This image also displays pre fabricated screw holes placed to secure both wall-to-walls as well walls-to-loading posts. (c) The access point for the 9 volt AC/DC supply unit which feeds the motors switches with constant and equal power spread in parallel. (d) The pulse width modulator board is displayed which controls the speed of each motor. (e) The RJ11 ports used to connect the magnetometers, located underneath the apparatus, to the Arduino micro-controller.

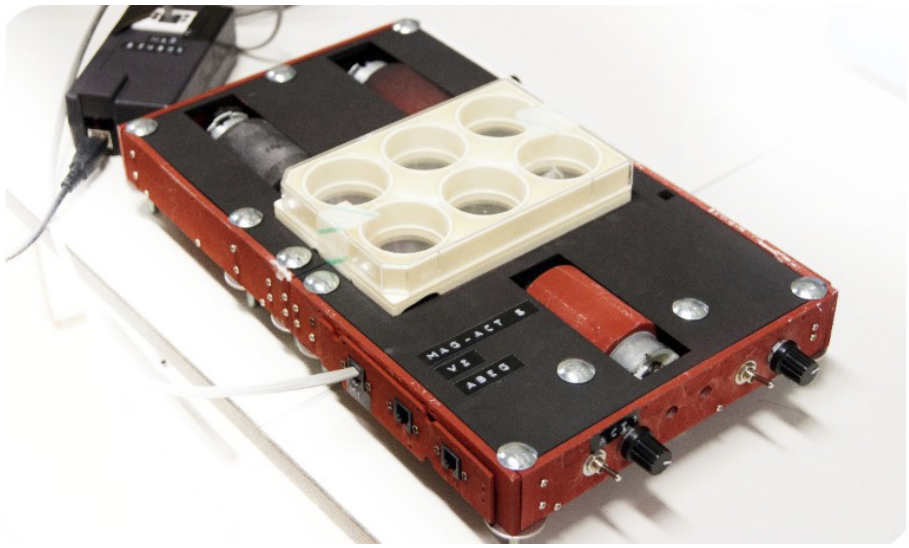

Figure 2.22
Completed MagAct. Image of MagAct after assembly including all circuitry, motors and peripheral components. The BioFlex® plates sits snugly within an indentation designed to hold the plate so that actuated wells are precisely above the centroid of the rotating magnets.

lubricating silicone to the FlexCell® loading posts as discussed in the introductory chapter. The FlexCell® system, as discussed in Section 1.1.2; page 27, is unable to deliver differing strain regimes at any given time; all plates running on the system can only be actuated with the same parameters. MagAct, with independent motor control for each well, allows a greater variety of experimental conditions within the same experiment and thus goes a step further in terms of throughput.

Another advantage of this system is portability. Weighing only a few kg, the device can be transported with ease and accompanying software for the MagSensor can be loaded from a lightweight laptop. The FlexCell® system is heavy in both the number of components involved as well as the weight of each, with the vacuum pump and the vacuum pump controller being the most cumbersome items.

In summary, MagAct is the novel low cost refinement of the original prototype from Section 2.3.2. Together with precision crafted housing of both the motors and apparatus in general, MagAct offers a built in feedback mechanism to report and control the oscillation frequency of strain as well as a constant, mains driven, power supply. Through addressing critique generated through analysis of the original prototype, this body of work has therefore delivered apparatus more suitable for a proof of concept.

Table 2.2
Comparative Costing Between MagAct and FlexCell®
FlexCell® costings provided by Dunn Labortechnik in Euros and are correct as on 7th September, 2015.

MagAct		FlexCell	
Item	**Cost (£)**	**Item**	**Cost (£)**
Apparatus 3D Printed Parts	105	FlexCell® Tension System	35,833.22
Motor Related 3D Printed Parts	30	Trivac D8B Vacuum Pump	2921.27
Arduino UNO	47.91	FlexStops	86.29
Magnetometers	11.85	Shipping and Installation	1096.85
Pulse Width Modulators	11.97		
Peripheral Circuitry Components	10		
Screws & Bolts	8.88		
Total	**225.61**	**Total**	**37,019.86**

Table 2.3
Feature Comparison Between FlexCell® and MagAct.

	FlexCell®	MagAct
Strain Distribution	Homogeneous	Heterogeneous
Method of Delivery	Vacuum	Magnetism
Contact	Lubricated Post	Contact Free
Control	No Well Specific Control	Well Specific Control
Portability	Fixed	Transportable
Strain Feedback	No	No
Frequency Feedback	Yes	Yes
Cost	High	Low

2.8 Chapter Summary

In relation to the original chapter aims in Section 2.1, this body of work has fulfilled the requirement for building a system capable of delivering heterogeneous strain across a BioFlex® plate where the period of oscillation is controllable for each well. Although it has been designed with consistency in mind, this has yet to be proven but further addressed in later chapters. Similarly, although at this point intuitive, the distribution of strain across each membrane is heterogeneous, however the precise values and variance of this distribution is not known but explored in later chapters. In summary, this chapter addressed these aims by:

1. Describing a novel prototype system for delivering strain to cells using magnetic actuation.

2. Analysing the original prototype system in order to refine and develop the ideas.

3. Constructing a novel, refined prototype which encapsulated the following:

   (a) A refined and precise method for EM augmentation of BioFlex®
   plates which allow for whole membrane imaging (to be discussed in Chapter 3).

   (b) A redesign of motor constructs to generate consistency and control in actuating the membranes.

   (c) The development of a motor frequency feedback method which consists of microprocessor together with novel, bespoke control software.

   (d) A redevelopment of circuitry for the purposes of control and consistency.

   (e) The construction of cost effective and precise apparatus housing.

The outcome of this chapter is a novel alternative to the FlexCell® system and apparatus to facilitate the central goals of this thesis. With the ability to deliver a heterogeneous strain distribution, the next two chapters each explore (i) imaging membranes for phenotype map development and (ii) physical analysis to generate the corresponding strain stimulus map.

Chapter 3

Imaging and Automated Analysis

Chapter 2 refined the original prototype and engineered a new apparatus. The assumption at this point is that it satisfies a requirement of this thesis by delivering a controlled heterogeneous strain distribution to a monolayer of cells.

This chapter is concerned with the imaging of these cells over a large area and the automated image analysis required as a result. This section of work spans the duration of the research years and forms the 'right' branch of the research plan – that of generating high resolution phenotype maps from fluorescent imaging. Although the work is presented in two distinct sections – 'Acquiring Images' and 'Automated Analysis', ultimately progress made in each was dependent on progress made in the other.

There is a choice over which strategy to employ when using image analysis for high content screening - utilising commercial softwares, open source applications, or creating bespoke in-house applications. This choice is arguably dependent on the context of the requirement together with the cell assay being performed. Here, the context of utilising image analysis pipelines is in the development of a proof of concept system for arbitrary phenotype assays.

Image analysis suites bundled with microscopy systems are usually a first port of call for researchers wishing to quantify images. However, these often have proprietary data formats, obfuscated image analysis algorithms, and are often impossible/difficult to extend beyond general functionality to make custom updates to software or hardware, (Eliceiri et al., 2012; Lamprecht et al., 2007). Customisation is crucial for the purposes here where all cells on a disc membrane are to be imaged and analysed to a high resolution and such that the behaviour of each cell can be related to the position of that cell on the membrane. Indeed, the software accompanying the imaging system used in later chapters, **MetaXPress**, does allow for customised macros but only through using existing procedures within the software. Coupled with this, the software was available only on the machine running the microscope at the time which meant that algorithm and pipeline development would have been sub optimal.

Open source platforms and plug-ins are far more appropriate to enhancements and development to suit experimental needs. For purposes here, data handling before and

after image analysis protocols is vital as a component to have strict control over. Tools such as **ImageJ (Fiji)** (Schindelin et al., 2012) and **Cell Profiler** (Carpenter et al., 2006) are popular open source platforms where scripts and macros are contributed by the research community and are all customisable. The requirements on the image pipeline here require specific data handling and analysis of images such that there is high unlikelihood that something exists which fit these needs. Therefore, even with an open source platform, scripting and development of existing functionality is likely needed. Together with this, substantial understanding of the scripting languages these tools use is vital to be able to develop anything meaningful.

Therefore, for the establishment of a pipeline consisting of sample preparation, imaging, image preprocessing, image analysis, post processing and data visualisation, a bespoke and customisable application is easier to construct in a familiar programming language than learning something new within open source platforms where several applications and macros within the platform may need to be strung together. Because of this a proof-of-concept pipeline is here developed in **Wolfram Mathematica** which allows for pipeline customisation, data handling, image analysis and data visualisation within a handful of scripts. As part of proof-of-concept development, creating a bespoke application in this way allows for rapid changes dependant on a biological feature of interest and therefore doesn't restrict development to any particular niche.

3.1 Chapter Aims

The aims of this chapter is to develop an end to end pipeline designed specifically for capturing, processing and analysing the cells adhered to BioFlex® membranes. In particular:

1. A method to efficiently image the entirety of a BioFlex® membrane after actuation from the MagAct system developed in the previous chapter.

2. Defining protocols for handling images such that they can all be inputted into a single image analysis pipeline.

3. Develop and script algorithms to extract relevant information within acceptable error from images. Here, this information is colorimetric behaviour of cell nuclei.

4. Demonstrate the end to end pipeline through the creation of phenotype maps - the end result of analysis.

3.2 Acquiring Images

The principle idea of this thesis requires that all cells adhered to the BioFlex® membrane can be imaged to a resolution which allows automated analysis. The analysis should extract the phenotypic state of each cell together with the position of the cell on the

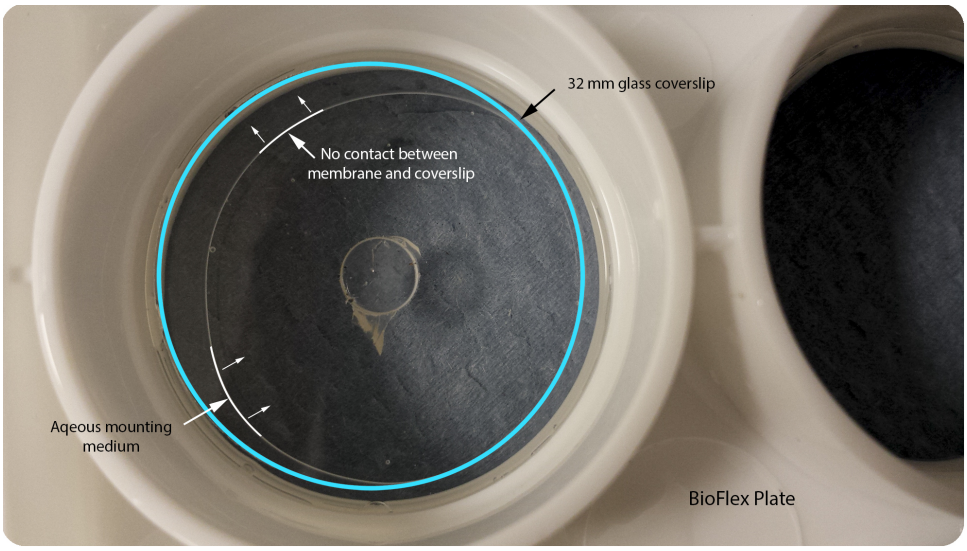

Figure 3.1
Attempt to mount a large glass cover-slip on top of the membrane which has undergone EM augmentation. Here the EM has been carefully removed using a scalpel whilst keeping the membrane intact. The membrane can't be imaged *in situ*. Full coverage of the mounting medium – in this case glycerol based – over the membrane is not achieved. Therefore, to image the membrane it has to be removed from the BioFlex® plate.

membrane. It is only through this that the proposal of heterogeneous stimulus correlation can be evaluated. To do this, the following is required from an image acquisition method:

1. The membrane is mounted for microscopy following cell fixation and fluorescent staining.
2. The membrane must be imaged on a computerised and automated microscope platform.
3. The membrane must be mounted in-plane with the microscope stage.
4. A logical acquisition of multiple images across the membrane is taken with a logic allowing each image to be related to a point in space on the membrane.

The initial stages of this investigation made it quickly clear that membranes had to be excised from the BioFlex® plate in order for whole membrane imaging. This was because the *in situ* BioFlex® membrane does not sit completely flat. Either the weight of fluid (culture medium or fluorescent mounting medium) or the augmentations made by embedding magnets (EMs), distort the membrane in its natural state. This is shown in the photograph in Figure 3.1. In this image attempt has been made to place a cover-slip over the membrane with a layer of fluorescent mounting medium in between. However, coverage of the medium across the membrane was not achieved and is demonstrated by the crescent region of membrane where mounting medium is absent. This indicates that the membrane cannot be held flat for imaging whilst it is part of the BioFlex® plate.

Excision of the membrane in the early stages of this work was conducted carefully using 15A disposable scalpels. The protocol was to cut at at the membrane boundaries, and is detailed later in a more developed form. Excision and membrane mounting is dependent on the microscope used for image capture. The following two sections detail the exploration undertaken for two microscopes.

3.2.1 The Zeiss SteREO Lumar V.12

Preliminary investigation in capturing and analysing all cells of the BioFlex® membrane was conducted using the Zeiss SteREO Lumar V.12 microscope. This was chosen due to its programmable and automated stage capable of capturing fluorescent imaging of large areas.

Efforts were conducted through engineering new microscope platforms using 3D printing, development of membrane mounting protocols and processing and analysis pipelines to handle the outputted images. Figure 3.2 displays images generated using this microscope on both a small cover slip as well as an excised and mounted BioFlex® membrane.

Use of this microscope was deemed not to be appropriate to achieve the aims of this chapter. This was due to a number of factors:

1. The membrane was never in plane to the optics and so multiple $z-$stacks were required. This resulted in a massive dataset as well as the need for intelligent algorithms to determine optimal images from stacks as part of processing. This is seen in Figure 3.2(b).

2. The resolution of the images was poor and such that complex image analysis algorithms would be needed to extract relevant information. The balance between complexity of post processing and image analysis with with quality of image acquisition was sub optimal in terms of efforts.

3. The system, and controlling computer, were not powerful enough to handle the volume of images required and on many occurrences would crash resulting in total data loss.

Although this work was not carried forward lessons were learned about what the imaging pipeline would need to contend with. In particular, because images are not preselected for analysis, the analysis pipeline would need to contend with image artefacts. Investigation using the Zeiss highlighted artefact types detailed in Figure 3.3. In the following section, utilisation of the ImageXPress system is found to be a more efficient way of imaging as well as fostering minimisation of image artefacts.

3.2.2 The ImageXPress System

Around the same time as the development of the membrane augmentation 2.2 in Section 2.6.1; page 72 (where the EM is fixed using glue rather than an additional layer of silicone), a new imaging system was sought after rejecting the Zeiss SteREO. Since the

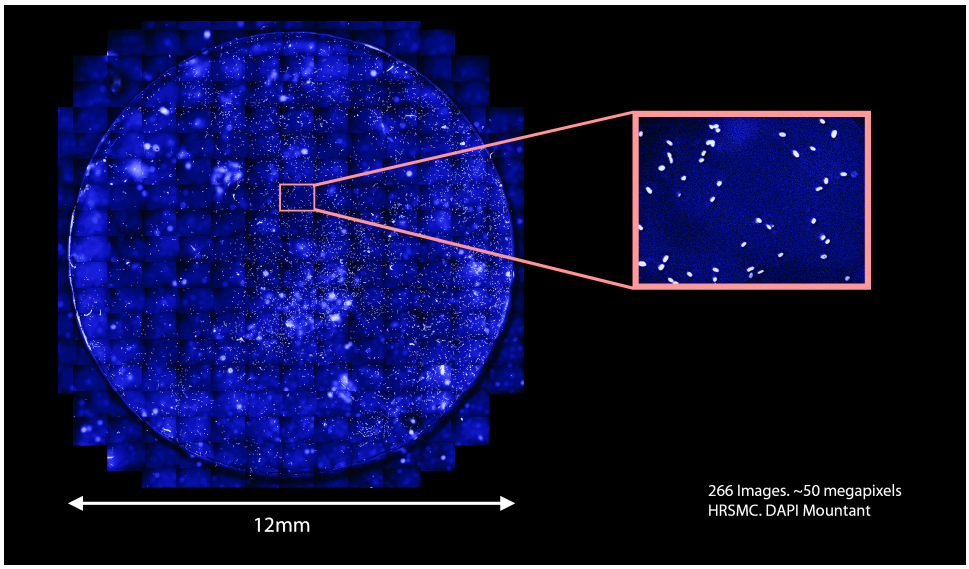

(a)

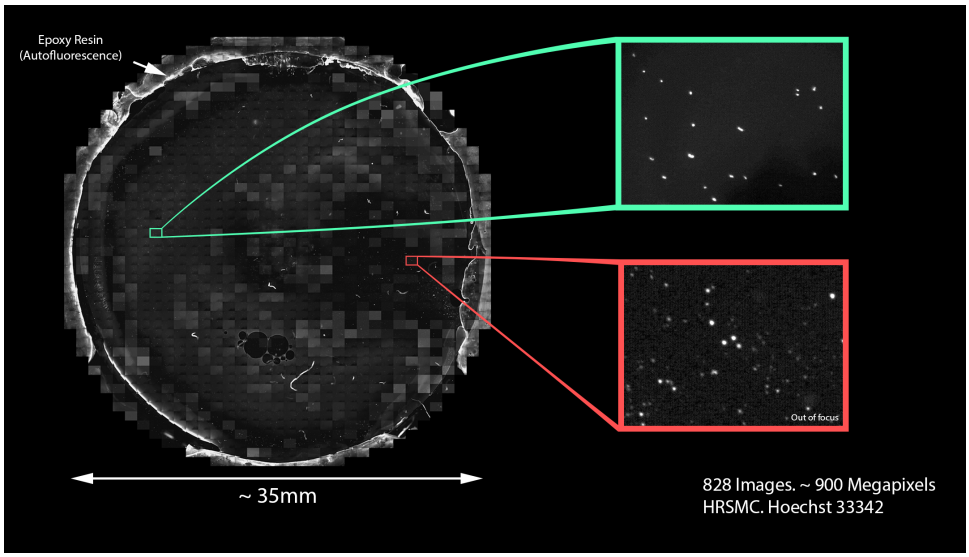

(b)

Figure 3.2
HRSMC Cultured on a Small Cover-slip. Cells were fixed in 4% formalin before mounted on a slide using a DAPI mountant. Imaged using the Zeiss SteREO Lumar V.12 and serves as a proof of capability.

membrane is free of an additional layer of silicone elastomer, it was now more pliable and assumed to be flatter. Consequently, it no longer needed the magnetic pressure clamps and epoxy resin for flat mounting. An alternative mounting protocol was developed to accommodate the ImageXPress Micro XL Widefield High Content Screening System (Molecular Devices). The objective lens for this system, as opposed to the Zeiss SteREO, is below the sample.

A feature of the ImageXPress system is the ability to load 6-well tissue culture plates for automated high throughput image capture of each well. Therefore a protocol was

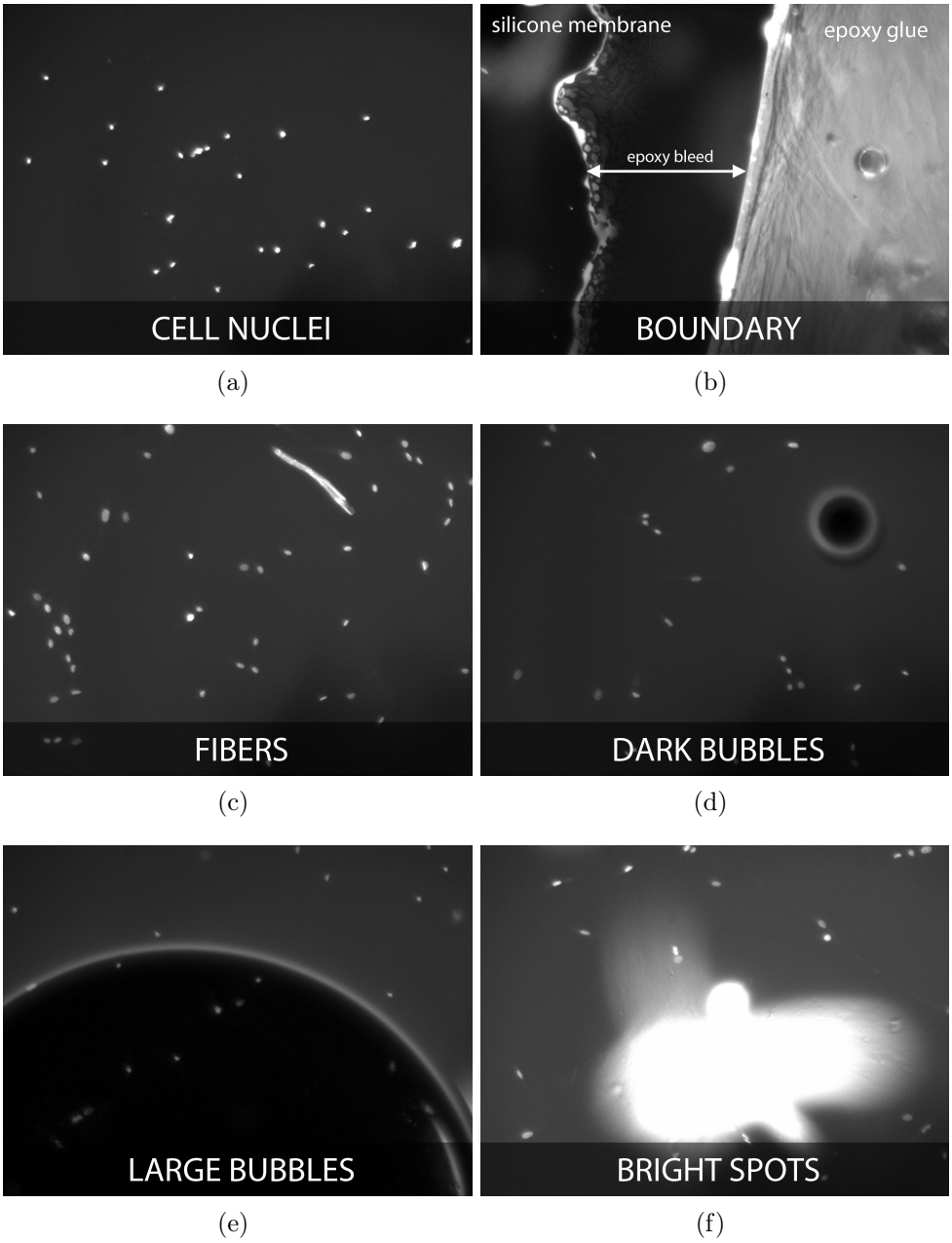

Figure 3.3
Category of microscopy images gathered from pilot data from the Zeiss SteREO. An image analysis algorithm needs to identify inevitable problematic images since manual filtering is impractical. Problematic images include those with fibres, dark bubbles, large bubbles and bright spots. As well as cell nuclei segmentation, the boundary of the membrane has to be identified in order to build the phenotype map.

developed where, after membrane excision from the BioFlex® plates, the membrane were mounted cell-side down into a black walled, glass bottomed 6-well tissue culture plate (P06-1.5H-N; CellVis). These plates are herein referred to as the 'imaging plates'. The protocol is detailed at the end of this section in detail, but in brief, after excision of

the membrane using a scalpel, the membrane is carefully picked up using clean tweezers and a magnetic rod is used to connect with the embedded magnet. The membrane is then lowered into the glass well which has been pre coated with 40 μL of an appropriate mounting medium (20 μL from top to bottom in a line, and 20 μL from left to right in a line resulting in a cross). The magnetic rod is weak enough magnetically to manually separate the membrane magnet from the rod once the membrane has been lowered into place in the well. This is schematised in Figure 3.4(a) and the mounted membrane in the imaging plate is shown photographed in Figure 3.4(b).

The ImageXPress system was programmed using its accompanying software – **Meta Xpress** – with dimensions of the imaging plate provided by the manufacturer. Preliminary tests were conducted to acquire images from BioFlex® membranes seeded with C2C12 cells. Two of the wells from Figure 3.4(b) are shown imaged and stitched (using scripts written in **Wolfram Mathematica**) in Figure 3.5. These images are from the 'UV' channel and show the nuclear Hoechst 33342 staining of C2C12 cells. For print, the images have been colour inverted and enhanced in **Adobe Photoshop CC**. Figure 3.5(a) shows images from a membrane having undergone augmentation 2.2. The bubbles present around the center left of the membrane in Figure 3.5(a) are typical of many images acquired at this time. The absence of these bubbles in membranes which have not been augmented – as in Figure 3.5(b) – indicated that the augmentation protocol cures the membrane in a deformed state. When mounted flat on the bottom of the imaging plate the resting tension of the membrane causes the center to rise up. Usually bubbles which occur in mounting procedures like this can be gently guided to the edge of a sample where they can diffuse. Here however, due to the upward force of the center of the membrane, the bubbles were always drawn to the center, despite guidance. This implied that under augmentation 2.2 the membranes undergo permanent deformation with magnet augmentation.

It is precisely this which drove the redevelopment of the augmentation procedure 3.1 in 2.6.1; page 73. Following this refinement of protocol, the ImageXPress system showed better capability of achieving the aims of the imaging component of this project. Figure 3.6, having been imaged at a higher magnification, demonstrates this. With it's built in automated focusing algorithms, the ImageXPress system both captures images of cells with a clarity far superior than the Zeiss SteREO and with fewer images.

3.2.3 BioFlex® Membrane Excision and Mounting Protocol

The development conducted with respect to the imaging portion of this thesis culminates with the use of the ImageXPress system to provide the cellular data in order to extract phenotype maps using image analysis. The protocol for preparing the BioFlex® membranes for imaging has been refined through many iterations with the primary purpose of minimizing artefacts in images – for example, bubbles and fibres. Measures were introduced which used cling-filmed surfaces to prevent debris and fibres from making contact with either side of the excised membrane. Alongside this, cling

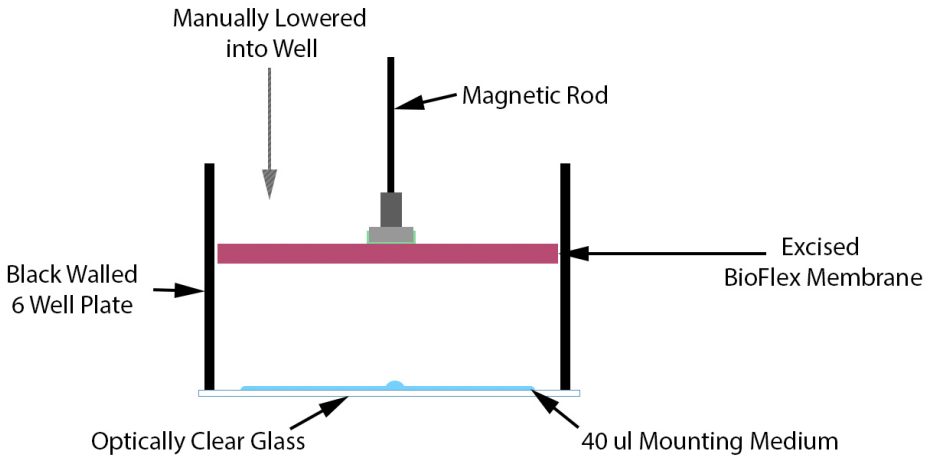

(a) Schematic of Membrane Mounting Procedure.

(b) Image of Membranes Following Mounting.

Figure 3.4
Mounting Membrane in a 6-Well Plate.
(a) Schematic representation of the method of mounting membranes. This replaces the magnet clamp procedure discussed previously. A magnetic rod is used to lower the membrane into a glass well coated with an appropriate mounting medium. Once the membrane is in place, the rod can be removed with a little pressure. (b) A photograph of the membrane in the glass 6-well plate after mounting. Membranes are mounted cell-side down.

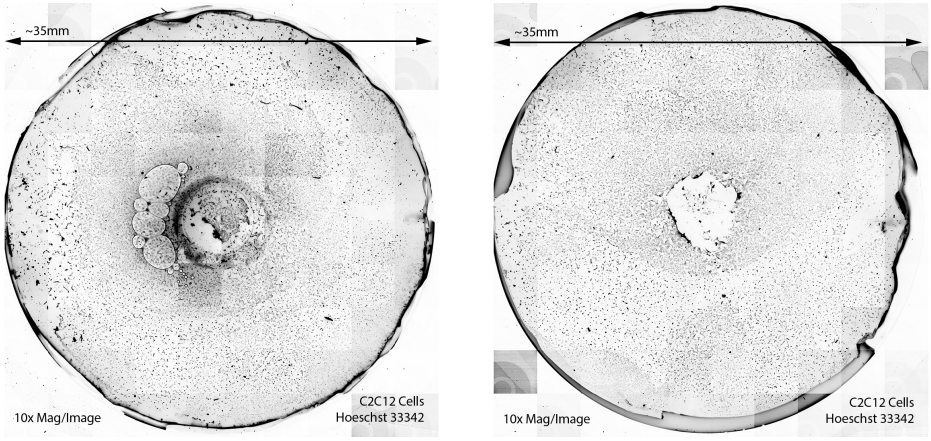

(a) Augmented (b) Not Augmented

Figure 3.5
ImageXPress Imaging 1.
(a) shows a membrane which has undergone magnet augmentation 2.2. The formation of bubbles to the left of the center – which were not possible to guide to the borders of the membrane – indicate the membrane is deformed in its resting state. This spurred the redevelopment of magnet augmentation which resulted in Protocol 2.1; page 74. (b) shows a membrane which has not undergone any augmentation.

film was also used to protect the underside of BioFlex® plates during experimentation to minimise debris making contact with the membrane and therefore minimising image artefacts. This is possible due to the method of actuation being non-contact. These processes are fully described in Protocols 3.1 and 3.2.

Protocol 3.1. BioFlex® Image Artefact Prevention
Once EM's are cured to membranes using Protocol 2.1; page 74, preparation for experimental use should follow these steps to minimise artefacts for imaging purposes.

1. In sterile conditions remove the loading posts and cling film used in Protocol 2.1.
2. Place the lid of the BioFlex® back onto the plate and affix with a small amount of autoclave tape to ensure it does not accidentally fall off.
3. Place the BioFlex® upside down and overlay a large sheet of cling film with one edge aligned with an edge of the plate. Affix the edge of the cling film to the BioFlex® plate using autoclave tape.
4. Repeat with all other edges using a blade to trim cling film edges and ensuring that the cling film is affixed taught.

End of Protocol 3.1.

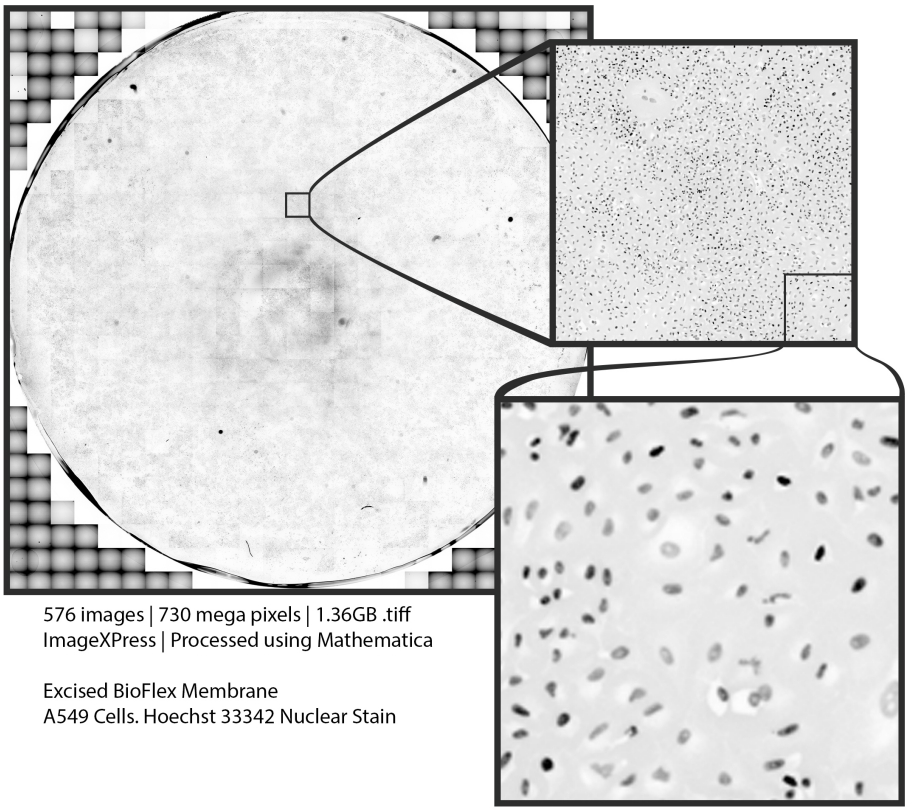

Figure 3.6
ImageXPress: Whole Membrane Imaging.
This image set is the result of having refined the magnet augmentation protocols (Protocol 2.1; page 74). As can be seen, there are no bubble type artefacts. This is typical of images acquired using this Protocol. The membrane here has been imaged at a higher magnification. The clarity of the cell nuclei in these images and the number of images which has been acquired demonstrates this systems power over the original Zeiss platform initially explored.

Protocol 3.2. BioFlex® Membrane Excision and Mounting Protocol

1. On a clean bench with minimal draft, such as that caused by air conditioning systems, lay down several sheets of tissue paper, enough to create a soft cushion. On top of the cushion lay down a clean sheet of cling film, enough to sufficiently cover the area of tissue paper. Using autoclave tape, seal the edges of the cling film to the bench ensuring a taught surface. This is the work surface for excision.

2. Take the cling film-protected and augmented BioFlex® plate (Protocols 3.1 and 2.1; page 74), and carefully remove the cling film protecting the underside of the plate. Place the plate right-way-up on the working surface.

3. In the imaging plate in which the membrane will be mounted, dispense 20 μL of mounting medium (Fluoromount^{TM} Aqueous Mounting Medium, Sigma Aldrich) in a line from one end of the well to the other. Repeat with 20 μL creating a second line so forming a cross of mounting medium in the well.

4. Aspirate and discard any fluid in the well from the BioFlex® plate to be mounted. Using a clean scalpel of size 15A (Swann-Morton Disposable Scalpel 15A, VWR), slowly pierce the membrane at its edge and trace around the edges of the well to excise the membrane. Allow the excised membrane to fall onto the cling-filmed working surface and move the BioFlex® plate to the side. Due to the tacky surface generated by the cling film any debris on the underside of the membrane has an increased chance of being removed.

5. Using clean tweezers, lift the membrane by its edge and, from underneath the membrane, allow the embedded magnet to make contact with a magnetic rod (this is done here using a flat-top torque screwdriver). Whilst holding the membrane by the magnetic rod, inspect the cell side for debris and carefully remove any fibres or particles using fine tweezers. Often during excision the scalpel catches the plastic rim of the BioFlex® plate causing plastic fragments to disperse on the membrane. These should be large enough to be carefully removed.

6. Hold the membrane upside down (cell side facing down) and lower the entire membrane into the imaging well. Once the membrane is in complete contact with the glass well, gently separate the magnetic rod from the embedded magnet.

7. Using a non-magnetic object, for example, a 1 mL pasteur pipette, apply pressure to the membrane to ensure an even distribution of mounting medium across the membrane. If bubbles have formed, gently push the bubbles to the edge of the membrane so that they pop and dissipate. Under the magnet augmentation 3.1 (Protocol 2.1; page 74), this should be possible.

8. Repeat for all other BioFlex® wells requiring imaging, and image within the same day. Do not use clear nail varnish to seal the membrane into place for risk of the varnish bleeding into the cells.

End of Protocol 3.2.

3.3 Automated Analysis

The ability to capture cellular data on the BioFlex® membrane is the first step in forming the phenotype map discussed in the introductory chapter. Given the size of each membrane image set, illustrated by Figure 3.6, it is clear that an automated image analysis pipeline is required to extract relevant information.

The images shown in the previous section have been for a single fluorescence channel – namely UV (488 nm) – intended for a background stain. Together with the data set in Figure 3.6, there would also be at least one more image set for a separate fluorescent channel describing the phenotypic state of each cell. The objectives of the automated analysis are therefore simple, identify all the nuclei across the membrane, and for each cell nuclei, decide, from the second imaging channel, whether it is positive or negative for a phenotype of interest.

Imaging systems like the ImageXPress are equipped with image processing software similar to what is developed in this section. The primary reason for designing something bespoke rather than relying on commercial software is control, as discussed previously. Often commercial softwares do not detail the algorithms behind automation to protect intellectual property. The benefit of creating a bespoke pipeline is to allow full customisation, optimisation and control of data structures.

The remainder of this section is split in two parts: the first defines and introduces preliminary concepts to understand the second part, the development of a nucleus identification and phenotype decision making algorithm.

The field of image analysis is not one of focus for this thesis. Rather, the tools employed in this body of work are used only as a means to an end. It is helpful, however, to clearly define the terminology for context of the methodology and algorithms developed here.

3.3.1 Preliminaries and Definitions

3.3.1.1 Digital Images

An image is here defined as a graphical representation of a matrix where each element is a single value or a vector of values which maps to a pixel, a digital representation of colour, by the colour space the image is defined within.

For example, in the 8-bit Grayscale model, each element has a single integer value from 0 to 256. In this model, each element is interpreted as an intensity which ranges from 0 – complete absence of intensity (black) – to 256 – maximum intensity (white) – with all other values ascribed to 'greyness' in between.

In the 8-bit RGB colour model each pixel is a triplet of values where each takes a single integer value from 0 to 256. Each element of the triplet represents the level of total red, green, and blue, respectively, to be summed giving a specific pixel colour. In this model there are 256^3 colour options available.

In terms of notation, we define an image in standard matrix notation as, $\mathbf{I} = I_{ij}$ where I_{ij} is the element in the i-th row and j-th column where $i \in \{1, \ldots, n\}$ and $j \in \{1, \ldots, m\}$. Thus, the resolution of the image, defined as the total number of pixels, is equal to $n \times m$.

3.3.1.2 Algorithmic Manipulation

Digital images are a representation of numerical matrices and thus images can be algorithmically transformed by manipulating this matrix. Furthermore, through suitable manipulations, 'features' can be extracted from images. A feature is here defined as an object of interest, be it the eye colour of all faces in photographic images, or more particular to this thesis, specific biological aspects in microscopy images.

3.3.1.3 Image Arithmetic

Just as with mathematical matrices, images also have basic algebraic properties for image operations. For example, if $\mathbf{I}^1 = I^1_{ij}$ and $\mathbf{I}^2 = I^2_{ij}$ are images then the following is possible:

1. Addition. Images can be added together:

$$(\mathbf{I}^1 + \mathbf{I}^2)_{ij} = I^1_{ij} + I^2_{ij}. \tag{3.3.1}$$

2. Subtraction. Images can be subtracted from one another:

$$(\mathbf{I}^1 - \mathbf{I}^2)_{ij} = I^1_{ij} - I^2_{ij}. \tag{3.3.2}$$

3. Scalar Multiplication. If $c \in \mathbb{R}$ then:

$$(c\mathbf{I}^1)_{ij} = c \times I^1_{ij}. \tag{3.3.3}$$

3.3.1.4 Thresholding

Often in digital image processing, thresholding is employed to binarize a grayscale image into either black or white. The simplest method of doing this is by replacing pixel values below a set threshold, I_{crit}, with 0 if I_{ij} is below and 1 if it is above. With this, it is hoped that the pixels equal to 1 are only those of the features of interest in the original image. The choice of this value can be set manually, however, and as discussed later, for processing of many images in a batch, the choice of I_{crit} is likely to cause error.

Methods to calculate the best shareholding value for an image exist. For example, a common method is Otsu's Thresholding Algorithm (Otsu, 1979). Broadly, this method is based upon minimizing intra-class variance. Otsu's method is packaged with **Wolfram Mathematica** and is used in this chapter for the construction of an image analysis pipeline.

Although there are many choices of thresholding algorithm to use, none may be suitable for use on a large collection of images and this is a subject discussed in later sections. Table 3.1 displays the application of several algorithms to an image of cell nuclei. As can be seen, none are able to threshold only cell nuclei.

For work in this thesis the Otsu method is chosen as the algorithm of choice. However, this choice is arbitrary. Instead of refining algorithms for thresholding, the focus in this

body of work is to standardise images through pre processing such that thresholding becomes trivial. Therefore, the choice to use Otsu's method is one of convenience.

Table 3.1
Examples of thresholding algorithms applied to a microscope image of cell nuclei. Thresholds performed in **Wolfram Mathematica**.

Threshold Description	Image
Original Image Image shows HUVEC's nucleii stained with Hoechst 33342.	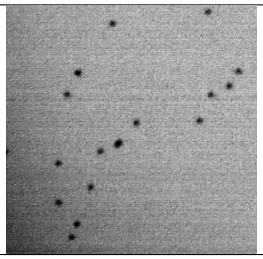
Cluster Method Otsu's method; cluster variance maximisation.	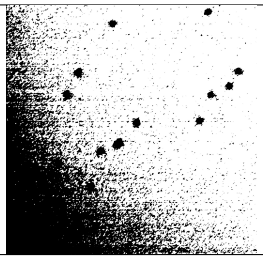
Entropy Method Kapur's method; histogram entropy minimisation.	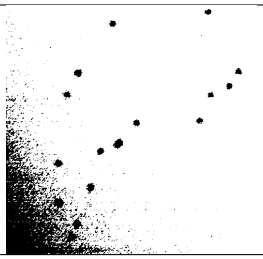
Mean Uses the mean pixel in the image value as the thresholding value.	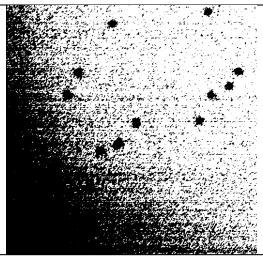
Median Uses the median pixel value in the image as the thresholding value.	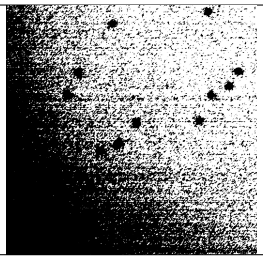
Minimum Error Kittler-Illingworth minimum error thresholding method.	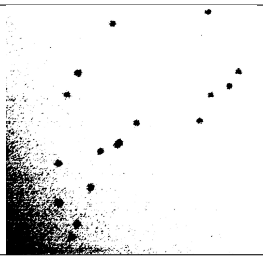

3.3.1.5 Image Kernels

Image kernels are heavily used in image processing applications to extract or enhance features of interest in an image. These kernels are usually small, square matrices 'convolved' with the matrix representation of an image. Convolution is an operation loosely related to mathematical convolution but not the same as matrix multiplication. Given a kernel, $\mathbf{K} = K_{kl}$ where $\{k, l\} \in \{1, \ldots, N\}$, convolution with an image, $\mathbf{I}$, can be written mathematically in two dimensional discrete form as:

$$(\mathbf{I} \star \mathbf{K})_{i,j} = \sum_{\beta=1}^{2\theta+1} \sum_{\alpha=1}^{2\theta+1} I_{i+\alpha-\theta-1, j+\beta-\theta-1} K_{-\alpha,-\beta}, \tag{3.3.4}$$

for $(2\theta + 1)^2 = N^2$ and $\theta \in \mathbb{Z}$. Equation 3.3.4 can be understood by considering the following small kernel and image:

$$\mathbf{K} = \begin{pmatrix} a & b & c \\ d & e & f \\ g & h & i \end{pmatrix}, \qquad \mathbf{I} = \begin{pmatrix} I_{11} & I_{12} & I_{13} & I_{14} \\ I_{21} & I_{22} & I_{23} & I_{24} \\ I_{31} & I_{32} & I_{33} & I_{34} \\ I_{41} & I_{42} & I_{43} & I_{44} \end{pmatrix}, \tag{3.3.5}$$

such that

$$\mathbf{I} \star \mathbf{K} = \begin{pmatrix} I'_{11} & I'_{12} & I'_{13} & I'_{14} \\ I'_{21} & I'_{22} & I'_{23} & I'_{24} \\ I'_{31} & I'_{32} & I'_{33} & I'_{34} \\ I'_{41} & I'_{42} & I'_{43} & I'_{44} \end{pmatrix}. \tag{3.3.6}$$

Then, to take I'_{22} and I'_{23} as an example, equation 3.3.4 gives

$$\begin{aligned} (\mathbf{I} \star \mathbf{K})_{2,2} = I'_{22} =& iI_{11} + hI_{12} + gI_{13} \\ &+ fI_{21} + eI_{22} + dI_{23} \\ &+ cI_{31} + bI_{32} + aI_{33}; \end{aligned} \tag{3.3.7}$$

$$\begin{aligned} (\mathbf{I} \star \mathbf{K})_{2,3} = I'_{23} =& iI_{12} + hI_{13} + gI_{14} \\ &+ fI_{22} + eI_{23} + dI_{24} \\ &+ cI_{32} + bI_{33} + aI_{34}. \end{aligned} \tag{3.3.8}$$

Image kernels transform each element in an image through a linear combination of surrounding elements. In photographic manipulation software, as well as image feature extraction algorithms, kernels can be used for blurring, sharpening, detecting edges and gradients amongst others. Table 3.2 gives examples of various kernels convolved with an image for context and reference for kernels used in algorithms developed later in this chapter.

Table 3.2
Examples of image kernels convolved with 'Lena' – the archetypal image used in exploration of image analysis techniques. Convolutions performed in **Wolfram Mathematica**.

Description	Kernel	Convolved Image
Identity Similar function as the identity matrix in linear algebra. This kernel leaves the image unchanged.	$\begin{pmatrix} 0 & 0 & 0 \\ 0 & 1 & 0 \\ 0 & 0 & 0 \end{pmatrix}$	
Gaussian Blur (Approx) This blurs the images by reducing the pixel value differences in adjacent pixels.	$\frac{1}{16}\begin{pmatrix} 1 & 2 & 1 \\ 2 & 4 & 2 \\ 1 & 2 & 1 \end{pmatrix}$	
Sharpening This does the opposite of blurring; this kernel enhances the pixel value differences in adjacent pixels.	$\begin{pmatrix} 0 & -1 & 0 \\ 1 & 5 & -1 \\ 0 & -1 & 0 \end{pmatrix}$	
Embossing A popular filter in image processing applications. This filter enhances the pixel value differences in a given direction and creates the illusion of depth.	$\begin{pmatrix} -2 & -1 & 0 \\ -1 & 1 & 1 \\ 0 & 1 & 2 \end{pmatrix}$	
Outline This kernel helps to detect edges in an image by enhancing the large differences in neighbouring pixels.	$\begin{pmatrix} -1 & -1 & -1 \\ -1 & 8 & -1 \\ -1 & -1 & -1 \end{pmatrix}$	
Bottom Sobel Like the 'Outline' kernel above. This filter highlights the large differences in neighbouring pixels in a given direction. In this case it is the differences from bottom to top.	$\begin{pmatrix} -1 & -2 & -1 \\ 0 & 0 & 0 \\ 1 & 2 & 1 \end{pmatrix}$	

Table 3.3
Histogram Matching
Histograms of example images 1 and 2 are shown underneath. By matching the histogram of Image 2 to Image 2, the image becomes visually comparable (Image 2 HM).

Image 1	Image 2	Image 2 HM
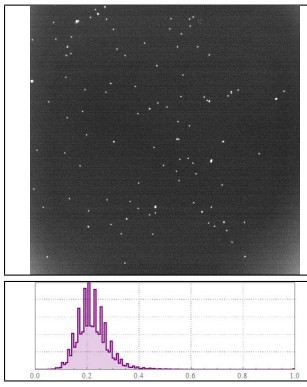	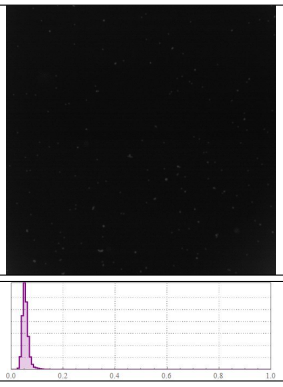	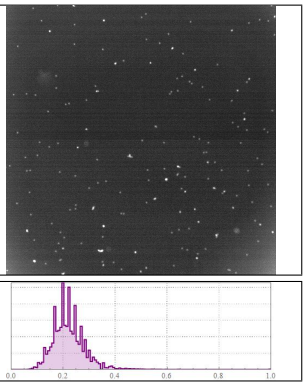

3.3.1.6 Histogram Matching

The histogram of a grayscale image is the discrete probability distribution of all the pixels in the image. Histogram matching is the process of transforming one image so that its histogram matches the histogram of another image. This is a useful tool to standardise images in order to maintain constant brightness and contrast levels.

Table 3.3 shows this in practice. Image 1 and Image 2, although captured from a single sample using the ImageXPress system, are visually different. This is because the software controlling the microscope also controls how the system processes the image. The second row shows the histograms of each image which are also notably different. By matching the histogram of Image 2 to Image 1 the image and histogram becomes visually comparable.

This process is useful when automation is required. Standardising all images by a single image helps to ensure that an algorithm based on defining specific parameters will work in the same way across all images.

3.3.1.7 Image Partitioning & Image Stitching

Image partitioning is used later in this chapter. It is the process of dividing an image into smaller images. Image stitching is the process of assembling a single image from joining smaller images.

3.3.1.8 Watershedding

Watershedding is a commonly used method in image analysis to segment features within an image. The details of watershedding algorithms go beyond the scope of this project but because they were packaged with **Wolfram Mathematica**, are used in incoming development of image analysis pipeline.

3.3.2 Nucleus Identification: Algorithm Building

In the research conducted in this thesis, fluorescent staining is predominantly in the cell nucleus. Thus for quantification, cell nucleus identification from fluorescent images needs to be automated. This section leads to and details an algorithmic processes to identify cell nuclei in images to achieve the aims of this research. Once every cell nuclei has been identified, a secondary step in the pipeline decides whether for each cell nuclei, the cell is positive or negative for a phenotype of interest.

The image in Figure 3.7(a) is frequently used as an example in the coming sections. For completeness, the image is of Human Umbilical Vein Endothelial Cells stained with Hoechst 33342 and taken from a set of images acquired on the ImageXPress system.

By considering a greyscale image to be a density plot, it is useful here to view the image as a 3-dimensional surface plot. This is shown in Figure 3.7(b) where pixel values of the image in 3.7(a) are considered as physical heights. Viewing the image in this way shows the level of noise generated by the grainy background. Pre processing the image using a Gaussian Filter with a radius of 5, defined in Table 3.2, decreases the effect of this noise and accentuates the spikes representing the cell nuclei. The representation of this as a surface is shown in Figure 3.7(c).

3.3.2.1 The Problem With Thresholding

Thresholding an image to extract objects of interest is a useful tool when the value of I_{crit} is selected manually. However, for large numbers of images where unbiased automation is required – that is, images which cannot be preselected for analysis – it is not always the case that a single value of I_{crit} will successfully binarize only the objects of interest. Further to this it is not true that a value of I_{crit} exists that successfully binarizes only the objects of interest. This is demonstrated in Figure 3.8. In terms of surface representations of images, thresholding can be considered as a cut-off plane (shown in green) where everything above the plane is characterised uniquely from everything below. In Figure 3.8, there exists no thresholding plane which separates the cell nuclei from the background.

In the original image (Figure 3.7(c)), there is lens shadowing in the bottom left corner. This amounts to a steady gradient increase in the background of the image seen in Figure 3.7(c). It is thus impossible to find a cut-off plane value which separates cell nuclei from background. In Figure 3.8, the cut-off plane varies from 0.5 to 0.8 illustrating that either to much of the background is captured or too little of the feature of interest.

3.3.2.2 Conical Specific Enhancement

Given thresholding is so useful for feature identification, research was focussed on methods to solve the thresholding issue discussed above. If images can be reliably thresholded so that only cell nuclei were included, then a watershedding algorithm would be able to segment the nuclei.

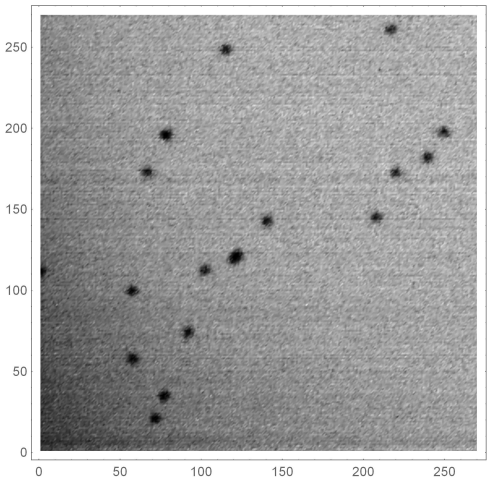

(a) Hoechst Stained Nuclii

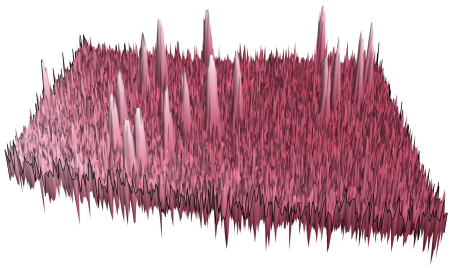

(b) Pixel as Height

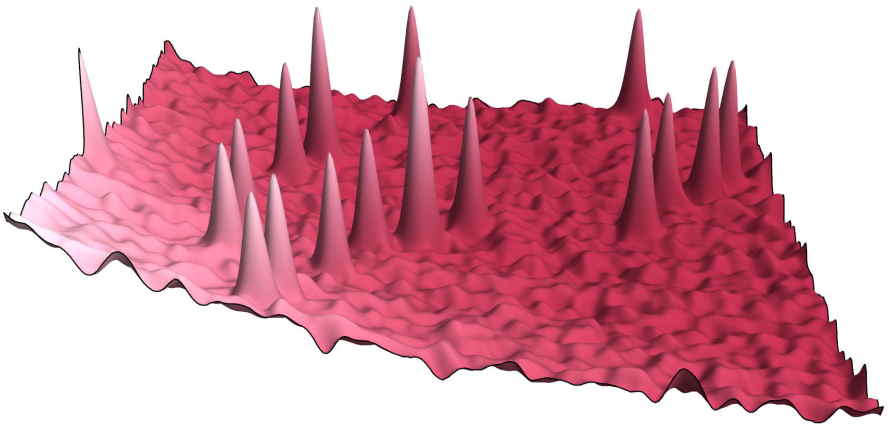

(c) Pixel as Height: Gaussian Filtered

Figure 3.7
Grayscale Image Visualised as A Surface Plot
(a) Shows the original microscopy image taken from an image set acquired using the ImageXPress system. The image is of Human Umbilical Vein Endothelial nuclei stained with Hoechst 33342. (b) Here the image is expressed as a surface plot where each pixel value translates to height. The surface plot is clearly noisy. (c) Here the image is represented as a surface plot after the application of a Gaussian filter with a radius of 5. The background noise has been diminished and cell nuclei are clearly visibly as spikes resembling cones.

A solution to this problem began with the realisation that in 3-Dimensional space (Figure 3.7(c)) cell nuclei appear as cones. The geometry of a cone is such that there is a symmetry in the gradient around the z-axis. Along with this, the second derivative of the cone is both non-zero and recovers the 'cone spike' but in the opposite direction. This

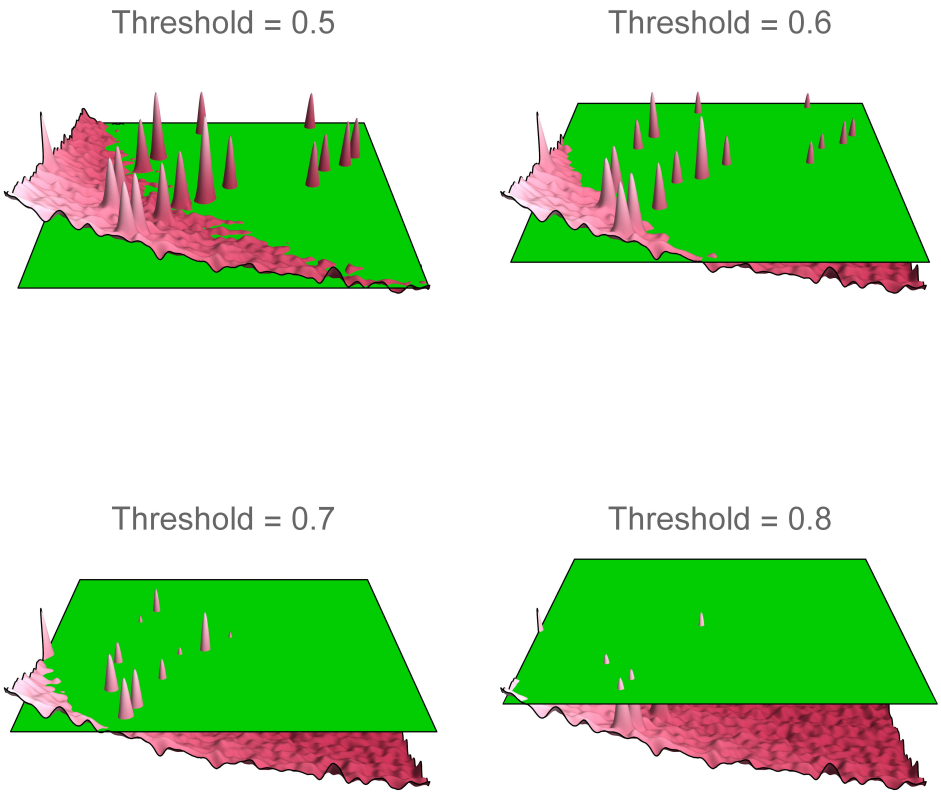

Figure 3.8
The Difficulty of Single Value Image Thresholding
Thresholding can be considered as a plane cutting through the surface plot of Figure 3.7(c). The images here demonstrate that for this image, no thresholding plane exists which successfully seperates the image features (cell nuclei) from the background. In this image, this is because the background is not flat, and instead increases in gradient towards the left corner.

is visualised in 2-dimensions in Figure 3.9. The curve in Figure 3.9(a) is differentiated to give the curve in Figure 3.9(b). The second differentiation in Figure 3.9(c) produces a cone like curve with additional spikes at what would be considered the edge of the original cone. The increasing gradient in the background of the original image, because it is linear, would not be recovered in the second derivative and would be zero.

To exploit this conical feature of cell nuclei, kernel operations were defined and used. The gradient of an image can be computed by subtracting each pixel value from a chosen value neighbouring the pixel. Here, four kernels were defined in four spatial directions across the image. Equation 3.3.9 produces the first derivative in the x direction (i.e. from left to right in the image), 3.3.10 gives the first derivative in the y direction (top to bottom), 3.3.11 gives the first derivative in the diagonal direction (top left to bottom right), and 3.3.12 gives the first derivative in the opposite diagonal direction (top right

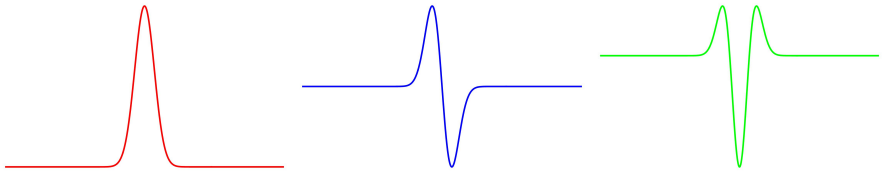

(a) C (b) C' (c) C''

Figure 3.9
Gradients of a Conical Projection. The shape of cell nuclei is conical after a Gaussian filter. It follows that the spatial derivative (and 2nd derivative) of the nucleus will be symmetric in every direction and suggests the use of 2nd derivatives to specifically enhance cell nuclei in an image. (a) shows a 2-D cone shape. (b) shows the first derivative of (a). (c) shows the second derivative of (a).

to bottom left);

$$\mathbf{d_x} = \begin{pmatrix} 0 & 0 & 0 \\ -1 & 1 & 0 \\ 0 & 0 & 0 \end{pmatrix}, \tag{3.3.9}$$

$$\mathbf{d_y} = \begin{pmatrix} 0 & -1 & 0 \\ 0 & 1 & 0 \\ 0 & 0 & 0 \end{pmatrix}, \tag{3.3.10}$$

$$\mathbf{d_{xy}} = \begin{pmatrix} -1 & 0 & 0 \\ 0 & 1 & 0 \\ 0 & 0 & 0 \end{pmatrix}, \tag{3.3.11}$$

$$\mathbf{d_{yx}} = \begin{pmatrix} 0 & 0 & -1 \\ 0 & 1 & 0 \\ 0 & 0 & 0 \end{pmatrix}. \tag{3.3.12}$$

Two convolutions of the image with each kernel would produce an approximation of the second derivative of the image for each of the four directions. Given the symmetry of the cone, it was hypothesised that by adding the second derivative images for each of the four directions, the resulting image would be an enhancement of the original where only conical type features are emphasized. In terms of mathematics, this process can be understood through:

$$(\mathbf{I} * \mathbf{d_x}) * \mathbf{d_x} + (\mathbf{I} * \mathbf{d_y}) * \mathbf{d_y} + (\mathbf{I} * \mathbf{d_{xy}}) * \mathbf{d_{xy}} + (\mathbf{I} * \mathbf{d_{yx}}) * \mathbf{d_{yx}}. \tag{3.3.13}$$

The application of Equation 3.3.13 can be seen in Figure 3.10. In this figure the resulting images for each kernel convolution can be seen for each of the four directions. Even after the first derivative operator has been applied, the lens shadowing which caused major problems with thresholding (Figure 3.8) has been filtered out. This is

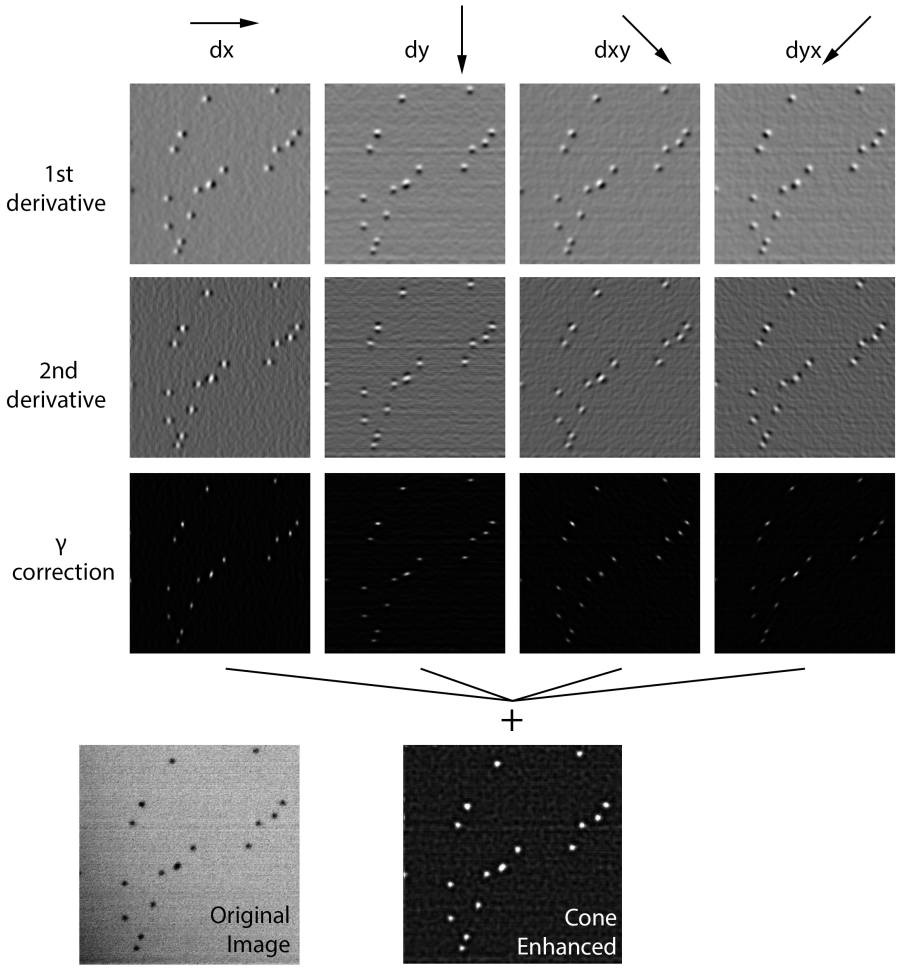

Figure 3.10
Example of Conical Specific Enhancement. The original image from Figure 3.7(c) has been convolved with the four conical specific enhancement kernels. The results upon adding the resultant images (Cone Enhanced) show an enhancement of cell nuclei against the Original Image.

expected as this gradient is approximately linear. The cells themselves have become split between being half black and half white as expected from Figure 3.9(b). Extending to the second derivative returns a slightly skewed version of the cell nuclei. Adding these images together produces a version of the original image where the cell nuclei have become enhanced. Note also that in the second derivative images there is a dark halo around each white cell nuclei – this corresponds to the peaks around the base shown in Figure 3.9(c) and further helps to enhance the shape of the nuclei. The effect of this 'conical specific enhancement' can be easily visualised by looking at thresholding planes. Figure 3.11 shows that even a thresholding plane of a value of 0.5 is now able to distinguish all cell nuclei from the image background.

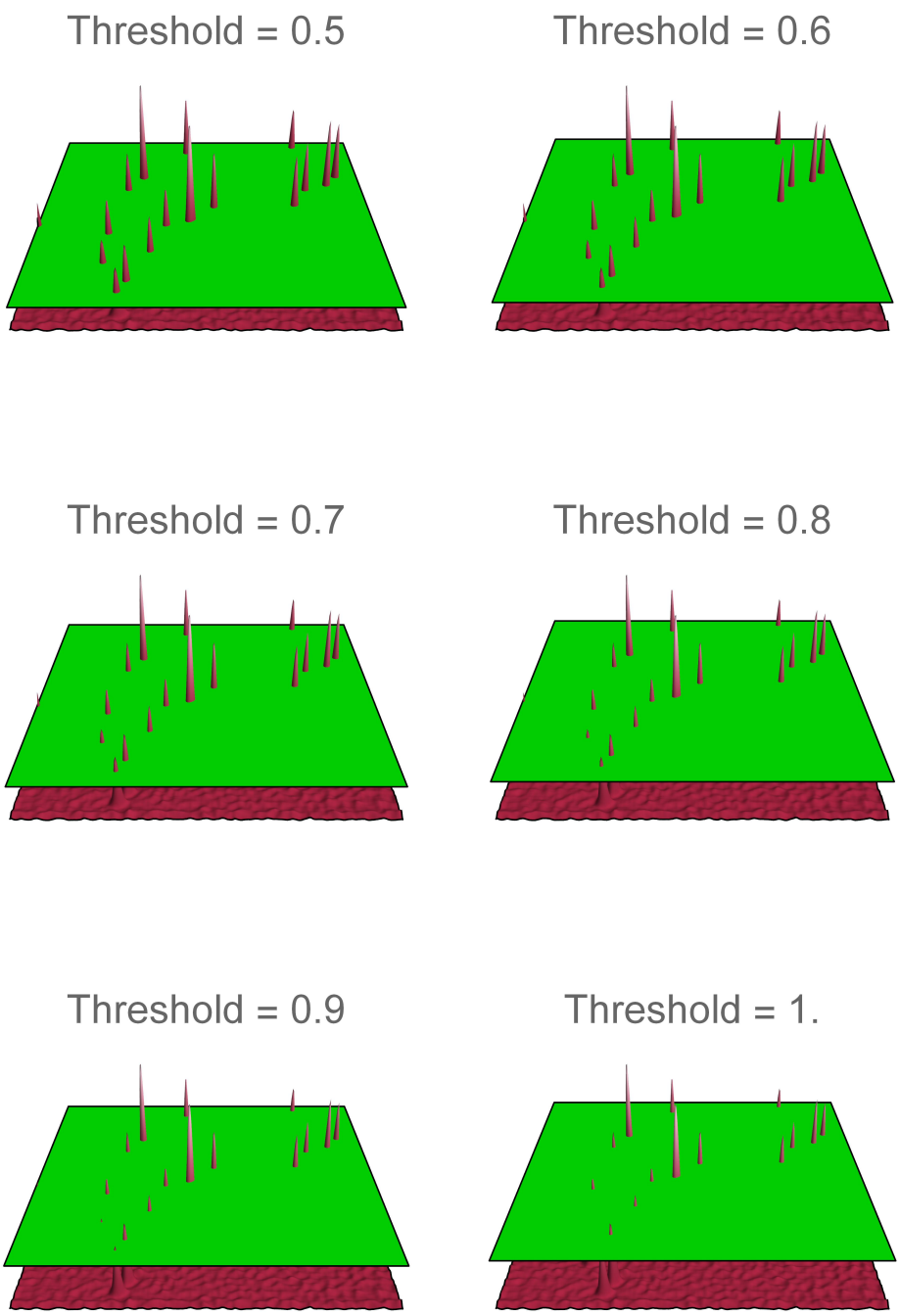

Figure 3.11
Thresholding After Conical Specific Enhancement.
Once the original image in Figure 3.7(a) has undergone this conical specific enhancement, by visualising again as a surface plot, it is immediately clear that a single thresholding value exists and can be easily found which separates cell nuclei from the background of the image.

3.3.2.3 Further Notes on the Conical Specific Enhancement

Mathematically, kernel convolution is associative. Therefore Equation 3.3.13 can be re-written as:

$$\mathbf{I} * \mathbf{D}, \tag{3.3.14}$$

where $\mathbf{D} = (\mathbf{d_x} \star \mathbf{d_x}) + (\mathbf{d_y} \star \mathbf{d_y}) + (\mathbf{d_{xy}} \star \mathbf{d_{yx}}) + (\mathbf{d_{yx}} \star \mathbf{d_{yx}})$. Computing the kernel convolution (by padding the matrix) gives:

$$\mathbf{D} = \begin{pmatrix} 1 & 0 & 1 & 0 & 0 \\ 0 & -2 & -2 & 0 & 0 \\ 1 & -2 & 4 & 0 & 0 \\ 0 & -2 & 0 & 0 & 0 \\ 1 & 0 & 0 & 0 & 0 \end{pmatrix}. \tag{3.3.15}$$

It was realised retrospectively that this kernel is simply the backward difference approximation to the first derivative. For example, the backward difference approximation to the first derivative is given as:

$$\left(\frac{\partial \mathbf{I}}{\partial x}\right)_{i,j} \approx I_{i,j} - I_{i-1,j}. \tag{3.3.16}$$

The backwards difference approximation to the second derivative is therefore calculated as follows:

$$\frac{\partial}{dx}\left(\frac{\partial \mathbf{I}}{\partial x}\right)_{i,j} \approx \frac{\partial(I_{i,j})}{dx} - \frac{\partial(I_{i-1,j})}{dx} \tag{3.3.17}$$

$$= I_{i,j} - I_{i+1,j} - (I_{i-1+1,j} - I_{i-1-1,j}) \tag{3.3.18}$$

$$= -I_{i-2,j} - 2I_{i-1,j} + I_{i,j}. \tag{3.3.19}$$

Note that the coefficients of Equation 3.3.19 – the 2nd derivative approximation in the x-direction – give the central row of $\mathbf{d}_x \star \mathbf{d}_x$.

With the realisation that the original conical specific enhancement (CSE) equation is, in reality, the well known backward difference approximation, the central difference approximation was also considered as a kernel;

$$\left(\frac{\partial \mathbf{I}}{\partial x}\right)_{i,j} \approx \frac{I_{i+1,j} - I_{i-1,j}}{2}. \tag{3.3.20}$$

The central difference approximation intuitively corresponds to the following kernels in

the x, y, xy and yx directions as:

$$\mathbf{d_x^{cd}} = \begin{pmatrix} 0 & 0 & 0 \\ -\frac{1}{2} & 0 & \frac{1}{2} \\ 0 & 0 & 0 \end{pmatrix}, \tag{3.3.21}$$

$$\mathbf{d_x^{cd}} = \begin{pmatrix} 0 & -\frac{1}{2} & 0 \\ 0 & 0 & 0 \\ 0 & \frac{1}{2} & 0 \end{pmatrix}, \tag{3.3.22}$$

$$\mathbf{d_{xy}^{cd}} = \begin{pmatrix} -\frac{1}{2} & 0 & 0 \\ 0 & 0 & 0 \\ 0 & 0 & \frac{1}{2} \end{pmatrix}, \tag{3.3.23}$$

$$\mathbf{d_{yx}^{cd}} = \begin{pmatrix} 0 & 0 & -\frac{1}{2} \\ 0 & 0 & 0 \\ \frac{1}{2} & 0 & 0 \end{pmatrix}. \tag{3.3.24}$$

Combining these kernels through Equation 3.3.14 gives the kernel $\mathbf{D^{cd}}$:

$$\mathbf{D^{cd}} = \begin{pmatrix} 1 & 0 & 1 & 0 & 1 \\ 0 & 0 & 0 & 0 & 0 \\ 1 & 0 & -8 & 0 & 1 \\ 0 & 0 & 0 & 0 & 0 \\ 1 & 0 & 1 & 0 & 1 \end{pmatrix}. \tag{3.3.25}$$

With Equation 3.3.25, it became immediately clear that the development of the 'conical specific enhancement' had implicitly been a deduction of a kernel which approximates the well-used discrete Laplace operator:

$$\mathbf{D^{LAP}} = \begin{pmatrix} 1 & 1 & 1 \\ 1 & -8 & 1 \\ 1 & 1 & 1 \end{pmatrix}. \tag{3.3.26}$$

A lack of baseline knowledge in the fundamentals of image analysis renders the development of the conical specific enhancement somewhat naive. However, beginning from a naive perspective has forced the development of a logical argument for why second derivative kernel approximations enhance cell nuclei in fluorescent images. As such, the utility of this section is self evident.

The three kernels defined here: $\mathbf{D}$, $\mathbf{D^{CD}}$, and $\mathbf{D^{LAP}}$ are tested in oncoming sections through image analysis validation using ground truth.

Table 3.4
Example of Image Normalisation Difficulty With Bright Spots.
Image 1 and 2, due to the large bright spot in Image 2, have the same histograms. In brightening Image 2 by +4, the cell nuclei can now be seen as in the native version of Image 1. But under this same brightness increase, Image 1 is completely bleached.

Brightness	Image 1	Image 2
+0	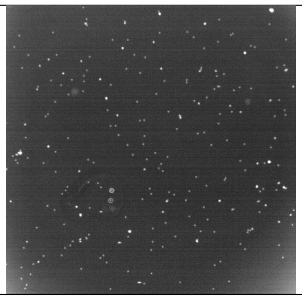	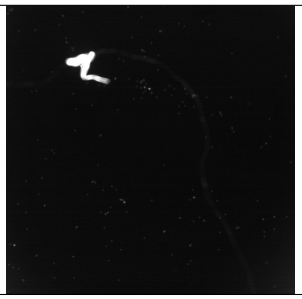
+4	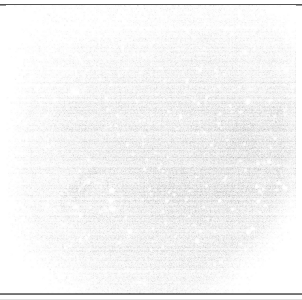	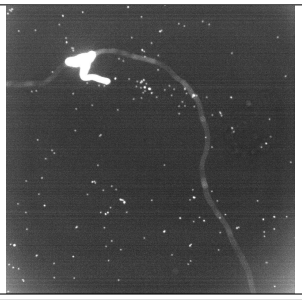

3.4 Image Sorting and Preprocessing

Before information can be extracted from the microscopy data set, images require extensive sorting and preprocessing.

One of the obstacles involved in analysing images indiscriminately is the potential existence of one of many types of artefact in images such as shown in Figure 3.3. A consequence of these types of artefacts is a mishandling of the image by the controlling software of the ImageXPress system. For example, the ImageXPress system attempts to standardise each image it captures against images it has already captured. One way it does this is assumed to be through histogram matching. However, when bright spots are inherent in an image due to some artefact, the images produced are not capable of being standardised to look similar. This is seen in the images in Table 3.4. In their raw form, Image 1 and Image 2 appear completely different. When the brightness is enhanced on both by +4, the cell nuclei in Image 2 can be seen together with the bright spot/fibre. Image 1 is now, however, completely bleached. The presence of artefacts makes it impossible to standardise images using histogram transforms because their histograms already match.

This section develops methodology to prepare the images up until the point in the pipeline where nucleus identification occurs.

3.4.1 Correction/Information Metadata Mask (CIMM)

Given images will need to be indiscriminately fed into an analysis algorithm the question of how to deal with artefacts in images has been long drawn. Artefacts in images are typically either fibres picked up from the environment during membrane mounting or bubbles incurred from the mounting process. Before the final protocol for mounting membranes (Protocol 3.2), fibres were often present in images. Much image analysis research was focussed on automated steps to manage these artefacts. The difficulty with this task directly guided refinement of the BioFlex® plate augmentation procedure, plate preparation, and membrane mounting procedure culminating in Protocols 2.1; page 74, 3.1, 3.2. These steps drastically reduced the presence of fibre artefacts. The methodology described here to counteract the presence of inevitable artefacts is a semi automated approach based on user made annotations of the images. These annotations are defined as the Correction/Information Metadata Mask (CIMM).

The CIMM is, in essence, an image created by the user which using various colour codes indicates the presence of various features in an image. This image is then used by a bespoke image processor as metadata to correct for artefacts and standardise all images. and as well creating informative reference points for later use in data handling.

The process is expanded upon in the following sections but in brief the steps required are:

1. Visualise the whole imaged membrane.
2. Create the CIMM using tools in **Adobe Photoshop CC**.
3. Automatically process the images using the CIMM.

3.4.1.1 CIMM Processing 1: Image Stitching

Images from the ImageXpress system are saved according to the following file name structure:

$$\text{ExperimentName } \_ \ \alpha \_ \ \text{s}\beta \_ \ \text{w}\gamma \ .\text{TIF}$$

where $\alpha \in \{\text{A01,A02,A03,B01,B02,B03}\}$ which describes the well the image belongs to in the 6 well format, $\beta \in \{1 \dots m^2\}$ describes the position in the $m \times m$ imaging grid from each well, and $\gamma \in \{1, 2\}$ represents the fluorescent channel.

With this, and using basic string manipulation in **Mathematica**, the file names of all images are selected and sorted to give a vector of file names per well: $\mathbf{N}^{\alpha} = N^{\alpha}_{\gamma}$. The images the file names represent are imported in turn giving the corresponding vector of images $\mathbf{I}^{\alpha}$. Partitioning this vector into m subunits produces an $m \times m$ matrix of images which corresponds spatially to the original well. Using Mathematica's *ImageAssemble* function, this matrix is exported as a single stitched image with an image resolution of $1.2 \times m^2$ megapixels and a file size $2.22 \times m^2$ megabytes. This step is shown in Figure 3.12(a) to 3.12(b) for two rows of images.

Table 3.5
CIMM Colour Key.

Colour	RGB Representation	Annotation Key
Green	{0,255,0}	Outside well.
Black	{0,0,0}	Membrane border.
Blue	{0,0,255}	Prime Image.
Red	{255,0,0}	Image Artefacts.
Yellow	{255,255,0}	Alignment.

3.4.1.2 CIMM Processing 2: Mask Creation

The CIMM is a secondary image created to store crucial information about the stitched image. Namely, annotations of image artefacts (bright spots, fibres, bubbles etc.), the orientation of the membrane, the borders of the membrane, the center point as well as the most visually 'ideal' image (herein referred to as the 'prime image'). The mask is created here in **Adobe Photoshop CC** but could equally be created in a variety of other image and graphics editors.

In simple terms, after importing the stitched image into **Photoshop**, the mask is created by 'painting' over artefacts in the stitched image in an independent image layer, in predefined colours and saved as a separate image. Features are marked with colours according to Table 3.5. Protocol 3.3 lists the steps involved in fully creating the mask. Once Protocol 3.3 has been completed, the CIMM will be as in Figure 3.12(c).

*Protocol 3.3. Creation of the CIMM (**Adobe Photoshop CC** Version)*

1. Import the stitched image for both fluorescent channels into **Photoshop CC** and layer them on top of each other in the same Photoshop page.
2. Create a new, clean layer over the stitched images.
3. Create a circle with a black border and transparent inner section and place as close as possible so that the circle is concentric with the image of the well and the black border straddles both the inside and outside of the edges of the well. Ensure that no edges of membrane are visible outside the black border.
4. Colour the area outside the membrane green.
5. Select the paintbrush tool with soft edges and set the colour to red. Carefully paint over all fibres, bubbles, and other artefacts.
6. Although the image has been stitched, it should still be possible to make out the individual images. Choose the image which is visually best in brightness and contrast and free from any artefacts. Place a small blue circle inside this image.

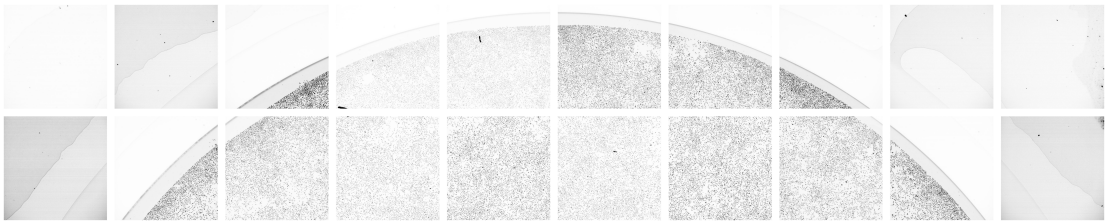

(a) 2 Rows of Images Pre Processing.

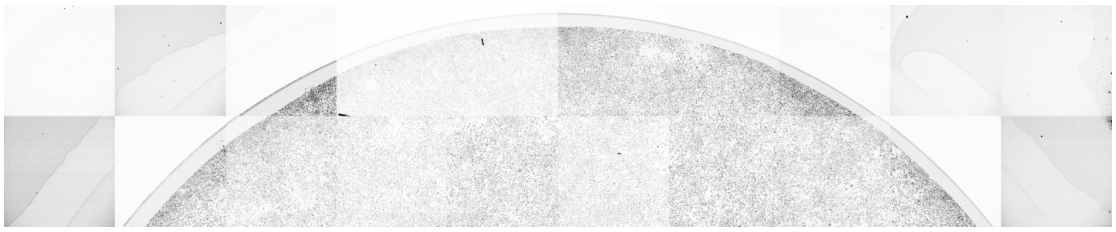

(b) Image Stitching

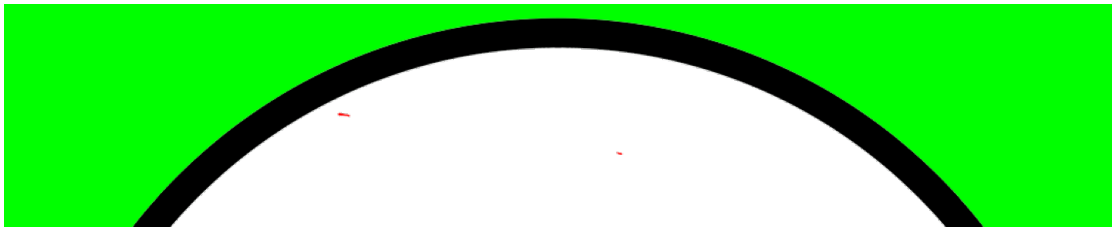

(c) CIMM Creation

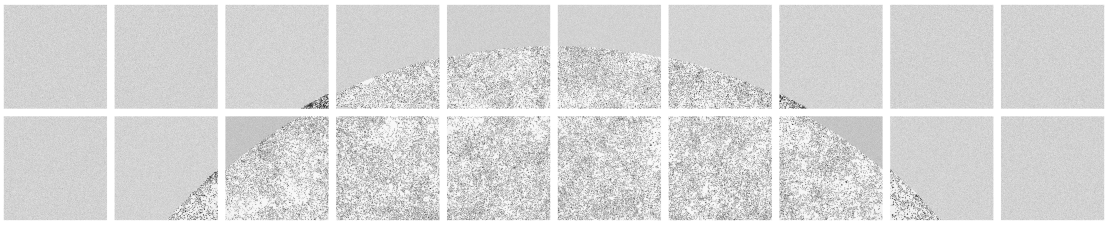

(d) CIMM Guided Processing

Figure 3.12
Example of processing images using the correction mask. The regions outside the well are replaced (according to the green areas in the mask) with pseudo random pixel values as well as regions of artefact (according to the red areas). After this each native image is histogram transformed with the image corresponding to the blue dot in the information mask.

7. Draw a line which corresponds to the marked line on the membrane. This is usually visible in the GFP channel.

8. Reduce the size of the CIMM layer to 10% and save as a **.tif** file.

End of Protocol 3.3.

3.4.1.3 CIMM Processing 3: Image Processing

A bespoke program was written in **Wolfram Mathematica** to process the images together with the CIMM.

In brief, the CIMM **.tiff** file is imported into the program and scaled up to 100%; that is, to match the size of the stitched image. The CIMM, partitioned into sub images with the same dimensions as the images in $\mathbf{I}$, produces a vector of 'mask images', $\mathcal{M} = \mathbf{M}_k$ with $k \in \{1 \dots m^2\}$.

The first step in the processor is to find the prime image – in the CIMM this corresponds to the blue dot. Since this blue is unique in the CIMM, the algorithm searches through $\mathbf{M}$ for the presence of blue pixels, that is, pixels in RGB space with a value of $\{0, 0, 255\}$. If blue pixels are present in say $\mathbf{M}_{Pr}$ then the 'prime image' is $\mathbf{I}_{Pr}$.

The next step is artefact correction. For each of the mask images, only those pixels which are either green ($\{0, 255, 0\}$), black ($\{255, 255, 255\}$), or red ($\{255, 0, 0\}$) are selected from the CIMM. This vector of these mask images is denoted $\mathcal{M}^{'} = \mathbf{M}'_k$. If for each $\mathbf{M}'_k$ we define $\mathbf{P}_k$ to be the matrix positions of $\mathbf{M}'_k$ where $(\mathbf{M}'_k)_{ij} \neq \{0, 0, 0\}$, i.e. the green, red and black pixels, then the 'mask corrected image', $\mathbf{I}'_k$, is defined as:

$$(I'_k)_{ij} = \begin{cases} \text{RND}(\bar{\mathbf{I}}_k, \sigma(\mathbf{I}_k)), & \text{if } (i,j) \in \mathbf{P}_k, \\ (I_k)_{ij}, & \text{otherwise,} \end{cases} \tag{3.4.1}$$

where $\text{RND}(\bar{\mathbf{I}}_k, \sigma(\mathbf{I}_k))$ is a pseudo-random number from a normal distribution with mean= $\bar{\mathbf{I}}_k$ and standard deviation=$\sigma(\mathbf{I}_k)$. This step replaces all the pixels in the microscopy image coinciding with the non-zero pixels in the mask with a random number based on the mean pixel value of the image. Thus, artefacts are removed and substituted with pixel values likely to be similar to the background.

With artefacts removed from the images, histogram transformations can now be used to standardise the brightness and contrast in the images. The histogram of the prime image is used to histogram transform all other images. Figure 3.12(d) shows the total effect of artefact removal followed by histogram transforms. The removal of the artefacts in row 1 image 4 and row 2 image 6 have allowed the histogram transforms to standardise all images so they look visually similar. The green area of the CIMM undergoes the same procedure as the red artefacts and creates a standard image type for areas outside the membrane – this is a useful step for later in the pipeline.

3.4.2 x-Pixel Voxel Partitioning - Data Resolution

In the introductory chapter the idea of virtual fencing to exploit the heterogeneity of a stimulus was discussed. That is, averaging cellular behaviour on a scale where the stimulus can be considered homogeneous.

Each image in $\mathbf{I}'_k$ is split into smaller pieces which are here termed voxels. Voxels can be considered the area over which analysis between the stimulus and phenotype map is

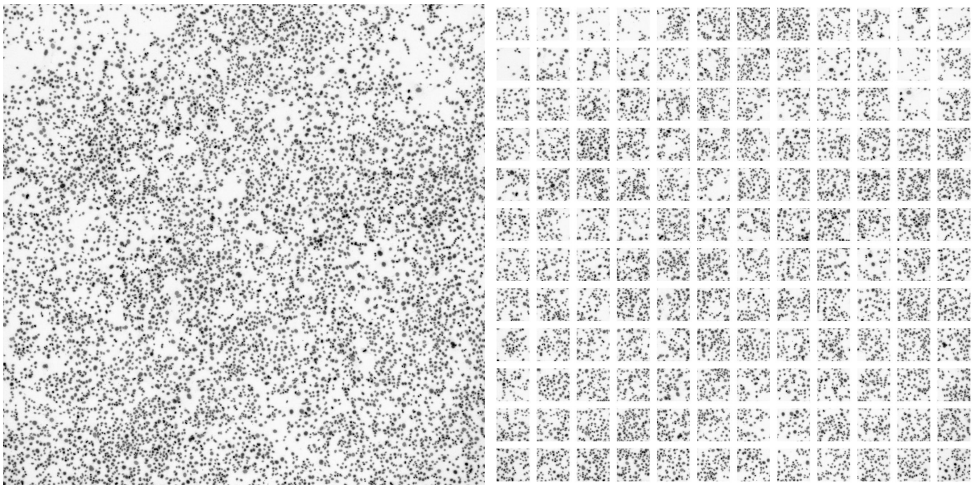

(a) Native Image. (b) 90-Pixel Voxel Partitioning.

Figure 3.13
Example of image partitioning with a voxel size of 90 pixels. Each voxel image in (b) is 90x90 pixels. The size of this voxel, and so the resolution of the phenotype map, can be chosen from the list of integer divisors of 1080 - the native image resolution.

considered. A large voxel size results in greater heterogeneity of the stimulus over each voxel. Thus, the decision of what resolution is needed is dependent on 3 factors:

1. The spatial heterogeneity of the stimulus.

2. The integer divisors of the resolution of the native images.

Each image given by ImageXPress is at a pixel resolution of 1080x1080. Thus, the set of possible voxel sizes, $\mathbb{V}$, is given by:

$$\begin{aligned}\mathbb{V} = \{&1, 2, 3, 4, 5, 6, 8, 9, 10, 12, 15, 18, 20, 24, 27, 30, 36, 40, 45,\\ &54, 60, 72, 90, 108, 120, 135, 180, 216, 270, 360, 540, 1080\}.\end{aligned} \tag{3.4.2}$$

Figure 3.13 shows a native image partitioned into 90-pixel voxels using **Wolfram Mathematica's** inbuilt **ImagePartition** function. The entire membrane image set split in this way therefore produces 14400 'virtual fences'.

3.4.3 Logistic Regression Classifier

In using the ImageXPress system to image the entire well it is necessary that images taken from outside the well are also recorded. The usage of the correction mask standardises these areas as seen in Figure 3.12(d). As nucleus identification here relies primarily on gradient based methods, and since all images are fed into an analysis algorithm without pre-selection, images from outside the well produce false results. This is shown systematically in Table 3.6. This occurs because the image outside the boundary contains

no features which comparatively minimise the effect of the noise. For the cells inside the boundary, the gradients of the backgrounds are entirely diminished by the gradients of the cell nuclei.

To overcome this problem Mathematica's inbuilt classification function is used: *Classify*. This is a machine learning classification algorithm which works on images. Given a set of images annotated with either a '0' or '1', the algorithm seeks to find a way based on this 'training data set' to decide whether an image is a '0' or '1'.

At stage 3 in Table 3.6, the images look distinctively different. A training set devised of random 90-pixel voxel images (from a single well imaged in the ImageXPress) are manually classified as being from inside or outside the well. These are fed into the classification function to automatically develop a set of rules to distinguish images at stage 3 as being images of cells or images of outside the well.

A small script was written in Mathematica to both generate and save training data, as well as train the classifier. The script does the following:

1. From a set of images from a single well after CIMM correction, a random choice is made 200 times. For each choice the image is partitioned into the desired voxel size, and 1 random choice is made from this list.

2. A pop-up dialogue window presents each image and a user choice is made between 'CELL' or 'NO CELLS'.

3. The images are exported to a designated folder with the classification embedded into each file name for later availability.

4. 150 images were used to train the classifier (using logistic regression) and the remaining 50 used as the test for classifier accuracy.

The classifier is judged by the accuracy against the 50 images used as testing. In general, this method works well for classifying images. The downside, however, is that for each set of images taken from the imaging plate, this process has to be completed at least once, and so reducing the automation of the pipeline..

3.5 Feature Extraction Algorithm

With images preprocessed and standardised, this section details the algorithmic steps taken to extract relevant cellular information from each x-pixel voxel to build the phenotype map. For illustration of the algorithm, the images in Figure 3.14(a) to 3.14(b) are used as an example. In this example, the images are the result of an experiment designed so that cells positive for a successful pEGFp-C1 plasmid transfection express green fluorescent protein. This is from work relevant to Chapter 5.

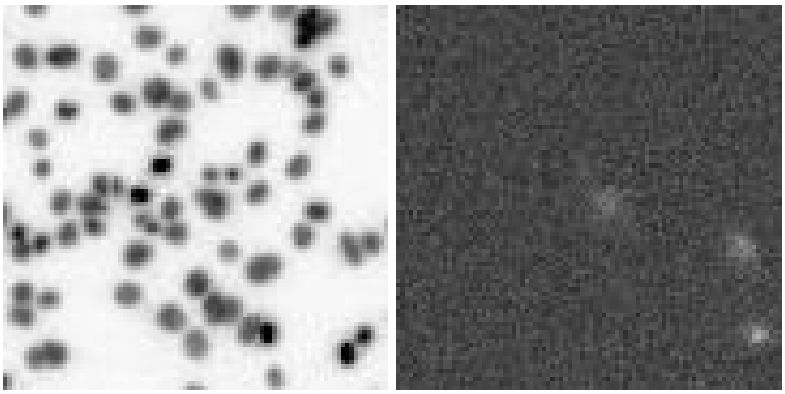

(a) Hoechst 33342 Cell Nuclei. (b) All GFP Positive Cells.

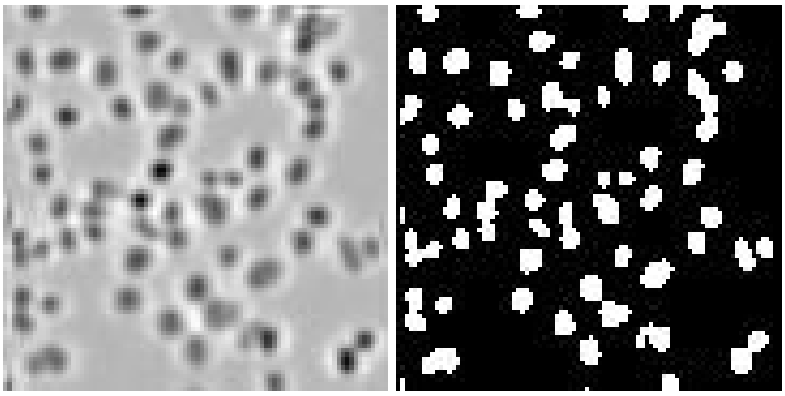

(c) Conical Specific Enhancement. (d) Otsu Binarization.

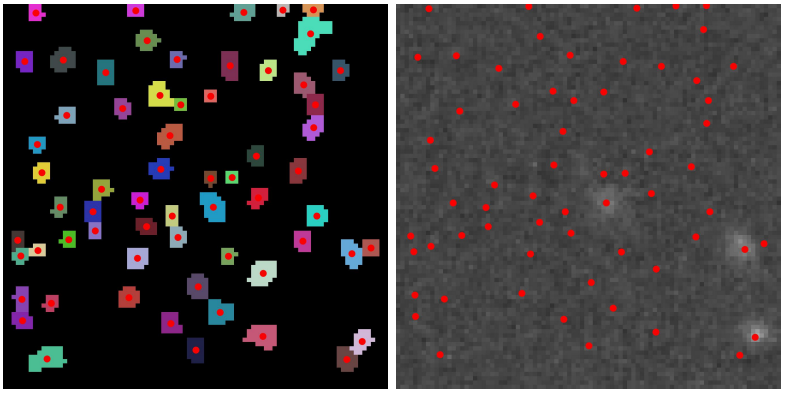

(e) Watershedding. (f) Location Matching on Second Channel.

Figure 3.14

Feature Extraction Algorithm Example. 90-pixel voxels. For C2C12 cells having undergone pEGFp-C1 plasmid transfection and subsequently fixed and stained with Hoechst 33342. (a) Hoechst channel (UV) and (b) is from the GFP channel. (c) shows the application of the conical specific enhancement filter. (d) is image (c) after an automatic thresholding algorithm (Otsu) has been applied. The use of the watershedding algorithm segments cells which are touching and the centres of each unique cell are shown in (e) marked by a red dot. (f) shows the GFP image with each of these dots overlaid.

Table 3.6

Demonstration of Errors Produced With Images Outside of Cell Region. The details of each step are provided in the next section. Images from outside the boundary result in errors. This is caused by the stage in row 2. In row 4 the binarized image from row 3 are watershed and results in visual error. In row 5 red dots are placed at the center of a uniquely identified nucleus given by watershed segmentation. The images in row 3 are visually distinct which allows a machine learned algorithm to automatically distinguish between images from outside the boundary or inside. This is done using a 'black box' approach with **Mathematica**'s **Classify** function.

Process	**Outside Boundary**	**Cells Inside Boundary**
1. 90-Pixel Voxel Example Image	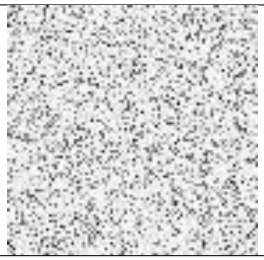	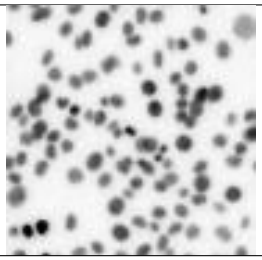
2. Cone Enhancement Kernel	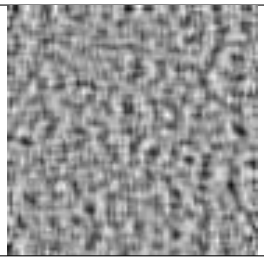	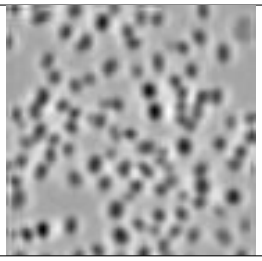
3. Binarization (Otsu's Method)	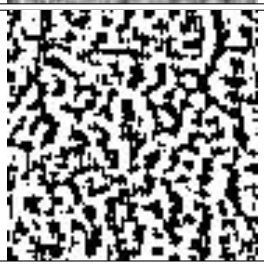	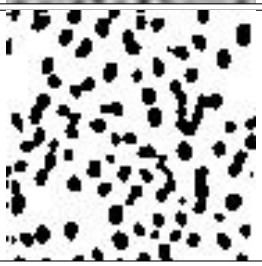
4. Watersheding Segmentation	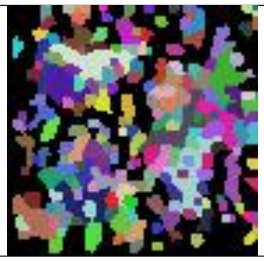	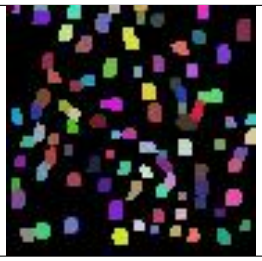
5. Centroid Overlay with Original Image	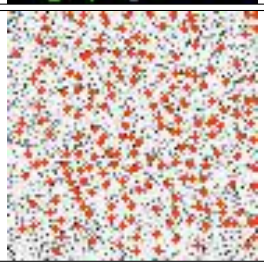	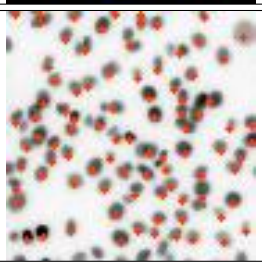

Step 1: Classification

For each image fed into the algorithm, the logistic regression classifier decides if the image contains cell nuclei or whether the image is from outside the well. If the image is not one containing cells, the algorithm stops and moves onto the next image in the sequence. If it does, the algorithm commences with Step 2.

Step 2: Nucleus Identification

For images which have been classified as containing cells, the following steps are applied to identify each nucleus:

1. A Gaussian filter is applied with a radius of 3.
2. The conical enhancement filter (Equation 3.3.26) is convolved with the image as shown in Figure 3.14(c).
3. The Otsu binarization method is applied to the filtered image in order to generate Figure 3.14(d).
4. The watershedding method described in Section 3.3.1.8 is applied to segment objects from the binarized image on the condition that objects are generally circular. This process is shown in Figure 3.14(e). In this image, each red dot represents the center of each identified cell nucleus and so completes nucleus identification.

Step 3: Phenotype Classification

Once the cell nuclei have been identified in the UV channel, the information is used to extract phenotype information from the secondary channel – in this case, the GFP channel. The steps used to identify whether each cell is positive or negative for a phenotype is detailed as follows:

1. For each identified cell nucleus, the pixel positions assigned to that nucleus are sampled from the the corresponding GFP image. The intensities of these pixel positions in the GFP are averaged. See Figure 3.14(f).
2. Once all nuclei have been sampled, each mean intensity is normalised by the average of all intensities. Figure 3.15(a) shows the result of this when displayed in ascending order.
3. Much like in cell analysis in flow cytometry, manual gating is here required to decide which of these cells is positive or negative for GFP. In the case presented here, prior knowledge that the majority of cells are negative is used to define a gate equal to the 'major outlier' of the distribution. That is, if $\mathbf{T}$ is the set of mean intensities for each identified cell then the gating value, g, is defined as

$$g = 3[Q_3(\mathbf{T}) - Q_1(\mathbf{T})] + Q_3(\mathbf{T}), \tag{3.5.1}$$

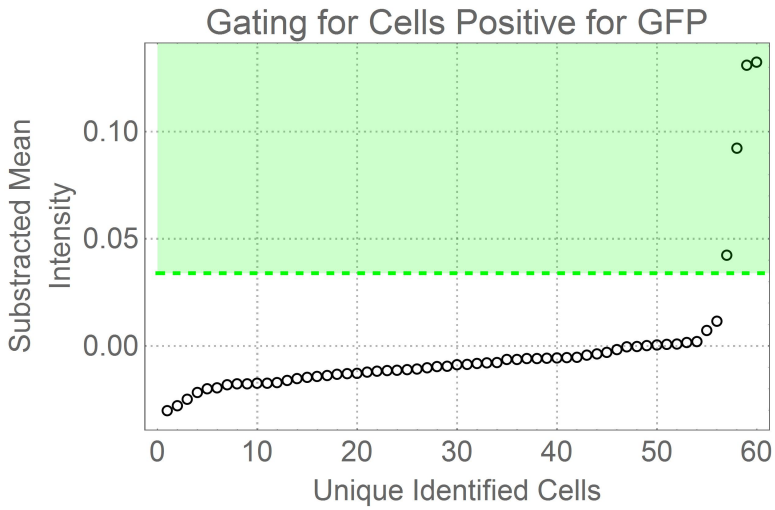

(a) Ordered List of Nuclei Intesities in GFP Channel. Figure continued overleaf.

where Q_i is the function calculating the interquartile range $i \in \{1, 2, 3\}$. The value of q for this example is shown by the green dotted line in Figure 3.15(a). Any cell caught above this line is deemed to be positive for GFP presence.

The result of this phenotype classification can be seen in Figures 3.15(b) and 3.15(c). Here, each number is a unique cell and numbers printed in green are those which are GFP positive.

It is important to note two points from this method. Firstly, that the choice of gating procedure is dependent on user interaction and setting which therefore reduces the level of automation of this pipeline. Secondly, the example displayed here erroneously identifies a cell nuclei as being positive for GFP. With a simple algorithmic procedure such as this, these errors cannot be avoided. A discussion of error is given in later sections in this chapter.

3.5.1 Phenotype Map

Once the cell nuclei have been identified and classified for phenotype, visualisation of the original well can be done through heat maps. In the example shown in Figure 3.16, 100,000 C2C12 cells were transfected with a pEGFP-C1 plasmid using Lipofectamine 2000. Cells successfully transfected with this plasmid produce GFP throughout the cytoplasm. Figure 3.16(a) shows the original image set from a 35 mm diameter well imaged on the UV channel and after preprocessing. Figure 3.16(b) shows the result of a 90-pixel voxel selection and the nucleus identification algorithm. The colour scale on the right indicates how many cells are present in each voxel. Figure 3.16(c) shows the result after phenotype classification for each cell evaluated using the corresponding image taken from the GFP channel. This map displays the total number of GFP positive cells in each voxel. Figure 3.16(d), on the other hand, displays a similar map but instead represents the percentage of GFP positive cells present in each voxel.

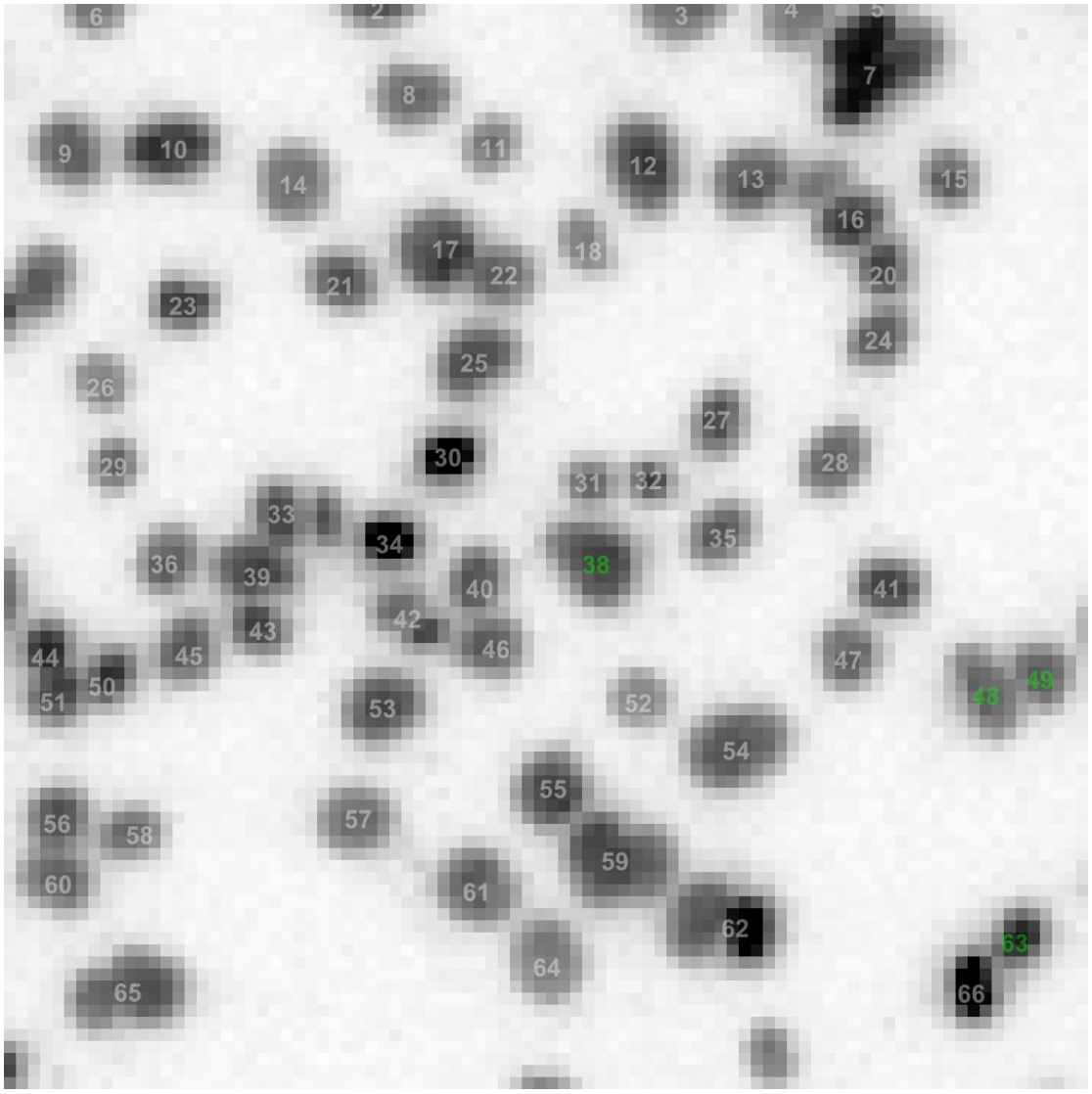

(b) GFP Positive Identified Nucleii on UV Channel Image. Figure continued overleaf.

There are a number of comments to be made regarding Figure 3.16. Firstly, there are regions across the sample where the analysis procedure fails. Note the bottom and right edge of Figure 3.16(b). This is due to the density of cells being sufficiently high that the logistic regression classifier cannot classify the voxel as 'contains cells'. This failure corresponds to when the voxel cell density is greater than 200 cells and roughly equates to a total well density of 3 million. The implication of this is that any experiment has to ensure that total cell density falls significantly short of this point.

The second point to note is in Figure 3.16(d), there is a notable heterogeneity in transfection efficiency distribution in the well with a visually higher efficiency percentage in the top left quadrant. This appears to correlate with a lower cell density in this region. Interpreted holistically, this demonstrates a proof of principle of using image based methods to capture single cell phenotype behaviour in order to generate a data map displaying heterogeneous behaviour.

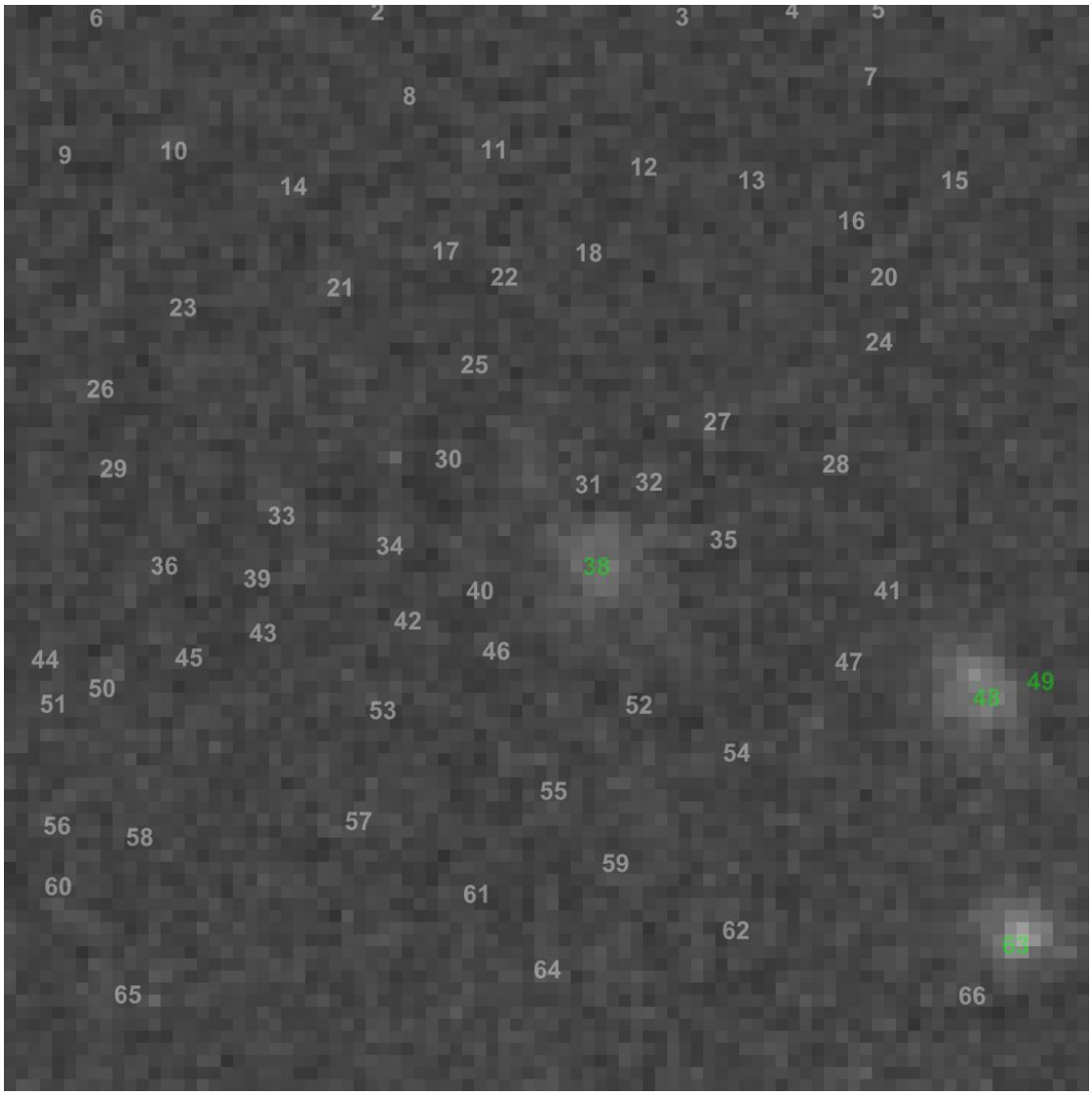

(c) GFP Positive Identified Nucleii on GFP Channel Image.

Figure 3.15
Phenotype Assignment of Identified Cell Nuclei.
(a) Shows a plot of the ordered list of identified cell nuclei against the mean intensities of each nuclei taken from the GFP channel. With the assumption that the majority of cells are negative for GFP, the 'major outlier' is used as a gating value to separate the two classes of cell. In this example, the gate is set by the green dashed line. Everything above this line is deemed GFP positive. (b)-(c) is the result of GFP positive identified cells overlaid on both the UV and GFP channels.

With the theme of this thesis, this completes the 'right branch', that of a generating a discrete data map by 'virtual fencing'. It remains now to develop a stimulus map on the same resolution where each voxel, instead of representing cellular behaviour, represents values of strain stimulus which can be considered the homogeneous stimulus of cells in that particular location.

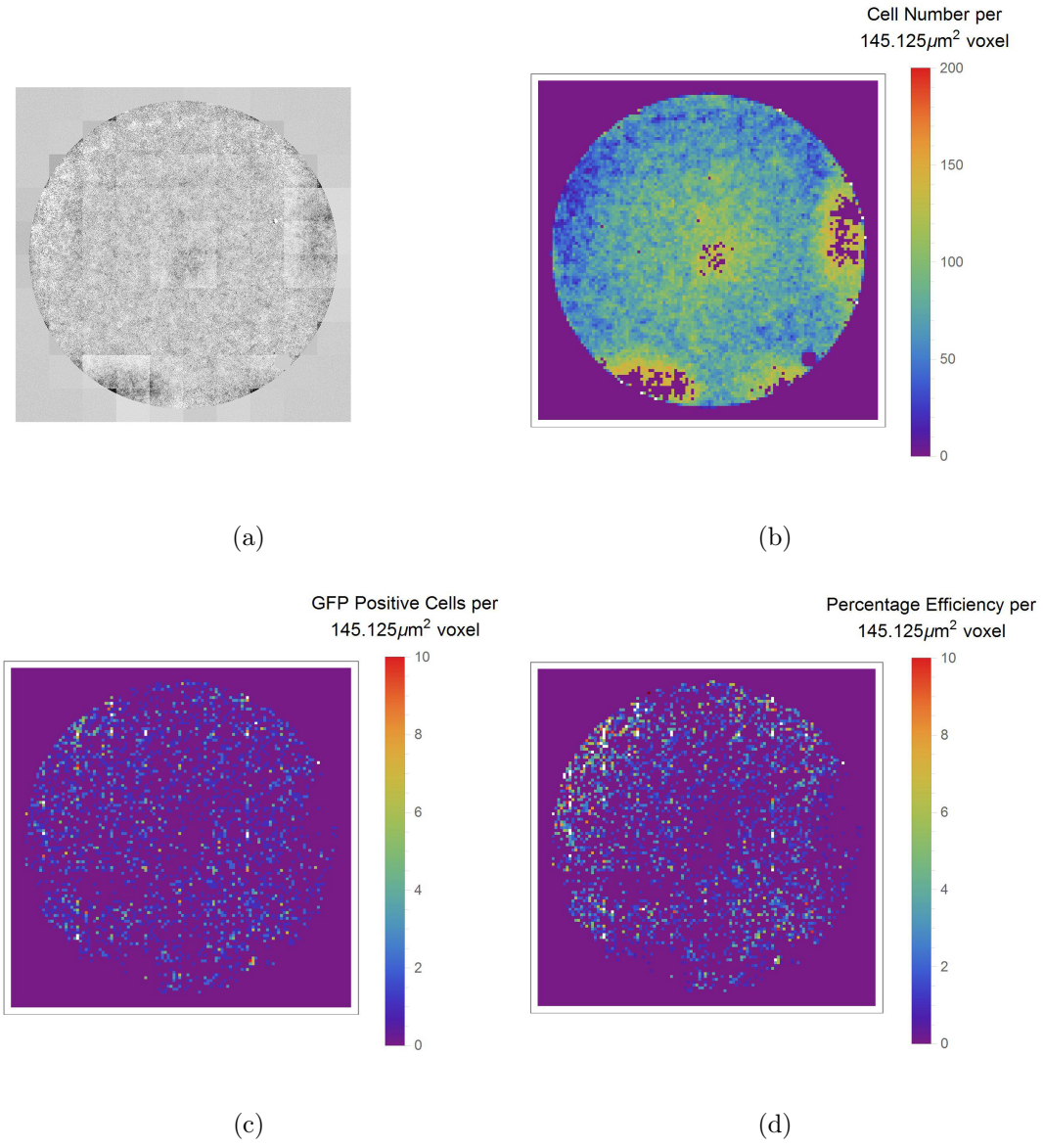

Figure 3.16

Visualising the Phenotype Map.

Where previous figures have shown examples of the analysis pipeline for single images, this figure shows the result of applying this procedure on an entire data set. (a) Shows the image set for a single well stitched after preprocessing. (b) maps the cell density across the well. Failures in the bottom and right edge are due to a cell density after which the algorithm falsely classifies images as being from outside the membrane. This implies a cell density limit for this analysis pipeline to work successfully. (c) and (d) show the maps after each cell nuclei has been classified for phenotype. (c) is the total number of each cells in each voxel which is expressing GFP whereas (d) is the percentage of cells in each voxel expressing GFP.

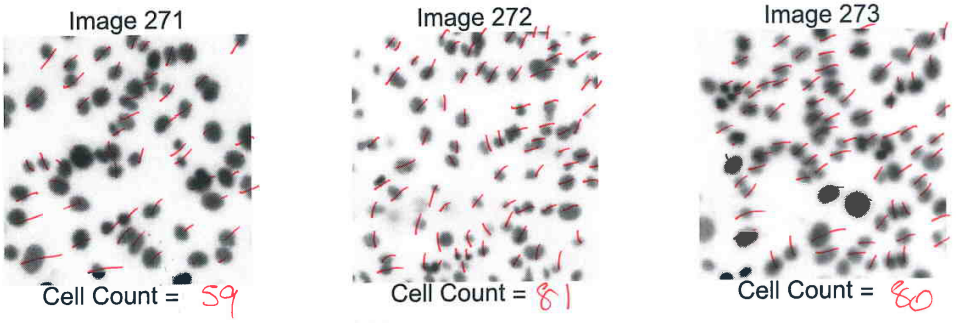

Figure 3.17
Scanned Ground Truth Annotation Example. 270 pseudo-random 90-voxel images of Hoechst 33342 stained C2C12 cells were printed to **.pdf** documents for manual cell nucleus counting.

3.6 Validation of Automation

The final section of this chapter details investigation to quantify the validity and error of the image based virtual fencing method.

Validation of the image analysis algorithms was conducted by first establishing ground truth; a set of images where features of interest have been manually identified. With this, statistical analysis is conducted against the automated feature extraction and ground truth.

Note that only the nucleus identification has been tested and validity of the phenotype assessment remains as an area of future work.

3.6.1 Cell Identification Validation

3.6.1.1 Methods and Materials

Images were used from a preliminary experiment investigating the Lipofectamine induced plasmid transfection of C2C12 cells (discussed in Chapter 5).

Cells on the surface of each well from a 6-well plate were imaged using the ImageXPress system. Following the mask correction stage and image classification stage of the analysis algorithm, two hundred and eighty 90-pixel voxel images were pseudo-randomly selected using a small script written in **Mathematica**. The images were assigned a unique number and printed to a **.pdf** page nine at a time in a grid resulting in thirty **.pdf** pages of images. The thirty **.pdf** pages were printed onto A4 paper for manual counting. Within each voxel cells were crossed out using red pen and at the same time tallied using the free application **Mouse Clickr**[1]. Following the completion of each voxel the cell count was written below the image. After all the images had been manually annotated, the data was entered into **Mathematica** where a small script exported the original images with a file name encapsulating both the unique number as well as the manual cell count into a pre-defined folder. Figure 3.17 shows a scanned copy of the

one row of these pages as an example. The cell identification stages of the analysis algorithm was then conducted over this sample of images under four separate analysis conditions (AC):

AC_1: In the absence of the convolution filter, that is without the process generating Figure 3.14(c).

AC_2: Using the convolution filter $\mathbf{D}$ given by Equation 3.3.15 (based on the backward difference approximation)

AC_3: Using the convolution filter $\mathbf{D}^{\mathbf{cd}}$ given by Equation 3.3.25 (based on the central difference approximation).

AC_4: Using the Laplace convolution filter given by Equation 3.3.26.

To analyse results, manually counted cell values for each voxel were plotted against machine generated cell count values and correlation statistics were used to assess linear dependence. Given that manual voxel cell counts are unlikely to be normally distributed, Pearson χ^2 tests were used to assess distribution fits. Percentage error is calculated for each voxel through the following equation:

$$err_i^{\%} = \frac{|t_i - p_i|}{t_i} \times 100, \tag{3.6.1}$$

where t_i is the true voxel count (given by ground truth), p_i is the machine counted value and $i \in \{1, \ldots, 270\}$.

3.6.2 Results

Figure 3.13(a) shows the results of the analysis under AC_1. For each voxel tested, the manual cell count is plotted against machine cell count. If the machine count is the same as the manual, all purple dots would lie on the red line. It is clear from the left figure that under this condition the algorithm does not count cells in each image with any accuracy. The Pearson χ^2 results, shown on the right, quantitatively agrees with this with a rejection of the null hypothesis.

Figures 3.18(b) and 3.19 show the same set of analysis results but for AC_2 - AC_4. In all of these cases the Pearson χ^2 test does not reject the null hypothesis suggesting on the whole the machine cell counts are on par with ground truth. The cell count plots on the left of these figures suggest that the Laplace filter condition (AC_4) gives machine counts which are closer to ground truth than in any other condition. This is made clear from the plots by the green dashed line (which is the line of best fit of the pairwise data points) being closer to the red line (the line of perfect identification).

These conclusions are solidified through consideration of error as defined by Equation 3.6.1. The results of the error analysis is shown in Figure 3.20. The median error

[1]Credited to *dejco*. http://dejco.deviantart.com/art/Mouse-Clickr-186410353

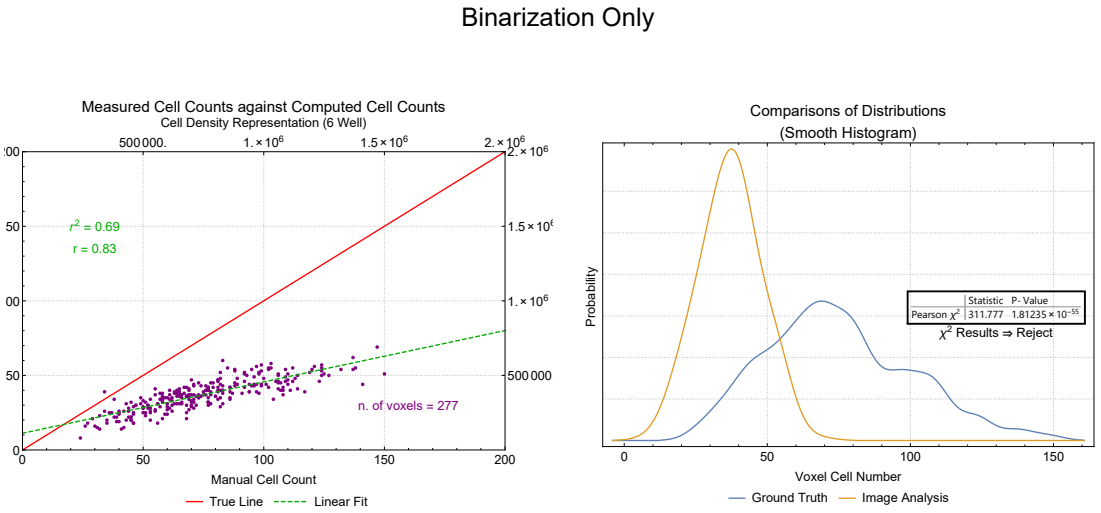

(a)

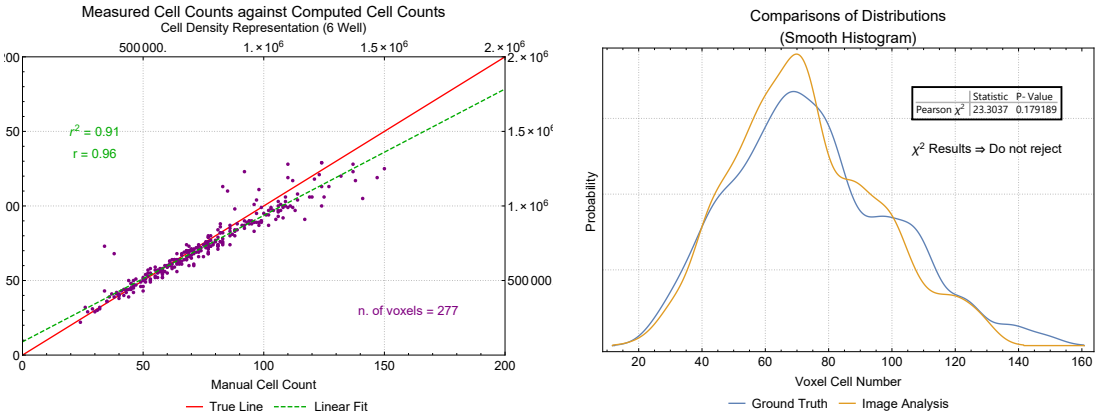

(b)

Figure 3.18

Cell Identification Error Analysis: No Kernel and Backward Difference Approximation. (a) shows the results from the analysis under the condition of AC_1. It is clear, that without the conical specific enhancement (CSE) step in the algorithm, cell identification performance is poor with a rejection of the null hypothesis under the Pearson χ^2 test. (b) shows the results from condition AC_2. This is the CSE filter generated by Equation 3.3.15. The performance of this is strikingly better than under condition AC_1.

(distance from ground truth) that each of the conditions produces is 50%, 5.1%, 5% and 4.1% for conditions AC_1 through to AC_4, respectively. To put this error into context, a separate analysis of error relating to the popular CyQuant assay for counting cells (a bi-

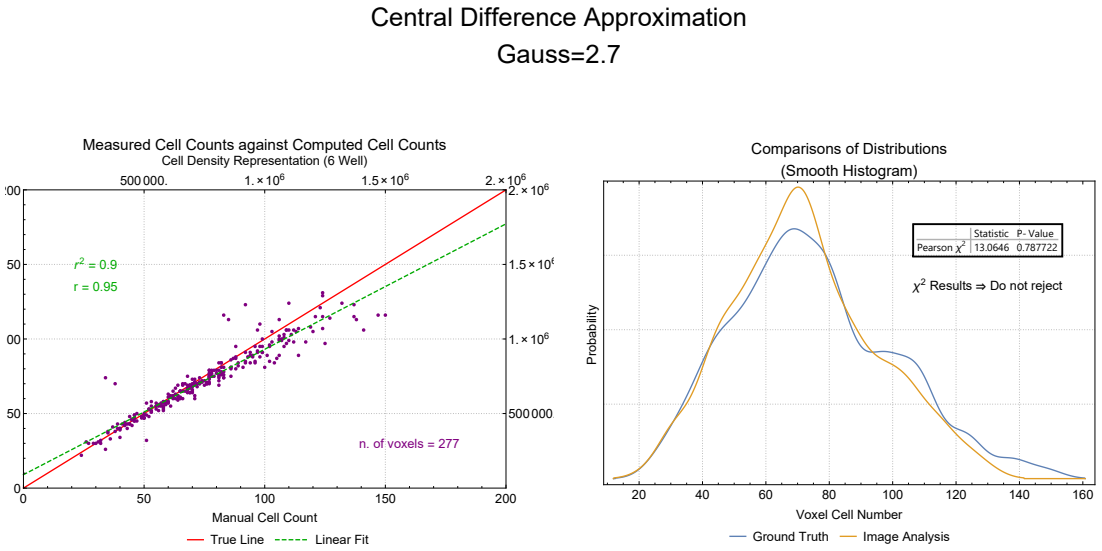

(a)

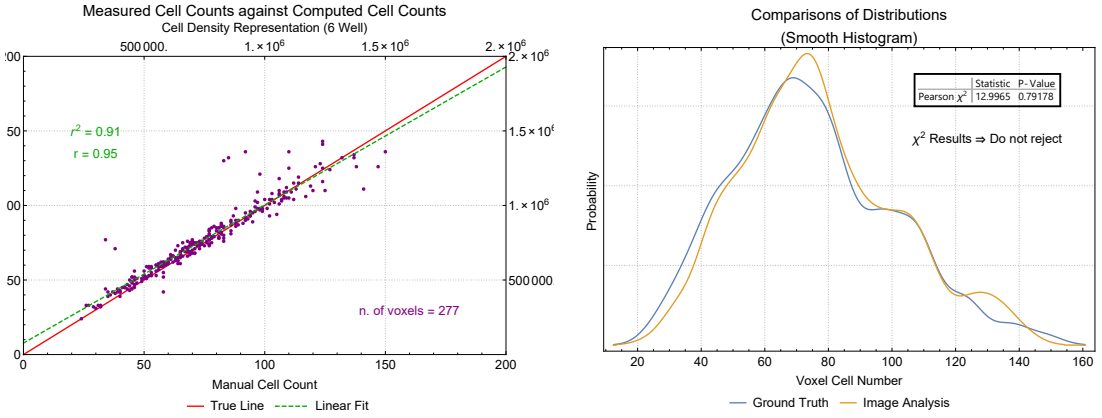

(b)

Figure 3.19

Cell Identification Error Analysis: Central Difference Approximation and Laplace Kernel. (a) and (b) show the results of conditions AC_3 and AC_4. Under these conditions, the algorithm performs much better than AC_1 and marginally better than AC_3.

ological method) resulted in errors ranging between 5.31% to 26.6% (results ommitted)[2].

The results of this section thus indicate that the cell identification algorithm performs within an acceptable level of error.

[2]This was an analysis of inter-sampling error of Cyquant readings for single cell samples. Cyquant data was provided by Eseelle Hendow of the Applied Biomedical Engineering Group, UCL.

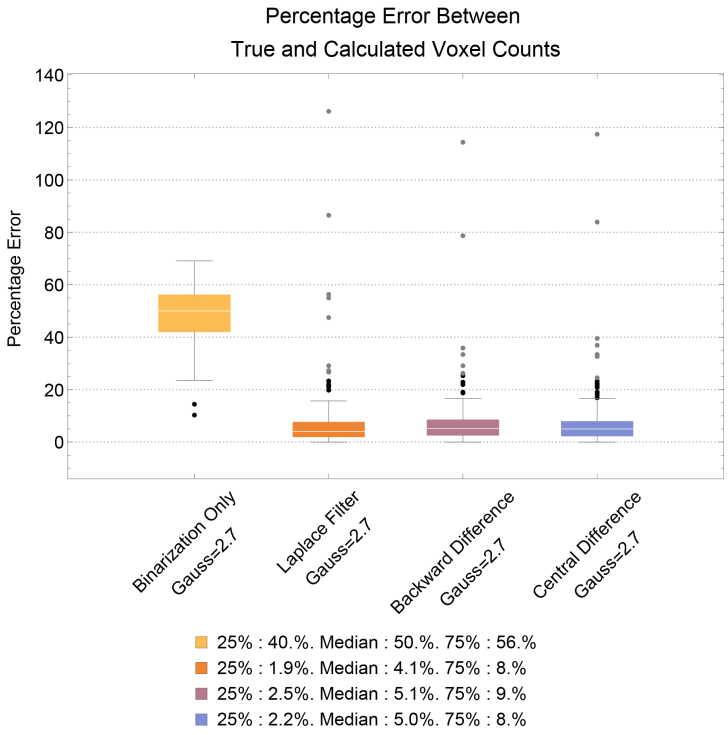

Figure 3.20
Cell Identification Kernel Error Comparison. The results of the analysis using Equation 3.6.1 as a marker for error. The results demonstrate that use of the Laplace Filter (Equation 3.3.26) for the CPE step is most optimal in terms of reducing error.

3.6.3 Discussion

This chapter was concerned with laying the groundwork to generate the right branch of the research aims as discussed in the introductory chapter. That is, to extract cellular data using large sample imaging together with a pipeline delivering automated image analysis. The purpose of this is to produce a 'phenotype map'; a spatial map which represents the behaviour of cells on the membrane. Theoretically, averaging the behaviour across this phenotype map should return precisely the same descriptions as would have been generated by biological population averaging assays and ELISA's. In a situation where the stimulus of the cells is heterogeneous, having a spatial map of cell behaviour allows for the use of statistical correlation between a heterogeneous stimulus and a heterogeneous response; such that population averaging methods will ultimately fail to do.

The beginning of this research, which also coincides with the beginning of this chapter, investigated an approach using the Zeiss SteREO imaging system. After a steep learning curve in both fluorescent microscopy as well as image analysis methods, it is noted that this approach is retrospectively naive. With hindsight, too much time was spent trying to make the Zeiss system work, both in terms of image acquisition and

image analysis. The approach here was one which dealt with inefficiencies in the quality of images by using image analysis algorithms and corrective measures. The research, therefore, was only advanced when the Zeiss system was abandoned and with the realisation that image acquisition should itself minimize the complexity of an image analysis pipeline, rather than image analysis correcting the weakness of image acquisition.

Together with appropriate protocols for sample handling and mounting, the acquisition and handling of a large number of images has been shown to be possible using the ImageXPress imaging system. The clarity of images this system provides, together with the need to capture only one focal plane of images despite the large diameter of the sample, allowed the development of a method for extraction of cellular data. At the beginning of the 'learning curve', during the 'Zeiss era', image analysis algorithms were complicated and inefficient. This period of time which produces nothing tangible is one which I think was absolutely necessary to learn the tools to create, in the end, a simple algorithm. Together with this, working from inexperience of image analysis allowed an approach based on first principles. This generated a logical argument of why the Laplace filter (CPE) enhances cell nuclei in images to better allow binarization methods to segment nuclei.

The novel pipeline developed in this chapter produces phenotype maps at user defined resolutions. The majority of investigation presented here utilises 90-pixel voxels. Viewing each voxel as a unique data point, this translates to 14,400 'virtual' data points across a single 6 well surface. This is in stark contrast to the 2 physical fences created by Basson et al. (1996) on the BioFlex® membrane as discussed in the introductory chapter.

Error analysis of this pipeline is also explored in this chapter. The results of this analysis suggest acceptable margins of error for cell nucleus identification benchmarked against standard protocols. Therefore, methods to generate phenotype maps for experiments using BioFlex® plates is complete. What remains in terms of methodology is the corresponding creation of stimulus maps generated on a resolution comparable to the phenotype maps described here.

3.7 Chapter Summary

With reference to Section 3.1, the aims of this chapter were achieved. In particular:

1. BioFlex® protocols for minimising artefacts in images were defined – both for pre and post experimentation.

2. A modality was established to acquire images of all cells on the BioFlex® membranes following experimentation.

3. An image analysis pipeline was established consisting of the following:

   (a) The manual creation of a metadata image (CIMM) to assist in image normalisation and corrections.

(b) A machine learning method to categorise cells as either inside the well or outside the well.

(c) A kernel convolution approach to enhance only cell nuclei in images based on mathematical arguments. This enables an arbitrary choice of thresholding algorithm.

(d) A nucleus identification, segmentation and phenotype identification protocol.

(e) Ground truth comparison to show error is within reasonable bounds.

4. Completion of the 'right branch' of the thesis design.

Through this, and taken together, the novelty of the pipeline is also established. Although designed specifically for MagAct experimentation, it applies equally to FlexCell®. This chapter demonstrates the feasibility of high throughput, single cell analysis using BioFlex® plates and indeed in any case where preservation of cell position relative to the cell substrate is crucial for meaningful information. That it was conducted with low cost demonstrates an advantage of bespoke, in-house pipeline development over utilising costly, black-box commercial software.

In the context of this thesis, establishment of the pipeline completes the right branch of the thesis and what remains is understanding the physical distribution of strain across the BioFlex® plate generated in MagAct and piecing all the components together to demonstrate a biological proof-of-concept.

Chapter 4

Strain Stimulus Mapping

Understanding the distribution of strain across membranes with as much accuracy as possible is imperative for the strategy proposed in this thesis. As discussed in the introductory chapter, Vande Geest et al. (2004) previously used finite element modelling to quantify the strain field for the FlexCell® system. With any complex *in silico* modelling assumptions have to be made in order to make computation simpler – assumptions for example in symmetries and material parameters. Indeed, a FEM analysis of the initial prototype conducted by a collaborator prior to this thesis (Section 2.3) made large simplifications in order to execute a model. Most notably it did this by calculating strain distributions through prescribing estimated displacements to the embedded magnet rather than, as would no doubt be more complicated but greater in accuracy, computing the time-dependent forces between all magnets and feeding this into the finite element analysis as appropriate boundary conditions.

An alternative to finite element modelling to understand strain distributions is the empirical approach. In general, markers are created on the membranes and through video capture the displacements of each marker between video frames can be measured and directly related to strain. Vande Geest et al. used this method to validate the finite element approach but don't specify how many markers used or the position of each marker. A similar approach was used by Colombo et al. (2008) who drew four lines on the membranes in a square formation centred at the origin of the membranes in a study of the post based FlexCell® system. Being empirical, this approach has the benefit over FEM purely because it is not a prediction of the strain but rather a measurement. However, in general, these types of empirical approaches are limited in resolution by the number of markers used.

This chapter is concerned with discovering the strain distributions generated on the BioFlex® membrane with the MagAct system. Given the importance of strain distribution maps for this thesis, a more advanced method to empirically quantify the apparatus was found in Dantec Dynamics Gmbh, a company which specialises in measurement systems, based in Ulm, Germany. An overwhelming advantage of their system is that deformation and strain of a material under load, although empirically acquired, is pro-

vided in a resolution on par as what would be expected from finite element approaches.

The aims of this body of work was to develop the strain 'stimulus map' for the virtual fencing method proposed in this thesis. To this end, together with the empirical approach given by using the system from Dantec Dynamics Gmbh, an FEM approach was also developed based upon this empirical data.

The outcome of this chapter highlights detrimental limitations of the MagAct system. This is due to the discovery that MagAct in its current form does not deliver a strain value greater than around 4%. Therefore the requirement of apparatus delivering a wide ranging heterogeneous stimulus is not met.

4.1 Chapter Aims

The aims of this chapter in general are to establish the profile of strain over the BioFlex® membrane when actuated using the MagAct system. In particular:

1. Exploration of the DIC method offered by Dantec Dynamics as a method for physically measuring strain.
2. Answering whether the MagAct system as it currently stands is capable of fulfilling the overall aims of this thesis. That is, delivering a variance of strain on par with the FlexCell® system but on a single membrane.
3. If the requirements of the MagAct system are not fulfilled, exploring methods to make it so.

4.2 Digital Image Correlation: Dantec Dynamics Gmbh

The digital image correlation (DIC) system was developed by Dantec Dynamics Gmbh and is a 3-dimensional, non contact optical method with full-field capability used to measure deformation and strain. Where the empirical methods mentioned previously use only a few number of markers on the membrane, the DIC method is principled upon creating thousands of markers across the entire surface. This is done through speckle coating a material or object of interest. The method uses two high resolution digital cameras to film the material, and so the speckle coating, as it goes through a deformation. The speckle coating is such that it is stochastic across the surface of material so that small segments of the coating can be considered unique. This uniqueness allows small segments to be automatically tracked throughout the video using image analysis methods. This is similar to the method of Colombo et al. but instead segments now cover the entire surface. Their segment correlation algorithms, use of stereoscopic cameras and calibration techniques allow for complete deformation to be digitally mapped in 3 dimensions, and in high resolution, through their software **Istra4D**[1].

[1]The principles of DIC may be found here:
http://www.dantecdynamics.com/measurement-principles-of-dic. Last accessed 28th Aug, 2017
and are discussed further in the following Section 4.2.1.

Owing to the compact and lightweight design of MagAct, the entire system was shipped to Dantec Dynamics headquarters in Ulm, Germany for testing on two occasions. On the first occasion the MagAct system using the BioFlex® augmentation 2.1 (Protocol C.1; page 233) was tested. Results from this indicated this EM augmentation method produced an insufficient range of strain and so, after redevelopment, the system was once again taken for testing under BioFlex® augmentation 3.1 (Protocol 2.1; page 74).

For the second set of measurements a different version of MagAct was also tested. This is described in later in Section 4.2.3. The results of the first set measurements were invalidated during this subsequent trip. Here, flaws were identified in protocols used by Dantec engineers. These are included here for both context and because they were the foundations for modifications made to the original MagAct system.

Building upon these second measurements, a FEM based approach was developed (discussed in Section 4.3) to define a characteristic strain map of the MagAct system.

4.2.1 DIC Methodology

An object which is speckle coated generates a stochastic pattern across the surface where, when breaking into smaller image chunks, here termed facets, each chunk can be considered unique. The DIC method records this speckle coated material during deformation using two high frequency capture cameras. Parameters relating to the positions of the cameras in relation to both the sample and each other are calculated using a calibration method. The greyscale images recorded for each frame of the recording are then discretised into facets. With the calibrated parameters together with image correlation algorithms, the software (**Istra4D**) tracks each facet through the frames and produces contour, deformation and strain data for the entire surface throughout the entire length of video capture and on a resolution governed by the size of the facet.

Figure 4.1 shows a magnified image of a speckle coated sample with facets created at a resolution of around 0.5 mm . In comparison to the resolution of the membranes images in Chapter 3, a facet size of around 0.5 mm is a resolution on par with the fluorescent microscopy images captured using the ImageXpress system. The high resolution capabilities of the DIC system therefore provide a promising method for generating high resolution strain 'stimulus maps'.

4.2.1.1 Data Handling and Analysis

The DIC system captures video of an object deforming at variable capture rates. In the experiments conducted in oncoming sections, the frame rate was 20 Hz (20 images per second of recording). The output of each **Istra4D** DIC analysis is a data set consisting of multiple **.ascii** files. For the analysis of one recording (here, the recording of a well undergoing deformation), the output of the analysis is an **.ascii** file for each frame (or step) with each containing the locations of all facet grid points together with every measurement **Istra4D** is capable of computing – for example, the (X, Y, Z) coordinate position of the mesh point; total displacement of the grid point relative to a reference

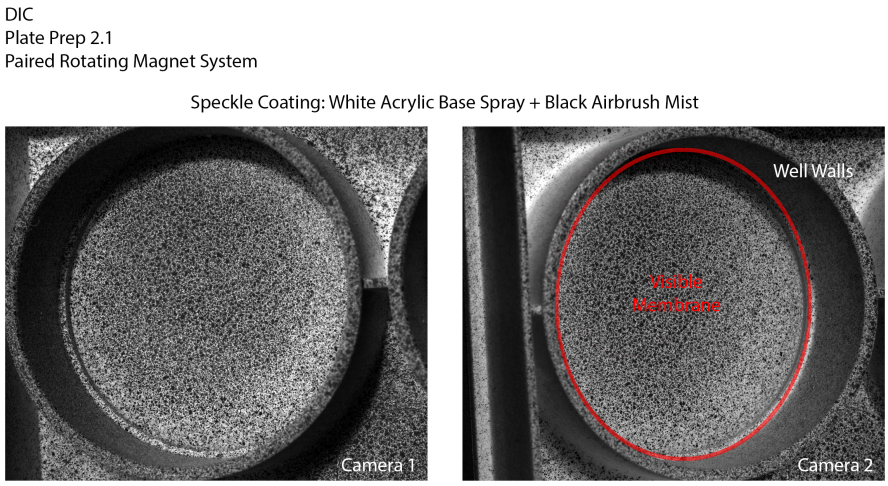

(a)

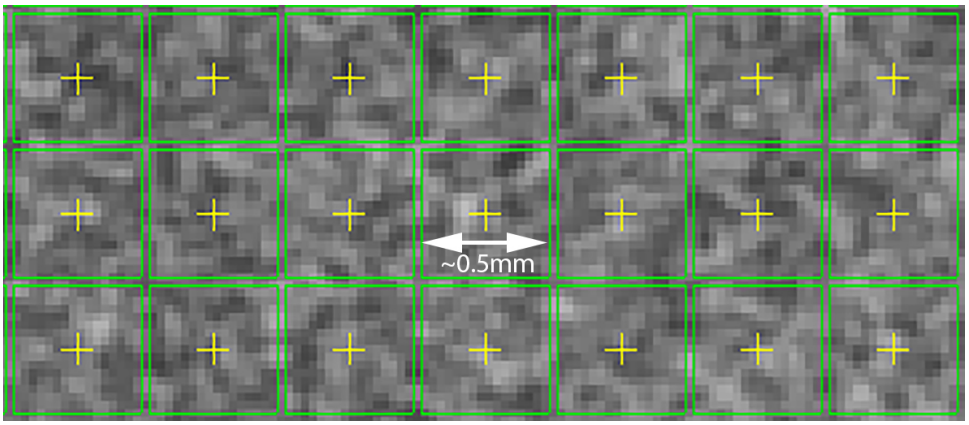

(b)

Figure 4.1
Digital Image Correlation.
(a) shows a single BioFlex® well after having been speckle coated and each image the vantage point of each of the stereoscopic cameras. (b) shows the discretisation of the speckle coated stochastic pattern – termed facets. Here each facet is on the scale of 0.5 mm, a resolution on par with microscopy imaging.

frame; the grid point displacement in the x-direction relative to a reference frame, and a variety of others (a full list of measurements is given in Appendix D.1; page 240)

A typical **.ascii** file here contains around 3500 entries. For 10 seconds of recording and analysis, a single data set therefore contains around 70,000 data entries. Data handling requires extracting relevant information from these data sets. In particular:

1. The (x, y) coordinate positions of all facet mesh points.

2. The DIC calculated displacements of each facet mesh point relative to a reference frame.

3. The DIC calculated maximum principle engineering strain values of each mesh point relative to a reference frame.

A script was written in **Mathematica** to run through each **.ascii** data set, extract relevant features and to produce information graphics of the results. The script extracts for each facet mesh point, the maximum and minimum values of displacement and engineering strain throughout the time series.

4.2.2 DIC Strain Analysis 1

The first measurements taken using the DIC system were for the MagAct system described in Chapter 2 with BioFlex® plates augmented with method 2.1 (Protocol C.2; page 233); the EM sandwiched between the membrane and an additional layer of silicone elastomer. The primary questions these experiments intended to answer were:

1. What is the range of strain magnitudes present on the membranes?
2. Can DIC be used to produce the strain 'stimulus map'?

4.2.2.1 DIC Method

The MagAct system was taken for testing to Dantec labs in Ulm, Germany. To create the speckle coating on the membranes two types of spray based paints were used by engineers working in the Dantec laboratories. A white primer was first applied using a spray-paint can ensuring complete coverage of BioFlex® membrane. After this had dried, an airbrush pen loaded with black paint was used to spray a spitting-type mist over the white; shown in Figure 4.2(a). This created a stochastic speckle coated pattern across the top of the membranes which were shown images through the stereoscopic cameras in Figure 4.1(a).

After calibration of the DIC system, the speckle coated plates were placed in the MagAct system and positioned underneath the stereoscopic camera system; Figure 4.2(b). Positioning is guided by the **Istra4D** capture software which shows real-time images from the stereoscopic cameras. The MagSensor and accompanying software (Section 2.6.4.2; page 82) were used to set the speed of the motors. Each of 12 augmented BioFlex® wells were recorded undergoing deformation with multiple motor speed – 1, 1.5 2, 3 Hz and for around 10 seconds each.

The image data was saved and the DIC analysis using **Istra4D** was conducted in UCL after having had tutorials in **Istrta4D** at the Dantec laboratories.

4.2.2.2 Results

As generated by the **Mathematica** script, Figure 4.3 is indicative of the results of this set of experiments. The figure shows the analysis from a single well having been recorded at three different frequencies. The top row shows the maximum displacement map for each recording relative to the first frame; here each facet is replaced by the maximum

(a) Speckle coating the magnet embedded BioFlex plate.

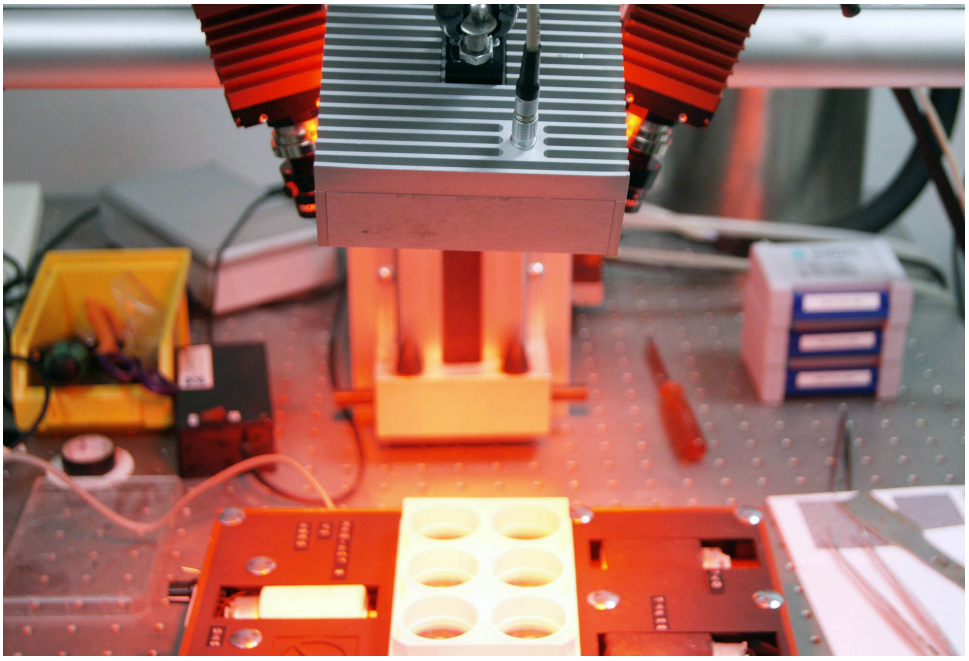

(b) DIC In Use

Figure 4.2

Images showing the DIC system in use. (a) Speckle coating the BioFlex plate. After a solid white primer has been sprayed onto the plate using a spray paint can, an airbrush pen paints a fine mist of black paint across the white undercoat to create a speckle pattern. This provides the stochastic pattern used for image correlation. (b) The MagAct system is positioned for each well under the stereoscopic cameras which feed the recording directly into the **Istra 4D** software. Red light is used to provide the highest contrast between white and black speckling.

displacement experienced at that point throughout the entire time series. The middle row shows density maps of the temporal change in position undergone by a line through the

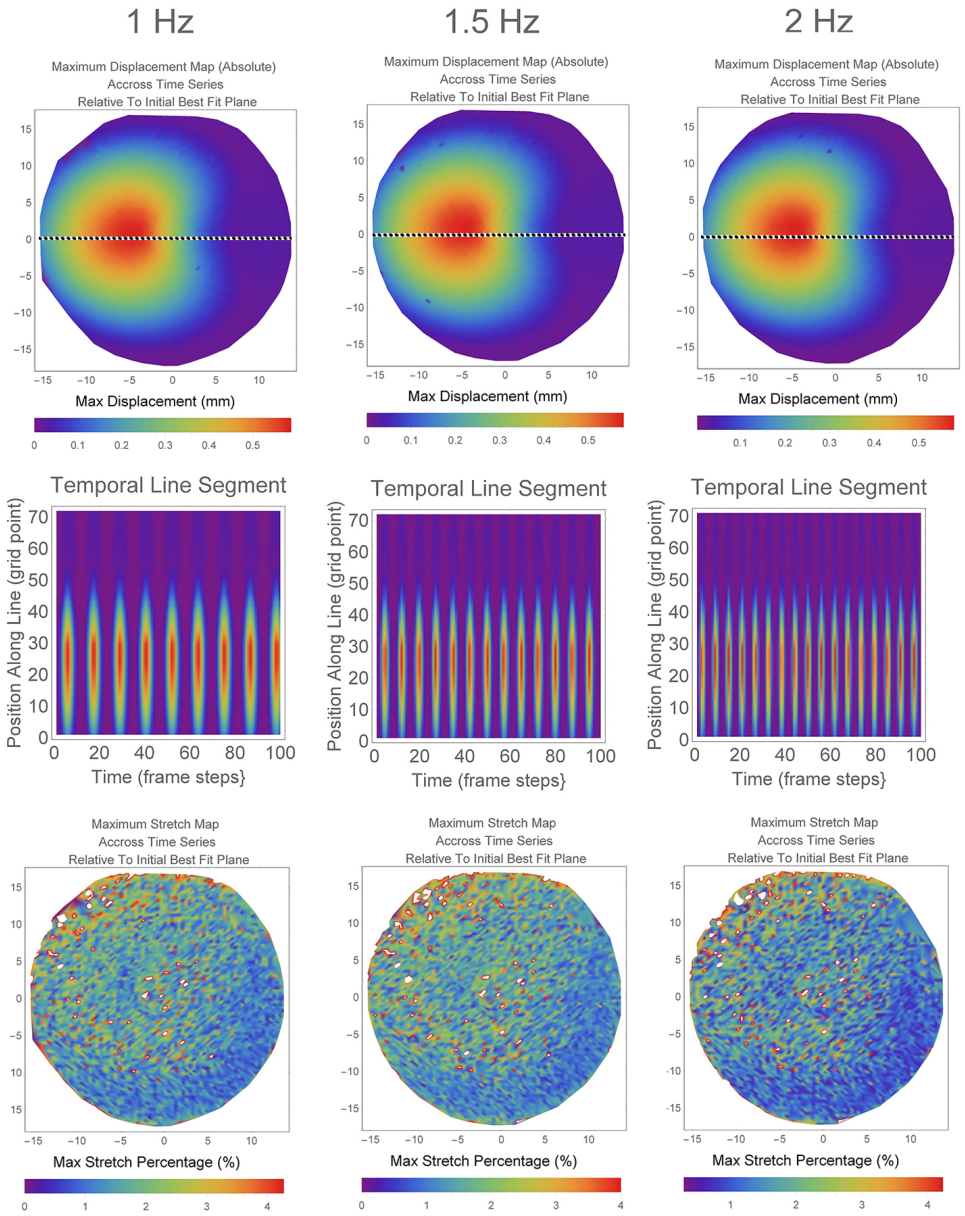

Figure 4.3

DIC Results of an Analysed Well Recorded at 3 Different Motor Frequencies. The top row displays the maximum displacement density maps for each frequency. Each facet is represented by the maximum displacement this facet undergoes throughout the time series. The middle row shows the time series of a line across the membrane (indicated by the dashed line in the top row). The density plot shows the displacement at each point in the line for all time steps and is therefore used as an indication of motor frequency. The bottom row displays the maximum stretch maps across the time series in a similar way to the first row. The stretch maps indicate a lack of discernible patterns of strain with this version of the MagAct system and that potentially no strain is present on the membrane.

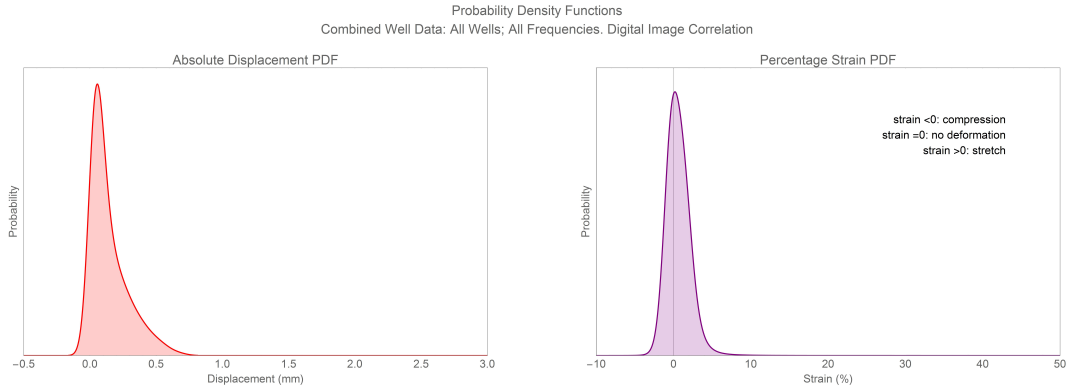

Figure 4.4
Probability Density Plots of DIC Results 1.
The left figure shows the probability density function (PDF) of facet displacement when all recorded wells and corresponding analysis have been amalgamated together. Similarly for strain (both compression and stretch) on the right. Assuming the DIC method has worked, these plots indicate that both very little displacement and very little strain are generated as a result. In general, the strain value across the membranes appears to average to 0.

membrane. This line segment is marked in the first row by the dashed lines. These plots qualitatively describe the frequency of the motors and therefore corroborate Algorithm 1; page 65 and its implementation using the MagSensor and accompanying software. The bottom row shows the maximum stretch maps throughout the time series using DIC maximum principal engineering strain values. These are generated and interpreted similarly as the displacement maps. The stretch maps lack the characteristic look and smoothness of the displacement maps. This indicates that either there is no strain generated by the MagAct system as it is, or the DIC method has not worked.

This type of behaviour was typical for all recordings of wells. To quantify this, the displacement and strain data was amalgamated for all DIC analysed wells at all frequencies and expressed as probability densities. These probability plots are shown in Figure 4.4. They indicate that, in general, the deformation of the wells is very low – the majority of the membrane doesn't move. As expected given Figure 4.3, the probability density for strain indicates that, in general, the majority of the membrane remains unstretched with the strain averaging close to zero. Under a MagAct system working well one would expect displacement distribution centered around a non-zero displacement.

4.2.2.3 Discussion

The results of Section 4.2.2.2 were at the time concerning. The DIC results were assumed to be true and the the absence of strain was attributed to the MagAct system – specifically the characteristics of the membrane as a result of augmentation 2.1. Because the silicone elastomer used to embed the EM was distributed with greater homogeneity, the result was a stiffer membrane than previously generated with Dr. Day's original

protocol (Protocol C.1; page 233). It stands to reason that given the same force to the stiffer membrane, the less movement is generated. Therefore stretch is greatly diminished. This was the driving force of the redevelopment of the BioFlex® augmentation 2.1 procedure which culminated with Protocol 2.1; page 74: the method which glues a magnet to the membrane using a silicone based glue and purpose built loading posts.

This work sought to discover whether the DIC could be used to build a characteristic strain 'stimulus map'. Attempt was made to amalgamate DIC outputs for each well to generate an averaged density map. The recordings in the Dantec laboratories required repositioning the MagAct system under the cameras when wells were swapped over. Any information regarding the positioning of each well relative to another is completely lost during the DIC analysis procedure. Therefore, normalising the data such that it could be amalgamated to generate an averaged stimulus map is near impossible.

Another difficulty with creating a characteristic map was related to the surface area of the membranes capable of DIC analysis. As the stereoscopic cameras are angled towards the membrane, the walls of BioFlex® obstructed the field of view. Analysis can only be conducted by areas of the membrane which are visible by both cameras. As annotated in Figure 4.1(a), the visible area is significantly less that the total area of the membrane. Therefore, even if data could be amalgamated, the characteristic strain map would not describe the entire membrane.

Subsequent usage of the DIC method, as will be discussed in Section 4.2.3, has resulted in an invalidation of these results. During the second trip to Dantec for repeated MagAct testing, cracking of the speckle coating was observed on the membranes during actuation. This observation led to the realisation – and major criticism of the DIC system – that whatever is used to create the speckle coating is assumed to deform and stretch in the same way as the underlying material. The cracking of the speckle coating suggests that the membrane is deforming underneath the speckle coated layer and the dynamics is hidden from the DIC cameras. For the measurements in this section, this implies the results do not represent the true dynamics of the membrane but instead the dynamics of the coating. Therefore, the results from this set of measurements are false.

4.2.3 DIC Strain Analysis 2

Although the first measurements made at Dantec Dynamics were uninformative, much was learned of the system so that methodologies were improved during a subsequent trip.

4.2.3.1 DIC Method

BioFlex® plates were prepared according to Protocol 2.1; page 74. To maximise the field of view the DIC system is able to capture, the plates were held in a vice and, using a hacksaw, the top half of the plate above the membrane was removed as shown in Figure 4.5(a). The increase in the DIC's field of view can be seen in Figure 4.5(b) relative to Figure 4.1(a).

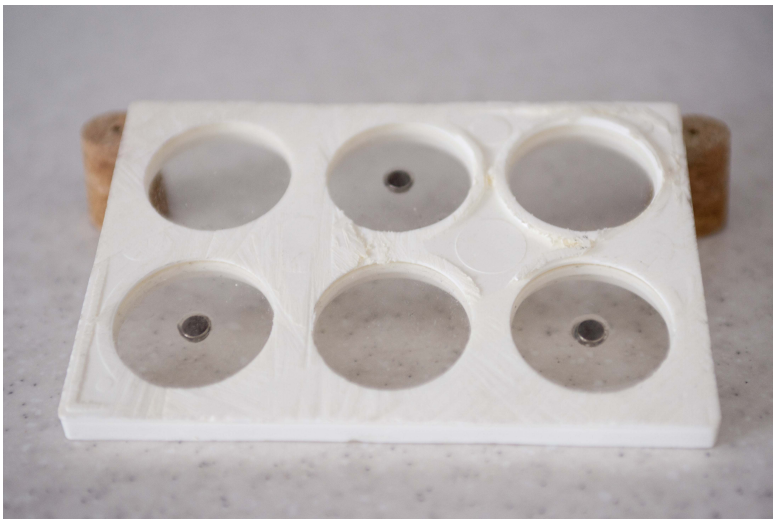

(a)

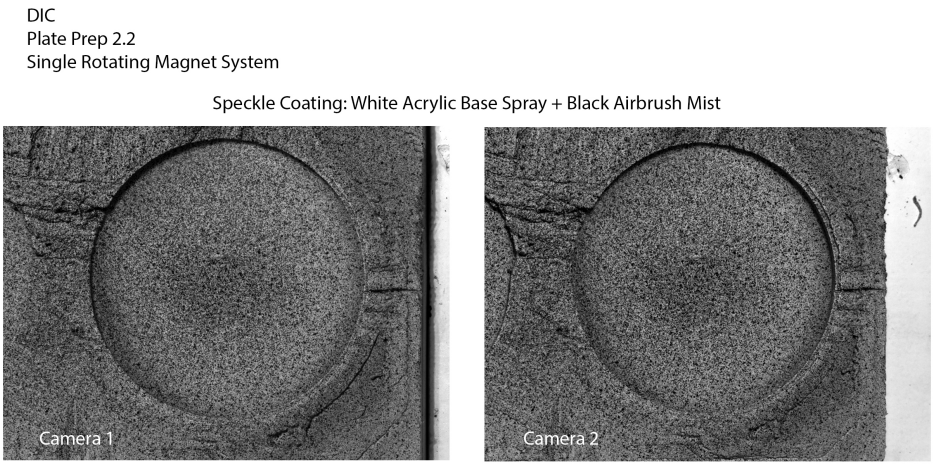

(b)

Figure 4.5

Field of view comparison to Figure 4.1(a). (a) Image of BioFlex® plate after cutting away the well walls. This was done to maximise DIC field of view. (b)Screen grab of speckle coated bioflex well as input into **Istra 4D**. The field of view from both cameras is now increased due to removing the upper portion of the BioFlex® plate using a hacksaw. Speckle coating is here generated using a chalk/solvent spray mixture together with a fine mist of black paint. By eye, this speckle coating deformed with the membrane better than the previously used white acrylic paint base coat.

To control the position of each well during DIC acquisition as much as possible relative to each other, a simple cross-hair laser system was constructed using generic 5 mW 650 nm cross-hair lasers purchased from ebay.co.uk[2]. Coupled with carefully marked points on the top plate of MagAct, this enables the MagAct system to be positioned such that

[2]Ebay Marketpalce. Seller: zhibinoppa.

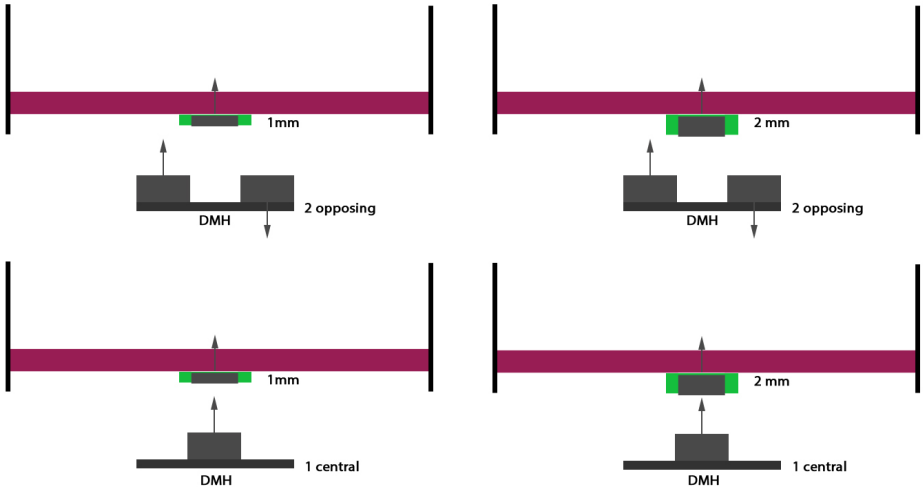

Figure 4.6
DIC 2: Conditions for DIC Testing. The top row shows the EM variations for MagAct v1.0. The bottom row shows the variations for MagAct v2.0. Both were tested using the DIC method with a chalk based speckle coating.

every well will have the same reference position and orientation.

Before the second trip, and based on the assumed true results of the first, modifications were made to the MagAct apparatus itself. It was anticipated that if there is only a single, centrally placed magnet in the DMH, then the EM would be pulled directly down from the center of the BioFlex® well as the DMH rotates to face the EM. Under perfect conditions, this was anticipated to produce a radially symmetric distribution of strain as would be seen in the FlexCell® system. If this was shown to be true, then amalgamation of data to create a characteristic (averaged) strain map would be easier to achieve. For nomenclature, the MagAct system with the double magnet actuator is referred to as 'MagAct v1.0' and the single magnet actuator is referred to as 'MagAct v2.0'.

A greater number of conditions were planned for testing using the DIC method under Protocol 2.1; page 74 (shown schematically in Figure 4.6). These are listed as follows:

1. 6(d)x1 mm EMs. MagAct v1.0.
2. 6(d)x2 mm EMs. MagAct v1.0.
3. 6(d)x1 mm EMs. MagAct v2.0.
4. 6(d)x2 mm EMs. MagAct v2.0.

The speckle coating had initially been performed using the same method as the previous section – acrylic white spray paint with a black mist. As previously noted, the observation of cracking suggests this coating deforms independently from the underlying membrane. Therefore a new method was developed by a Dantec engineer. Rather than spraying the membrane with an acrylic undercoat, he instead sprayed a mist of chalk

particles on the membranes. The chalk is delivered by aerosol can together with a solvent which, once the solvent evaporates, leaves a layer of chalk on the membranes. A fine spray of black paint using the spray-pen generates the speckle coating as seen in Figure 4.5(b).

DIC recordings were made using the conditions detailed above and for 1 and 2 Hz motor rotation speeds using the MagSensor and accompanying software. DIC analysis using **Istra4D** was conducted at UCL using similar data handling methods described in Section 4.2.2.1.

4.2.3.2 Results

In the following set of analysis all data (displacement, stretch and compression) is normalised to a reference frame chosen such that the membrane is flat and free from deformation. This occurs in practise when the DMC is pointing away from the membrane. All recordings are orientated in the same spatial directions using the cross-hair laser system for positioning.

Figure 4.7 shows the results of a single 6(d)x1 mm augmented BioFlex® well recorded at both 1 and 2 Hz using MagAct v2.0. The DMH rotates along the axis of the dotted line in the maximum displacement map. The plots are read similarly as in Section 4.2.2. Here however the strain map has been separated into two maps – compression and stretch[3]. The compression map represents the greatest amount of negative strain for each facet. The maximum displacement plot indicates the maximum displacement achieved by the membrane. This is no more than 1.25 mm and corresponds to a small area of stretch at the right hand side of the EM with a magnitude up to around 6%. Slight compression is measured at the left hand edge of the magnet reaching around 2.5%. The results for 1 and 2 Hz are visually and qualitatively similar which suggests, as before, that frequency does not affect membrane dynamics. The smooth histogram plots of both maximal displacements indicate on average low levels of both displacement and strain.

Figure 4.8 shows the results in the case of the 6(d)x1 mm EM using MagAct v2.0. Maximum displacement maps indicate for both 1 and 2 Hz a slightly greater maximum displacement than in Figure 4.7 at around 2.5 mm. As intended, the maximum displacement maps are approximately radially symmetric. Maximum stretch and compression maps are also approximately radially symmetric. The maximum stretch is around 6% around the periphery of the EM. There is an annular region around the EM with zero stretch. The compression maps suggest this area, rather than stretching, compresses by around 1%. Outside of this area there is maximal stretch of around 2% which through a gradient drops to zero. The presence of bi-modality in the smooth histogram plots of strain suggest that the area of membrane which is stretching is greater than with MagAct v1.0.

[3]This is only possible when the reference frame in **Istra4D** is chosen to be in the undeformed state. For the first set of measurements taken at Dantec this was not the case.

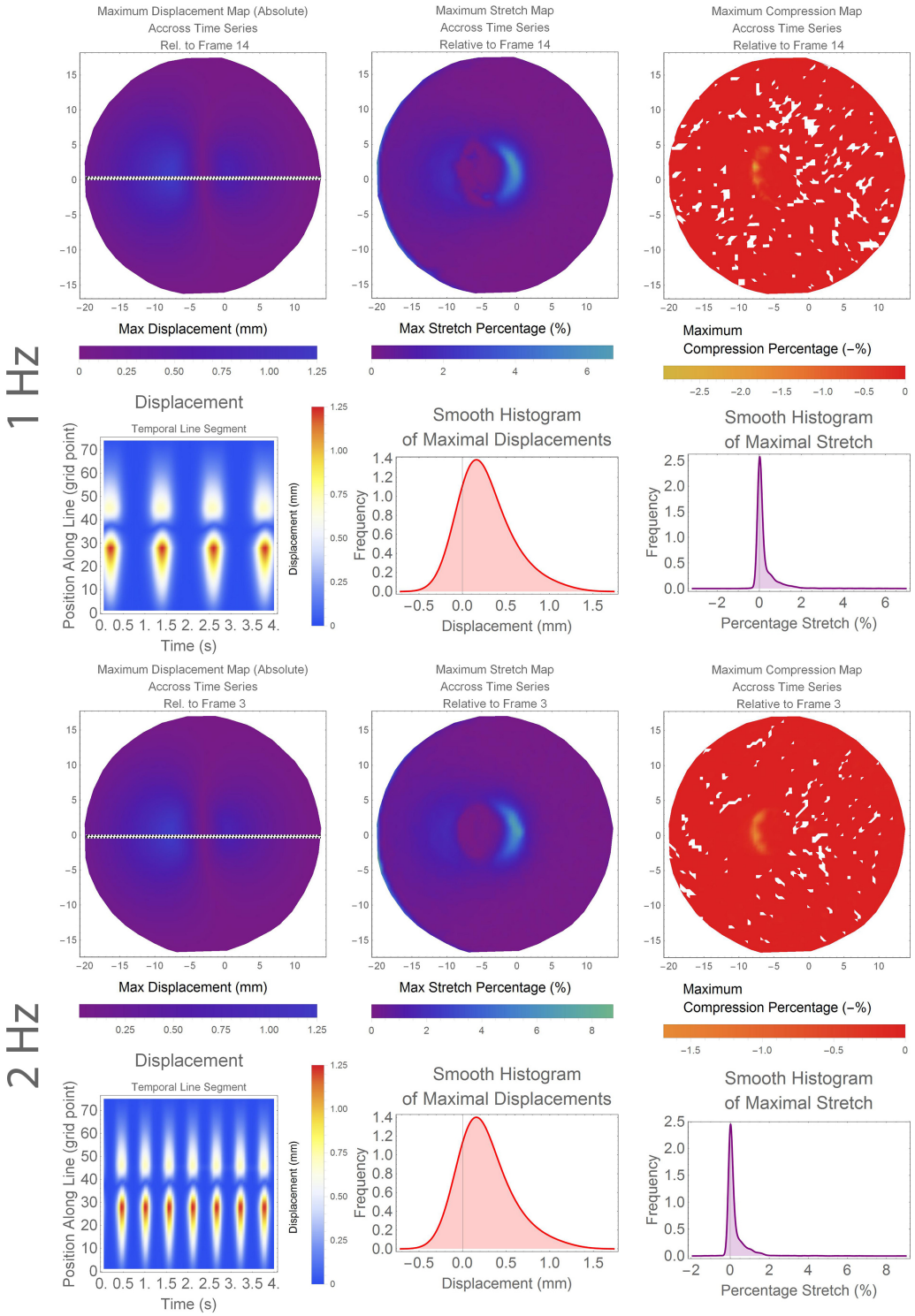

Figure 4.7

DIC Results 2: 6(d)x1 *m*m EM | MagAct v1.0.

Results for a single well recorded at both 1 Hz and 2 Hz motor frequency. 1st and 3rd row show the maximum displacement, maximum stretch, and maximum compression maps. As before, the maps show the maximum (and minimum) values each facet point reaches throughout the time series. 2nd and 4th row show the temporal line density plot (indicating motor frequency), and the probability density plot of both the maximal displacements and stretch.

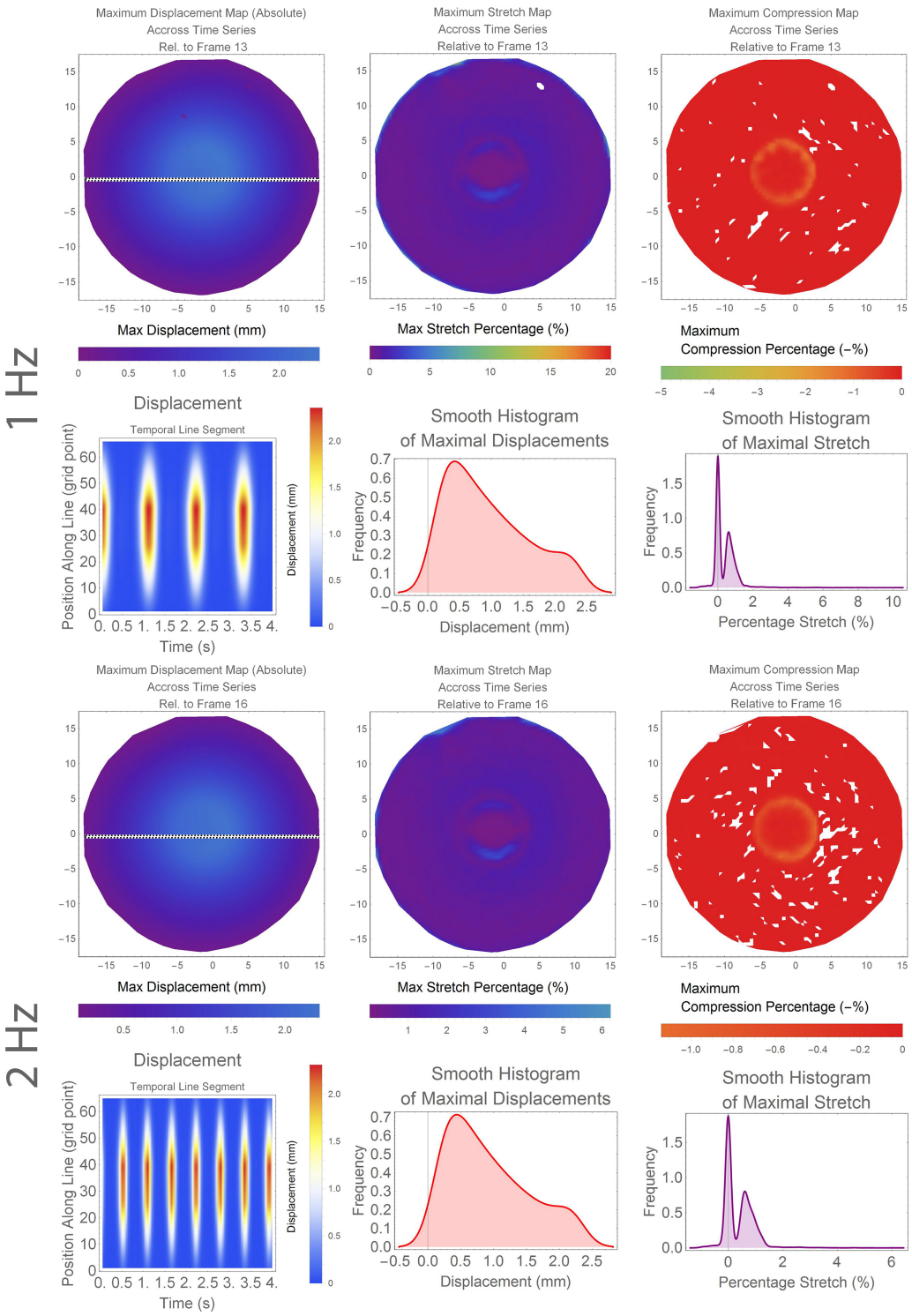

Figure 4.8
DIC Results 2: 6x1 mm EM | MagAct v2.0.
See caption to Figure 4.7.

Figure 4.9 shows the results from the case of 6(d)x2 mm EM with MagAct v1.0. The additional 1 mm thickness of the EM (compared to Figure 4.7) causes an increase of the maximal displacement reaching 3 mm and the maximal stretch reaching at most 10%. With the increase in stretch and under this colour scale a 'comet trail' type distribution of stretch is observed with the tail towards the left side of the magnet. Around 3 - 4% compression is seen at the left periphery of the EM.

Figure 4.10 shows the case with the 6(d)x2 mm EM using MagAct v2.0. Similar to before, displacement and stretch maps show approximately radially symmetric distributions. Maximal displacements are between 5-6 mm in the center of the membrane and maximal stretches are around 7%. Similar to the case with 6(d)x1 mm EM (Figure 4.10), compression is seen in an annular region around the EM with a magnitude of around 2%. The bi-modality in the smooth histogram plots indicate that a significant portion of the membrane experiences a non zero strain and displacement.

4.2.3.3 Discussion

This second trip to the Dantec laboratories in Germany produced results which were more informative than the first. As was discovered, the set of results generated from the first trip were unusable due to flawed methodology used to create the speckle coating. Cracking of the white acrylic base coat implies that the speckle coating acts independently of the membrane and therefore any readings calculated by the DIC system are not representative of the dynamics of the membrane.

The use of a white chalk/solvent aerosol to provide a speckle base coat have produced results that are in general more expected than that produced before; deformation and displacement maps are intuitively correct. However, given the error incurred with the acrylic coating, it is reasonable to question the validity of any DIC results. The system is entirely based on the assumption that whatever is used to create the speckle coating sticks to, and deforms with, the object to be measured. The particles of chalk which stick to the membrane will not stretch with the membrane but instead move apart. This was observed during the DIC recording process; as the membrane was fully stretched the speckle coating separates, exposing the membrane, and returns together upon the membrane relaxing. This is expected behaviour of particles on a stretching membrane. However, if visible by eye, then these areas of exposed membrane result in the DIC method (which operates on a sub millimetre resolution) to ultimately have pockets of complete data loss. For example, if it is only in regions of high strain where membrane is exposed, then it could be argued that the DIC will not report the values at these regions. An understanding on the impact of this in DIC measurements is needed to fully trust the results from this section and this should be an area for continuing research.

A second observation of the chalk based method for create a speckle coated pattern is that it was temporally short. After 5 to 7 seconds of actuation chalk was seen to come off from the membrane creating a mist above the membrane. This suggests that recordings can only be made in short intervals and highlight a limitation of the chalk

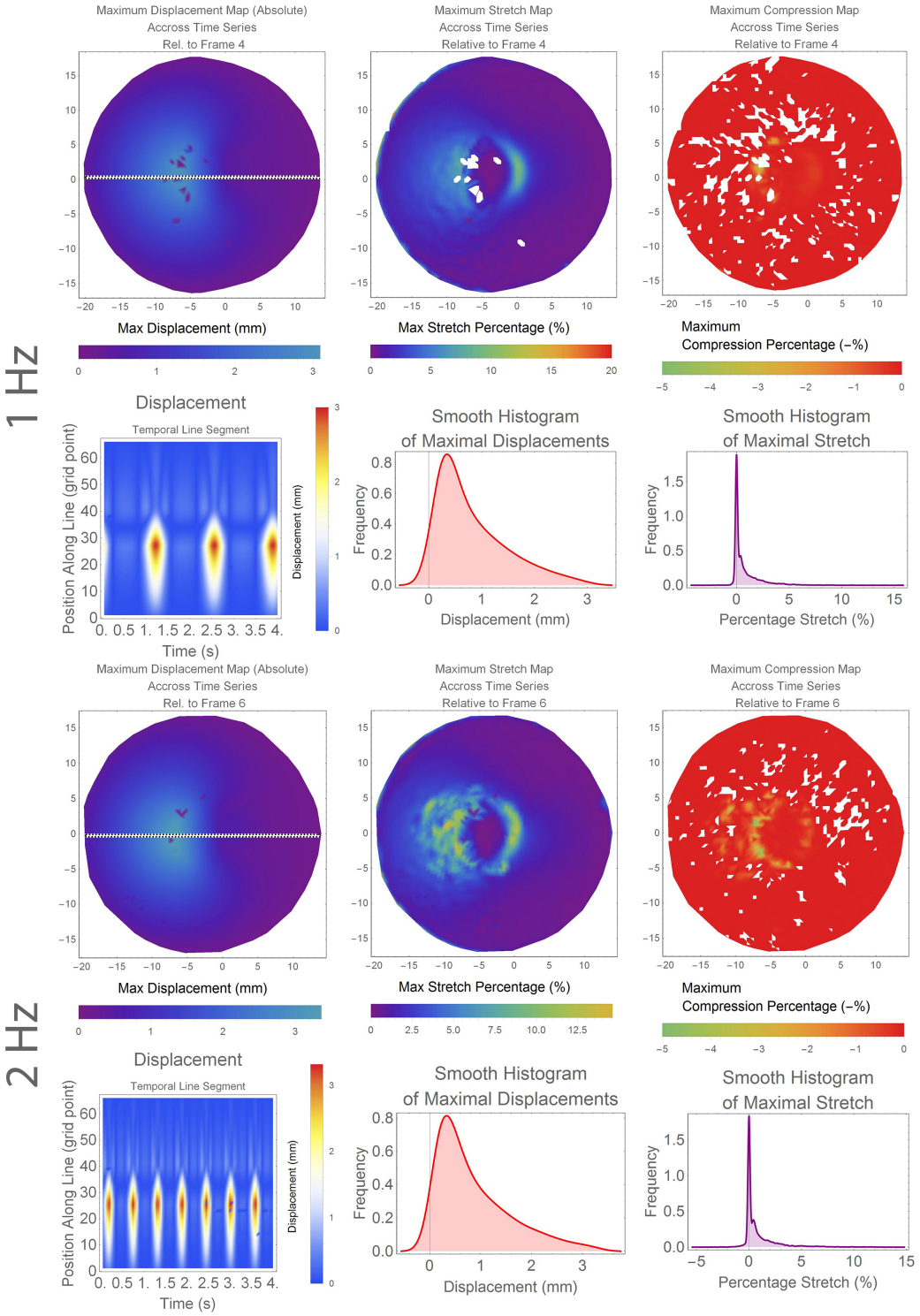

Figure 4.9
DIC Results 2: 6(d)x2 mm EM | MagAct v1.0
See caption to Figure 4.7.

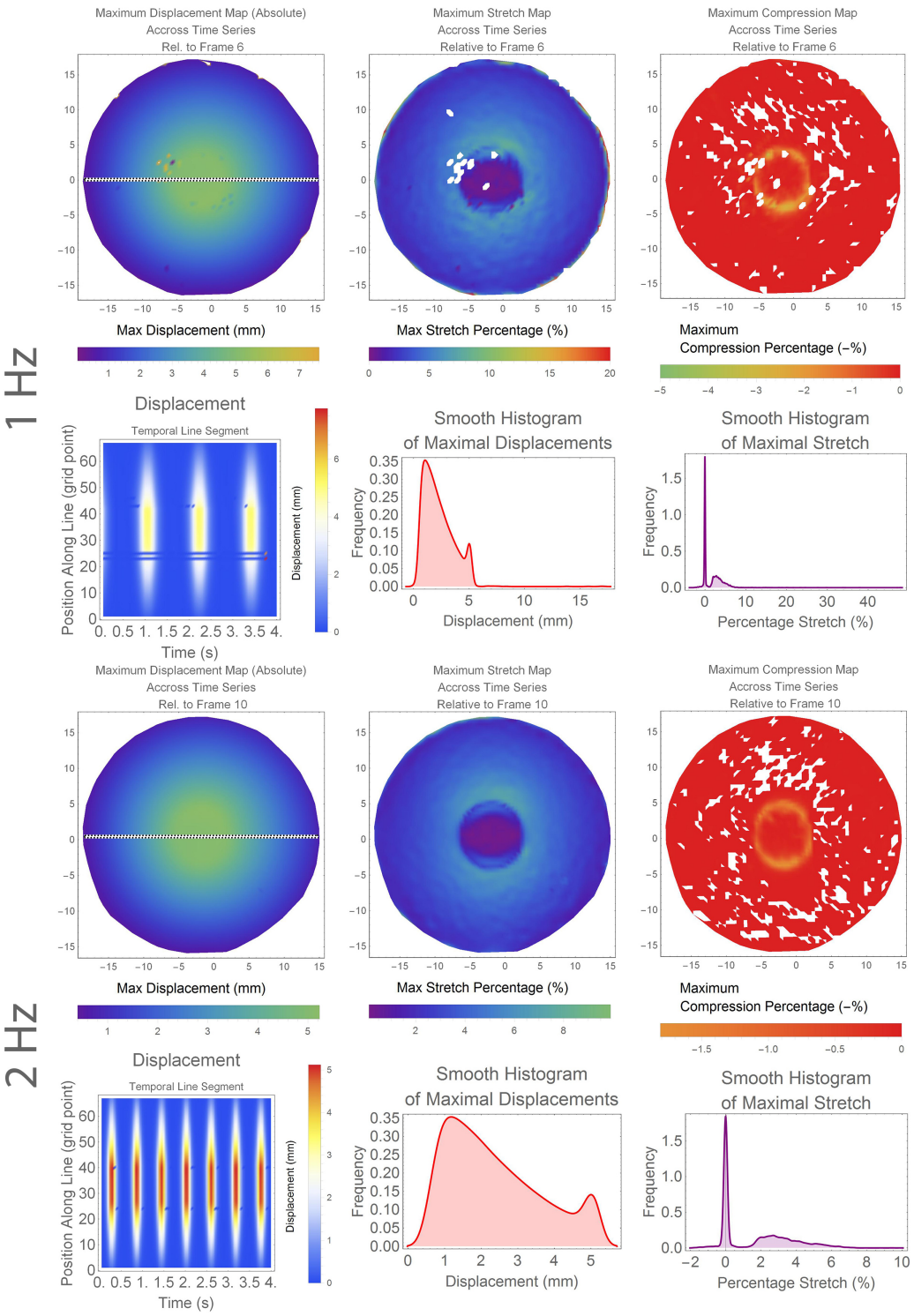

Figure 4.10
DIC Results 2: 6x2 mm EM | MagAct v2.0.
See caption to Figure 4.7.

based method for coating.

Under the assumption that the DIC results are accurate enough, MagAct v2.0 together with the 6x2 mm EM BioFlex® augmentation Protocol 2.1, was shown to deliver the greatest variance of strain across the membrane and with a general radial symmetry (Figure 4.10).

In some maximum strain maps for the 6x2 mm MagAct v2.0 the strain is not symmetric around the magnet but instead focussed to one side of the magnet with a crescent shape (not here presented). The implication of this is that the apparatus lacks a precision originally intended; either the EM is not mounted perfectly in the center of the BioFlex® well and/or the rotating magnet in the DMH is not placed centrally underneath the EM. Through retrospect it is clear that any apparatus not constructed by machine but constructed manually will unlikely be consistent and therefore, in the case of MagAct v2.0, no empirically measured strain map may exist which is free of inconsistencies between measurements. Therefore, efforts to construct a single strain distribution map from the measurements made using the DIC method are hard to justify.

In light of this, focus was turned to supplementing the DIC results with FEM methods. MagAct v2.0 system produces an approximate radial symmetry which is useful for analytics (Figure 4.8 and 4.10). This is made clear by Figure 4.11. Here, DIC results have been arranged frame by frame together with a visual description of the geometry of the membrane as it undergoes deformation. Frame 13 and Frame 27 describe the membrane when the magnets in the DMH are facing away from the membrane. As they rotate towards the membrane, the membrane deforms as in Frames 15 to 19 before the closest point is reached and the membrane is maximally deformed as in Frame 21. Although there are intermediary dynamics, the action between Frame 13 (the un-deformed state) and Frame 21 (the fully deformed state) is simply a 1-dimensional (downward) displacement of the EM – a value given by the maximum value of the maximum displacement maps. Implementation in finite element models is made more simple than before in the case of MagAct v1.0.

The DIC system had been earmarked as a high resolution methodology to physically measure the strain and deformation distributions generated by MagAct. With the claim of the company to be able to empirically measure map strain deformations across large deformable surfaces, this method was explored as a way of providing the stimulus maps required to test the hypothesis of this thesis.

The results of the DIC system are indicative of that, at least compared to the FlexCell® system, the variance of strain delivered is unacceptably low for a high-throughput apparatus. FEM methods were explored to build upon DIC measurements to both establish a characteristic strain map and theoretically explore methods to increase the variance the strain distribution.

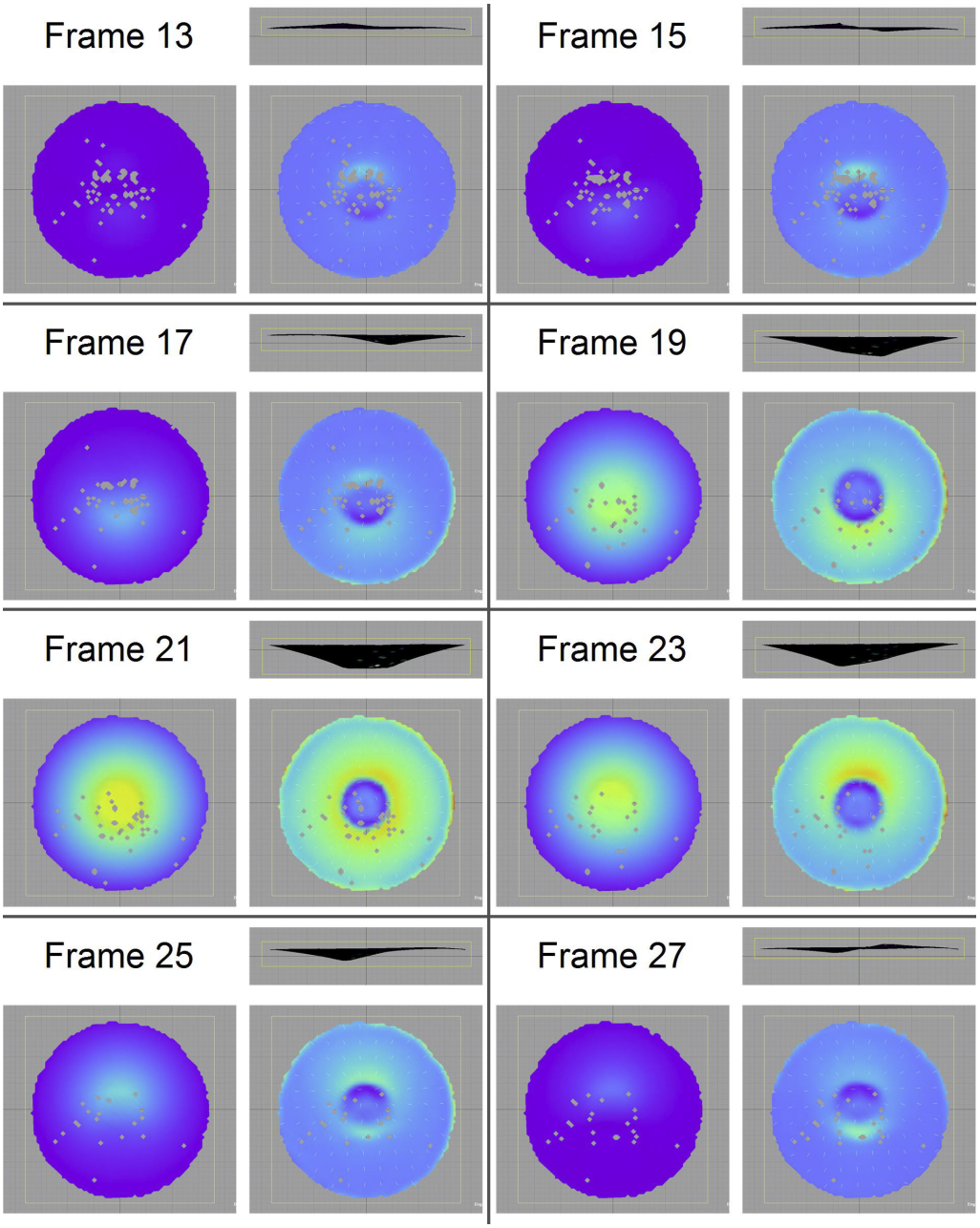

Figure 4.11

MagAct v2.0: A Basis for FEM. Figure shows viewpoints of a single membrane undergoing deformation using the single magnet actuator system as measured by DIC. The top right of each block is a side on view of the membrane. Bottom left is the deformation map relative to a reference frame. Bottom right is the engineering strain map relative to a reference frame. Frame 21 coincides with the magnets in the DMH being closest to the membrane and compared to the other Frames, the maximum downward displacement. As a result of the symmetry, finite elements may be used to model the membrane undergoing a fixed downward displacement from Frame 13 to Frame 21. Theoretically this should be the membrane in maximal strain configuration.

4.3 Finite Element Modelling

All FE approaches were conducted using **Ansys Workbench 17**, **Static Structural** together with **Rhino3D** for object construction. The BioFlex® membrane was modelled as a Neo-Hookean hyperelastic material. **Ansys Static Structural** requires the *initial shear modulus*, G_0, and the *incompressibility parameter*, D_1 to characterise the material. Vande Geest et al. (2004) and Chiang et al. (2010) both set the value of the material parameter C_1 to be 0.282 MPa. In both cases this value was verified by regression analysis of stress-strain measurements of the BioFlex® membrane. For a Neo-Hookean hyperelastic material, the initial shear modulus is determined by

$$G_0 = 2C_1 = \frac{E_0}{2(1+\nu)}, \tag{4.3.1}$$

where E_0 is the Young's modulus of the material and ν is the Poisson ratio (Jakel, 2010). The parameter $D1$ is related to material parameters through the initial bulk modulus, K_0:

$$K_0 = \frac{2}{D_1} = \frac{E_0}{3(1-2\nu)}. \tag{4.3.2}$$

Using Equations 4.3.1 and 4.3.2 and assuming $\nu = 0.499$ (a value indicating near incompressibility), $E_0 = 1.69$ MPa, $G_0 = 5.64$ MPa and $D_1 = 3.6 \times 10^{-8}$ Pa^{-1}. A material property sheet for the BioFlex® membrane was provided by Flexcell International Corporation and lists the Young's modulus of the membrane as 0.93 MPa but does not provide detail on methods of calculation. A copy of the material property sheet can be found in Appendix D.2. Despite the FlexCell® material property sheet, for initial FE investigation, E_0 is set to 1.69 MPa to remain consistent with previous studies.

4.3.1 FEM of FlexCell®

As an initial study, an FEM of FlexCell® was constructed for comparison against previous studies.

A 34.98 mm disc was constructed to sit upon a 25.4 mm diameter post with a top edge fillet of 1.778 mm as done by Vande Geest et al. (2004). The disc was constructed with an interior disc and outer annulus. Vande Geest et al. (2004) construct the membrane similarly with an inner disc equal to the diameter of the post. The outer annulus is then set to experience the force generated by the vacuum pressure. Chiang et al. (2010), however, argue that as the membrane begins to deform and stretch around the post there would be inner regions of membrane which should then become subject to the same force. By only prescribing force to the outer region, Vande Geest et al. are ignoring what could be an important element of the dynamics of the system. Here, the inner region is created with a diameter of 20 mm and the outer annulus straddles both the off- and on-post regions to account for this effect. This is shown schematically in Figure 4.12.

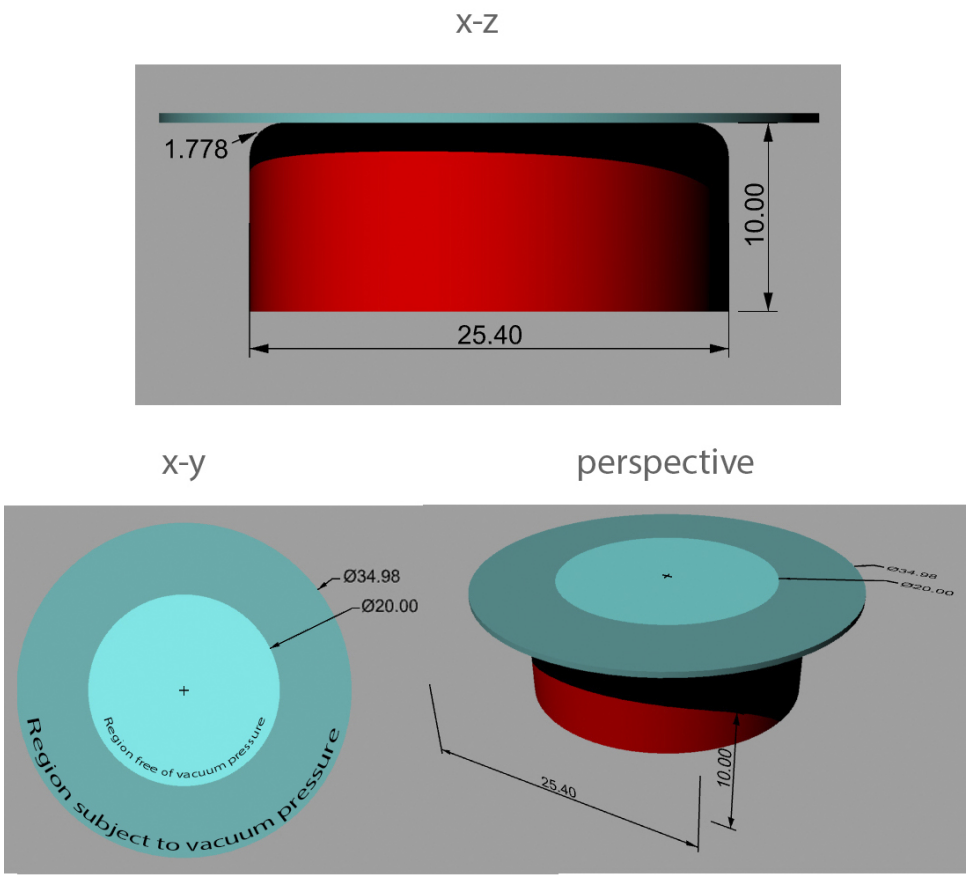

Figure 4.12
Model Schematic for FlexCell® FEM. Each colour represents a distinct object. The membrane is broken into two sections where the outer section is exposed to the vacuum pressure.

Once imported into **Ansys**, the post was rendered as a rigid body object while the membrane was meshed with tetrahedrons using a patch conforming algorithm. This generated 144,972 nodes and 87,845 elements with a minimum element size of 0.4 mm. In comparison, Vande Geest et al. (2004) used 5830 first order, quadrilateral elements. They, however, reported the conducting of mesh independency analysis which is missing from this work. As such, mesh density analysis is an important avenue for developing this work. A frictional contact region was prescribed between the post and the underside of the membrane with a friction coefficient of 0.03 (Vande Geest et al., 2004). The outer edge of the membrane and the base of the post were given zero displacement boundary conditions. The two membrane sections were paired as a 'glued contact region' so they would behave as one object. A normal surface pressure was applied to the underside of the outer annulus of the membrane. The **Ansys** Non-linear Mechanical FEM solver steps from a pressure equal to 0 until it reaches 80 kPa. This represents a vacuum pressure of -80 kPa which the FlexCell® manual claims to generate 20.2% strain on the membrane.

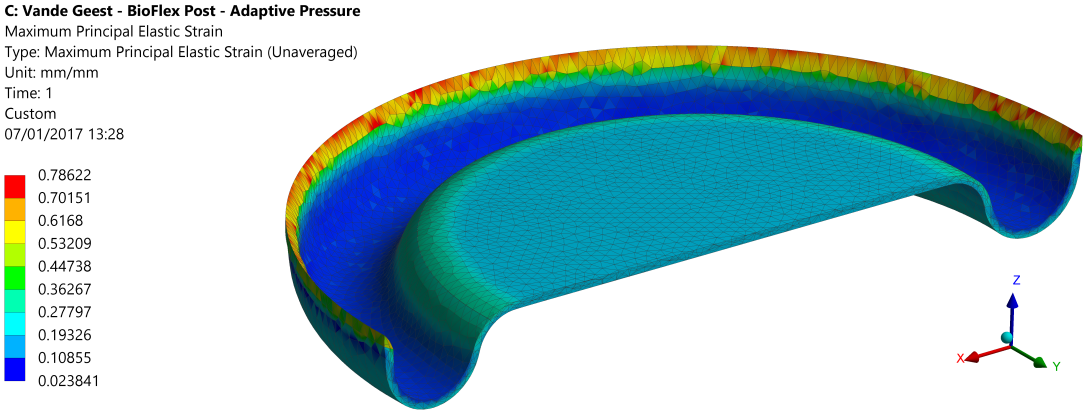

(a) Maximum Principal Elastic Strain

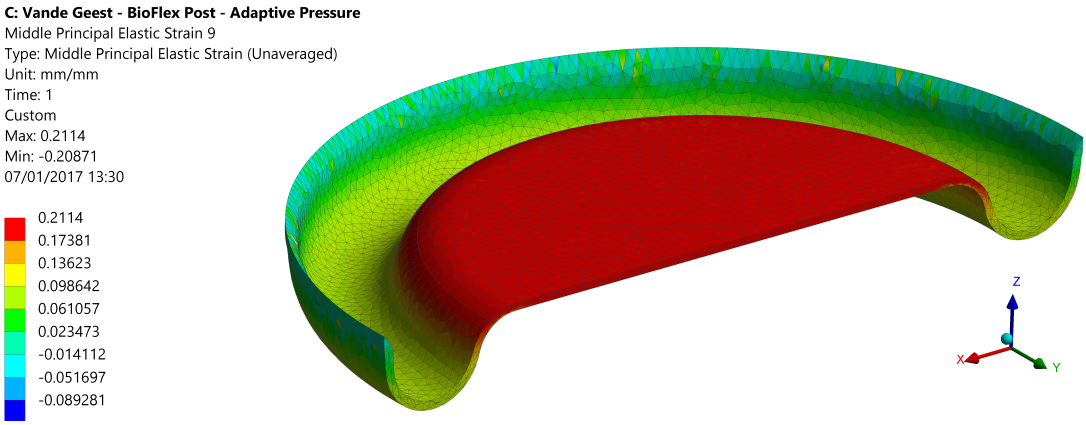

(b) Minimum Principal Elastic Strain

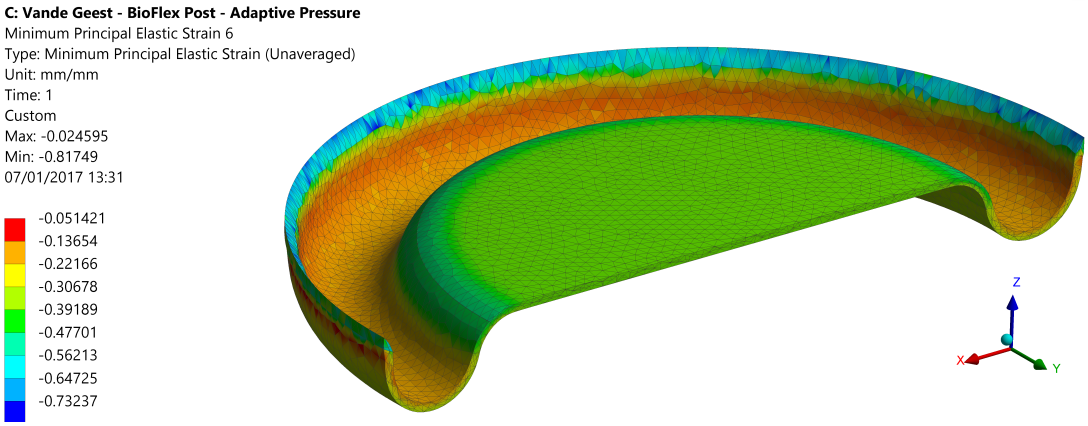

(c) Minimum Principal Elastic Strain

Figure 4.13
FEM of FlexCell® : 3D Visualisation of principal strain measurements when subject to 80 kPa of vacuum pressure. Images are shown in the deformed state.

Pressure (kPa)	Strain (%)			
	FlexCell®	VG	CH	JP
20	3.7	4/4.4	3	3.8
40	9.2	7/8	6.2	7.5
60	15.6	10.5/11.7	10.2	12
80	20.2	15.2/17	NA	19.3

Table 4.1
Multiple Source Comparison of Strain Values for FlexCell®. VG=Vande Geest et al. (2004); CH=Chiang et al. (2010); JP=current study.

4.3.2 Results and Discussion

Figure 4.13 shows the 3-dimensional FEM results of the membrane having undergone 80 kPa of vacuum pressure. The plots show the maximum, middle and minimum principal elastic strains, respectively. The deformation of the membrane around post is as would be expected. The principal directions are indicated by the arrows along the radial line of the membrane in Figure 4.14(a). The maximum and middle principals remain in plane with the membrane but does not consistently point in the same direction. The minimum principal is always directed normal to the membrane.

Figure 4.14(b) shows the z-displacement of the radial line along the top of the membrane for four vacuum pressures: 20, 40, 60, and 80 kPa, respectively. The region where the post is underneath the membrane as well as the curved edge of the post are indicated on the graph. The separation of the curves on the on-post region indicate that as pressure is increased the membrane is increasingly compressed towards the post in the z-direction. This directly contradicts Chiang et al. who claim their FEM results suggest the membrane located over the post moves upwards, perpendicular to the membrane. They, however, do not report the detail or data of this result. They speculate this occurs in their models due to a 'leak' of vacuum underneath the membrane early into the vacuum cycle. This is not seen here or suggested by these FEM results. Further investigation would be needed to assess these dissimilarities.

Figures 4.14(c) to 4.14(e) show the equivalent maximum, middle and minimum principal strains. The first two principals are tangential to the membrane plane and the equality of results up until the post edge indicate a biaxial strain. On the on-post region, the biaxial strain is 3.8%, 7.5%, 12% and 19.3% for the pressures 20, 40, 60, and 80 kPa, respectively when taking the value of strain at the center. These values are shown in Table 4.1 for comparison to those provided from the Flexcell Cooperation, Vande Geest et al. and Chiang et al.. The results from the FEM here are closer to those associated with FlexCell® than in other studies. Despite a request to Flexcell, the methodology used to calculate the values for the FlexCell® system are not known and therefore it is difficult to judge whether the values discovered here are better or worse than those in previous studies.

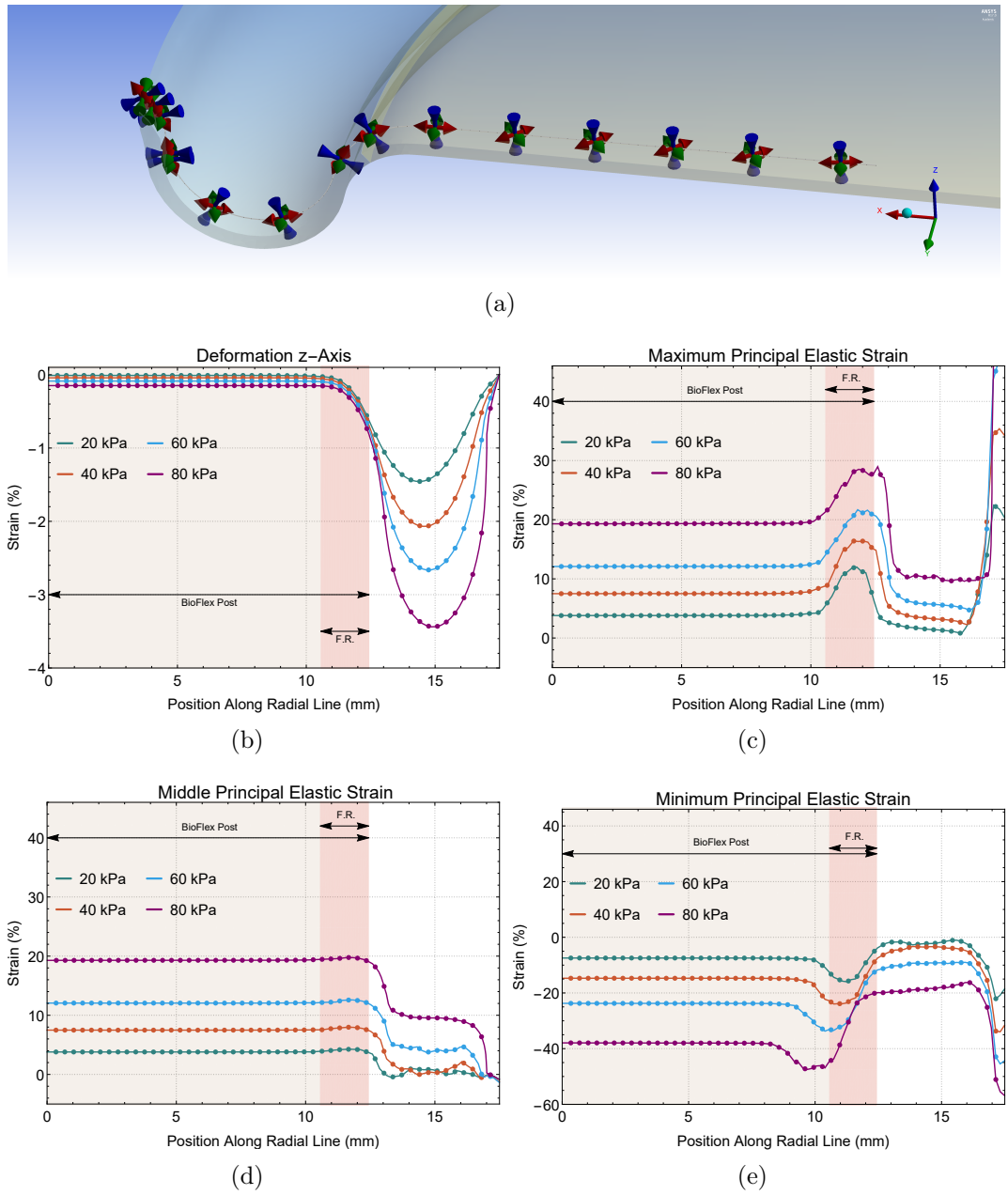

Figure 4.14

FEM of FlexCell®. (a) Shows the principal strain directions along the radial line for the x,y and z planes. (b) to (e) show deformation, maximum, middle and minimum principals along the radial line for four applied pressures.

Vande Geest et al. express their FEM results through radial and circumferential strain components, E_{rr} and $E_{\theta\theta}$, respectively, along the radial line. A method in the **Ansys Workbench** user interface to extract these components was not found. Therefore to calculate E_{rr}, 100 node coordinates were taken along the line going from $(x, y) = (0, 0)$ to $(17.49, 0)$ (the radial line) in the FE model from the undeformed configuration together with the corresponding nodes in the fully deformed configuration. This is shown in Figure 4.15(a) where each white line connects corresponding nodes. For each un deformed node,

N_i^u, and the corresponding deformed node, N_i^d ($i \in [1, 100] \in \mathbb{Z}$), E_{rr} was calculated through:

$$E_{rr}^i = \frac{ed(N_i^d, N_{i+1}^d) - ed(N_i^u, N_{i+1}^u)}{ed(N_i^u, N_{i+1}^u)}, \tag{4.3.3}$$

where $ed(s1, s2)$ is the Euclidean distance between $s1$ and $s2$. Equation 4.3.3 calculates strain by measuring the change in node to node distance from the deformed to the un-deformed configuration as a fraction of the un-deformed distance. Figure 4.15(b) compares the output of this to the data from Vande Geest et al. as extracted from Section 1.3; page 39. It is clear that there are strong discrepancies when comparing the two data sets. In particular, there is a complete absence of strain gradient in the FE results generated here when compared to the Vande Geest et al. data in the case of 80 kPa of vacuum pressure. Discrepancies are also notable in the regions at the fillet region of the post where a jump in radial strain is predicted here. Within the off-post region the membrane is here predicted to sharply decrease in radial strain. In the case of the lower vacuum pressure of 20 kPa the radial strain becomes compressive which is not predicted by the VG data.

The absence of the strain gradient in the region over the post has been difficult to account for and despite investigations not presented here, an answer has not been reached. However, the decrease in radial strain in the off-post region, when considering Figure 4.15(b), appears reasonable. As the membrane deforms downwards a bending moment may be expected such that the bottom of the membrane radially stretches compensated by the top of the membrane radially compressing. The presence of bending moments in membranes such as these are briefly mentioned in Gilbert et al. (1994), albeit, for a thicker membrane. It isn't clear from either Vande Geest et al. or Chiang et al. from where throughout the thickness of the membrane radial lines are measured. If radial strain is averaged throughout the thickness of the membrane then perhaps this could account for the discrepancies seen here. However, a definitive explanation has not been reached and since empirical data has never been measured for strain at the off-post region, any explanation here will only ever be speculative.

Justified by strain values measured here being closer to those offered by FlexCell® in Table 4.1, the membrane model was developed further for MagAct v2.0.

4.3.3 FEM of MagAct v2.0

An FE model of the MagAct v2.0 system was constructed in four parts given by:

1. The membrane is modelled as a single 0.5 mm disc with a diameter of 34.96 mm as before.

2. The EM is a 6(d)x2 mm cylinder directly underneath the center of the membrane.

3. From observation of augmented BioFlex® plates, the glue used to embed the mag-

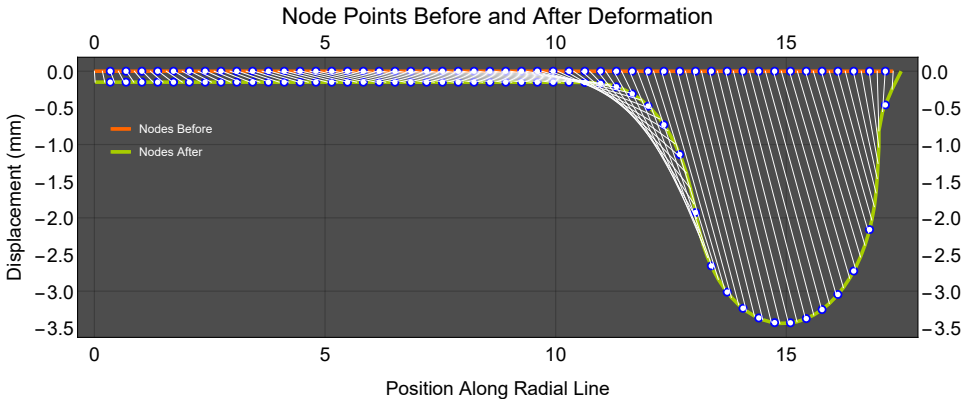

(a)

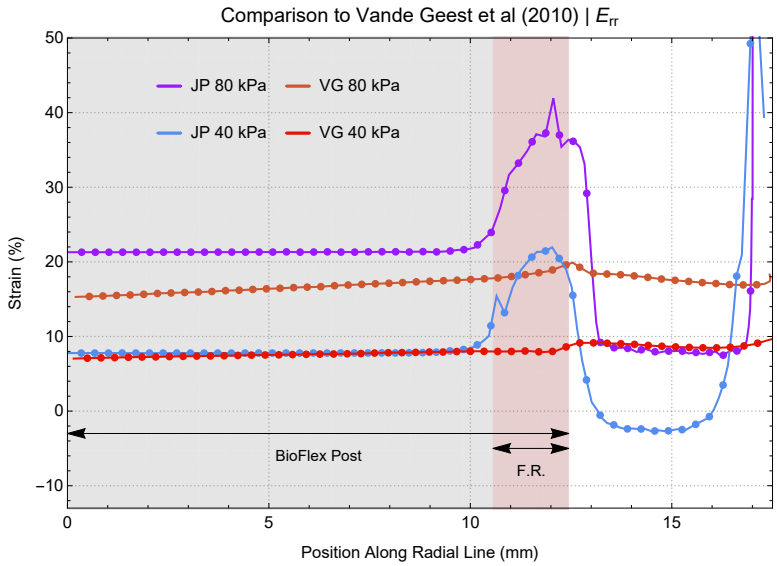

(b)

Figure 4.15

Comparison of FlexCell® FEM to Vande Geest et al. (2004). (a) Plots the relationship between position along the radial lines in both the deformed and un-deformed state in order to calculate E_{rr}. (b) Comparisons between the data from Vande Geest et al. (VG) and the equivalent measurements made here (JP).

net ridges around the EM before dropping off to form a peripheral mound of glue. The glue section was designed in two parts (Figure 4.16):

(a) An inner cylindrical annulus of glue with an outer diameter of 8 mm and height of 1 mm.

(b) A second component with a height of 1 mm which decays in height towards the membrane surface.

The silicone glue was given the same material properties of the membrane. The glue did not undergo any material testing so this assumption is a limitation of the FE model constructed here.

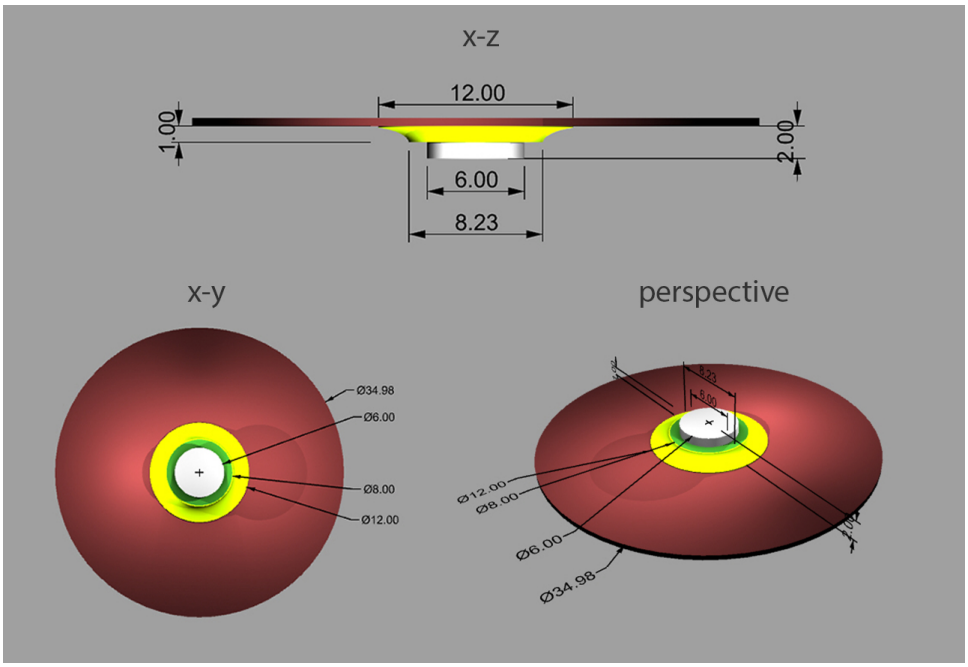

Figure 4.16
FE Model Schematic for MagAct. Colours represent distinct objects. Green and yellow objects are two stages of glue binding the EM to the membrane. Measurements are given in mm.

Once imported into **Ansys** all objects were meshed with tetrahedrons using a patch conforming algorithm. This generated 154,131 nodes with 93,541 elements with a minimum element size of 0.4 mm. Each of the objects were paired to have 'glued contact regions'. A z-displacement of 10 mm was applied to the magnet through which the **Ansys** Non-linear Mechanical FEM solver steps from 0 mm until 10 mm is reached.

4.3.4 Results and Discussion

Figure 4.17, similar to the previous section, shows the 3-dimensional results of the membrane having undergone 5 mm of EM downward displacement. The plots show the maximum, middle and minimum principal elastic strains, respectively. The deformation of the membrane is as expected. The principal directions are indicated by the arrows along the radial line of the membranes in Figure 4.18(a). Unlike the FE models of FlexCell®, the maximum and middle principal vectors are not always tangential to the membrane. In general, the maximum principal is in the radial direction. Directly over where the magnet is situated, however, the maximum principle is in the z-direction. This suggests the predominate strain in the region over the magnet is one which is vertically stretching – i.e., bulging.

Figure 4.18(b) shows the z-deformation of the radial line for the cases when EM displacement is 2.5, 5, 7.5 and 10 mm, respectively. As the EM displacement has been set to these values, this plot serves as a useful cross-check that the model is running as expected. Figures 4.18(c) to 4.18(e) show the corresponding strain principals for the four

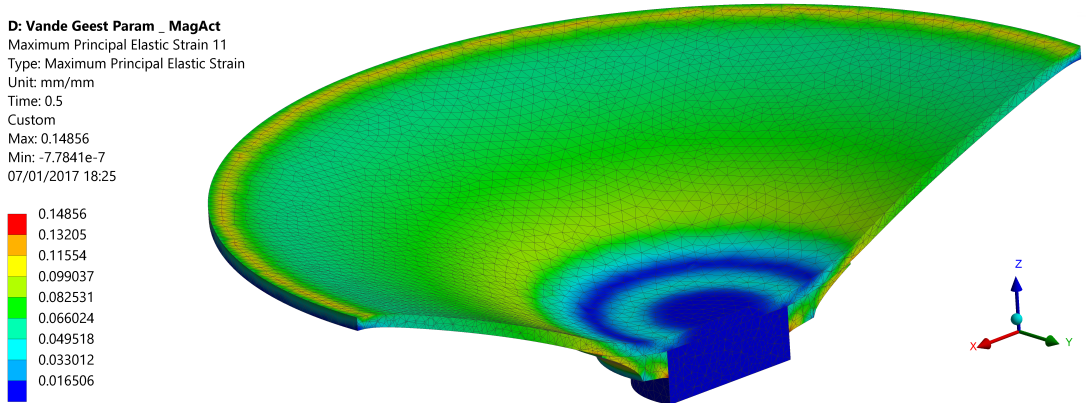

(a) Maximum Principal Elastic Strain

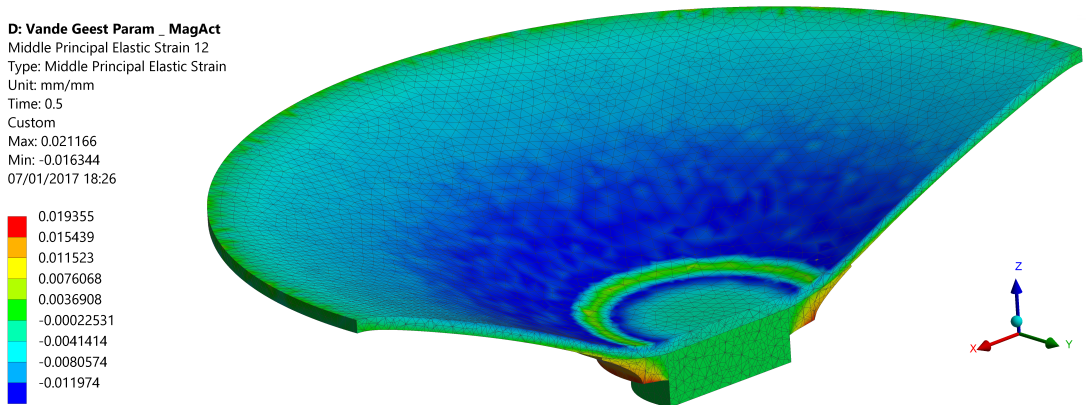

(b) Middle Principal Elastic Strain

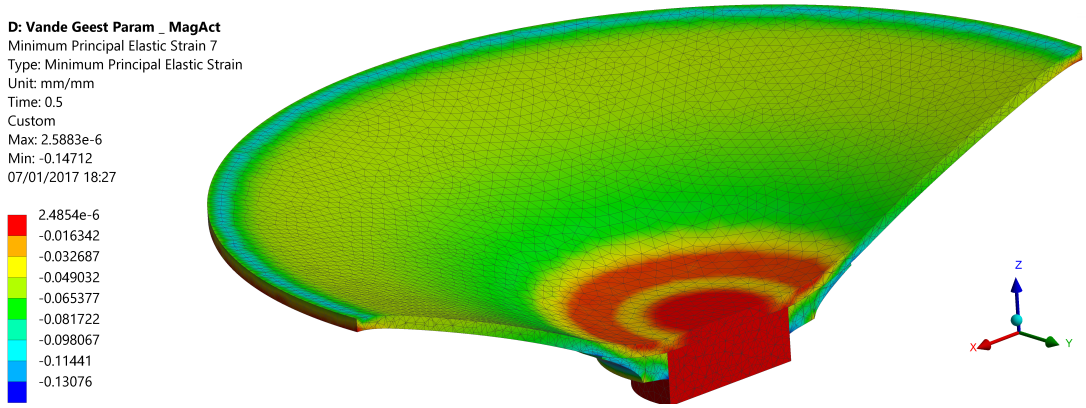

(c) Minimum Principal Elastic Strain

Figure 4.17
FEM of MagAct: 3D visualisation of principal strain measurements when subject to a 5 mm EM downward displacement.

displacement lines. The plots also indicate the spatial regions where the membrane is over either over the EM, the first glue section (G1), and the second glue section (G2). In the region over the EM the maximum principal, which is pointing in the z-direction, displays a strain of around 13% percent for the 10 mm distension. This suggests, coupled with the observation that the middle and minimum principals (in plane with the membrane) are

compressive, that at 10mm of downward pull the region over the EM bulges upwards with a (non-biaxial) compression in the membrane plane. These observations make intuitive sense. As the membrane is pulled down from the middle the free regions of the membrane (the parts not glued directly to the EM) will be pushed inwards towards the middle, and since the top of the membrane is unrestricted, it bulges upwards to compensate.

When in the G1 phase in the radial line plots (Figure 4.18), strain always tends towards 0. Considering this section is essentially a thicker area of membrane it makes sense that it would be less pliable and therefore exhibits less strain than neighbouring sections. As the membrane thins in the G2 phase the principal direction of strain points in the radial direction and increases in magnitude sharply. After the G2 phase the membrane is free of interfering components and quickly reaches a maximum radial strain before decaying towards the membrane edge.

The results in Figure 4.18 are indicative of several key theoretical features of the MagAct system. Firstly, the strain across the membrane is not biaxial. In comparison, this is a feature at the core of the FlexCell® system. Secondly, the MagAct v2.0 system does appear to generate a heterogeneous strain gradient. When pulled down to 10 mm the results suggest a range of strain between 5 - 30%. However, as will be discussed later, the variance of strain produced in MagAct v2.0 is much smaller.

Just as the FEM of FlexCell® was compared to previous studies, the FEM results from MagAct is here compared to the DIC data from Section 4.2.3. Based on visual inspection of the clarity of data and visual symmetry, the 2 Hz data set previously shown in Figure 4.10 was chosen for further analysis.

4.3.4.1 Comparison to DIC

One of the major limitations of the DIC system is the absence of a standard coordinate system from which to work from. To compensate for this, a script was written in **Mathematica** to interactively move the DIC membrane in its native coordinate system to align with the FE system. This is shown as a before and after screen-shot in Figure 4.19(a). In the Figure the outer blue circle is the same diameter as the BioFlex® membrane whilst the inner is the diameter of the EM. The sliders were manually dragged to visually align the DIC membrane with the circles. The x and y correction values were then used to transform the coordinate system of the DIC membrane. Figure 4.19(a) demonstrates both the partial loss of membrane edge from the DIC data as well as suggesting a strong glue related effect in terms of strain around the EM.

Following coordinate transformation, radial lines going through the origin in the DIC data were then sampled from the membrane. In total 64 lines were sampled. This was also repeated for the corresponding compression map (see Figure 4.10). The corresponding values of strain along these lines are shown plotted in Figure 4.19(b). Superimposed on the plot are the lower and upper quartiles of the distribution of radial strain as well as the mean. The variance is relatively consistent for the data set. The EM, G1 and G2 regions used in the FEM model are also superimposed. The result suggests that the

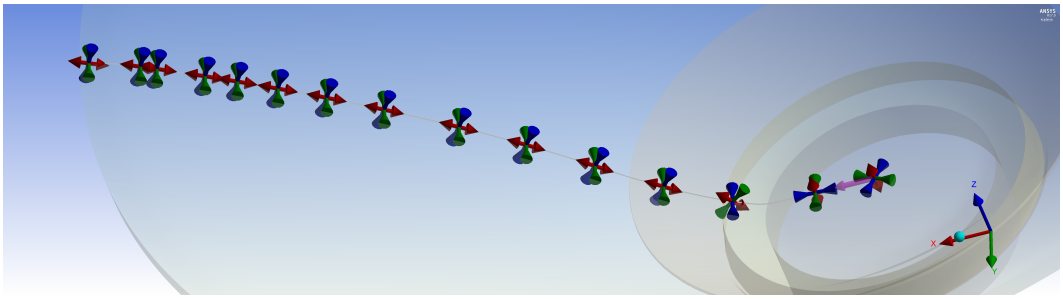

(a) Direction of Strain Principals

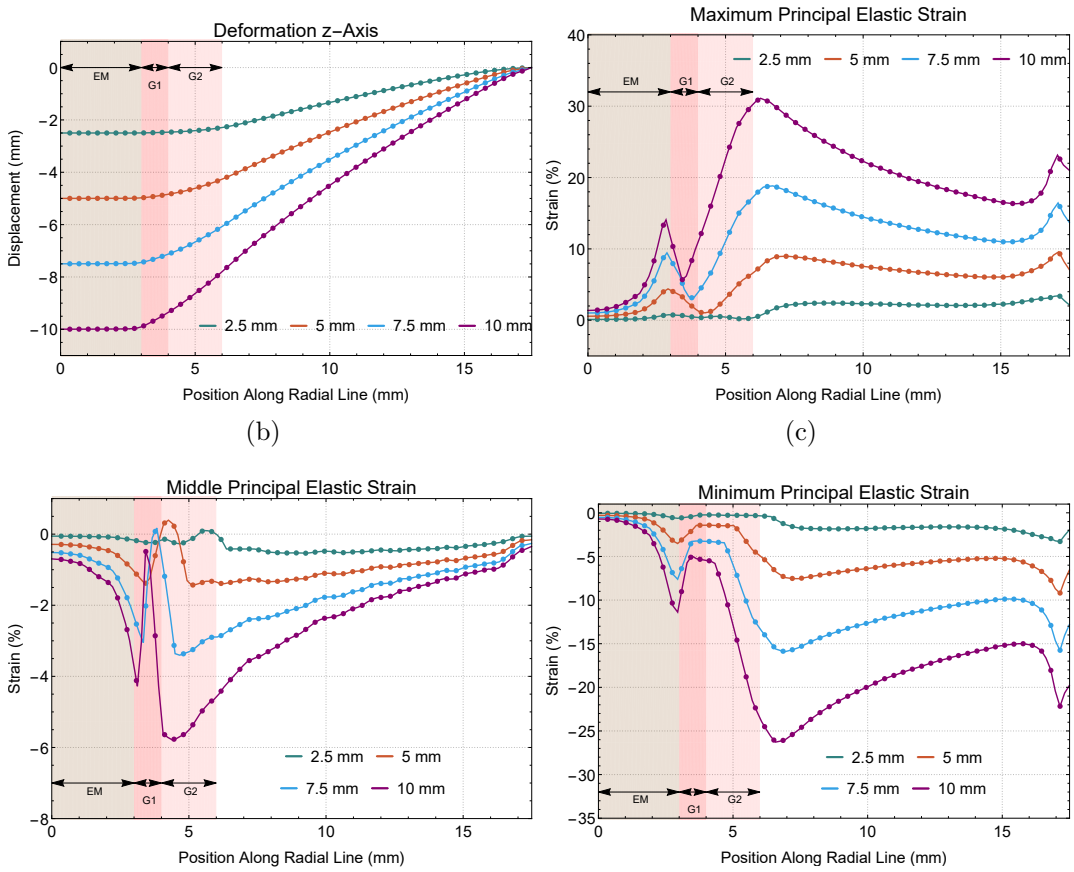

Figure 4.18

FEM of MagAct v2.0. (a) Shows the principal strain directions along the radial line. (b) to (e) show deformation, maximum, middle and minimum principals along this line for four applied displacements.

placement of the G1 phase in the FE model is consistent with the DIC data but that the G2 phase may not have been wide enough.

For this DIC measured membrane the maximum z-displacement of the EM was measured at 5.5 mm. Figure 4.20 shows the comparison between the maximum principal elastic strain from the FE model when the EM has been distended by several distances. It is immediately clear that there are stark differences between the FEM at 5.5 mm and the DIC data. The DIC system does not concur with the sharp increase seen in

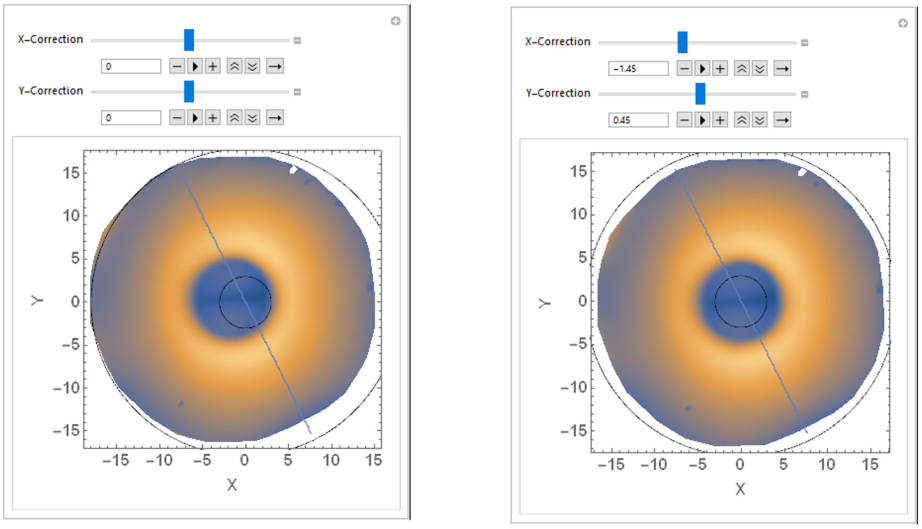

(a) Coordinate Transformation

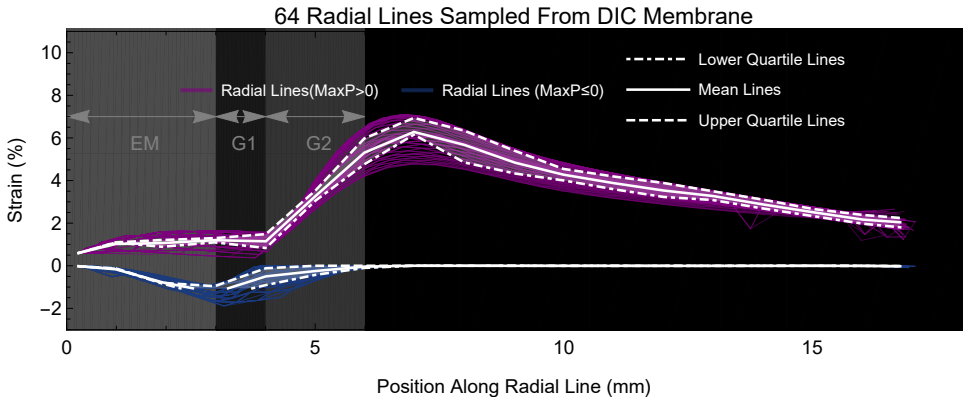

(b) DIC Principal Strain Radial Lines

Figure 4.19

Preparation of the DIC Data.

(a) shows the application of the methodology being used to transform the native coordinate system of the DIC data to one which is symmetric around the origin. Manual sliders were used to move the DIC membrane to fit visually within an outer circle (representing the BioFlex® dimensions) and an inner circle (representing the EM dimensions). (b) Shows the results from sampling 64 radial lines rotating around the origin of the transformed DIC membrane. The plot shows the EM, G1, and G2 phases that were used in the FE model as a point of comparison.

maximum principal strain towards the edge of the EM phase where, as discussed previously, is directed with the z-axis. The strain incline after the G1 phase is higher with the FEM results than DIC, reaching a peak of around 11% before declining throughout the rest of the membrane to around 6.5%. Instead, the DIC measurements show a peak of around 7% declining throughout the rest of the membrane to around 2%. Despite this, the gradient of decline for both the DIC and FEM results are qualitatively similar suggesting that the FEM results capture the spatial dynamics of the system in form,

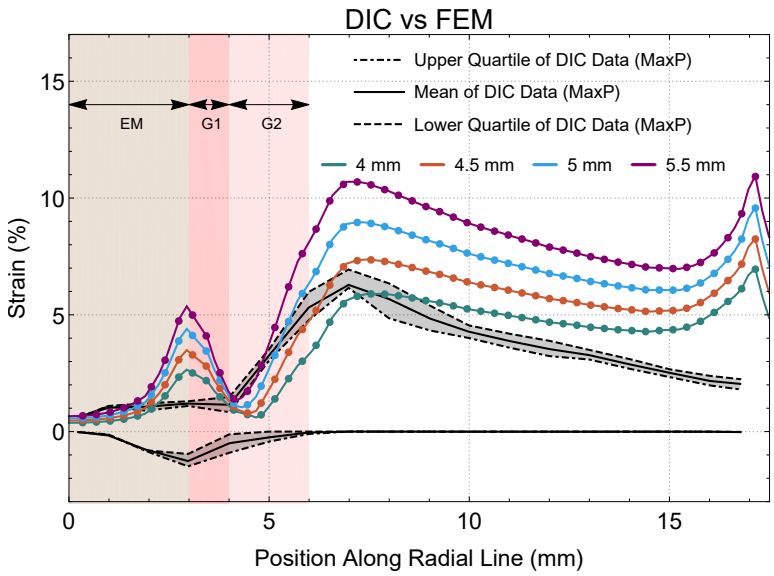

Figure 4.20

DIC Data (black) Compared to FEM of MagAct (colour). FEM of MagAct is presented for four EM displacements – 4, 4.5, 5 and 5.5 mm. After transforming the coordinate system of the DIC data the maximum principal strain given by the FEM model for a radial line displaced by 4, 4.5, 5, and 5.5 mm is compared.

but not in magnitude. Attempts to correct the discrepancy by comparing strain lines for various EM displacements (shown on the same plot, Figure 4.20) suggest a decrease of EM displacement may better replicate the initial peak of the DIC data but that the similar gradient of decline is lost. In other words, the 4.5 mm FEM model describes the magnitude but not the spatial dynamics.

To explain the discrepancy, the possibility that the BioFlex® manufacturers are incorrect in consistently creating 0.5 mm thick membranes was tested. Similar iterations were conducted for membrane thickness whilst keeping the EM displacement fixed. FE models were conducted for membranes that were 0.5, 0.8 and 1.4 mm thick and compared similarly to the DIC radial data. These results are shown in Figure 4.21. Additional in these plots is the E_{rr} component calculated similarly as before using Equation 4.3.3. The E_{rr} curves in all of the plots confirm that after the G1 phase the principal direction is radial. Figure 4.21(b) suggests the a membrane with a thickness of 0.8 mm may better represent the DIC data than the original model. When the membrane is even thicker (Figure 4.21(c)) the gradient of decline deviates from the DIC data and the improvement is lost. However, fitting the model to the DIC data is not a sensible approach given the doubts regarding the DIC methodology.

4.4 Conclusion

The aim of the work in this chapter was to analyse the strain distributions generated by MagAct in order to generate a characteristic strain distribution map. With this

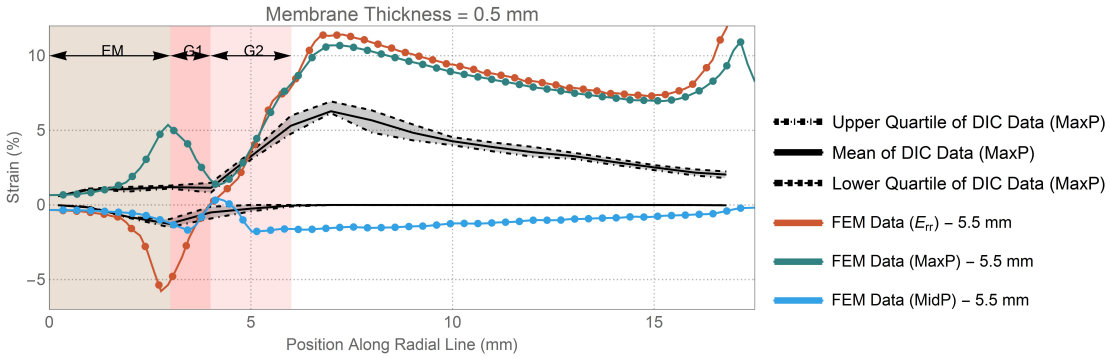

(a)

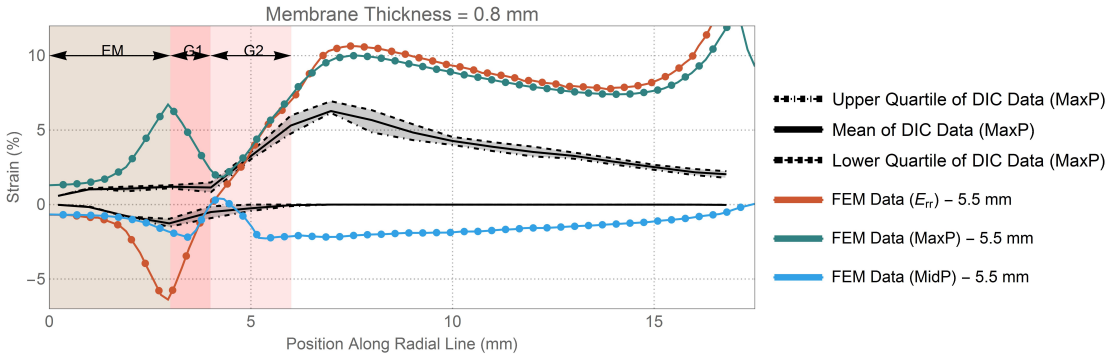

(b)

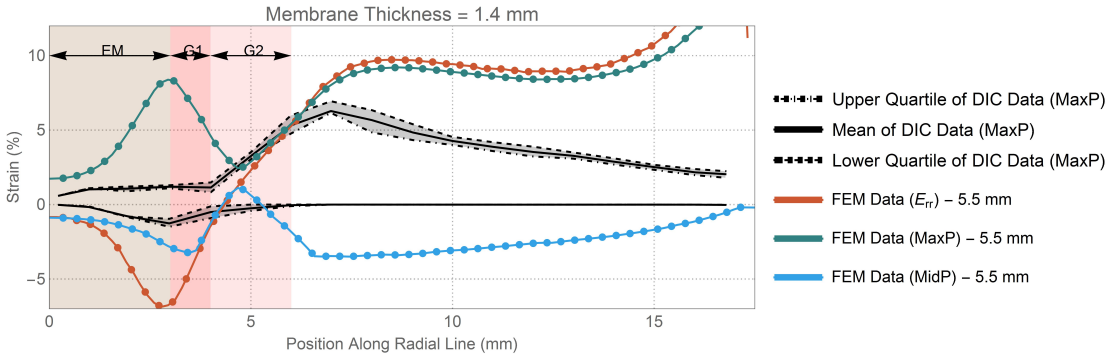

(c)

Figure 4.21
Comparison of DIC (black) to FEM Data (colour) of MagAct With Variable Membrane Thickness. E_{rr} is calculated for the radial line FEM results for MagAct v2.0 and compared to the DIC data. (a), (b) and (c) show the results for membranes of 0.5, 0.8, and 1.4 mm thickness, respectively.

'stimulus map', the left branch of this thesis' hypothesis would be complete. To do this, two methods of investigation were employed: empirical measurements using the digital image correlation (DIC) system from Dantec Dynamics GmbH, and theoretical calculation in the form of finite element modelling (FEM) approaches.

The DIC measurements at first indicated a failure of the MagAct system in producing any strain at all. Subsequent investigation found this was attributed instead to a detrimental flaw within the DIC methodology. Upon rectifying this through employing a different method of creating a speckle coated pattern, the system began producing results closer to intuitive expectations. These results indicated that the most varied but symmetric distributions of strain are generated by using a single magnet actuator system (MagAct v2.0) and marks a distinct departure from Dr. Day's original prototype.

Analysis of the DIC results also pointed to the difficulty in averaging DIC results to produce a characteristic strain map. At the heart of this was the realisation of the challenges of the MagAct system. Although every attempt was made, manual construction of the apparatus together with manual augmentation of the BioFlex® plates results in either/both the EM placement or placement of magnets in the DMH being non-central.

A beneficial consequence of MagAct v2.0 is the ease at which FEM approaches can be used to theoretically investigate the system. Due to the symmetry of the system, investigation of maximal strains can be reduced to a simple z-displacement of the EM as being the key model dynamics. This is in contrast with the previous expectation of having to model the force interactions between magnet pairs in MagAct v1.0.

The FEM was build upon previous work conducted predominantly by Vande Geest et al. (2004) who theoretically investigated the FlexCell® system. The FEM results of the FlexCell® conducted here do not fully concur with previous studies. Despite this, the strain values theorised for the FlexCell® system are closer to those provided by the manufacturers than previous studies. The FEM was then considered robust enough in terms of validation to justify extension to MagAct v2.0.

The theoretical result for the MagAct system were directly compared to measurements made using DIC. Although there are similarities between the two sets of data, a close match was not observed. There are, however, obvious limitations to both methods. FEM is a theorised simplification of the MagAct system based on untested material parameters and which rely on precedent set by previous studies. The DIC system on the other hand is left open to considerable criticism with respect to the speckle coating procedure. As discussed earlier, the speckle coating is assumed to deform in the same manner as the material to be measured. This assumption is the main reason for the failure during the first set of tests to produce any meaningful results using the DIC system. There is reasonable doubt whether by trying to observe the deformation using DIC, the deformation can truly be measured. There is also the possibility that the stereoscopic camera set up of the DIC system is not able to accurately measure this extent of out-of-plane deformation. Other versions of the system exist which utilise a five camera system. Such could increase the accuracy of out-of-plane deformation measurement.

If a characteristic map of strain stimulus were to be produced from this work, it would be through FEM results. The DIC results, however, guide the FE models in providing a maximum distension of the EM – that of 5.5 mm.

With this, the result of this chapter suggests that the range of strain MagAct v2.0

is capable of theoretically delivering is between -5-11% using the radial strain as the measurement of choice. As well as not having anticipated compression, the range of strain is lower than ideal for experimental purposes given, for example, pathological strain may be as high as 15% (as discussed in the introductory chapter). Original goals for a high throughput strain apparatus had desired ranges of strain covering, at the very least, the full spectrum of the FlexCell® values: 0-25% strain. Theoretical modelling suggests a further distension of the EM by up to 5 mm could generate strain gradients up to 30% and thus serves as a topic for future development of this work.

To conclude, the strain delivered using the MagAct v2.0 system is non-biaxial, approximately radially symmetric, and can be approximated using FEM in radial strain components with a resolution on par with the microscopy in Figure 3.16; page 130.

4.5 Chapter Summary

With reference to Section 4.1, the aims of this chapter have been achieved. In particular:

1. DIC methods were intuitively shown to measure strain distributions.
2. Driven by initial measurements, the MagAct system was developed to use a single magnet actuation method encouraged. This resulted in MagAct v2.0.
3. Physical measurements suggested that the range of strain generated by MagAct v2.0 is no more than 0 to 5%. Therefore, MagAct v2.0 does not fulfil the original aims of this thesis.
4. Finite element models were created to theoretically describe strain distributions. These are only partially in agreement with DIC measurements and suggest that strain ranges are between -5 to 11%.

There is no rational consensus about which of the DIC measurements or the theoretical FEM analysis is closer to describing the truth of the MagAct system. However, it is clear that MagAct does not deliver the variance of strain originally desired by the aims of this thesis - 0 to 25%.

The DIC system appears to be a relatively trustworthy tool for measuring strain and to date a method as high in resolution as this has not been applied to the FlexCell® system. Aside from an analysis of the MagAct system this chapter also demonstrates a novel alternative to standard measurements of strain across BioFlex® plates in the FlexCell® system. It therefore serves as a promising area of future work to expand analysis of FlexCell® experiments to a degree which has not been done before.

Chapter 5

Explorative Study of Cyclic Strain and Proliferation

When this thesis was in its planning stage the research plan for this chapter was focused on answering biological questions rather than the development of the technology to do so. This chapter was intended to showcase experimentally gathered information greater in volume than previous literature of the correlation between strain and cellular proliferation. However, biological complications coupled with an underestimation of the time required to develop the technology leaves this work in flux. This chapter instead describes and discusses biological experimentation undertaken during the course of this research, it's purpose within the context of the development of MagAct, and a discussion of limitations and future work.

5.1 Introduction

Biological experimentation has served two purposes in this thesis: firstly as a tool for development of the technology, and secondly to form the foundations for a complete proof of concept demonstrating the validity of the method.

For development, in particular, the image acquisition and analysis work has been driven by repeated experimental work. For establishing the proof of concept of the MagAct system, preliminary experimental work was driven by the strategy defined as follows:

1. Find a cell type together with a set of FlexCell® strain parameters where a notable proliferative change is observed. This is referred to as 'ground truth'.
2. With the same cell type, perform experiments using the MagAct work flow.
3. If, as part of the high throughput MagAct pipeline, the results derived encapsulate the ground truth results from 1, then a proof of principle is established.

Proliferation as a phenotype of interest was chosen as a proof of principle candidate for a number of reasons. Primarily, this was because of Dr. Day's original proof of

concept using the original prototype discussed briefly in Chapter 2.3.3; page 61, and described in detail in Appendix C.2; page 234. Building upon this work is of interest to our research group; engineering tissue both *ex vivo* and *in vivo* is greatly enhanced as a therapeutic by controlling the rate of proliferation in cells. This is particularly notable considering the wide use of non-human animal serum as a growth supplement in cell culture.

Ultimately, a proof of principle was not established using proliferation as a phenotype of interest. This is discussed in this chapter and in the final chapter of this thesis.

5.2 Chapter Aims

The aims of this chapter are to establish a biological paradigm to be used within a proof of concept study of MagAct and the imaging pipeline established in previous chapters. In particular:

1. Find a set of parameters for a specific cell type using the FlexCell® system which exhibits strong correlation with strain and proliferation measure using the Roche BrdU proliferation ELISA.

2. Using the established cell type, conduct experiments using the MagAct system and imaging pipeline.

3. Demonstrate proof of concept by showing the results of 1. are encapsulated in the results of 2.

5.3 Quantifying Proliferation

Results based on Dr. Day's original prototype used the Roche BrdU Colorimetric Cell Proliferation ELISA. 5-bromo-2'-deoxyuridine (BrdU) is a synthetic nucleoside analogue of thymidine. BrdU can be incorporated into newly synthesised DNA of in-tact cells through a substitution of thymidine for BrdU. A BrdU antibody can then be bound to BrdU but only after denaturing of the DNA in the cells. The protocol for the Roche BrdU ELISA is described here by Protocol A.15; page 226. Note that this protocol has been developed for 6-well cell culture analysis.

The immediate criticism with the usage of this ELISA in Dr. Day's original prototype, and indeed on any experiment where the stimulant is not homogeneous, is that the ELISA is population averaging. Consequently, not only are any heterogeneous effects ignored, but the results may not be an indicator of the true biology.

Given the method developed in this thesis relies on stimulant heterogeneity, an alternative method for assessing proliferation was found in the Click-it® EdU Alexa Fluor® 488 imaging kit from ThermoFisher. Like BrdU, 5-ethynul-2'-deoxyuridine (EdU) is a nucleoside analogue of thymidine and is incorporated into newly synthesised DNA

Cell Type	Analysis Method	Apparatus	Stetch Regimes	Surface Coatings	Basic Finding
HAEC	BrdU	FlexCell® †⋆	5%; 15 %	Pronectin Collagen 1	Inhibition of Proliferation
HRSMC	BrdU	FlexCell® †⋆	5%; 15 %	Pronectin	Inhibition of Proliferation
HASMC	BrdU	FlexCell® † MagAct v1.0	15% Heterogeneous	Collagen 1	No Significant Change
HUVEC	BrdU	MagAct v1.0 MagAct v2.0	Heterogeneous	Fibronectin	No Significant Change
C2C12	BrdU	MagAct v2.0	Heterogeneous	Fibronectin	Stimulation of Proliferation

Table 5.1
Proliferation Studies: Basic Experimental Findings.
†: with BioFlex® post. ⋆: without BioFlex® post.

of in-tact cells through a substitution of thymidine for EdU. Mild fixation and permeabilisation is sufficient for the molecule based detection reagent to gain access to the EdU in the DNA which means that cells no longer need to be denatured. This kit allows fluorescent tagging using a variety of Alexa Fluor® dyes. In this way, cells are fixed in place following strain stimulus for quantification of proliferative state through fluorescent microscopy – a method suitable for the MagAct work flow developed here. The protocol for the Click-it® EdU Alexa Fluor® 488 method is described in Protocol A.16; page 227. Note that this protocol describes a method which utilises several ThermoFisher products rather than the single imaging kit which the company offers. This was done due to the cost effective nature of utilising several products; more experiments can be conducted for less cost. Similar to the BrdU ELISA it has also been scaled for 6-well cell culture analysis.

5.4 Experimental Exploration

Exploration to find a suitable proof of concept use case made use of several cell types. The following section details a variety of results related to each. Table 5.1 summarises select experimental results. In brief, no cell type was found to be suitable and results are often contrary to what would be expected given previous literature. Reasons for why this may the case be are explored in the discussion in Section 5.5.

5.4.1 General Methods and Materials

5.4.1.1 Culturing Protocols

For any given cell type, the first suspension of cells from cryopreservation was conducted according to Protocol A.7; page 222. Cells were cultured and passaged according to Protocol A.8; page 224. When there was a surplus, cells were aliquoted and cyropreserved according to Protocol A.10; page 225.

5.4.1.2 BrdU Titration and Serum Starvation

For serum starvation studies, cells were seeded into a 96 well tissue culture plate at a specified density in 100 μL of complete (cell specific) medium. Approximately 24 hours later half of the wells were replaced with complete medium and the other half replaced with serum free (cell specific) medium. Following 24 hours of incubation the BrdU ELISA was conducted according to Protocol A.15; page 226, with volumes scaled by 1/10.

For BrdU titration studies, cells were seeded into a 96 well place at a density of $10{\times}10^3$ per well in 100 μL of complete medium. Approximately 24 hours later half the wells were replaced with complete medium and the other half replaced with serum free medium. Following 24 hours of incubation, BrdU labelling solution was added to wells at specified time intervals so that by the final time point cells would have been exposed to a defined variety of times of BrdU incubation. The BrdU ELISA was then continued according to Protocol A.15; page 226, with volumes scaled by 1/10.

5.4.1.3 FlexCell® and MagAct

A FlexCell® 3000FX was made available by Dr. Petros Syrris in the Institute of Cardiovascular Science, UCL. BioFlex® plates were purchased from Dunn Labortechnik GmbH. Untreated (BF-3001U), ProNectin coated (BF-3001P) and Collagen Type 1 coated (BF-3001C) were purchased. FlexCell® lubricating grease was also purchased from Dunn Lavarotechnik GmbH.

Cells were seeded onto BioFlex® plates according to Protocols A.8; page 224, and A.11; page 225. After a specified time of incubation, medium was replaced with pre-warmed complete (cell specific) medium before being mounted onto the FlexCell® system for stretching. Prior to mounting, the 25 mm loading posts of the FlexCell® system were coated lightly by finger with lubricating grease and the software was programmed to deliver appropriate strain parameters. The loading posts can be removed from the FlexCell® system and when done this step was ignored. The BioFlex® plate was then mounted on top of the loading posts as per manufacturers instructions and removed only if the experiment required replenishment of medium. Otherwise the plate was removed at the end of the experiment and quantified using the BrdU ELISA (Protocol A.15). For every actuated BioFlex® plate a control plate is prepared the same way and at the same time but is not subject to BioFlex® actuation.

For experiments involving MagAct, BioFlex® plates and control plates are seeded and handled in the same way as above. The actuation period was set using software developed in previous sections.

5.4.2 Human Aortic Endothelial Cells (HAEC)

Human Aortic Endothelial Cells (HAEC) were purchased from Gibco (COO65C) as a frozen vial cryopreserved in medium containing 10% DMSO.

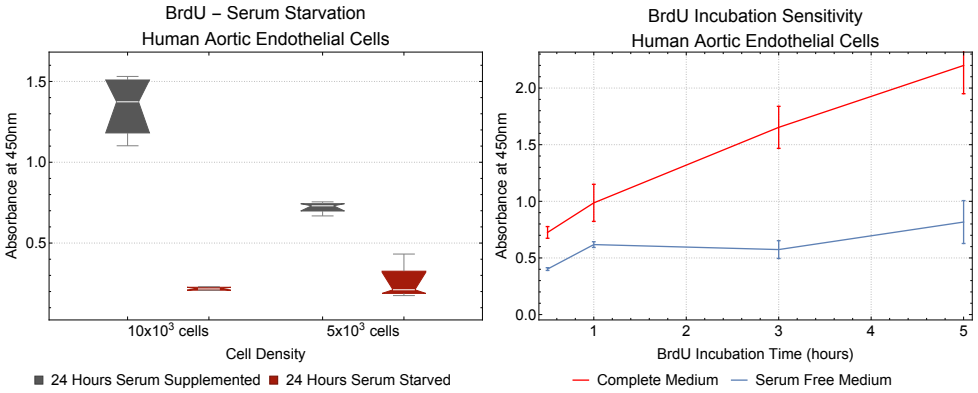

(a) Serum Starvation (b) BrdU Sensitivity

Figure 5.1
BrdU sensitivity and serum starvation experiments. (a) Shows the colorimetric absorbance of HAEC having undergone 24 hours of serum starvation and quantified using the BrdU ELISA. (b) Shows the results of titrating BrdU incubation times.

5.4.2.1 BrdU Titration and Serum Starvation

For serum starvation studies, cells were seeded into a 96 well tissue culture plate at a density of 10×10^3 and 5×10^3 per well in 100 μL of Medium 200 with Low Serum Growth Supplement (LSGS) and antibiotics/antimycoctics (AB/AM) (complete medium; see Table A.1; page 223). Serum free medium is described as Medium 200 with ABAM only.

For the BrdU titration studies, cells were seeded into a 96 well plate at a density of 10×10^3 per well in 100 μL of complete medium. BrdU labelling intervals resulted in final exposure time points of 0.5, 1, 3 and 5 hours. Three wells were recorded for each experimental condition.

Results

Figure 5.1(a) shows the results of the serum starvation experiment. As expected, it suggests a complete arrest of DNA synthesis activity after 24 hours of serum starvation.

Figure 5.1(b) shows the results of the BrdU titration. As expected from 24 hours of serum starvation, DNA synthesis activity is inhibited compared to cells exposed to fully supplemented medium. After 1 hour of BrdU labelling solution incubation the difference between the colorimetric signals of serum starved and fully supplemented cells increasingly becomes larger. For experimental work, an incubation time of around 3 hours is suggested in order to clearly differentiate signals from proliferating and non-proliferating cells.

This set of experiments suggests the cells are behaving as expected and 3 hours is a sufficient time for BrdU labelling solution incubation.

5.4.2.2 FlexCell® Experimentation

As mentioned earlier, the purpose of testing these cells on the FlexCell® system is to establish a ground truth from which the MagAct system can be tested against as a proof of concept. From the results of Li et al. (1994) (see Table 1.1; page 37) the expectation was that HAEC would be stimulated to proliferate when stretched at an amount between 7-25% at a frequency of 1.6 Hz. This was partially tested as well as a handful of other parameters on the FlexCell® system.

For all variations of the experiments HAEC of passage 5-8 were seeded onto 6-well Collagen Type 1 or ProNectin BioFlex® .

In attempt to replicate the results of Li et al. (1994) HAEC were stretched continuously for 5 days with programmed strain of 25% at a frequency of 1.6 Hz. For this 100×10^3 cells were initially seeded. For exploration of proliferative responses to various stretch parameters the following conditions were also explored:

Exp 1: Initial seeding of 65×10^3 cells on ProNectin treated plate; 24 hours actuation; 15% stretch. Including loading post.

Exp 2: Initial seeding of 65×10^3 cells on ProNectin treated plate; 24 hours actuation; 15% stretch. No loading post.

Exp 3: Initial seeding of 65×10^3 cells on ProNectin treated plate; 24 hours actuation; 5% stretch. Including loading post.

Exp 4: Initial seeding of 65×10^3 cells on Collagen Type 1 treated plate; 24 hours actuation; 15% stretch. Including loading post.

It should be noted that microscopes available in the lab at this time did not have focal lengths which were capable of viewing the cell plane on the membranes; the culture height in BioFlex® plates is much higher than standard tissue culture plates. As a result, visual confirmation before and after experiments was not conducted.

Results and Discussion

For the Li et al. (1994) replication experiment the results are presented as the BrdU colorimetric reading for both the actuated wells and control wells. For Exp 1 to Exp 4 results are presented as BrdU fold increases of the actuated wells relative to the control wells. In this way results can be presented in the same plot and interpreted in the same way.

Figure 5.2(a) shows the results from the 5 day actuation experiment. Contrary to what was expected from Li et al. (1994) there is no marked difference between actuated and control wells. However, by the final day there was significant condensation of medium on the underside of the lid in the BioFlex® plate which was being actuated. This was not present in control plates. Visually, there was also a significant loss of medium due to evaporation in the actuated wells compared to the controls. As no positive

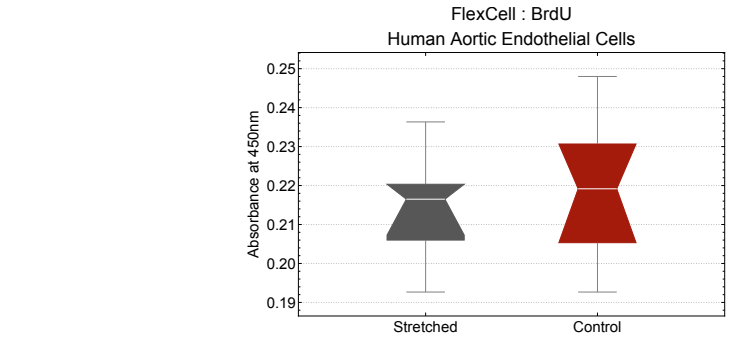

(a)

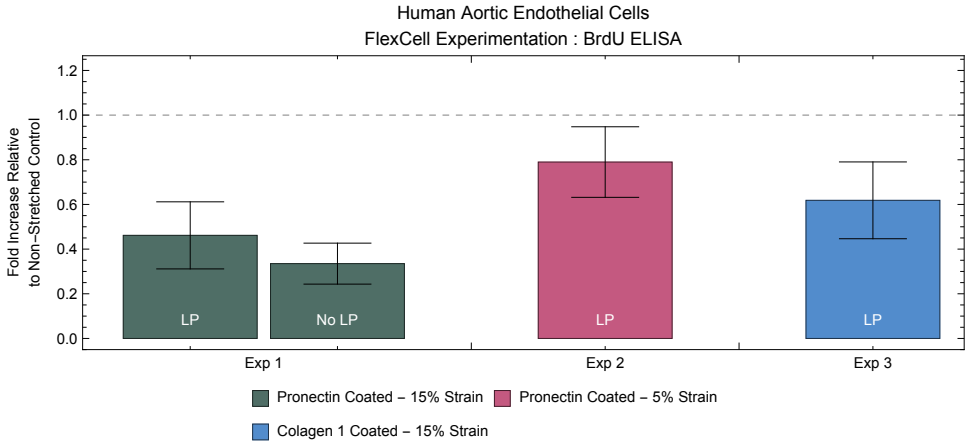

(b)

Figure 5.2

Human Aortic Endothelial Cells: FlexCell® Experimentation Results. (a) Replication of experiment of Li et al. (1994); shows the colorimetric reading when quantified using BrdU. (b) Provides the fold increase relative to an unstretched control plate. In this way results can be better compared. No experiments here show an increased level of proliferation as a result of of cyclic stretch.

controls or standardised readings were used in the experiments these results can't be definitively compared against other experiments. The colorimetric readings, however, resemble those of serum starved cell cycle arrest seen in Figure 5.1(a). This indicates, but doesn't definitively point to, 5 days being too long an actuation period without medium replenishment.

Figure 5.2(b) shows the results of conditions Ex 1 to Ex 4. Expressed as ratios of the control measurement, each result is interpreted as the fold increase in proliferation as a result of stretch. A fold increase greater than 1 indicates an induced proliferative response. Here, all measurements are indicative of significant inhibition of proliferation as a response to stretch. Again, this is contrary to the results of Li et al. (1994). Given that these experiments were not repeated, the assumption is that there were flaws in the experimental protocol or faults in the FlexCell® apparatus. Figure 5.3 shows the result of a subsequent test where a ProNectin BioFlex® plate is compared to a 6-well

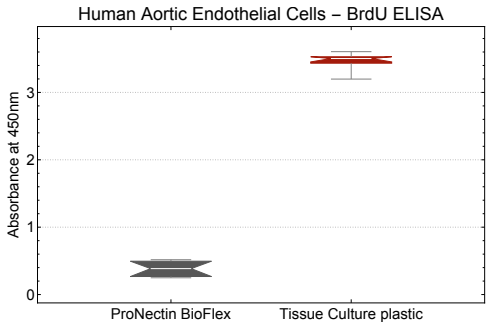

Figure 5.3
HAEC: Growth on plastic versus ProNectin BioFlex® . Cells grown on plastic are in a significantly more proliferative state than cells grown the exact same way on ProNectin BioFlex® plates.

tissue culture plastic plate. Both plates were seeded with 100×10^3 cells and treated in the same way as described in Section 5.4.1. BrdU analysis suggests that by virtue of being on ProNectin BioFlex® , the HAECs are either arrested in their cell cycle – not proliferating – or cells have not adhered, or cells do not grow on ProNectin. The lack of a microscope to visualise cells on the BioFlex® plates and without a repeat which quantifies total cell number, a definitive answer cannot be concluded.

For the purposes of finding a suitable cell type for use as a proof of concept, HAEC were deemed an unsuitable candidate due to both contrary behaviour and a lack of a suitable response.

5.4.3 Human Rectal Smooth Muscle Cells (HRSMC)

HRSMC were previously used by Dr. Richard Day in establishing his original prototype for this project. This cell type was also explored as a suitable candidate here.

5.4.3.1 Serum Starvation and BrdU Titration

Similarly to Section 5.4.2.1, the BrdU ELISA was titrated across BrdU incubation times and assessed using a serum starvation experiment as a preliminary step for the use of HRSMC.

For the the serum starvation study, HRSMC of passage 11 were seeded into a 96 well tissue culture plate at a density of 10×10^3 and 3.4×10^3 per well in 100 μL of complete medium (A.1; page 223). Approximately 24 hours later one third of the wells were replaced with complete medium, one third replaced with complete medium without FBS and the remaining third with complete medium with the addition of human basic fibroblast growth factor (hbFGF) at a concentration of 1 μg/10 mL . The inclusion of a group with added hbFGF was to provide a positive control. hbFGF is used by others in the lab to stimulate the proliferation of cells and concentrations were established through recommendation and experience of other lab members.

For the BrdU titration study, HAEC of passage 11 were seeded into a 96 well plate

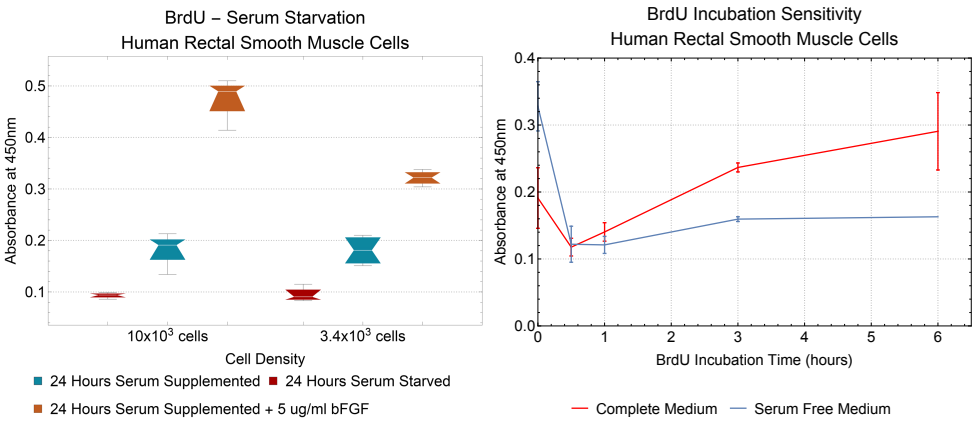

(a) (b)

Figure 5.4
BrdU sensitivity and serum starvation experiments. (a) Shows the colorimetric absorbance of HRSMC having undergone 24 hours of serum starvation and quantified using the BrdU ELISA. (b) Shows the results of titrating BrdU incubation times.

at a density of $10{\times}10^3$ complete medium.

Results and Discussion

Figure 5.4(a) shows the results of the serum starvation experiment. As expected, it suggests a complete arresting of DNA synthesis activity after 24 hours of serum starvation. The positive control shows a large increase in proliferation and shows that cells are capable of proliferating at a rate higher than their base rate.

Figure 5.4(b) shows the results of the BrdU titration. As expected from 24 hours of serum starvation, DNA synthesis activity is inhibited compared to cells exposed to fully supplemented medium. After 1 hour of BrdU labelling solution incubation the difference between the colorimetric signals between serum starved and fully supplemented cells increasingly becomes larger. For experimental work, an incubation time of around 3 hours is suggested in order to clearly differentiate signals from proliferating and non-proliferating cells.

5.4.3.2 FlexCell® Experimentation

The method and materials for FlexCell® experimentation of HRSMC is the same as described in Section 5.4.1. However, in line with Dr. Day's original prototype experiments, the period between seeding cells onto BioFlex® plates and the time the first actuation occurs is different. Here, cells are seeded 3 days before actuation, typically on a Friday for actuation beginning on the following Monday. Each well in the BioFlex® plate is replaced with pre-warmed complete medium immediately before FlexCell® actuation as before.

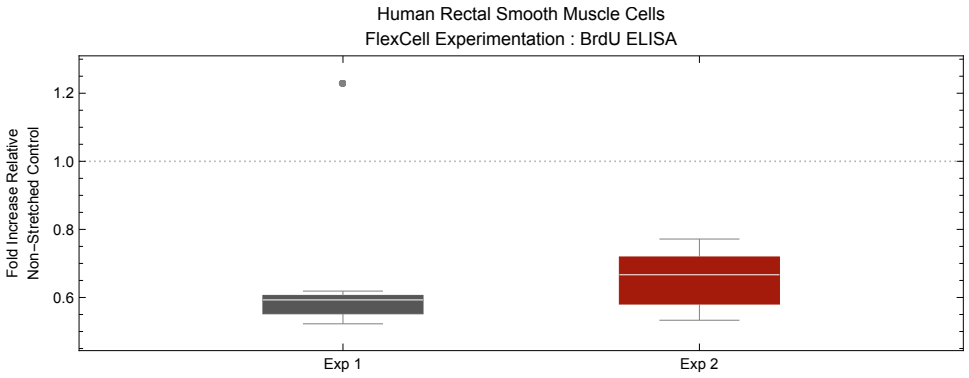

Figure 5.5
HRSMC FlexCell® Experimentation. Results show the fold increase of two FlexCell® experiments, Exp 1 and Exp 2, using HRSMC relative to unstretched controls for two independent plates.

HRSMC's were the cell type of choice for Dr. Day's original prototype. Of the two experiments detailed here, Exp 2 follows in a similar vein with periodic actuation over several days for only 1 hour per day. Much work in the literature with similar smooth muscle cell types instead expose the cells to a continuous actuation for several days. The experiments presented here using FlexCell® to assess suitability for HRSMC as a candidate for a proof of concept for the MagAct pipeline was conducted through the following experimental parameters:

Exp 1: Initial seeding 300×10^3 cells on ProNectin treated plates; 24 hour actuation; 15% stretch; 1 Hz; with loading post.

Exp 2: Initial seeding 360×10^3 cells on ProNectin treated plates; 1 hour actuation per day for 5 days; 10% stretch; 1 Hz; with loading post.

For Exp 1 cells of passage 7 were used and for Exp 2 cells of passage 9 were used.

Results and Discussion

Figure 5.5 shows the results of the two exploratory experiments. Similar to the experiments for HAEC's, contrary to what is expected, there appears to be an inhibition of proliferation in cells which have been stretched. Again, there was no visual confirmation that cells were adhered to the membrane following actuation and without adequate repeats the result can not definitively say that there is an inhibition of proliferation.

Although only a few experiments with HRSMC are presented here, because an increase in proliferation was not observed, this cell type was also deemed to be unsuitable.

5.4.4 Human Aortic Smooth Muscle Cells (HASMC)

Human Aortic Smooth Muscle Cells (HASMC) were purchased from Gibco (COO75C) as a frozen vial cryopreserved in medium containing 10% DMSO.

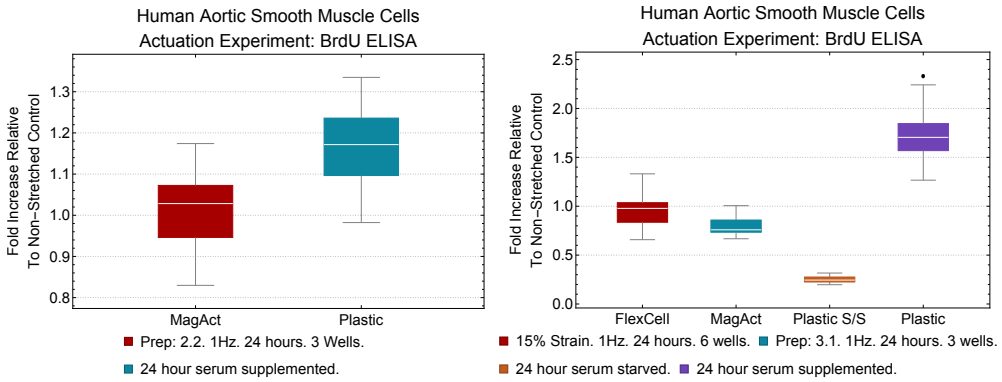

(a) (b)

Figure 5.6
HASMC MagAct v1.0 and FlexCell® Experimentation. (a) shows the results of an experiment using MagAct with augmentation 2.2. (b) shows the results of a comparison experiment between FlexCell® , MagAct 1.0 augmentation 3.1, a serum starved (S/S) control and cells grown on tissue culture plastic.

5.4.4.1 FlexCell® and MagAct Experiments

In a conscious move away from FlexCell® experimentation, experiments using HASMC were conducted predominantly on the MagAct v1.0 system. Two experiments are presented here, the first uses MagAct v1.0 with augmentation 2.2 (Protocol C.2; page 233), and the other uses MagAct v1.0 with augmentation 3.1 (Protocol 2.1; page 74). In both cases HASMC are seeded onto Collagen 1 coated BioFlex® plates at a density of 100×10^3 cells. 24 hours after seeding, plates are placed on the MagAct system having been set to run at 1 Hz and were actuated for 24 hours. Plates prepared in the same way are placed next to MagAct in the incubator to serve as a control.

In the second experiment, a plate was also prepared for use on the FlexCell® system and the method and materials are the same as described in Section 5.4.1. Cells seeded on two 6-well plastic tissue culture plates served as extra controls and are treated the same way as the BioFlex® control. In the second experiment however, a tissue-culture plate was serum starved during the 24 hour actuation period. This was to provide a negative control. Following actuations, the BrdU ELISA is used to quantify proliferation. Cells in both experiments were seeded at passage 6.

5.4.4.2 Results and Discussion

Results are presented as fold increases relative to the BioFlex® control. Figure 5.6(a) suggests that there is no effect of MagAct strain upon proliferation when using plate preparation method 2.2. Given what was deduced in Chapter 4, this is expected. Even if there was an effect generated by the limited strain this method creates, it would be so localised that averaging the membrane using the BrdU ELISA would obfuscate these effects. Figure 5.6(a) suggests also that cells grown on tissue culture plastics are

naturally in a more proliferative phenotype than cells grown statically on a Collagen 1 coated BioFlex® plate.

Figure 5.6(b) shows the result from the second experiment utilising MagAct v.1.0 with plate preparation 3.1. BioFlex® membrane augmented using this preparation method are thinner and should therefore deliver higher levels of strain. In comparison to FlexCell® , when actuated on MagAct there is a marginally significant decrease in proliferation relative to control. The significant difference between the serum starved negative control and all other conditions suggest that it is not the case that there are no proliferating cells on the BioFlex® membrane – this was a question raised as a result of the first experiment. Again, cells grown on tissue culture plastic are naturally in a more proliferative phenotype than cells grown both statically and dynamically on Collagen 1 coated BioFlex® plates.

Based on the Mills et al. (1997), it was expected that a significant stimulation of proliferation would be observed using FlexCell® at 15%. However, the group used cells derived from rabbit rather than human and so a legitimate comparison cannot be drawn. Together with a difficulty experienced in expanding these cells and a lack of significant experimental effect this cell type was regarded as not being suitable as a candidate for a proof of concept.

5.4.5 Human Umbilical Vein Endothelial Cells (pooled) (HUVECp)

Human Umbilical Vein Endothelial Cells (pooled) (HUVECp) were purchased from Gibco (C0155C) as a frozen vial cryopreserved in medium containing 10% DMSO.

5.4.5.1 MagAct Experiments

Testing was conducted with HUVECp's towards the later stages of this project. Unlike before, no tests were conducted using the FlexCell® system and an affect was only explored using MagAct. Two experiments were conducted; one using MagAct v1.0 and plate preparation 2.2 and the other using MagAct v2.0 plate preparation 3.1. Although the differences between plate preparations are minimal in terms of strain distribution, as seen in Chapter 4, the difference between strain distribution between v1.0 and v2.0 are far greater.

Testing parameters were here conducted closer to Dr. Day's original prototype experiments. Uncoated BioFlex® plates were treated with bovine fibronectin through Protocol A.13; page 225. $100{\times}10^3$ HUVEC were seeded onto BioFlex® plates on a Friday and left to attach over the weekend for actuations beginning on the following Monday. Plates on a Monday were replaced with complete pre-warmed medium and actuated on the MagAct system for 1 hour per day for a total of 3 days before being quantified using the BrdU ELISA. Cells used were between passages 3 and 5. As before, both BioFlex® and tissue culture plates were used as static controls.

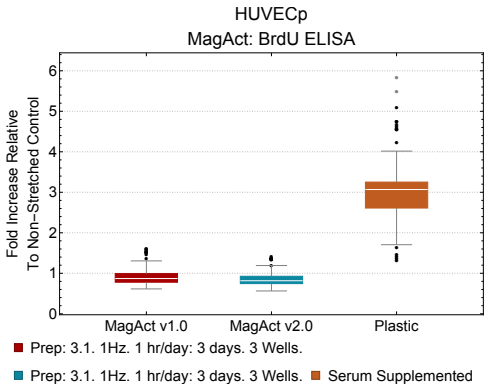

Figure 5.7

HUVECp MagAct Experimentation. Fold increases are displayed for actuation of HUVECp using both MagAct v1.0 and MagAct 2.0 relative to unstretched control. The comparison against cells grown on plastic are also shown.

5.4.5.2 Results and Discussion

Figure 5.7 shows the results of BrdU quantification expressed relative to unstretched controls. As before, it suggests there is no significant change in fold increase in proliferative behaviour as a result of MagAct stimulus. The results also suggest that cells grown on tissue culture plastics are naturally in a more proliferative phenotype than cells grown statically on a bovine fibronectin coated BioFlex® plate.

Given the results from Chapter 4, MagAct v2.0 still does not generate strains that could be generated by the FlexCell® system, and the area where it does provide a strain greater than zero is sufficiently small such that any possible effect will be obfuscated by averaging across the whole membrane.

At the time, the lack of significant effect this cell type was regarded as enough to not be being suitable as a candidate for a proof of concept.

5.4.6 C2C12 Cells

C2C12 cells had previously been purchased as a frozen vial cryopreserved in medium containing 10% DMSO.

5.4.6.1 MagAct Experiments

Experiments using C2C12 cells were conducted in exactly the same way as described in Section 5.4.5.1. Through 2 separate experiments, three plates were actuated using MagAct v2.0 and plate preparation 3.1. Cells were seeded at passage 12. As well as BrdU ELISA quantification, duplicate wells were used for EdU Proliferation staining (Protocol A.16; page 227) and imaging (Protocol 3.2; page 100).

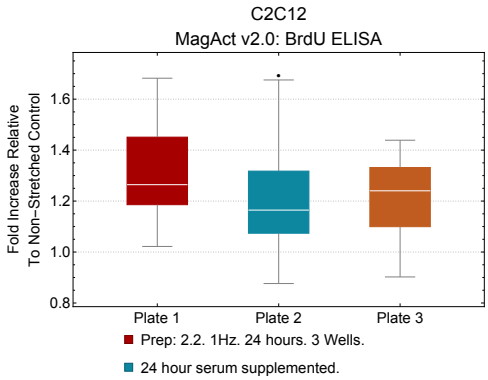

Figure 5.8
C2C12 MagAct v2.0 Experimentation. Results are expressed as fold increases relative to unstretched controls.

5.4.6.2 Results and Discussion

Figure 5.8 shows the BrdU ELISA results relative to the unstretched BioFlex® control. Although the variance is high in each plate, there is a trend towards an increased level of proliferation across each of the 3 plates tested. Given what is understood by the strain distribution for MagAct v2.0 from Chapter 4, this suggests a sensitivity of C2C12 cells to even a small strain magnitude.

Although an effect is observed with C2C12 cells, suitability for use as a proof of concept is complicated by their behaviour on the substrate. At the end of the 3 days of actuation, cell sheets could be observed by naked eye on the BioFlex® membranes. EdU staining and whole membrane imaging confirmed the formation of cell sheets. This is shown in Figure 5.9. Whole membrane imaging also reveals that cells are not evenly distributed where in the previous cell studies (images not here presented) cells show a homogeneous distribution. For the image analysis pipeline developed in Chapter 3, the complexity of analysing cell sheets goes beyond the capabilities of what has been developed. Therefore, despite C2C12 cells appearing to be a suitable candidate for a proof of concept biologically, in terms of the overall pipeline, this is not the case.

5.4.7 Imaging for Proliferative Phenotypes

For the majority of cell studies described above, parallel studies were also conducted to explore suitability of fluorescent staining using the Click-it® EdU proliferation assay as described by Protocol A.16; page 227, and imaging using Protocol 3.2; page 100. Since no cell type was discovered to be a suitable candidate for proof of concept, documentation of these experiments is not provided in this thesis. However, Figure 5.10 highlights the ability to stain cell types for proliferation and their suitability for proof of concept had a biological response been found.

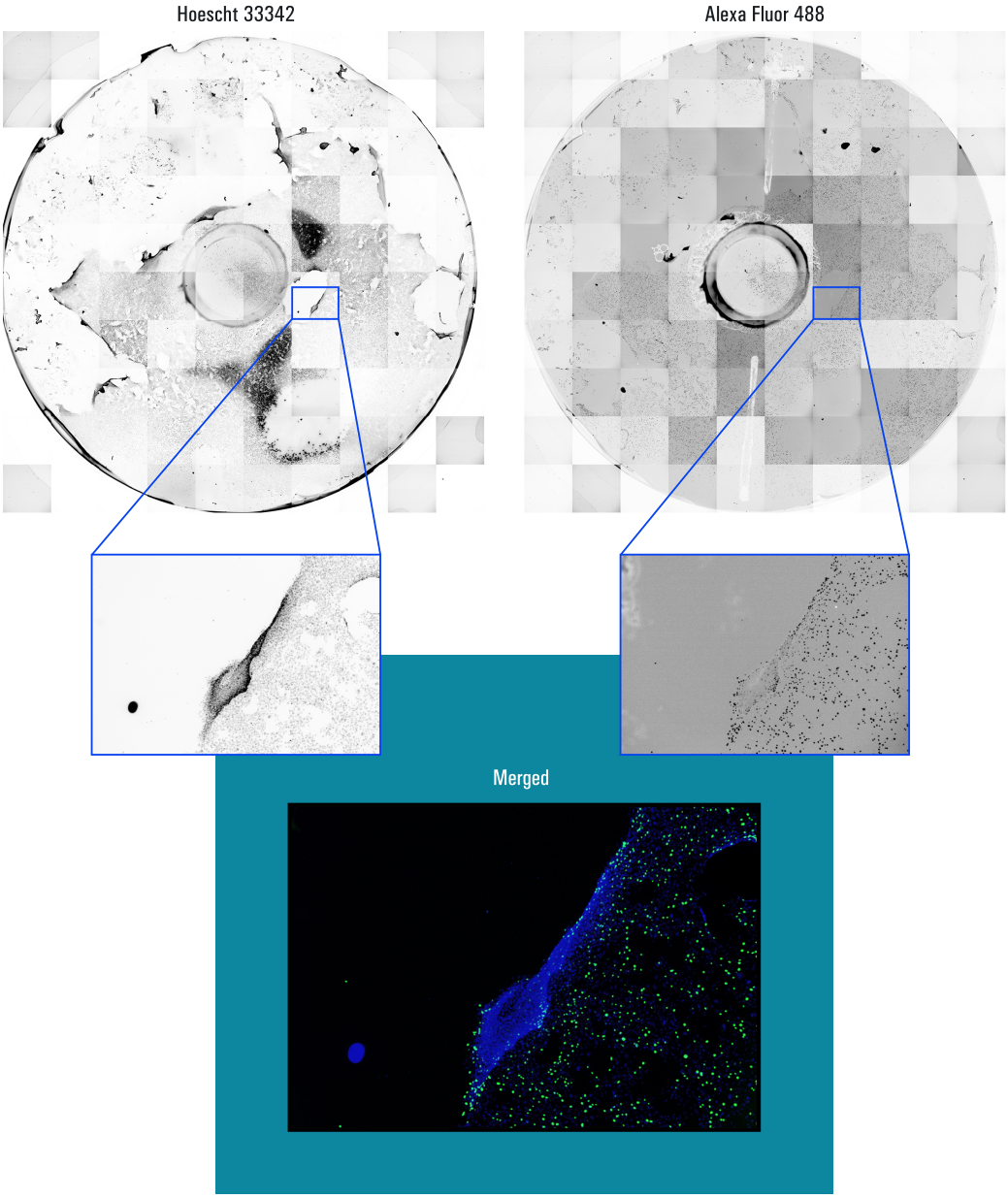

Figure 5.9
C2C12: Formation of Cell Sheets Example. C2C12 cells imaged using ImageXPress after having been strained with the AlexaFluor Click-it Proliferation ELISA. Cell sheet formation can be observed.

5.5 Discussion

The search for a cell type established to have proliferative responses to strain to be used as a proof of concept for MagAct has proven to be challenging. No cell type was found which, given previous literature, achieved expected results. A selection of studies conducted here are compared to those which are closest matched in the literature in Table 5.2 where rows highlighted in yellow are results from this chapter. There are a

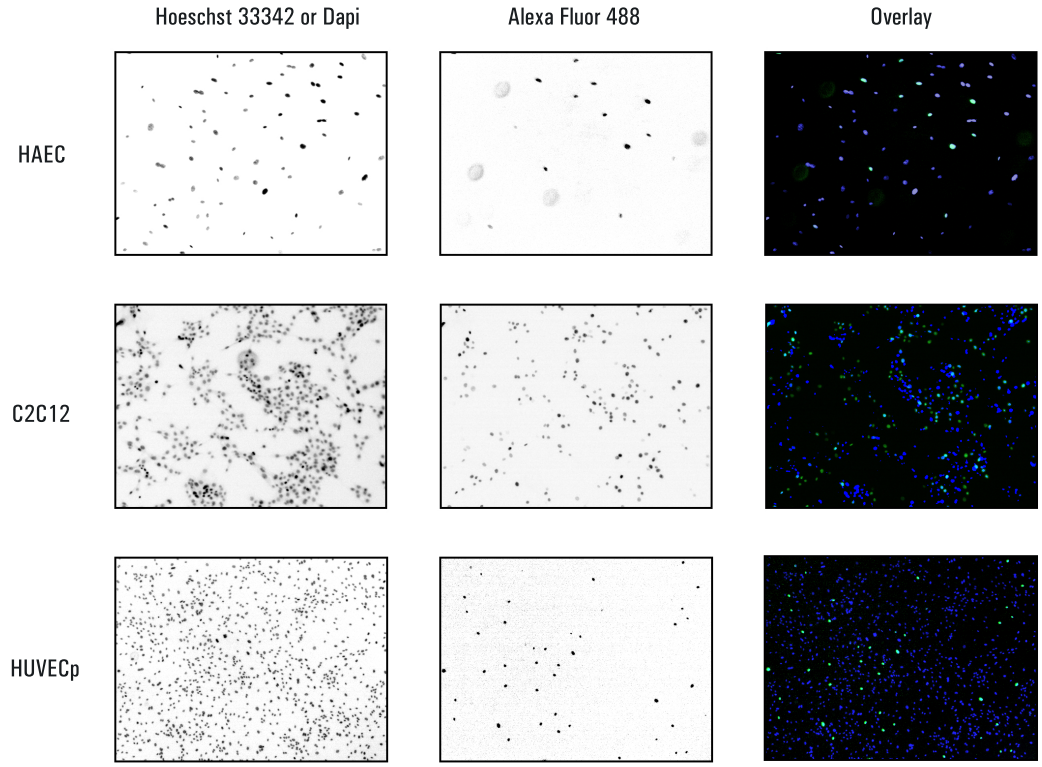

Figure 5.10
Example of EdU Staining for HAECs, C2C12 cells and HUVECps.

number of reasons which could explain this these discrepancies.

The FlexCell® apparatus which was used here was dated. The platform in which the BioFlex® plates sit shows obvious signs of warping and was too expensive to replace. Not only this, but strain regimes which were programmed into the software were not reported by the on-screen monitor. Occasions where 15% strain was proscribed, the monitor reported only a maximum of 11.6%. When 25% was proscribed, often only a maximum of 15% was reported. From the strain analysis of Colombo et al. (2008), the value reported by the software is based on pressure-strain relationships hard coded into the software. As Colombo et al. have suggested, these relationships should be assessed on a case by case basis and coded into the software. Warping of the platform suggests an inherent shelf life of the system and therefore care should be taken over results.

Although the FlexCell® apparatus may have inherent problems, methodology may also allude to why no appropriate cell type was found. A lack of consistency between experiments makes it difficult to progress with any cell type evaluated; experiments were conducted with MagAct v1.0, v2.0, plate preparation 2.1, 2.2 and 3.1.

The possibility also exists that the incubator these experiments were conducted in was malfunctioning. It was an incubator outside the control of the Day lab and therefore its upkeep could not be accounted for. Therefore, it is possible that if CO_2 or temperature

levels were misreported then cells would in a sub-optimal environment and may not behave as expected.

Alternatively, these results may in fact be true which indicates a heterogeneity inter-species, and possibly intra-species, in the behaviour of cells when responding to physical stretch. If this is the case it further highlight the need for higher throughput tools to understand these differences.

In terms of the cell-substrate dynamics, it is conceivable that as a result of the stretch generated by the membrane cells would detach. Therefore, based on the experimental methods used here, non-actuated control wells are not adequate as a reference point to compare actuated wells against. A solution to this would be to use more appropriate actuated controls. For example, actuated BioFlex® plates that are serum starved could be used as a negative control. Actuated wells which are supplemented with hbFGF could be used as positive controls, as done in Section 5.4.3.

Proliferation as a biological paradigm was sought throughout this thesis because of Dr. Day's original experiments. An increase in proliferation due to the original prototype had been established as discussed in Section 2.3.3; page 61. Despite these possible explanations for not finding a suitable cell type, a more damning critique is found in the consideration of a study by Wilson et al. (1993). The group subjected neonatal rat vascular smooth muscle cells to strain using the Flex I system (15-20 kPa of pressure was delivered but strain values aren't reported). They showed, with the use of Platelet Derived Growth Factor (PDGF) antibodies, that an autocrine secretion of PDGF was the driving force of strain induced proliferation in the cells. If strain related increase in proliferation is indeed driven by autocrine factors then general strain-proliferation relationships can never be uncovered by the methods proposed in this thesis. The release of PDGF from cells, even if they were stimulated to do so by particular strain amounts, would diffuse through medium and act upon all cells in the culture. Ultimately this renders any proliferation analysis obfuscated by a combination of autocrine and paracrine effects. Therefore the 'stimulus' for proliferation in this case is not heterogeneous, and therefore strain cannot be directly related to proliferation.

5.5.1 A Different Biological Paradigm

Based on the argument that no cell type can exist which is suitable for a proliferation based proof of concept, a seperate idea which was conceived early in the project but left on the back burner was revisited. This is the model where cellular strain modifies plasmid transfection efficiency. As discussed in Section 1.2.2.2; page 36, Taylor et al. (2003) demonstrated that A549 cells having undergone as little as 30 minutes of stretch on the FlexCell® system demonstrate significantly greater expression of transfected plasmids than unstretched controls. This idea was evaluated as an initial investigation in the late stages of this project.

Cell Type	Quie.L.	ρ ($x10^3$)	Hz	%	Time	Method	Fence	Surf.	Phenotypic Output	Reference
BAEC	0	96	1.6	0-7/7-25	5	Flex I	Yes	Collagen 1	(Strain Dependent) Stimulation of Proliferation	Li et al. (1994)
BAEC	0	10	0.05	10	7 days	Flex I	No	N/A	Inhibition of Proliferation	Sumpio et al. (1987)
BAEC	0	$\star$	0	4	4 hours	BioFlex® w. Post	Yes	Collagen 1	Inhibition of Proliferation	Woodell et al. (2003)
BAEC	0	$\star$	0.1	4	4 hours	BioFlex® w. Post	Yes	Collagen 1	Inhibition of Proliferation	Woodell et al. (2003)
HAEC	0	65	1	15	24 hours	BioFlex® w. Post	No	ProNectin	Inhibition of Proliferation	Present Study
RASMC	24	300	1.25	5	1	BioFlex® w. Post	No	N/A	Inhibition of Proliferation	Qi et al. (2010)
RASMC	24	300	1.25	15	1	BioFlex® w. Post	No	N/A	Stimulation of Proliferation	Qi et al. (2010)
BASMC	0	96	1	0-7/7-25	3-5 days	Flex I	Yes	type 1 collagen	(Strain Dependent) Stimulation of Proliferation	Mills et al. (1997)
HASMC	100	65	1	15	24 hours	BioFlex® w. Post	No	Collagen 1	No significant difference	Present Study
HRSMC	300	300	1	15	24 hours	BioFlex® w. Post	No	ProNectin	Inhibition of Proliferation	Present Study

Table 5.2

Comparison of Experimental Parameters Conducted Here Against Those in Literature. Column titles provide information on experimental design and results. **Quie.L.** is the length of time cells were serum starved before experimentation. ρ ($x10^3$) is the cell seeding density. **Hz** and % are the strain parameters frequency and stretch percentage. **Time** is the time spend in actuation. **Fence** indicates whether the fencing method was used. **Surf** is the membrane surface coating.

5.5.1.1 C2C12 Cell Transfection

As an initial investigation C2C12 cells were transfected using a pEGFP-C1 plasmid donated by Dr. Paul Frankel (Division of Medicine, UCL) originally purchased from Clon Tech (6084-1). The original donation of plasmids were expanded in colonies of Stellar Competent Cells (Clon Tech 636763) according to Protocol A.17; page 229 and purified using the Maxi-Prep Purification kit (QIAGEN, 12145X4) according to manufacturers instructions. Transfection of cells using Lipofectamine was conducted through Protocol A.19; page 230.

100×10^3 C2C12 cells at passage 10 were seeded onto 6-well glass bottom black walled culture plates. Following 24 hours of incubation, cells were transfected with the pEGFP-C1 plasmid. Cells successfully transfected produce Green Fluorescent Protein (GFP). 24 hours following transfection cells were fixed and stained with Hoeschst 33342 according to Protocols A.12; page 225, and A.14; page 226. Wells were then imaged using the ImageXPress system as described in Chapter 3. Quantification was conducted using the image analysis pipeline developed in the same chapter.

Results

Figure 5.11 shows the stitched image of a single well for both channels: Hoechst 33342 and GFP. The zoomed image shows a small section which has been merged and pseudo coloured in **Adobe Photoshop**. The white circles indicate those cells which are expressing GFP. Given that only 24 hours had passed after transfection, it is reasonable to assume that not enough time was given to cells which had been successfully transfected to begin expressing GFP, and this is an explanation for such a low efficacy of transfection.

Figure 5.12 shows the output of the image analysis pipeline for 3 transfected wells. For each subfigure, 'cell density' maps, 'cell number expressing GFP per voxel' maps, and 'percentage expressing GFP per voxel' maps are shown. Across all 3 wells, total percentage transfection is an average of around 0.7%.

Interestingly, because the cell distribution shown on the cell density map is heterogeneous, the percentage efficiency per voxel map qualitatively suggests that there is a relationship between percentage efficiency and cell density – the top left section of the map displays a higher expression of transfection which coincides with a localised cell density (blue) of around 30 cells per voxel. Where typically transfection percentages would be assessed by trypsinising all cells and quantifying expression levels through tools such as flow cytometry, image based systems such as this may have the power to extract more information than is often generated. This is demonstrated here by localised peaks of transfection associated to a heterogeneous stimulus, here heterogeneous cell density. This is a promising area of future work.

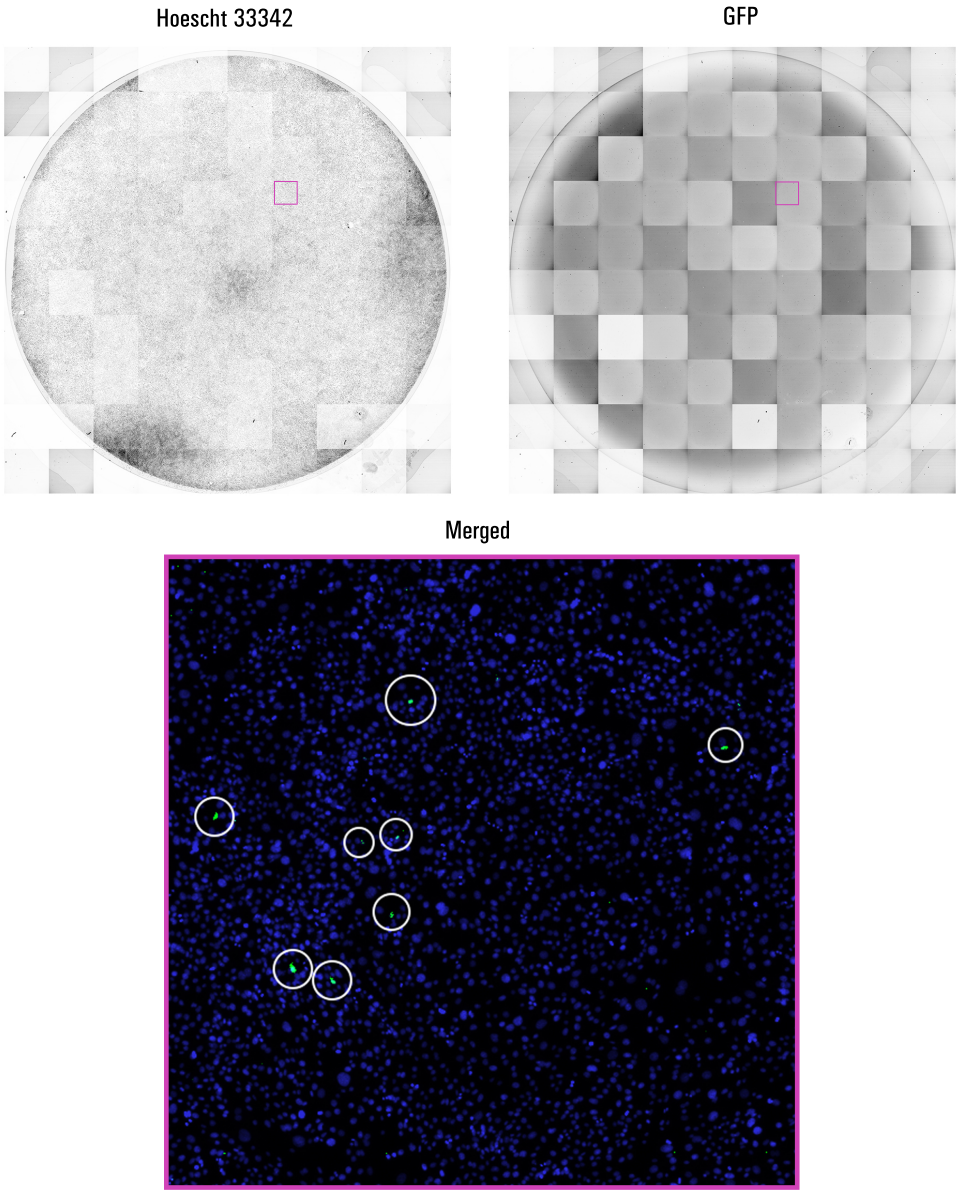

Figure 5.11
Transfection of C2C12 Cells with pEGFP-C1. Following fixations cells have been stained with Hoechst 33342 and imaged using the ImageXPress system. The white circles in the merged image show those cell nuclei which are expressing both Hoechst 33342 and GFP.

Discussion

Although no actuation experiments are here presented using the transfection paradigm, initial experimentation suggest is may be better suited for proof of concept of the MagAct system. As well as being a cheaper experiment to run, there is less doubt between the cause and effect between strain and transfection owing to an educated assumption that the biological method behind this phenomenon is intracellular.

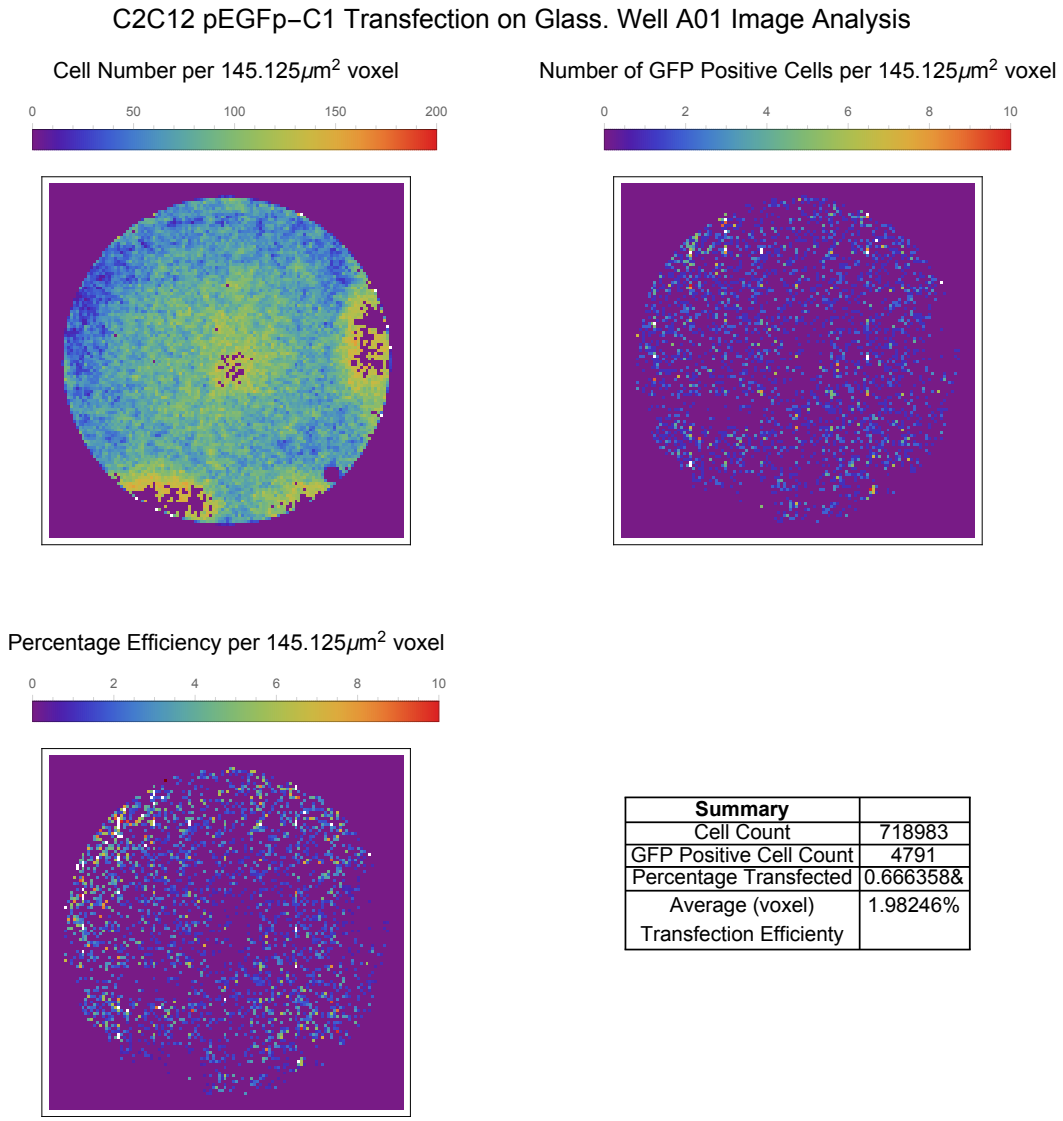

(a) C2C12 Transfection Image Analysis - Well A01. Figure continued overleaf.

It is regrettable that this wasn't explored further as the primary biological paradigm in which to test the system, but it serves a solid starting point for future work.

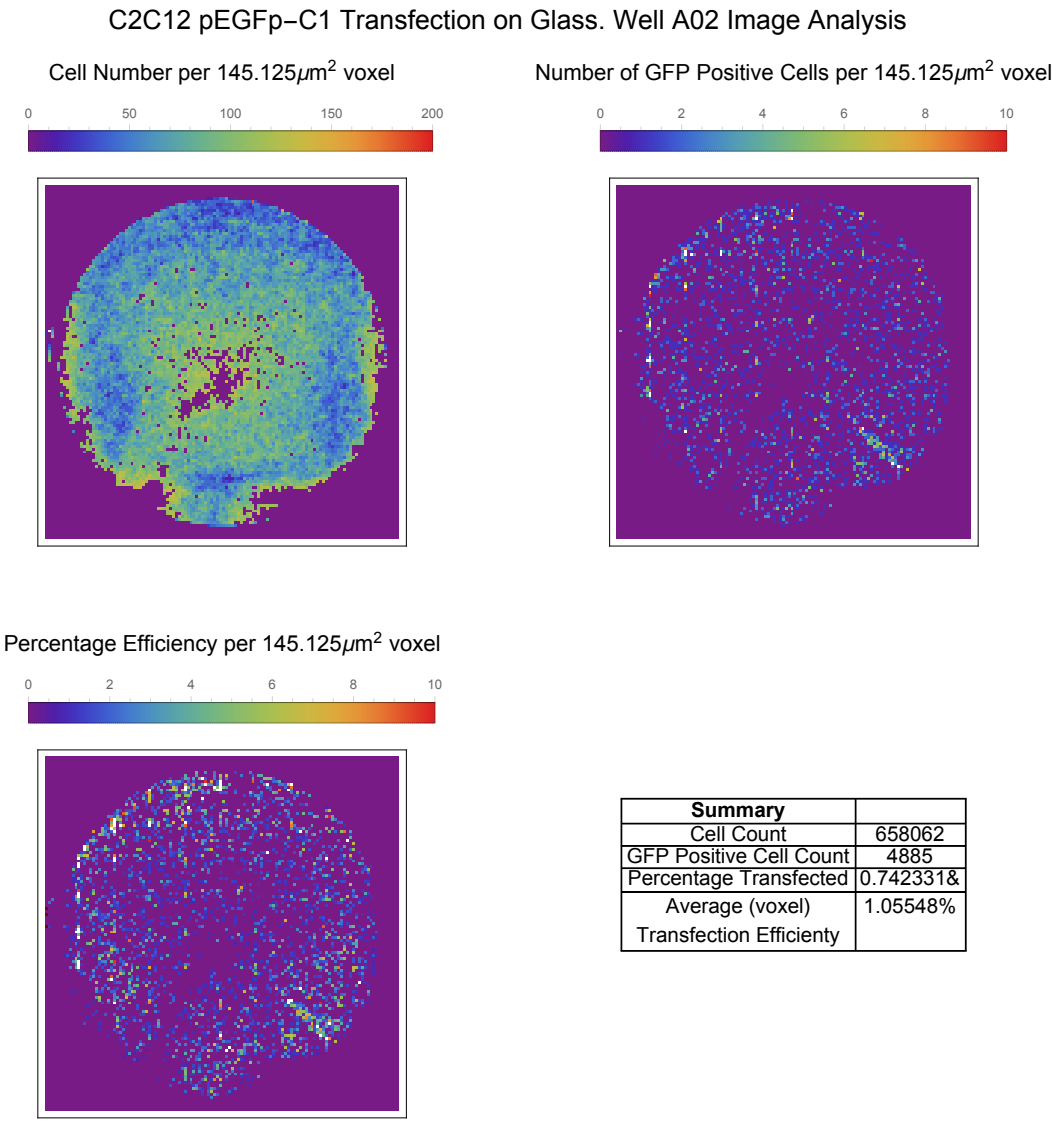

(b) C2C12 Transfection Image Analysis - Well A02. Figure continued overleaf.

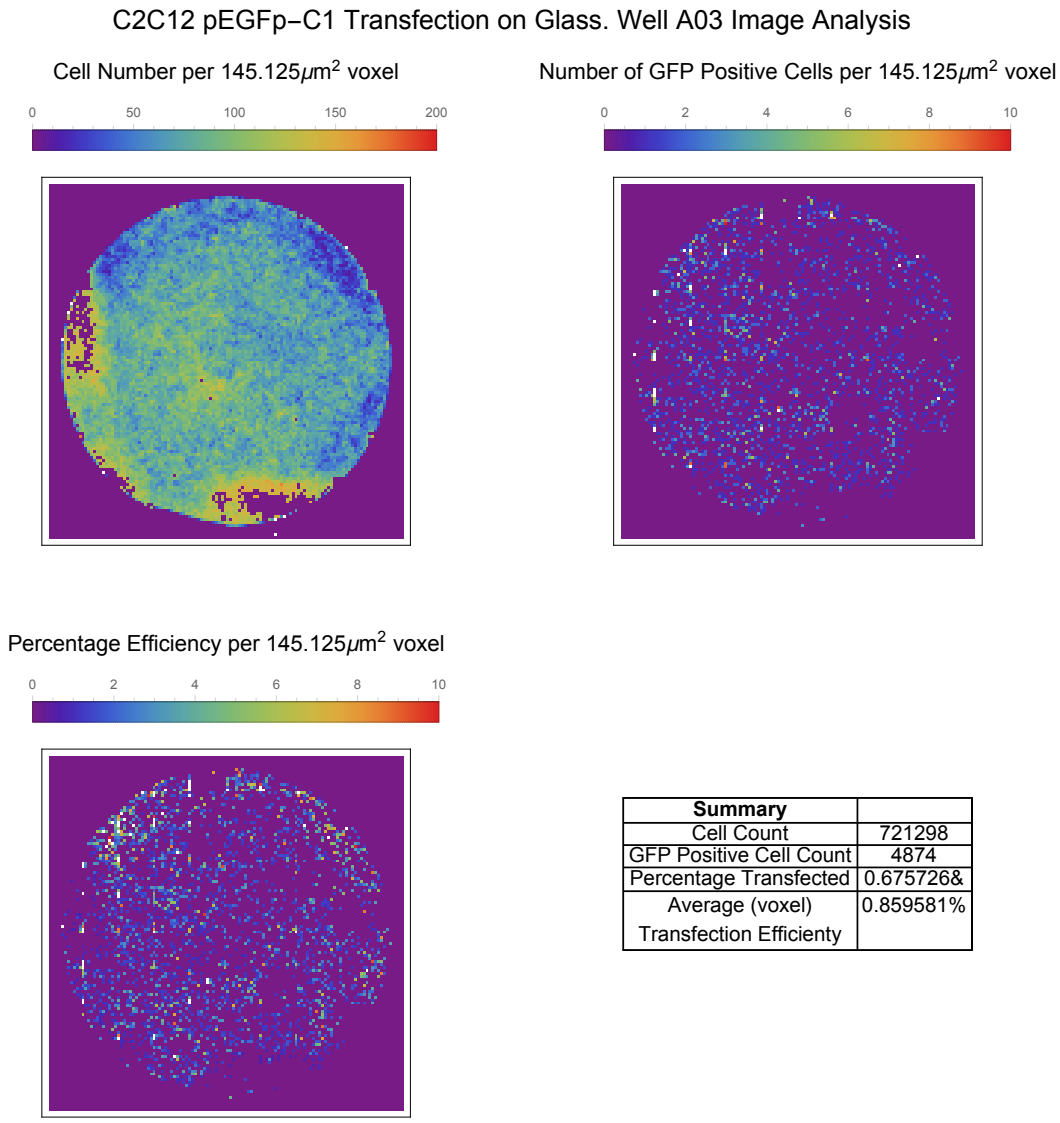

(c) C2C12 Transfection Image Analysis - Well A03

Figure 5.12

Analysed Images for C2C12 Transfection. Images recorded using the ImageXpress system have been analysed using the image analysis pipeline developed in Chapter 3. The results indicate a very low percentage of transfected cells as well as visual observations that transfection is heterogeneous across the well. This heterogeneity visually appears related to cell density.

5.6 Chapter Summary

With reference to Section 5.2, the aims of this chapter have not been met. A set of parameters for a specific cell type using the FlexCell® system which exhibits strong correlation with strain and phenotype was not found for a variety of cell types. Judgement of this was driven by not being to replicate results in the literature. However, there may be experimental reasons for this as well as biological, as discussed in Section 5.5. Similarly, strong correlation was not observed in the handful of experiments conducted on the MagAct system. However, this may be explained by the results of Chapter 4. Ultimately, the lack of finding a suitable biological paradigm has resulted in not having the capability of establishing an end-to-end proof of concept. In summary:

1. In light of Dr. Day's results using the original prototype, efforts were predominantly focused on finding a cell type where a notable increase in proliferation was observed as a response to FlexCell® generated strain.

2. No cell type was found which was suitable as a paradigm in which to test MagAct. This could be due to:

   (a) Apparatus flaws - both FlexCell® and culturing equipment.

   (b) Experimental design flaws.

   (c) Inherent biological heterogeneity between cell samples.

3. Proliferation as a paradigm may not be suitable due to studies suggesting the method of stimulation being autocrinous PDGF.

4. Transfection as a paradigm would have been a better model to investigate from the start, but is a solid foundation for continuing research.

Chapter 6

Discussion

The aim of this thesis was to develop a new system for conducting stretch based experiments on biological cells, an important component of cell biology research. The principle of this system was rooted in increasing the volume of information returned from each conducted experiment in order to maximise the information from research output. In part this differs from the current popular tool for stretching cells; the FlexCell® system. The FlexCell® system is designed both for uncovering relationships between strain and phenotype as well as providing a culturing environment which delivers a reasonably controlled environment which better mimics the mechanical environment from which cells are naturally derived. Arguably, this balance results in a low throughput in terms of uncovering relationships; each experiment delivers only a single strain parameter and therefore dozens of experiments are required to elucidate relationships in general. The strategy employed in this thesis was to design a system primarily for the purposes of uncovering relationships. In this respect the system is not a replacement for one which is used to culture cells in a mechanical environment, but one only to rapidly understand strain-phenotype relationships. Considering the heterogeneous nature of the distribution of strain generated by the MagAct system, this distinction is important. The MagAct system and the pipeline built around it was constructed under the goal of rapidly understanding relationships by exposing cell substrates to as many strain values as possible. For culturing cells in a mechanically active environment, either to better mimic *in vivo* as a baseline for other biological studies, or to condition cells for engineering purposes, a uniform homogeneous strain is arguably better. The MagAct pipeline should therefore be treated as a precursory stage which informs what this homogeneous strain value should be. It is within this where the novelty and impact of this work resides.

To increase throughput in cyclic strain experimentation there are two strategies which can be taken. The first is scaling down and increasing experimental variation of homogeneous strain regimes. This is equivalent to a system where the 6 well BioFlex® plate becomes a 24 or 48 well plate where each well can be prescribed individual strain regimes. As demonstrated by Balestrini et al. (2010), such could be achieved through retrofitting the FlexCell® system such that each well in the 6-well BioFlex® can be prescribed dif-

ferent strain regimes despite a uniform vacuum pressure across the plate[1]. Although scaling down is a sensible strategy for increasing throughput this thesis attempted the second, and perhaps the more unorthodox, strategy of maintaining scale but increasing experimental variation with heterogeneous strain regimes. This itself is not without issues. As has been discussed here (and elsewhere in Moraes et al. (2010)) for any autocrine/paracrine stimulation of a phenotype associated with stretch, trying to uncover this relationship using a heterogeneous stimulus is a complex problem. Diffusion of signalling agents through medium undoubtedly obfuscates the correlation of heterogeneous stretch with heterogeneous phenotype. Indeed, signalling agents seems to be the driver of stretch induced proliferation changes (Wilson et al., 1993). This has significant implications for the heterogeneous strategy employed in this thesis and suggests the caveat that the strategy can only work where imaging the behaviour of a cell is not dependent on cell signalling mechanisms. For example, the EdU proliferation assay would not be sufficient for understanding stretch induced proliferation as each cell may have been impacted upon by another cell's secretion of Platelet Derived Growth Factor (PDGF). This can be overcome in this strategy by not imaging for a proliferative phenotype but instead imaging the production of PDGF. Ultimately, it suggests a limitation of using the MagAct pipeline without understanding something of the strain-phenotype relationship *a priori* to mitigate for heterogeneous related obfuscations.

Completion of the MagAct pipeline was, however, only part realised. Despite this, and the above, there is still potential for considerable value with the system. In part this value lies in the potential to truly increase the volume of information from experimental practises. With this, not only will our understanding of mechanobiology increase but will also allow us to be better informed when designing further studies.

This chapter serves as both a summary of the work conducted throughout this thesis as well as a retrospective analysis in order to answer why this work was not fully successful, and therefore provide a platform for future research.

6.1 Summary of Work

Chapter 1 provided an introduction to the motivations of this work. Investigation of cyclic strain on cellular phenotype modulation is a field which has been under investigation for decades given its significant biological implications. However, through synthesis of previous research an argument was made that throughput is not high enough to significantly progress the field. This is evidenced by a review of the literature surrounding modulations in proliferative behaviour of cells as a result of cyclic strain and the observation that there is no key literature which describes this relationship in general terms or recommends best practise in investigating these relationships. A review of apparatus both commercially available as well as built in-house shed light on why this may be the case. The FlexCell® corporation have cornered the market for this type of research but

[1] As the authors note, however, this itself it not without problems

it transpires that their system is severely lacking in throughput. Perhaps due to cost, iterative experiments where strain regimes are titrated are not conducted and therefore general relationships are not recorded in the literature.

The field of tissue engineering utilises mechanical conditioning of tissue to better create tissues for therapeutics. It was argued that to build anything new it is beneficial to know more than you use than to use only what you know. That is, without having a general understanding of the *strain-phenotype* relationship, further research may be sub-optimal. A general understanding would provide rational foundations for further research to be based upon. Arguably, this is more likely to advance the field. Coupled to this, on the issue of FlexCell®, this chapter provided a small but novel theoretical analysis of the system based on results published in the literature. This demonstrated that the current utilisation of FlexCell® may not return true strain-phenotype relationships and further highlighted the need for developing something new.

A model to enhance throughput was subsequently defined. Instead of delivering a homogeneous strain regime, the ambitions of this thesis were instead to exploit a heterogeneous regime where image analysis methods together with a solid understanding of the strain distribution could be used to extract general relationships from minimal experiments. This principle was encapsulated in Figure 1.8; page 53.

Chapter 2 detailed the design and development of new apparatus to deliver a heterogeneous strain stimulus. The system used magnetic actuation to create deformations in BioFlex® membranes. A magnet embedded to the underside of BioFlex® membranes is displaced by magnets rotating underneath the membrane using brush motors. The system was engineered and constructed using 3D printing technology. Software was developed to allow control of the periodic strain through magnetic sensors and Arduino microcontrollers. In comparison to the FlexCell® system, MagAct is lightweight, portable and cheap to produce.

Chapter 3 detailed efforts to image the monolayer of cells on BioFlex® membranes with an effort focused on imaging every cell. A number of obstacles were overcome to do this. Despite an early focus making use of the Ziess Axiovision microscope, feasibility was demonstrated using the ImageXpress microscopy system. Protocols for preparing the membranes for imaging were developed and iterated to allow for close to every cell on the membrane to be imaged, such that the location of each cell on the membrane would be known. This chapter is in many respects coupled to Chapter 2 given that protocols to facilitate successful imaging necessitated changes to the apparatus. In light of these changes whole membrane imaging was achieved and as well the capability to analyse these images. For the scenario where cell nuclei are the features of interest, both bespoke algorithms and computational pipelines were developed to process the images. As part of this pipeline manual intervention to create metadata to normalise images was developed. Despite many efforts, manual intervention was needed as image artefacts and aberrations would always be present in membrane preparations conducted by hand – for example, caused by small fibres, invisible to the eye, falling on the top

of the membrane. The image analysis pipeline was evaluated in terms of error and was shown to be successfully working within reasonable bounds of error.

Chapter 4 detailed efforts to understand and evaluate the strain distribution generated by the MagAct system. Digital image correlation methods (DIC), conducted with Dantec Dynamics in Germany, as well as finite element modelling were employed. Two trips were made to Dantec Dynamics to conduct testing. The first analysed an earlier version of the MagAct system. Results indicated that strain was non-existent and so motivated a redesign of the system. The second trip showed that the results obtained using the first design were in fact due to an error in the applied Dantec system. Once corrected, analysis of DIC data showed the redesign to be providing a detectable strain across the membrane lower in magnitudes than expected. To understand this a finite element modelling pipeline was developed. Finite element analysis went some way to corroborate this and suggested that 3-5 mm of further distension of the embedded magnet was needed to achieve desired strain regimes.

Chapters 5 showcased efforts in biological experimentation. Experimentation heavily leaned towards finding a model to be used to test the MagAct system and in light of results on the original prototype, efforts were greatly focused on proliferation as a paradigm of choice. The strategy had been to use the FlexCell® system to generate what could be considered as ground truth data to be used later to validate/invalidate the MagAct system. For nearly every cell type tested, the proliferative response appeared counter-intuitive to expectations deduced from the literature. A definitive answer for why this is was the case was not reached, likely due to this being the result of a myriad of factors. Efforts were subsequently focused on plasmid transfection as a model of choice. Given plasmid transfection efficiencies have been shown to increase with cyclic strain, foundations for this as a model were investigated. Experimentation in transfection was geared towards use in image analysis rather than generating ground truth using FlexCell®. However, given the choice of proliferation and transfection, transfection was deemed to be a better candidate as a model for validating the MagAct system and a promising area of future research.

6.2 Critiques of Approach

The MagAct system ultimately did not deliver a wide enough variance of strain across the membrane of BioFlex® plates. Although FEM results provide a basis for increasing this variance allowing for continuation of this research it is prudent to offer critiques on the approaches used throughout this thesis to better facilitate this development. Two areas of criticism are in the absence of statistics and the need for a retrospective analysis on the project plan. These are here discussed in turn to provide a redesign of the project to better optimise development.

6.2.1 Critique: Absence of Statistics

A critique to the realisation of the aims of this thesis is a lack of discussion and development of the statistics which would be necessary for the method proposed in the introduction to succeed. This was in part due to a necessary focus given to other foundational elements of the work. By creating *virtual fences* through microscopy imaging, the act of relating each of these small areas to the underlying strain is far from trivial in terms of statistics. With reference to the matrices in Figure 1.8; page 53, this is because each element can not be treated as independent; it cannot be said that each element acts independently of its neighbouring elements. Therefore, standard methods in correlation statistics cannot be used.

One porential avenue of development is found in the work of Peiffer et al. (2013). Peiffer et al. investigated the relationship between blood flow characteristics and atherosclerosis. They generated disease distribution maps generated from *in vivo* studies together with computational fluid dynamics to associate patterns of wall shear stress to the presence of atherosclerotic lesions. They argue that conventional quantification methods lack robustness when comparing two spatial maps. In part, methods such as linear regression between spatial maps, having been discretised into small segments, necessarily assumes the experimental independence of each segment. In their datasets each segment cannot be considered independent and may be influenced by neighbouring segments. This has parallels to the maps generated in this thesis. In the case of this project, where whole membrane images have been discretised into smaller segments, cell to cell communication between neighbouring segments results in a dependency between data points, and therefore linear regression comparison fails.

Peiffer et al. devised a novel quantification method for comparing spatial maps. Their method is based on calculating discriminating statistics on multiple surrogate pairs. In brief, a statistic is used to compare the original two distributions through point wise comparison of segments. Swaps are then made in the point wise pairings and the statistic is recalculated. This process repeated multiple times with each swap pairing resulting in a distribution of statistics. The placement on this distribution of the original statistic for the two distributions is an indicator of confidence in the correlation between maps. If the original statistic is high on the distribution of all statistics, it suggests that the maps are not correlated by chance, but that given random changes to one of the maps, the original is more likely correlated due to causality.

This principle applies to the spatial maps generated in this project (that of phenotype and stimulus). Therefore quantification methods to extract strain-phenotype relationships were to be based on the method of Peiffer et al.. This represents an important are of future development.

6.2.2 Critique: Retrospective Analysis

Although the work conducted in this thesis is presented as distinct chapters, in reality each was conducted simultaneously throughout the research period: minor results from each fed into other components. For example, struggles with whole membrane imaging discussed in Chapter 3 heavily influenced the protocols developed in Chapter 2 for augmenting the BioFlex® membrane to include the embedded magnet. However, changes to these protocols resulted in a differing strain distribution pattern, and so the decision of when to measure this using DIC becomes crucial. Retrospectively, a reason for why the initial aims were only part realised is because of time.

For a complex, interdisciplinary project such as this, without significant prior experience and expertise in the various components required to make it work, forward planning is easily misguided. Early in this project focus was given predominantly to the biology, and excessive biological experiments were conducted on early prototype systems. These results are not presented in this thesis as no significant value was added to this project.

In the scope of project planning, this project was naively *waterfall*; the structure was such that it would only be after the completion of every component and the integration of each that the success or failure of the system would be known. A result of this is that the design of MagAct continued from the beginning all the way through to the final months of this project, where sense would instead suggest it be the first component complete. Given the emphasis on working on all components simultaneously, which to some degree is needed owing to the interplay between components, realisation that MagAct v2.0 was not delivering a varied enough strain distribution was not realised until it was late in the project. The visits to the labs of Dantec Dynamics in Germany for DIC testing were separated by over a year. A reason for this is due to focus being diverted to imaging and image analysis after the first visit, which continuously changed the MagAct system. As the system was in flux, the return trip was delayed by a long period such that it was detrimental to this thesis.

As part of this discussion, and to understand the shortfalls of this project, an exercise based on retrospect was conducted to create a revised project plan. In doing so the limitations of this project are illuminated. Based on this, a platform for continuing research is established.

6.2.3 Redesigning the Project

The project was redesigned based on answering a series of questions:

1. What are the components?
2. What are the requirements/dependencies of each component?
3. What is the point at which a minimum viable product can be established?
4. How can progress be assessed?

Of these, only the first was fully established at the beginning of this project. As an argument to why, sufficient expertise did not exist to be able to legitimately answer the remaining questions. Answering them now is legitimised through an increased basic knowledge of the various components and together with a reverse engineering of experience.

Figure 6.1 shows a swimlane based project schematic constructed using the answers to the above questions. It is referred to as the Revised Project Plan (RPP) where each swimlane represents a distinct component of the project. This thesis treated apparatus testing and the biology as one and the same; in the beginning of the project, apparatus testing was a means to an end to generate biological results. In this redesign, the opposite is imposed: the role of the biology in this context is only to test apparatus as this is the only way to ultimately ensure biologically informative output. Therefore, these are here separate components.

The AND gates in the RPP are indicative of the dependencies throughout the project. In the apparatus swimlane relating to Chapter 2, both *Theoretical Optimisation* of the Apparatus *and* completed *Requirement Gathering* for Imaging are needed before apparatus should begin a construction phase.

Milestones are reached at various levels as a direct result of testing. For example, the first is reached after successful testing of a minimum viable product (discussed further below). The failure of a test results in a *stop point*. If the minimum viable product test has inconsistencies, for example, nothing should continue with the project until this has been assessed. Both milestones and stop points did not adequately exist in the project undertaken in this thesis. As there was a strong degree of parallel work across components, when a 'stop point' was reached in one component (i.e. something didn't work as required), adequate assessment was not conducted due parallel activities which demanded parallel focus. Although parallel efforts are undoubtedly required in this project, in retrospect efforts must be structured and guided by defined scope.

Below, each task/requirement box labelled in the RPP in Figure 6.1 is explained in more detail.

Theoretical Optimisation

In this project FEM of MagAct was conducted towards the end of the project period. Retrospect suggests that it would be more prudent to conduct it straight away. For example, theoretical optimisation was conducted here in Chapter 4 for the purposes of understanding DIC measurements. Development of a modelling approach, however, both explained these results partially but more importantly provided a rational to engineer the system further for achieving the requirements of the MagAct system – to deliver a wide ranging and heterogeneous strain stimulus. Construction of apparatus may have been aided with this as the primary driver.

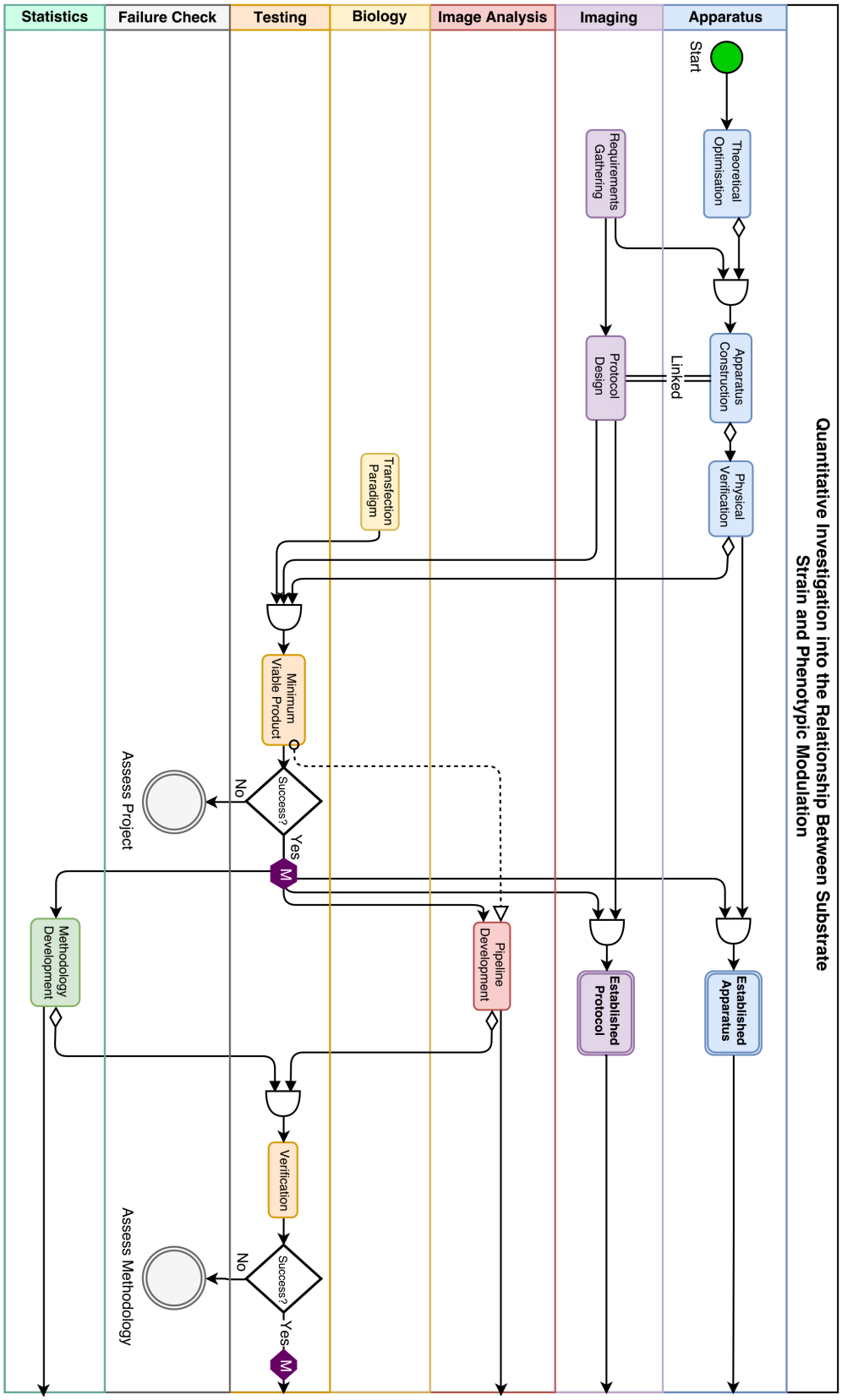

(a) Revised Project Plan. Swimlane style diagram presenting a redesign of the project as discussed in Section 6.2.3. Continued overleaf.

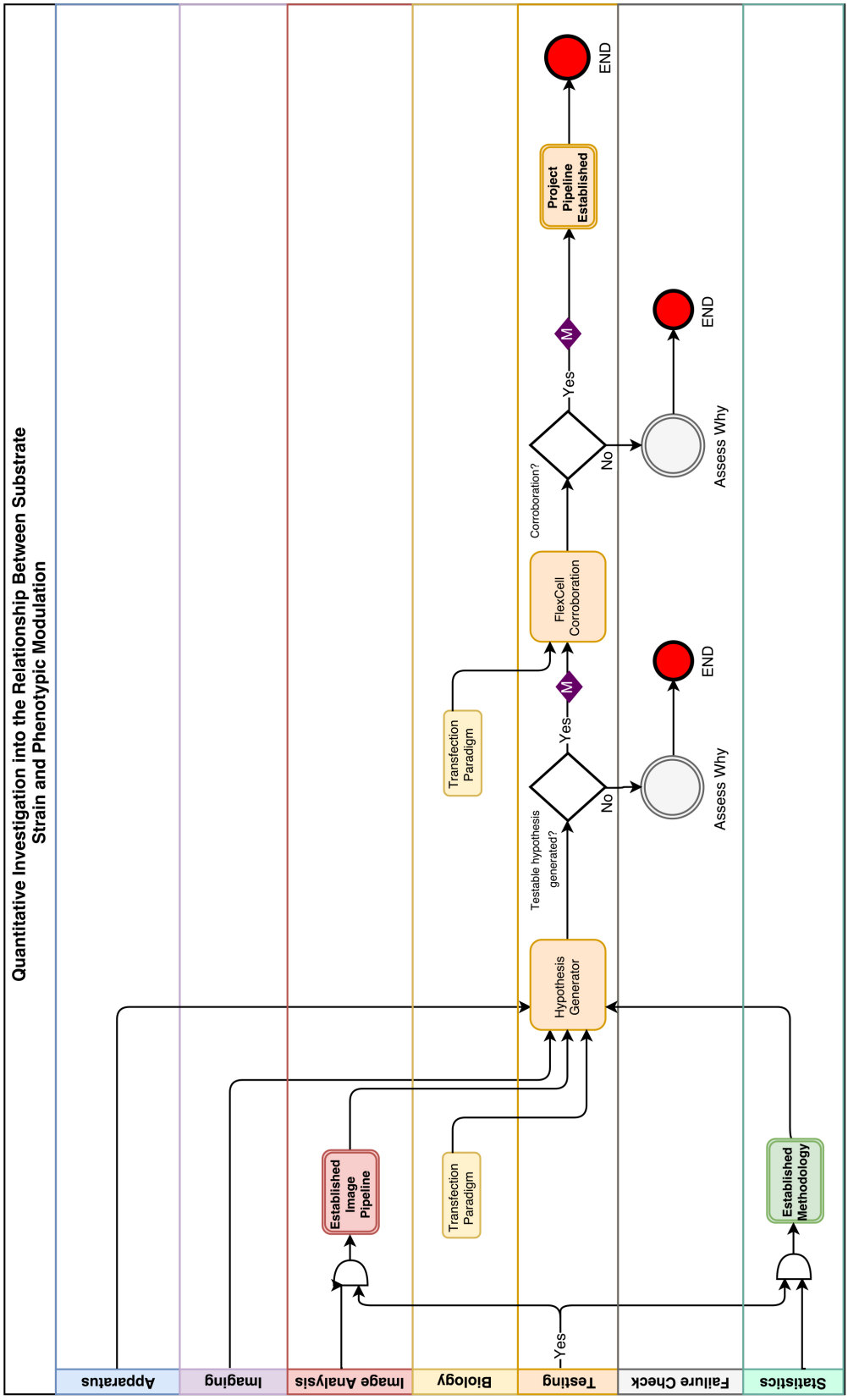

(b) Revised Project Plan Continued.

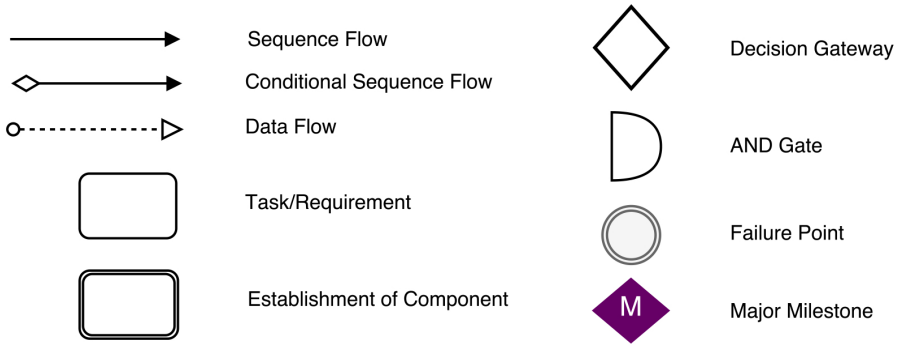

(c) Revised Project Plan Schematic Key

Figure 6.1
(a) and (b): Retrospective redesign of the project plan as discussed in Section 6.2.3. Each swimlane (row) is a distinct component.

Requirements Gathering (Imaging)

The building of MagAct and the ability to image whole membranes were deeply entangled throughout this thesis. MagAct was constructed first before properly exploring imaging systems, and as a result arguably an unnecessary amount of time was spent returning to and iterating the apparatus. Therefore, in the RPP, it is a dependency of apparatus construction that the requirements for imaging are fully understood and defined.

Apparatus Construction

Apparatus construction occurs after theoretical optimisation and imaging requirements have been ascertained. In this thesis, construction was conducted to refine a rudimentary but already existing system, and the aims of this refinement were to increase the accuracy and repeatability of Dr. Day's original prototype. Although the refinement was successful, it was not feasible, given the time of discovery, to conduct further redesigns and improvements.

Protocol Design (Imaging)

The methodology used for whole substrate imaging and the construction of the apparatus are undoubtedly linked. For agility, retrospect would suggest that these occur in parallel to optimise development time.

Physical Verification

In this thesis, DIC measurements in the Dantec Labs in Germany were conducted as a means of understanding the strain distribution across membranes. The RPP, however, uses these measurements as a means of corroborating the theoretical basis upon which the apparatus was constructed. A lesson informed by this thesis was that any apparatus

not machine constructed will undoubtedly have inconsistencies which result in variations. In the case here, augmenting BioFlex® plates manually will result in differences in magnet positions causing non-consistent strain distributions between wells as well as between experiments. Therefore, physical measurements do not offer much in the way of usable data to generate the 'stimulus map' defined in the Introduction chapter, and the apparatus here developed can only be a proof of concept and not a salient product.

Transfection Paradigm

A notable feature of this project redesign is the complete absence of proliferation as a phenotype of interest. For this thesis, from early on, a great amount of resource (both time and financial) was given to the proliferation of cells as a biological route of interest in accordance with Dr. Day's original prototype results as well as lab interests. This thesis began primarily as an investigation into proliferation caused by cyclic strain on smooth muscle cells, and the development of the technology was a means to an end to explore this further. The scale of the work required in developing the technology eventually obfuscated this investigation, and proliferation was benched as the paradigm in which to validate the technology. For the reasons discussed in Section 5.5; page 189, the evidence suggesting the involvement of autocrinicity in proliferation by cyclic strain may hinder the usefulness of proliferation as a validating model.

Based on this, the use of proliferation as a model is abandoned in favour of transfection studies. As discussion in Section 1.2.2.2; page 36, and based on the preliminary work in the same section, a strain induced increase in plasmid transfection efficiency is suited both in feasibility and by medical relevance to be used as a paradigm for testing the MagAct pipeline.

In this RPP, the primary focus is not to discover new biology regarding this phenomenon, but to use it instead as a means only to test. That is, a fixed experimental protocol and parameter set used repeatedly throughout the project. This stage is only to set these parameters. Working in this way has the potential to facilitate a much greater impact on biological output yielding both broader, repeatable, and more robust results.

Minimum Viable Product (Milestone 1)

The first milestone in this revised project plan is the completion of a minimum viable product. Together with the transfection paradigm, a completed version of the imaging protocol and a completed version of the apparatus, a test for viability to reach the aims of the project should be conducted.

Here there is no need for image analysis or statistical methods but rather simply answering the question of whether the apparatus, given it has been theoretically optimised, is capable of generating transfection efficiencies which vary (qualitatively) with locations of the membrane. It is a step which is minimal in terms of quantitative analysis but a qualitative answer serves as a potent indication of viability. If the system does show a spatial dependence then the first milestone is reached and both the method of imaging

and apparatus can be fixed without later needing change. If it does not, then a stop point is reached where reassessment of the steps preceding can be thoroughly evaluated.

Established Apparatus

The first milestone permits the establishment of the apparatus and no longer should be changed.

Established Protocol (Imaging)

The first milestone permits the establishment of the imaging protocol and no longer should be changed.

Pipeline Development (Image Analysis)

The point at which to start developing the computational pipeline for image analysis is a difficult one to place. During the requirement gathering and protocol design work surrounding the Zeiss Axio Scan microscope (Section **??**; page **??**), significant effort was also given to the development of a complementary image analysis pipeline (not presented in this thesis). This work added little value to the project other than serving as a sandbox for image analysis. With experience and hindsight, in the revised plan this stage should begin after the first milestone without allowance to revise the imaging protocol. As experienced in this thesis, the backlog of revisions to multiple components when imaging protocols are changed is a step which was challenging to the advancement of the project.

Methodology Development (Statistics)

As discussed in Section 6.1, together with the development of the image analysis pipeline, the statistical framework should be designed as a dependency before continuing with the project.

Verification (Milestone 2)

This verification phase is a test of both the development of statistical and image analysis methodology. It should be a stage which is independent of strain as a stimulus or the biological paradigm.

This stage, although not set in stone, is envisaged to involve simple cell experiments where a variable associated with the cells is dependent on spatial location. For example, low attatchment cell culture plates where the wells are selectively treated with extra cellular matrix proteins in, say, annular rings. Cells seeded to the cells would naturally adhere to the annulus of protein. Over time cells may gradually migrate out of the rings. Imaging all cell nuclei after a predefined time together with the statistical framework based on Peiffer et al. (2013) should be able to confidently correlate the spatial map of protein treatment and the map of cell density.

If the experiment shows successful methodology in correlating maps, then the second milestone is reached and both the imaging and statistical pipelines may be fixed without later needing change. If it does not, then a stop point is reached where reassessment of the steps preceding can be thoroughly evaluated.

Established Image Pipeline (Image Analysis)

The second milestone permits the establishment of the image analysis pipeline and should no longer be changed.

Established Methodology (Statistics)

The second milestone permits the establishment of the statistical methodology and should no longer be changed.

Hypothesis Generator (Milestone 3)

In the context of this thesis, this stage denoted the end goal. Experiments were conducted prematurely and data stored for later use in a complete image analysis and statistical framework. As the developed apparatus was found to not fully behave according to requirements, this data adds little value. More so, these experiments more often than not failed at some level due to incomplete protocols for imaging and/or because apparatus had not been finalised.

The emphasis in the revised project is not to use biological experimentation to provide a data set to validate MagAct, but instead to use MagAct to generate hypotheses to be validated after.

If a hypothesis is generated – that is, the MagAct pipeline generates an intuitively convincing relationship – then the third milestone is reached. However, if it does not, a stop point is reached. Different from the first and second stop points is that here, there is little reassessment of project, project plan and scope, but instead an informed end point to the project.

FlexCell® Corroboration (Milestone 4)

With respect to FlexCell®, efforts in this thesis were geared towards pre-emptively generating data using FlexCell® and a biological model. Here, this was the proliferation of cells. Data was sought as a means to verify any hypothesis generated from the MagAct pipeline. In the revised project plan the use of FlexCell® remains the same – it is a verification tool of the MagAct system – however, this is scheduled to happen only after the third milestone; only after hypothesis have been generated.

Conducting FlexCell® experiments alongside the development of everything else – as was the case in this thesis – proved to be a fruitless task and efforts would have been better spent focusing on other components rather than thinly spreading efforts in parallel. This will also reduce biological resources and therefore optimise spending.

If the FlexCell® system verifies the hypothesis of MagAct, then it confirms the system works and inductively that MagAct returns biological results rather than simply a biological hypothesis. At this stage the final milestone is reached and the project comes to a close.

Project Pipeline Established

The fourth milestone permits the fixation and validation of the project pipeline and brings the project to a successful close.

6.2.4 Continuing Research

The best strategy to continue this work is to follow the RPP (Figure 6.1). This thesis has made significant and novel contributions to key areas of the project. Given the imaging, image analysis and biological model are ready to be integrated, to course correct the project a theoretically driven redesign of the apparatus remains as the main blocker for reaching the first milestone. Therefore, this is the starting point to continue research for achieving the original aims of this thesis. Continuing with the plan set out in the RPP provides a defined, methodological approach.

A starting point here is exploration of a controlled increase of the membrane distension up to 10 mm where FEM suggests a greater strain heterogeneity will be observed with strain in the ranges of 0 to 30% (Figure 4.21; page 171). Such an increase could be achieved by changing the magnet dynamics: either stronger magnets or the rotating magnets being placed closer to the EM's.

6.3 Conclusions

The aims of this thesis were to to construct apparatus that would provide information regarding the relationship between substrate strain and phenotypic modulation in cells with greater throughput. Where popular existing apparatus delivers a homogeneous distribution of strain to a monolayer of cells – done to facilitate easier biological quantification – the principles explored here to increase throughput are to instead deliver a purposely heterogeneous distribution. In this way, by imaging every cell on the membrane, a quantitative relationship was sought between small, but well defined, areas of cells and the corresponding strain experienced by each. The more heterogeneous the strain, the more strain-cell associations can be drawn and therefore throughput, and subsequently biologically relevant information, increased significantly in each experiment. This has implications to the fields of tissue engineering and cell biology as a whole.

The complexity of purposely delivering heterogeneous strain required a multidisciplinary approach: physical and electrical engineering of the apparatus, software design, theoretical and physical analysis of strain, a reliable method of recording data through fluorescent microscopy, development of appropriate computational processes for analysing images, and a biological paradigm in which to test.

Tailor made apparatus (MagAct) was designed and developed based on magnetic actuation to deform the membranes of BioFlex® plates. This was accompanied by the creation of software to control the period of deformation based on magnetic sensors. Protocols for image acquisition of 35 mm diameter membranes were produced and implemented which allowed for the recording of every cell on the membrane. A bespoke image analysis pipeline which converts the images to a usable matrix of information was established and validated. This imaging pipeline, out-with the framework of MagAct, offers a novel methodology specifically for studies involving BioFlex® plates where imaging of the entire substrate is not reported in the literature. Due to its bespoke nature, this pipeline can be easily tailored to investigate any biological paradigm. Both finite element modelling and physical measurements in the form of digital image correlation were used to describe the strain deformation experienced by the membranes. In doing so the DIC method offered by Dantec Dynamics is demonstrated to be a novel tool for measuring strain in the FlexCell® system to a degree of resolution which has never been conducted before. Biological experimentation was conducted to facilitate testing of the apparatus and the entire pipeline. Finite element modelling and digital image correlation both highlighted that although succeeding in delivering a heterogeneous strain, the MagAct apparatus may not provide enough strain variance. Currently only a maximum strain of 4-5% is reached which is insufficient to provide biologically relevant results. Through a retrospective analysis methods to achieve the aims of this thesis are offered – in particular a change to the apparatus to achieve desired strain ranges is proposed as well as an alternative biological paradigm to investigate the pipeline and establish a proof-of-concept.

In whole, this thesis highlights a limitation with current methodology to understand strain-phenotype relationships and contributes to the field by developing a multidisciplinary novel methodology and pipeline to facilitate enhanced understanding.

Chapter 7

Bibliography

Arem, A. J. and Madden, J. W. Effects of stress on healing wounds: I. intermittent noncyclical tension. *Journal of Surgical Research*, 20(2):93–102, 1976. ISSN 0022-4804 (Print) 0022-4804 (Linking).

Asanuma, K., Magid, R., Johnson, C., Nerem, R. M., and Galis, Z. S. Uniaxial strain upregulates matrix-degrading enzymes produced by human vascular smooth muscle cells. *American Journal of Physiology: Heart and Circulatory Physiology*, 284(5):H1778–84, 2003. ISSN 0363-6135 (Print) 0363-6135 (Linking).

Balestrini, J. and Hinz, B. The mechanical regulation of myofibroblasts; mechanically-guided matrix remodeling and prevention of fibrosis in regenerative medicine. In *Cells, Forces and the Microenvironment*. Pan Staford Publishing Pte Ltd, Singapore, 2014.

Balestrini, J. L., Skorinko, J. K., Hera, A., Gaudette, G. R., and Billiar, K. L. Applying controlled non-uniform deformation for in vitro studies of cell mechanobiology. *Biomechanics and Modeling in Mechanobiology*, 9(3):329–44, 2010. ISSN 1617-7940 (Electronic) 1617-7940 (Linking).

Banes, A. J., Gilbert, J., Taylor, D., and Monbureau, O. A new vacuum-operated stress-providing instrument that applies static or variable duration cyclic tension or compression to cells in vitro. *Journal of Cell Science*, 75:35–42, 1985. ISSN 0021-9533 (Print) 0021-9533 (Linking).

Basson, M. D., Li, G. D., Hong, F., Han, O., and Sumpio, B. E. Amplitude-dependent modulation of brush border enzymes and proliferation by cyclic strain in human intestinal caco-2 monolayers. *Journal of Cellular Physiology*, 168(2):476–88, 1996. ISSN 0021-9541 (Print) 0021-9541 (Linking).

Birukov, K. G., Shirinsky, V. P., Stepanova, O. V., Tkachuk, V. A., Hahn, A. W., Resink, T. J., and Smirnov, V. N. Stretch affects phenotype and proliferation of vascular smooth muscle cells. *Molecular and Cellular Biochemistry*, 144(2):131–9, 1995. ISSN 0300-8177 (Print) 0300-8177 (Linking).

Boerboom, R. A., Rubbens, M. P., Driessen, N. J., Bouten, C. V., and Baaijens, F. P. Effect of strain magnitude on the tissue properties of engineered cardiovascular constructs. *Annals of biomedical engineering*, 36(2):244–253, 2008.

Brown, T. D. Techniques for mechanical stimulation of cells in vitro: A review. *Journal of Biomechanics*, 33(1):3–14, 2000. ISSN 0021-9290 (Print) 0021-9290 (Linking).

Bryer, S. C. and Koh, T. J. Mechanical strain increases gene transfer to skeletal muscle cells. *Journal of Biomechanics*, 40(9):1995–2001, 2007. ISSN 0021-9290 (Print) 0021-9290 (Linking).

Carpenter, A. E., Jones, T. R., Lamprecht, M. R., Clarke, C., Kang, I. H., Friman, O., Guertin, D. A., Chang, J. H., Lindquist, R. A., Moffat, J., Golland, P., and Sabatini, D. M. Cellprofiler: Image analysis software for identifying and quantifying cell phenotypes. *Genome Biol*, 7(10): R100, 2006. ISSN 1465-6906 (Print).

Cartmell, S. H., Keramane, A., Kirkham, G. R., Verschueren, S. B., Magnay, J. L., El Haj, A. J., and Dobson, J. Use of magnetic particles to apply mechanical forces for bone tissue engineering purposes. *Fifth International Conference on Fine Particle Magnetism*, 17(1): 77–80, 2005. ISSN 1742-6588.

Cha, J. M., Park, S.-N., Noh, S. H., and Suh, H. Time-dependent modulation of alignment and differentiation of smooth muscle cells seeded on a porous substrate undergoing cyclic mechanical strain. *Artificial organs*, 30(4):250–258, 2006.

Chapman, G. B., Durante, W., Hellums, J. D., and Schafer, A. I. Physiological cyclic stretch causes cell cycle arrest in cultured vascular smooth muscle cells. *American Journal of Physiology: Heart and Circulatory Physiology*, 278(3):H748–54, 2000. ISSN 0363-6135 (Print) 0363-6135 (Linking).

Chiang, M. Y., Cheng, T., Pakstis, L., and Dunkers, J. Solutions for determining equibiaxial substrate strain for dynamic cell culture. *Journal of Biomechanics*, 43(13):2613–7, 2010. ISSN 1873-2380 (Electronic) 0021-9290 (Linking).

Colombo, A., Cahill, P. A., and Lally, C. An analysis of the strain field in biaxial flexcell membranes for different waveforms and frequencies. *Proceedings of the Institution of Mechanical Engineers. Part H: Journal of Engineering in Medicine*, 222(8):1235–45, 2008. ISSN 0954-4119 (Print) 0954-4119 (Linking).

Davis, C. A., Zambrano, S., Anumolu, P., Allen, A. C., Sonoqui, L., and Moreno, M. R. Device-based in vitro techniques for mechanical stimulation of vascular cells: A review. *Journal of Biomechanical Engineering*, 137(4):040801, 2015. ISSN 1528-8951 (Electronic) 0148-0731 (Linking).

Eldib, M. and Dean, D. A. Cyclic stretch of alveolar epithelial cells alters cytoskeletal micromechanics. *Biotechnology and Bioengineering*, 108(2):446–53, 2011. ISSN 1097-0290 (Electronic) 0006-3592 (Linking).

Eliceiri, K. W., Berthold, M. R., Goldberg, I. G., Ibáñez, L., Manjunath, B. S., Martone, M. E., Murphy, R. F., Peng, H., Plant, A. L., Roysam, B., et al. Biological imaging software tools. *Nature methods*, 9(7):697–710, 2012.

Elsaadany, M., Harris, M., and Yildirim-Ayan, E. Design and validation of equiaxial mechanical strain platform, equicycler, for 3d tissue engineered constructs. *BioMed Research International*, 2017:3609703, 2017. ISSN 2314-6141 (Electronic).

Friedrich, O., Schneidereit, D., Nikolaev, Y. A., Nikolova-Krstevski, V., Schurmann, S., Wirth-Hucking, A., Merten, A. L., Fatkin, D., and Martinac, B. Adding dimension to cellular mechanotransduction: Advances in biomedical engineering of multiaxial cell-stretch systems and their application to cardiovascular biomechanics and mechano-signaling. *Progress in Biophysics and Molecular Biology*, 2017. ISSN 1873-1732 (Electronic) 0079-6107 (Linking).

Fuhrer, R., Hofmann, S., Hild, N., Vetsch, J. R., Herrmann, I. K., Grass, R. N., and Stark, W. J. Pressureless mechanical induction of stem cell differentiation is dose and frequency dependent. *PloS One*, 8(11):e81362, 2013. ISSN 1932-6203 (Electronic) 1932-6203 (Linking).

Geiger, R. C., Taylor, W., Glucksberg, M. R., and Dean, D. A. Cyclic stretch-induced reorganization of the cytoskeleton and its role in enhanced gene transfer. *Gene Therapy*, 13(8): 725–31, 2006. ISSN 0969-7128 (Print) 0969-7128 (Linking).

Gilbert, J. A., Banes, A. J., Link, G. W., and Jones, G. L. Video analysis of membrane strain: An application in cell stretching. *EXT Experimental Techniques*, 14(5):43–45, 1990. ISSN 0732-8818.

Gilbert, J. A., Weinhold, P. S., Banes, A. J., Link, G. W., and Jones, G. L. Strain profiles for circular cell culture plates containing flexible surfaces employed to mechanically deform cells in vitro. *Journal of Biomechanics*, 27(9):1169–77, 1994. ISSN 0021-9290 (Print) 0021-9290 (Linking).

Goriely, A., Geers, M. G., Holzapfel, G. A., Jayamohan, J., Jerusalem, A., Sivaloganathan, S., Squier, W., Van Dommelen, J. A., Waters, S., and Kuhl, E. Mechanics of the brain: Perspectives, challenges, and opportunities. *Biomechanics and Modeling in Mechanobiology*, 14(5):931–65, 2015. ISSN 1617-7940 (Electronic) 1617-7940 (Linking).

Harshad, K., Jun, M., Park, S., Barton, M. J., Vadivelu, R. K., St John, J., and Nguyen, N. T. An electromagnetic cell-stretching device for mechanotransduction studies of olfactory ensheathing cells. *Biomedical Microdevices*, 18(3):45, 2016. ISSN 1572-8781 (Electronic) 1387-2176 (Linking).

Hipper, A. and Isenberg, G. Cyclic mechanical strain decreases the dna synthesis of vascular smooth muscle cells. *Pflügers Archiv*, 440(1):19–27, 2000. ISSN 0031-6768 (Print) 0031-6768 (Linking).

Jakel, R. I. Analysis of hyperelastic materials with mechanica – theory and application examples. 2010.

Kamble, H., Barton, M. J., and Nguyen, N. T. Modelling of an uniaxial single-sided magnetically actuated cell-stretching device. *Sensors and Actuators a-Physical*, 252:174–79, 2016. ISSN 0924-4247.

Khademolhosseini, F., Liu, C. C., Lim, C. J., and Chiao, M. A magnetically actuated cellular strain assessment tool for quantitative analysis of strain induced cellular reorientation and actin alignment. *Review of Scientific Instruments*, 87(8):085004, 2016. ISSN 1089-7623 (Electronic) 0034-6748 (Linking).

King, J. D., York, S. L., and Saunders, M. M. Design, fabrication and characterization of a pure uniaxial microloading system for biologic testing. *Medical Engineering and Physics*, 38 (4):411–6, 2016. ISSN 1873-4030 (Electronic) 1350-4533 (Linking).

Lam, A. P. and Dean, D. A. Cyclic stretch-induced nuclear localization of transcription factors results in increased nuclear targeting of plasmids in alveolar epithelial cells. *Journal of Gene Medicine*, 10(6):668–78, 2008. ISSN 1521-2254 (Electronic) 1099-498X (Linking).

Lamprecht, M. R., Sabatini, D. M., Carpenter, A. E., et al. CellprofilerâĎć: free, versatile software for automated biological image analysis. *Biotechniques*, 42(1):71, 2007.

Lau, J. J., Wang, R. M., and Black, L. D. Development of an arbitrary waveform membrane stretcher for dynamic cell culture. *Annals of Biomedical Engineering*, 42(5):1062–73, 2014. ISSN 1573-9686 (Electronic) 0090-6964 (Linking).

Lee, K., Silva, E. A., and Mooney, D. J. Growth factor delivery-based tissue engineering: General approaches and a review of recent developments. *Journal of the Royal Society Interface*, 8 (55):153–70, 2011. ISSN 1742-5662 (Electronic) 1742-5662 (Linking).

Leung, D. Y., Glagov, S., and Mathews, M. B. A new in vitro system for studying cell response to mechanical stimulation. different effects of cyclic stretching and agitation on smooth muscle cell biosynthesis. *Experimental Cell Research*, 109(2):285–98, 1977. ISSN 0014-4827 (Print) 0014-4827 (Linking).

Li, G., Mills, I., and Sumpio, B. E. Cyclic strain stimulates endothelial cell proliferation: Characterization of strain requirements. *Endothelium*, 2(2):177–81, 1994. ISSN 1062-3329 1029-2373.

Li, Q., Muragaki, Y., Ueno, H., and Ooshima, A. Stretch-induced proliferation of cultured vascular smooth muscle cells and a possible involvement of local renin-angiotensin system and platelet-derived growth factor (pdgf). *Hypertension Research*, 20(3):217–23, 1997. ISSN 0916-9636 (Print) 0916-9636 (Linking).

Liu, B., Qu, M. J., Qin, K. R., Li, H., Li, Z. K., Shen, B. R., and Jiang, Z. L. Role of cyclic strain frequency in regulating the alignment of vascular smooth muscle cells in vitro. *Biophysical Journal*, 94(4):1497–507, 2008. ISSN 1542-0086 (Electronic) 0006-3495 (Linking).

Liu, X., Huang, X., Chen, L., Zhang, Y., Li, M., Wang, L., Ge, C., Wang, H., and Zhang, M. Mechanical stretch promotes matrix metalloproteinase-2 and prolyl-4-hydroxylase a1 production in human aortic smooth muscle cells via akt-p38 mapk-jnk signaling. *BC International Journal of Biochemistry and Cell Biology*, 62:15–23, 2015. ISSN 1357-2725.

Martin, I., Wendt, D., and Heberer, M. The role of bioreactors in tissue engineering. *Trends in Biotechnology*, 22(2):80–6, 2004. ISSN 0167-7799 (Print) 0167-7799 (Linking).

Miller, C. J. and Davidson, L. A. The interplay between cell signalling and mechanics in developmental processes. *Nature Reviews Genetics*, 14(10):733–44, 2013. ISSN 1471-0056.

Mills, I., Cohen, C. R., Kamal, K., Li, G., Shin, T., Du, W., and Sumpio, B. E. Strain activation of bovine aortic smooth muscle cell proliferation and alignment: Study of strain dependency and the role of protein kinase a and c signaling pathways. *Journal of Cellular Physiology*, 170 (3):228–34, 1997. ISSN 0021-9541 (Print) 0021-9541 (Linking).

Moraes, C., Chen, J. H., Sun, Y., and Simmons, C. A. Microfabricated arrays for high-throughput screening of cellular response to cyclic substrate deformation. *Lab Chip*, 10(2): 227–34, 2010. ISSN 1473-0197 (Print) 1473-0189 (Linking).

Mori, D., David, G., Humphrey, J. D., and Moore, J., J. E. Stress distribution in a circular membrane with a central fixation. *Journal of Biomechanical Engineering*, 127(3):549–53, 2005. ISSN 0148-0731 (Print) 0148-0731 (Linking).

Morrow, D., Sweeney, C., Birney, Y. A., Cummins, P. M., Walls, D., Redmond, E. M., and Cahill, P. A. Cyclic strain inhibits notch receptor signaling in vascular smooth muscle cells in vitro. *Circulation Research*, 96(5):567–75, 2005. ISSN 1524-4571 (Electronic) 0009-7330 (Linking).

Orr, A. W., Helmke, B. P., Blackman, B. R., and Schwartz, M. A. Mechanisms of mechanotransduction. *Developmental Cell*, 10(1):11–20, 2006. ISSN 1534-5807 (Print) 1534-5807 (Linking).

Otsu, N. A threshold selection method from gray-level histograms. *IEEE Transactions on Systems, Man, and Cybernetics*, 9(1):62–66, 1979. ISSN 0018-9472 2168-2909.

Pankhurst, Q., Thanh, N. K. T., Jones, S. K., and Dobson, J. Progress in applications of magnetic nanoparticles in biomedicine. *Journal of Physics D: Applied Physics*, 42(22), 2009. ISSN 0022-3727.

Paul, N. E., Denecke, B., Kim, B. S., Dreser, A., Bernhagen, J., and Pallua, N. The effect of mechanical stress on the proliferation, adipogenic differentiation and gene expression of human adipose-derived stem cells. *Journal of Tissue Engineering and Regenerative Medicine*, 2017. ISSN 1932-7005 (Electronic) 1932-6254 (Linking).

Peiffer, V., Bharath, A. A., Sherwin, S. J., and Weinberg, P. D. A novel method for quantifying spatial correlations between patterns of atherosclerosis and hemodynamic factors. *Journal of Biomechanical Engineering*, 135(2):021023, 2013. ISSN 1528-8951 (Electronic) 0148-0731 (Linking).

Pimentel, D. R., Amin, J. K., Xiao, L., Miller, T., Viereck, J., Oliver-Krasinski, J., Baliga, R., Wang, J., Siwik, D. A., Singh, K., et al. Reactive oxygen species mediate amplitude-dependent hypertrophic and apoptotic responses to mechanical stretch in cardiac myocytes. *Circulation research*, 89(5):453–460, 2001.

Predel, H. G., Yang, Z., Von Segesser, L., Turina, M., Buhler, F. R., and Luscher, T. F. Implications of pulsatile stretch on growth of saphenous vein and mammary artery smooth muscle. *Lancet*, 340(8824):878–9, 1992. ISSN 0140-6736 (Print) 0140-6736 (Linking).

Qi, Y. X., Qu, M. J., Yan, Z. Q., Zhao, D., Jiang, X. H., Shen, B. R., and Jiang, Z. L. Cyclic strain modulates migration and proliferation of vascular smooth muscle cells via rho-gdialpha, rac1, and p38 pathway. *Journal of Cellular Biochemistry*, 109(5):906–14, 2010. ISSN 1097-4644 (Electronic) 0730-2312 (Linking).

Richardson, W. J., Metz, R. P., Moreno, M. R., Wilson, E., and Moore, J., J. E. A device to study the effects of stretch gradients on cell behavior. *Journal of Biomechanical Engineering*, 133(10):101008, 2011. ISSN 1528-8951 (Electronic) 0148-0731 (Linking).

Riehl, B. D., Park, J. H., Kwon, I. K., and Lim, J. Y. Mechanical stretching for tissue engineering: Two-dimensional and three-dimensional constructs. *Tissue Engineering Part B: Reviews*, 18 (4):288–300, 2012. ISSN 1937-3376 (Electronic) 1937-3368 (Linking).

Riha, G. M., Wang, X., Wang, H., Chai, H., Mu, H., Lin, P. H., Lumsden, A. B., Yao, Q., and Chen, C. Cyclic strain induces vascular smooth muscle cell differentiation from murine embryonic mesenchymal progenitor cells. *Surgery*, 141(3):394–402, 2007. ISSN 0039-6060 (Print) 0039-6060 (Linking).

Rosenblatt, N., Hu, S., Chen, J., Wang, N., and Stamenovic, D. Distending stress of the cytoskeleton is a key determinant of cell rheological behavior. *Biochemical and Biophysical Research Communications*, 321(3):617–22, 2004. ISSN 0006-291X (Print) 0006-291X (Linking).

Ruwhof, C., Van Wamel, A. E., Egas, J. M., and Van Der Laarse, A. Cyclic stretch induces the release of growth promoting factors from cultured neonatal cardiomyocytes and cardiac fibroblasts. *Molecular and cellular biochemistry*, 208(1-2):89–98, 2000.

Schad, J. F., Meltzer, K. R., Hicks, M. R., Beutler, D. S., Cao, T. V., and Standley, P. R. Cyclic strain upregulates vegf and attenuates proliferation of vascular smooth muscle cells. *Vascular Cell*, 3(1):21, 2011. ISSN 2045-824X (Electronic) 2045-824X (Linking).

Schaffer, J. L., Rizen, M., L'italien, G. J., Benbrahim, A., Megerman, J., Gerstenfeld, L. C., and Gray, M. L. Device for the application of a dynamic biaxially uniform and isotropic strain to a flexible cell culture membrane. *Journal of Orthopaedic Research*, 12(5):709–19, 1994. ISSN 0736-0266 (Print) 0736-0266 (Linking).

Schindelin, J., Arganda-Carreras, I., Frise, E., Kaynig, V., Longair, M., Pietzsch, T., Preibisch, S., Rueden, C., Saalfeld, S., Schmid, B., et al. Fiji: an open-source platform for biological-image analysis. *Nature methods*, 9(7):676–682, 2012.

Seko, Y., Seko, Y., Takahashi, N., Shibuya, M., and Yazaki, Y. Pulsatile stretch stimulates vascular endothelial growth factor (vegf) secretion by cultured rat cardiac myocytes. *Biochemical and biophysical research communications*, 254(2):462–465, 1999.

Seriani, S., Del Favero, G., Mahaffey, J., Marko, D., Gallina, P., Long, C. S., Mestroni, L., and Sbaizero, O. The cell-stretcher: A novel device for the mechanical stimulation of cell populations. *Review of Scientific Instruments*, 87(8):084301, 2016. ISSN 1089-7623 (Electronic) 0034-6748 (Linking).

Smith, P. G., Janiga, K. E., and Bruce, M. C. Strain increases airway smooth muscle cell proliferation. *American Journal of Respiratory Cell and Molecular Biology*, 10(1):85–90, 1994. ISSN 1044-1549 (Print) 1044-1549 (Linking).

Standley, P. R., Cammarata, A., Nolan, B. P., Purgason, C. T., and Stanley, M. A. Cyclic stretch induces vascular smooth muscle cell alignment via no signaling. *American Journal of Physiology: Heart and Circulatory Physiology*, 283(5):H1907–14, 2002. ISSN 0363-6135 (Print) 0363-6135 (Linking).

Subramanian, G., Elsaadany, M., Bialorucki, C., and Yildirim-Ayan, E. Creating homogenous strain distribution within 3d cell-encapsulated constructs using a simple and cost-effective uniaxial tensile bioreactor: Design and validation study. *Biotechnology and Bioengineering*, 114(8):1878–87, 2017. ISSN 1097-0290 (Electronic) 0006-3592 (Linking).

Sumpio, B. E. and Banes, A. J. Response of porcine aortic smooth muscle cells to cyclic tensional deformation in culture. *Journal of Surgical Research*, 44(6):696–701, 1988. ISSN 0022-4804 (Print) 0022-4804 (Linking).

Sumpio, B. E., Banes, A. J., Levin, L. G., and Johnson, J., G. Mechanical stress stimulates aortic endothelial cells to proliferate. *Journal of Vascular Surgery*, 6(3):252–6, 1987. ISSN 0741-5214 (Print) 0741-5214 (Linking).

Sumpio, B. E., Du, W., Galagher, G., Wang, X., Khachigian, L. M., Collins, T., Gimbrone, J., M. A., and Resnick, N. Regulation of pdgf-b in endothelial cells exposed to cyclic strain. *Arteriosclerosis, Thrombosis, and Vascular Biology*, 18(3):349–55, 1998. ISSN 1079-5642 (Print) 1079-5642 (Linking).

Syedain, Z. H. and Tranquillo, R. T. Controlled cyclic stretch bioreactor for tissue-engineered heart valves. *Biomaterials*, 30(25):4078–4084, 2009.

Taylor, W., Gokay, K. E., Capaccio, C., Davis, E., Glucksberg, M., and Dean, D. A. The effects of cyclic stretch on gene transfer in alveolar epithelial cells. *Molecular Therapy*, 7(4):542–9, 2003. ISSN 1525-0016 (Print) 1525-0016 (Linking).

Toume, S., Gefen, A., and Weihs, D. Printable low-cost, sustained and dynamic cell stretching apparatus. *Journal of Biomechanics*, 49(8):1336–9, 2016. ISSN 1873-2380 (Electronic) 0021-9290 (Linking).

Tulloch, N. L., Muskheli, V., Razumova, M. V., Korte, F. S., Regnier, M., Hauch, K. D., Pabon, L., Reinecke, H., and Murry, C. E. Growth of engineered human myocardium with mechanical loading and vascular coculture. *Circulation research*, pages CIRCRESAHA–110, 2011.

Van Wamel, J., Ruwhof, C., Van der Valk-Kokshoorn, E., Schrier, P., and Van der Laarse, A. Rapid gene transcription induced by stretch in cardiac myocytes and fibroblasts and their paracrine influence on stationary myocytes and fibroblasts. *Pflügers Archiv*, 439(6):781–788, 2000.

Vande Geest, J. P., Di Martino, E. S., and Vorp, D. A. An analysis of the complete strain field within flexercell$^{\text{tm}}$ membranes. *Journal of Biomechanics*, 37(12):1923–28, 2004. ISSN 0021-9290.

Wilson, E., Mai, Q., Sudhir, K., Weiss, R. H., and Ives, H. E. Mechanical strain induces growth of vascular smooth muscle cells via autocrine action of pdgf. *Journal of Cell Biology*, 123(3): 741–7, 1993. ISSN 0021-9525 (Print) 0021-9525 (Linking).

Winston, F. K., Macarak, E. J., Gorfien, S. F., and Thibault, L. E. A system to reproduce and quantify the biomechanical environment of the cell. *Journal of Applied Physiology*, 67(1): 397–405, 1989. ISSN 8750-7587 (Print) 0161-7567 (Linking).

Woodell, J. E., Laberge, M., Langan, r., E. M., and Hilderman, R. H. In vitro strain-induced endothelial cell dysfunction determined by dna synthesis. *Proceedings of the Institution of Mechanical Engineers. Part H: Journal of Engineering in Medicine*, 217(1):13–20, 2003. ISSN 0954-4119 (Print) 0954-4119 (Linking).

Yang, Z., Noll, G., and Luscher, T. F. Calcium antagonists differently inhibit proliferation of human coronary smooth muscle cells in response to pulsatile stretch and platelet-derived growth factor. *Circulation*, 88(3):832–6, 1993. ISSN 0009-7322 (Print) 0009-7322 (Linking).

Appendix A

Biological Experimentation Related Methods and Materials

A.1 Cell Culture Methods and Materials

A.1.1 Preparation of General Reagents

Protocol A.1. Sterile Dulbecco's phosphate buffered saline (D-PBS) for Tissue Culture
10x Dulbecco's phosphate buffered saline (D-PBS) was purchased from Sigma Aldrich (D1408-500ML). 1x D-PBS is a cell culture grade water used for washing.

1. In sterile conditions mix 90 mL of autoclaved deionized water (dH_2O) with 10 mL of 10x PBS to give a 1X working solution. Solutions are stored between 2-6°C.

End of Protocol A.1.

Protocol A.2. Non-sterile phosphate buffered saline (PBS)
Non-sterile PBS is used for reagent dilutions and washing when tissue culture sterility is not an issue. PBS tablets are puchased from Sigma-Aldrich (P4417-50TAB).

1. Dissolve two PBS tablets with 400 mL dH_2O to give a 1X working solution consisting of 0.01 M phosphate butter, 0.0027 M potassium chloride and 0.137 M sodium chloride with a solution pH of 7.4.

End of Protocol A.2.

Protocol A.3. 4% Formalin
4% formalin is a used as a general purpose fixative to preserve biological samples - in particular here, as preparation for fluorescent staining.

1. In a fume hood, mix 20 mL of 10% formalin with 30 mL of 0.01 M PBS to give a 4% solution of formalin. Store solutions at room temperature in a safety cabinet.

End of Protocol A.3.

Protocol A.4. 3% bovine serum albumin (BSA)
bovine serum albumin (BSA) is used here as a reagent for fluorescent staining. BSA is purchased from Sigma-Aldrich (A2153) as a lyophilized powder.

1. Using scales, dispense 1.5 g of BSA powder on a weighing boat before fully dissolving in a bottle with 50 mL of 0.01 M PBS. Store solution between 2-6°C and are discard a month after preparation if not used.

End of Protocol A.4.

Protocol A.5. 0.5% Triton X-100
0.5% Triton X-100 is used here as a reagent for fluorescent staining and is purchased from Sigma-Aldrich (T8787).

1. In a fume hood, mix 0.5 mL of Trixon X-100 with 95.5 mL of deionized water to make a 0.5% working solution. Store solutions between 2-6°C and are discard a month after preparation if not used.

End of Protocol A.5.

A.1.2 Cell Culture Protocols

The protocols listed here are for use in the following cell types:

- Human Rectal Smooth Muscle Cells (HRSMC).
- Human Aortic Smooth Muscle Cells (HASMC): Gibco (C0075C): primary cells.
- Human Aortic Endothelial Cells (HAEC): Gibco (C0065C): primary cells.
- Human Umbilical Vein Endothelial Cells (pooled) (HUVECp): Gibco (C0155C): primary cells, pooled from multiple donors.
- Mouse Myoblast Cells (C2C12).

Protocol A.6. Preparation of Complete Cell Culture Medium
Complete cell culture medium (herein referred to as 'complete medium') is made up of components specific to the cell type being cultured. Table A.1 lists and details the components of each complete medium.

1. Thaw frozen aliquots of appropriate supplements in a water bath heated to 37°C ensuring that the water level does not reach the lid of each aliquot.
2. Before being transferred to a class 2 type A laminar flow culture hood (herein referred to as the 'culture hood'), spray thawed tubes with 70% IMS.
3. In aseptic conditions, transfer supplements to a bottle of basal medium using serological pipettes.
4. Gently rotate the medium bottle to ensure even mixing.
5. Store at 2-6°C and discard a month after preparation if not already completely used.

End of Protocol A.6.

Protocol A.7. Suspension of Cells from Cryopreservation - First Suspension
Vials of cells which are delivered are stored in a −80°C freezer at the point of arrival and should be seeded within at most 24 hours.

1. Remove the vial of frozen cells from −80°C freezer and transfer to a water bath heated to 37°C for rapid thawing ensuring the water level does not reach the lid of the vial.

Cell Type	**Basal Medium**	**Supplements**	**Supplement Concentration**
HRSMC	MEME (Sigma, M2279)	L-Glutamine (Sigma, G7513) NEAA (Sigma, M7145) AB/AM (Sigma, A5955) FBS (Gibco, 10270-106)	1% v/v L-Glutamine; 1% v/v NEAA; 1% v/v AB/AM 10% v/v FBS
HASMC	M231 (Thermo-Fisher, M231500)	SMGS(Thermo-Fisher, S00725) AB/AM	4.9% v/v FBS; 2 ng/mL bFGF; 0.5 ng/mL hEGF 5 ng/mL heparin; 2 $\mu g/mL$ rHIGF 0.2 $\mu g/mL$ BSA 1% v/v ABAM
HAEC	M200 (Thermo-Fisher, M200500)	LSGS(Thermo-Fisher, S00310) ABAM	2% v/v FBS; 1 $\mu g/mL$ hydrocortisone; 10 ng/mL hEGF 3 ng/mL bFGF; 10 $\mu g/mL$ heparin; 1% v/v AB/AM
HUVECp	M200	LSGS ABAM	2% v/v FBS; 1 $\mu g/mL$ hydrocortisone; 10 ng/mL hEGF 3 ng/mL bFGF 10 $\mu g/mL$ heparin; 1% v/v AB/AM
C2C12	DMEM (Thermo-Fisher, 41966029)	FBS AB/AM	10% v/v FBS 1% v/v AB/AM

Table A.1

Components of Complete Medium for Used Cell Types

Acronyms: fetal bovine serum (FBS); human basic fibroblast growth factor (hbFGF); human epidermal growth factor (hEGF); recombinant human insulin-like growth factor (rhIGF); antibiotics/antimycoctics (AB/AM); bovine serum albumin (BSA); Non-Essential Amino Acids (NEAA); Minimum Essential Medium Eagle's (MEME); Dulbecco's Modified Eagles Medium (DMEM); acrfulllsgs; Smooth Muscle Growth Supplement (SMGS).

2. Before being transferred to the culture hood, spray the vial with 70% IMS.
3. In sterile conditions, pipette the contents of the vial up and down using a 1 mL serological pasteur pipette to disperse the cells. In the same way, transfer the contents of the vial to a 20 mL universal tube with 10 mL of cell specific complete medium.
4. Centrifuge the tube for five minutes at 1000 revolutions per minutes to gather the cells as a pellet at the bottom of the tube.
5. In sterile conditions, re-suspend the pellet in an appropriate volume of complete medium.
6. Aspirate the cell suspension equally among the desired number of T75 flasks and supplement each flask with medium such that the cell suspension totals 12 mL of medium.
7. Incubate at 37°C at 5% CO_2.
8. 24 hours after incubation replace the medium in each flask with complete and pre-warmed medium.

End of Protocol A.7.

Protocol A.8. Culturing and Passaging Cells

Culturing Cells

1. Replenish medium of cells cultured in T75 flasks ever 2-3 days using complete, pre-warmed medium prepared according to Protocol A.6.
2. When cell confluency reaches 70%, cells should be passaged.

Passaging Cells

1. In sterile conditions aspirate and discard medium from the T75 flask and gently clean the cell layer using 10 mL of pre-warmed PBS (Protocol A.1).
2. Add 3 mL of freshly thawed Trypsin EDTA (Sigma, T3924) to the flask and tilt the flask to ensure complete coverage of the cells.
3. Incubate at room temperature or at 37°C depending on the distributor's instructions for each cell type. Incubation should be no longer than around 5 minutes and only until cells detach from the flask and with a gently rasping of the flask.
4. Immediately dispense 10 mL of complete, pre-warmed medium in the flask ensuring coverage of the flask surface. Transfer the contents to a sterile 15 mL centrifuge tube.
5. Centrifuge the tube for 5 minutes at 1000 revolutions per minutes to gather the cells as a pellet at the bottom of the tube.
6. In sterile conditions, re-suspend the pellet in an appropriate volume of complete medium.
7. Aspirate the cell suspension equally among the desired number of T75 flasks and supplement each flask with medium such that the cell suspension totals 12 mL of medium.
8. Incubate at 37°C at 5% CO_2.

End of Protocol A.8.

Protocol A.9. Preparation of Freezing Medium
To make x mL of freezing medium.

1. in sterile conditions add $\frac{4}{5}x$ mL of FBS to $\frac{x}{5}m$L of Dimethyl sulfoxide (DMSO).
2. Aliquot into $5m$L bijou tubes and store at -20°C .

End of Protocol A.9.

Protocol A.10. Cryofreezing and Re-suspending Cells

1. Trypsinise and centrifuge cells according to Protocol A.8 but ignore Step 6 onwards.
2. Re-suspend the cell pellet using the drop-wise addition of freshly thawed freezing medium as prepared through Protocol A.9.
3. Transfer 2 mL of cell suspension to a cryofreezing tube and place in a freezing container (C1562-1EA, Sigma) which inside a -70°C freezer, cools the cell suspension at a rate of 1°C per minute.
4. For long term storage transfer to an appropriate liquid nitrogen storage facility.

End of Protocol A.10.

Protocol A.11. Cell Counting and Seeding

1. Re-suspend a pellet of cells after trypsinisation and spinning (Protocol A.8, Step 6) in x mL of complete medium.
2. On a clean glass hemocytometer dispense 10 μL of the suspension in each chamber underneath the glass coverslip.
3. Using a microscope, count the cells in the central nine squares of each chamber.
4. Clean the hemocytometer and glass coverslips and repeat the process.
5. Take the average hemocytometer cell count and calculate the total number of cells in the suspension by multiplying the average by $x \times 10^4$.
6. Based on a desired cell seeding density, dilute an appropriate fraction of the cell suspension with complete medium and distribute amount cell culture wells.

End of Protocol A.11.

Protocol A.12. Fixation of Cells

1. In a fume cupboard, aspirate well contents and discard.
2. Add enough 4% formalin (prepared according to Protocol A.3) to cover the cell layer.
3. Incubate at room temperature for 15 minutes before aspirating and appropriate disposing of the formalin.
4. Rinse the cells three times with PBS solution. Store in PBS until further use.

End of Protocol A.12.

Protocol A.13. Fibronectin Coating of Untreated BioFlex® Plates
This protocol applied to untreated BioFlex® plates (Dunn Labarotechnik GmbH, BF-3001C). Bovine Fibronectin (Sigma F1141) is used to coat untreated membranes for cell culture.

- In sterile conditions, dilute freshly thawed bovine fibronectin in sterile PBS (Protocol A.1) to give a working concentration of 5 μg/mL fibronectin in PBS. Prepare 3 mL of this solution per 6-well plate to be coated.
- In sterile conditions, dispense 3 mL of the working solution into a well of a BioFlex® plate and swirl for 5 seconds to ensure even coverage.
- Transfer the solution to the next well and repeat.
- Repeat for each well in the plate.
- For each plate, use 3 mL of fresh fibronectin solution.

End of Protocol A.13.

A.2 Cell Analysis

Protocol A.14. Hoechst 33342 Staining

Stock Preparation

Hoechst 33342 is prepared as a stock solution according to manufacturers instructions. Here, stock is prepared at a concentration of 10 mg per mL in DMSO.

Working Protocol

1. Freshly prepare working solutions by diluting the stock solution in PBS to give a Hoechst 33342 concentration of 10 μg per mL.
2. Following Protocol A.12, aspirate any PBS in the well and add enough working solution of Hoechst 33342 to cover the cell layer. For 6-well plates, 1 mL of solution is added to each well.
3. Incubate at room temperature in darkness for 15 minutes.
4. Rinse three times with PBS.

End of Protocol A.14.

Protocol A.15. Cell Proliferation ELISA, BrdU (colorimetric) - 6 Well Format
The BrdU colorimetric cell proliferation ELISA was purchased from Roche Diagnostics (11647229001). The protocol used here is scaled from the 96 well format given in the product documentation to a 6 well format.

Stock Preparation

1. Bottle 3 (Anti-BrdU-POD) is dissolved in 1.1 mL of double distilled water for 10 minutes and thoroughly mixed resulting in 100 times working concentration stock solution. Stored at 2 - 8°C the solution is stable for several months.

Working Protocol

1. Prepare BrdU labelling solution shortly before use. For each well to be assessed add 100 μL of fresh culture medium to 1 μL of stock BrdU labelling reagent (bottle 1). Regardless of the number of wells to be assessed, prepare an extra 100 μL of labelling solution to account for solution lost to bubbles. For example, for 6 wells 700 μL should be mixed with 7 μL of BrdU labelling reagent.
2. In the culture hood, adjust the medium in each well in the 6-well to 1000 μL of original medium.
3. Aspirate 100 μL of the BrdU labelling solution into each of the adjusted wells and swirl to ensure mixed before returning to the incubator for at least 3 hours depending on the cell type.
4. Remove medium from each well. Add 1 mL of the fixing/denaturing reagent (bottle 3) to each well and incubate at room temperature for 30 minutes.
5. Prepare the Anti-BrdU-POD working solution prepared shortly before the fixing/denaturing step is complete. For each well mix 10 μL of Anti-BrdU-POD stock solution with 1000 μL of the antibody dilution solution (bottle 4). Regardless of the number of wells to be assessed, prepare an extra 500 μL of antibody solution to account for solution lost to bubbles. For example, for 6 wells 6500 μL of dilution solution should be mixed with 65 μL of Anti-BrdU-POD stock solution. Remove the fixing solution thoroughly by aspiration and/or tapping. Add 1000 μL of working Anti-BrdU-POD to each well and incubated at room temperature for 90 minutes.
6. During the 90 minute incubation prepare a 96 well plate for colorimetric reading. For each well assessed three to four wells in the 96 well plate are prepared. In each well of the 96 well plate to be used, aspirate 25 μL of 1 M H_2SO_4.
7. Remove the Anti-BrdU-POD solution thoroughly by aspiration and/or tapping and rinse each well using a 1 times concentration of PBS.
8. Add 1 mL of substrate solution (bottle 6) to each well and incubate in the dark at room temperature for 10 to 15 minutes depending on the strength of the colour produced. After a chosen time, for each well, aspirate 300 - 400 μL of the substrate solution deposit equally into 3 - 4 wells of the pre-prepared 96 well plate. The H_2SO_4 in the 96 well plate works to stop the colour development process.
9. Plate the 96 well plate on a plate shaker for 1 minute at 200 revolutions per minute to ensure even mixing before read on an ELISA plate reader at 370 nm with a reference wavelength of 492 nm.

End of Protocol A.15.

Protocol A.16. Click-iT® EdU Alexa Fluor® 488 Imaging - 6 Well Format
Click-iT® EdU Alexa Fluor® 488 is available as a complete imaging kit but is for the most part used here in component form. Click-iT® Cell Reaction Buffer Kit, Alexa Fluor® 488 Azide and 5-ethynul-2'-deoxyuridine (EdU) is purchased from ThermoFisher (C10269, A10266 and A10044 respectively). Copper(II) Sulfate ($CuSO_4$) and Dimethyl sulfoxide (DMSO) is purchased from Sigma-Aldrich (C1297-100G and D8418, respectively).

Stock Preparation

1. EdU Solutions:
   (a) If using stand alone component: Dissolve the 50 g EdU dessicate in 2 mL of DMSO to give a 100 mM stock solution. Once dissolved, aliquot by mixing 200 μL of stock with 1800 μL of DMSO to give a concentration of 10 mM. Stock solutions are stable up to a year when stored at $\leq -20°$C.

(b) If using Imaging Kit: Dissolve the 50 g EdU dessicate in 2 mL of DMSO to give a 10 mM stock solution. Stock solutions are stable up to a year when stored at $\leq -20°$C.

2. Reaction Buffer Additive:

   (a) If using reaction buffer kit: Dissolve the 80 g of reaction buffer additive desiccate in 4 mL deionized water (dH_2O) to give a 1X working solution. Stock solutions are stable up to a year when stored at $\leq -20°$C and should be discarded if the solution develops a brown colour.

   (b) If using the imaging kit: Dissolve the 400 g of reaction buffer additive desiccate in 2 mL deionized water (dH_2O) to give a 10X working solution. Stock solutions are stable up to a year when stored at $\leq -20°$C and should be discarded if the solution develops a brown colour.

3. $CuSO_4$: Dissolve 0.08 g of $CuSO_4$ in 5 mL dH_2O to give a 100 mM aqueous solution and is stored between 2-6°C.

4. AlexaFluor® 488 Azide: Dissolve 0.5 mg of AlexaFluor® 488 azide desiccate in 1.5 mL DMSO to give a 0.39 mM stock solution. The solution is stored protected from light at $\leq -20°$C .

Working Protocol

1. Prepare EdU labelling solution shortly before use. For each well to be assessed, add 1000 μL of fresh culture medium to 2 μL of 10 mM stock EdU solution resulting in a 20 μM solution. Regardless of the number of wells to be assessed, prepare an extra 500 μL of labelling solution to account for solution lost to bubbles. For example, for 6 wells 6500 μL should be mixed with 13 μL of EdU labelling reagent. Before use, warm the EdU working solution to 37°C in an incubator.

2. In the culture hood adjust each well in the 6 well plate is adjusted to 1000 μL of original medium.

3. Add 1000 μL of the EdU labelling solution into each of the adjusted wells, and swirl to ensure mixed. Return the plate to the incubator for at least 3 hours depending on the cell type. The concentration of EdU in each well is now 10 μM/mL .

4. Remove the medium in each well of the plate thoroughly by aspiration. Fix the cells using Protocol A.12 but rinse with 3% BSA (Protocol A.4) instead of PBS.

5. Thoroughly remove the BSA and add 1 mL of 0.5% Triton® X-100 in PBS (Protocol A.5) to each and incubate at room temperature for 20 minutes.

6. Prepare the reaction buffer cocktail no more than 15 minutes before use through the following:

   (a) Reagent preparation for n wells:

      i. Reaction buffer working solution: dilute 88×n μL of stock reaction buffer in 792×n μL of dH_2O to give a 1X working solution.

      ii. Reaction buffer additive (if from imaging kit): dilute 10×n μL of stock reaction buffer additive in 90×n μL of dH_2O to give a 1X working solution.

   (b) Add the components listed in Table A.2 in order to prepare the reaction buffer cocktail. This results in a final AlexaFluor® azide concentration of 5 μM/mL . Regardless of the number of wells to be assessed, prepare an extra 500 μL of reaction cocktail to account for solution lost to bubbles

7. Rinsed each well three times with 3% BSA.

8. Add 1 mL of the reaction buffer cocktail to each well and incubate at room temperature in the dark for 30 minutes.

9. Rinse each well three times with PBS.

Table A.2
Click-it® EdU Reaction Cocktail Preparation Table

Component	n**-wells** (μ**L**)	**6.5 wells** (μ**L**)
1X reaction buffer	$880\times n$	5720
$CuSO_4$	$20\times n$	130
AlexaFluor® azide (stock)	$13\times n$	84.5
1X reaction buffer additive	$100\times n$	650
Total	$1013\times n$	6584.5

10. Stain each well with Hoechst 33342 using Protocol A.14.
11. Rinse each well three times with PBS.
12. Image using a fluorescent microscope. Alexa Fluor® 488 has an excitation of 495 nm and an emission of 519 nm. Hoechst 33342 has an excitation wavelength of 350 nm and an emission of 461nm.

End of Protocol A.16.

A.2.1 Cell Manipulation: Plasmid Transfection

Protocol A.17. Colony Expansion of Plasmid

pEGFP-C1 Plasmid Transformation

1. Prepare an Agar plate with Kanamycin according to manufacturers protocols such that the Kanamycin concentration is 1 mL per litre.
2. Mix 1 muL of stock pEGFP-C1 plasmid to 50 muL of Stellar™ competent cells (Clontech, 636763) in a microcentrifugue tube and incubate on ice for 10 minutes.
3. Heat shock the solution at 42°C for 45 seconds and then return to ice for 2 minutes.
4. Mix 250 uL of SOC Medium (Sigma, S1797) with the solution and incubate at 37°C for 1 hour.
5. Spread the solution on the agar plate and incubate at 37°C for 24 hours.

Colony Expansion

1. The agar plate should have visible colonies of Stellar™ competent cells following 24 hours of incubation.
2. Prepare 100mL of autoclaved LB Broth (Sigma, L7275) with 50 mg/mL of Kanamycin in a conical flask according to manufacturers instructions .
3. Using a colony picker, scrape a single colony of cells on the agar plate and stir into the LB broth. Incubate the flask at 37°C in an 3D shaker for 16 hours.

End of Protocol A.17.

Protocol A.18. Plasmid Purification Maxi Prep
Purifcation of plasmids from colony expansions (Protocol A.17) is conducted according to manufacturers instructions (Qiagen, C1562-1EA). Quantify yield using spectrophotometry.
End of Protocol A.18.

Protocol A.19. Lipofecatmine Induced Plasmid Transfection of Cells
For x number of wells in a 6-well plate.

1. Bring Opti-MEM (ThermoFisher, 31985070) and Lipofectamine 2000 (ThermoFisher, 11668019) to room temperature.
2. Tube A: In sterile conditions mix x μg of plasmid with $250x$ μg of Opti-MEM.
3. Tube B: In sterile conditions mix $5x$ μL of Lipofectamine 2000 to $250x$ μL of Opti-MEM.
4. Incubate Tubes A and B at room temperature for 5 minutes.
5. Tube C: Gently mix Tube A with Tube B and incubate for 20 minutes at room temperature.
6. In sterils onditions replace the medium in each well to be transfected with 1.5 mL of prewarmed DMEM containing 10% FCS.
7. Dropwise add 500 μL of solution from Tube C to each well.
8. Incubate at 37°C and 5% CO_2 for 6 hours before rinsing three times with PBS.
9. Add complete medium to each well and return to the incubator.

End of Protocol A.19.

Appendix B

Appendices For Chapter 1

B.1 Literature Keyword Removal

Table B.1
Key word removal for high level overview in Figure 1.3(b)

of	in	on	stretch
via	by	a	tensile
strain	mechanical	for	mechanotransduction
stress	is	to	the
cyclic	cultured	not	study
but	and	as	with
an	from	during	stretch-induced
strain-induced	role	cellsthe	ii
exposed	cellsmechanical	model	cells:
stretchÃćÂĂ	ÃćÂĂÂęcyclic	cellscyclic	stretched
stretchÃćÂĂ	stretching	under	shear
cells	2		

Appendix C

Appendices For Chapter 2

C.1 BioFlex® /EM Augmentation Protocols

Protocol C.1. BioFlex® Plate Augmentation 1 (Dr. R. Day)

1. Open an individually sealed BioFlex® plate (Dunn Labortechnik, BF-3001U) inside a class 2 laminar flow culture hood. Seal the lid to the base with autoclave tape so to not contaminate the wells.
2. Prepare 8 mL of Sylgard® 184 elastomer as per manufacturers instructions (Dow Corning) ensuring the two part elastomer is thoroughly mixed.
3. On a bench, upturn the BioFlex® plate. Suction 1 mL of Sylgard® elastomer into a 1 mL syringe. Aspirate a small amount of elastomer into the middle of each well. Place a 6(d)x2 mm N42 nickel plated disc magnet (e-magnets, EP390) onto the middle of 3 wells (A1, A3 and B2). Gently syringe the remainder of each 1 mL syringe over the magnets ensuring an even coating across the membrane and over the magnet.
4. Syringe 1 mL of the remainder of the elastomer mix into each of the remaining wells to act as controls.
5. Cure in an empty incubator at 37° Celsius for 24 hours.

End of Protocol C.1.

Protocol C.2. BioFlex® Plate Augmentation 2.1

1. For each BioFlex plate prepare 6 magnet containing loading posts by placing them in a class 2 safety cabinet and dousing with 70% IMS. Allow to air dry fully.
2. Open an individually sealed BioFlex® plate inside the safety cabinet.
3. Remove the lid of the plate and hold upside down before fully inserting one loading post into each well. Place the plate upside down so that the plate is resting on the loading posts.
4. Place the magnet spacer on the membrane. Orient a 6(d)x2 mm magnet so that the magnetic poles are consistent with a reference magnet. Allow the magnet to drop in the middle of the spacer and attract the magnet inside the loading post. Remove the magnet placer and repeat for the remaining wells.

5. Suction 1 mL of Sylgard® elastomer, prepared according to manufacturers instructions, into a 1 mL syringe. Gently syringe 1 mL syringe over the magnets ensuring an even coating across the membrane and over the magnet. Cure *in situ* in the biosafety cabinet for at least 72 hours. (72 hours as opposed to 24 in Protocol C.1 due to the temperature difference in the biosafety cabinet.)
6. In aseptic conditions, remove the loading posts by hand remaining careful not to contaminate the lids of the well.
7. Using a sharp scalpel, slice over the elastomer in wells A2, B1 and B3 and allow the embedded magnet to be removed by magnetic attraction to the scalpel. These wells are used as controls.

End of Protocol C.2.

C.2 Initial Prototype Proof of Concept

Within the context of studying strain induced proliferation, initial experiments using the prototype magnetic actuator were conducted using Human Rectal Smooth Muscle Cells (Human Rectal Smooth Muscle Cells (HRSMC)). This work was conducted by Dr. Richard Day.

C.2.0.1 Materials

HRSMC were obtained from ScienCell (2985). Bovine fibronectin was obtained from Sigma-Aldrich. HRSMC was cultured with Minimum Essential Medium Eagle (M 2279 Sigma-Aldrich) supplemented with 1% non essential amino acids (M7145 Sigma-Aldrich),1% L-Glutamine (Sigma-Aldrich), 1% antibiotic/antimycotic solution (A5955 Sigma-Aldrich) and 10% fetal bovine serum (10270 Life Technologies). Cells were grown in standard T75 tissue culture treated flasks with medium replaced over 2-3 days and passaged at 70% confluency using Trpsin/EDTA (T3935-100ml Sigma-Aldrich). The Roche BrdU Proliferation Elisa was purchased from Abcam (AB126556).

C.2.0.2 Methods

BioFlex® plates were prepared according to Protocol C.1. Subsequently they were opened in class 2 safety cabinet in sterile conditions. 1 mL of fibronectin in PBS (5μg/mL) was swirled in each well to create a matrix for cells to bind to. In a solution of 3 mL of complete medium, HRSMC were seeded on each well at a density of 500×10^3/well. Plates were left unagitated in a humidified incubator at 37 degrees Celsius with 5% CO_2. After 24 hours the plate was moved to the prototype actuator apparatus. Magnets were lined up by eye with pre-marked cross hairs (as in Figure 2.4(d)) and taped into position. The motors were initiated with fresh AA batteries and set to speed setting 1 as indicated by the LEGO® speed remote controller. The actuator device and BioFlex® plate were placed inside a humidified incubator at 37 degrees Celsius with 5%CO_2. The actuator was run for 1 hour per day for 5 days.

At the end of the actuation period the proliferation status of each well was assessed using the BrdU Proliferation Elisa according to manufacturers instructions with all volumes scaled up for use with a 6 well plate.

Concurrent with this, through a collaboration with Dr. Guitano Buriescci (Department of Engineering, UCL), a finite element model (FEM) of the system was derived and the strain distribution across the membrane generated by the magnets theoretically calculated. Other than knowing that the magnetic forces were not, in fact, part of the model but the embedded magnet was prescribed a displacement based on an educated assessment of the system, the details of the model and implementation are not available.

C.2.0.3 Results

The results of the effect of a 1 hour actuation for 5 days on HRSMC are shown in Figure 2.6(a). A significant increase is seen in the actuated wells compared to control. Results are given with 3 actuated wells and 3 control wells.

The FEM calculations are shown in Figure 2.6(b) as supplied by Dr. Burriesci. Although the model heavily based on estimates, alongside intuition, it becomes apparent that a characteristic of this system is a highly heterogeneous strain distribution, both in direction and magnitude.

C.3 Arduino Magnetometer Control Code

```
#include <Wire.h>
#include <Adafruit_Sensor.h>
#include <Adafruit_HMC5883_U.h>

/* Assign a unique ID to this sensor at the same time */
Adafruit_HMC5883_Unified mag = Adafruit_HMC5883_Unified(12345);

void displaySensorDetails(void)
{
  sensor_t sensor;
  mag.getSensor(&sensor);
  mag.setMagGain(HMC5883_MAGGAIN_8_1);
  delay(500);
}
void setup(void)
{
  Serial.begin(115200);
 /* Initialise the sensor */
  if(!mag.begin())
  {
    /* There was a problem detecting the HMC5883 ... check your connections */
    Serial.println("Ooops, no HMC5883 detected ... Check your wiring!");
    while(1);
  }
 /* Display some basic information on this sensor */
  displaySensorDetails();
}
void loop(void)
{
  /* Get a new sensor event */
  sensors_event_t event;
  mag.getEvent(&event);

  /* Magnetic vector values are in micro-Tesla (uT) */
Serial.println(event.magnetic.z,BIN);
  delay(10);
}
```

Table C.1
List of filenames in MagAct software with a brief description of the function of each.

File Name Title	Function
ABEG_ARDUINO_MAG.fig	Created using MATLAB Guide. GUI display code
ABEG_ARDUINO_MAG.m	Created using MATLAB Guide. Defines buttons and function calls.
connect.m	Connected to the Arduino COM port.
portopen.m	Opens the Arduino COM port.
portclose.m	Closes the Arduino COM port.
read_calculate.m	Reads the data stram from the COM port and computes magnetic field analysis.
logo.png	Image
logo2.png	Image
logo3.png	Image

C.4 MagSensor Software Notes

The un-compiled root folder *MagAct_Frequency* contains the file architecture listed in Table C.1. The *ABEG_ARDUINO_MAG .fig* and *.m* files were created with the assistance of MATLAB GUIDE: a simple environment for designing graphical user interface (GUI). These files form the front end of the program calling the other files in the root folder as MATLAB functions or images for reading and processing the data stream.

Appendix D

Appendices For Chapter 4

D.1 Istra4D Data Output Forms

- coordinate_x/mm
- coordinate_y/mm
- coordinate_z/mm
- coordinate_x_var/u(m^2)
- coordinate_y_var/u(m^2)
- coordinate_z_var/u(m^2)
- distance_to_plane/mm
- distance_to_sphere/mm
- variance_sphere/u(m^2)
- displacement_total/mm
- displacement_total_var/u(m^2)
- displacement_total_rbmr/mm
- displacement_total_rbmr_var/u(m^2)
- displacement_x/mm
- displacement_y/mm
- displacement_z/mm
- displacement_x_var/u(m^2)
- displacement_y_var/u(m^2)
- displacement_z_var/u(m^2)
- displacement_x_rbmr/mm
- displacement_y_rbmr/mm
- displacement_z_rbmr/mm
- strain_xx/%
- strain_yy/%
- strain_xy/%
- strain_p1/%
- strain_p2/%

- strain_xx_var/%^2
- strain_yy_var/%^2
- strain_xy_var/%^2
- strain_p1_var/%^2
- strain_p2_var/%^2
- engineering_strain_xx/%
- engineering_strain_yy/%
- engineering_strain_xy/%
- engineering_strain_p1/%
- engineering_strain_p2/%
- engineering_strain_xx_var/%^2
- engineering_strain_yy_var/%^2
- engineering_strain_xy_var/%^2
- engineering_strain_p1_var/%^2
- engineering_strain_p2_var/%^2
- true_strain_xx/%
- true_strain_yy/%
- true_strain_xy/%
- true_strain_p1/%
- true_strain_p2/%
- true_strain_xx_var/%^2
- true_strain_yy_var/%^2
- true_strain_xy_var/%^2
- true_strain_p1_var/%^2
- true_strain_p2_var/%^2
- Time/s"

D.2 Flexcell Provided BioFlex® Material Data Sheet

FLEXCELL INTERNATIONAL CORPORATION

Biotechnology Products for Cellular Biomechanics™

Material Properties Specification Sheet
Bioflex Membrane

Property	Test Method	BioFlex Membrane
Physical Properties: Durometer, Shore "A" (pts)	ASTM D2240	40
Tensile Strength, psi (MPa)	ASTM D412	1000 (6.9)
Modulus of Elasticity (Young's Modulus) (kPa) Modulus is measured in the strain region of 0 - 0.18 =>2mm/11mm	Flexcell Internal	930
Elongation, %	ASTM D412	450
Tear Strength, ppi (kN/m)	ASTM D624	125 (21.9)
Compression Set, % **70 hr @ 300°F (149°C)**	ASTM D395B	30
Effects of Dry Heat Aging: Change in Hardness, Shore "A"(pts) **70 hr. @ 437°F (225°C)**	ASTM D573	+/-5
Change in Tensile Strength, %	ASTM D573	-15
Change in Elongation, %	ASTM D573	-40
Effects of Oil Immersion (ASTM#1 Oil) Change in Hardness, Shore "A" (pts) **70 hr. @ 302°F (150°C)**	ASTM D471	+/-5
Change in Tensile Strength, %	ASTM D471	-35
Change in Elongation, %	ASTM D471	-40
Change in Volume, %	ASTM D471	+10
Electrical & Thermal Properties Dielectric Constant	ASTM D150	3.0
Dielectric Strength, Volts/mil	ASTM D149	400
Volume Resistivity (Ohm/cm)	ASTM D257	$>1x10^{14}$
Thermal Conductivity (BTU in/hr/ft^2/°F) (Wm/°K)	ASTM C-518	1.5 0.21

Culturing Cells in a Mechanically Active Environment™
Hillsborough Business Center • 437 Dimmocks Mill Road • Hillsborough, NC 27278
800-728-3714 • (919) 732-1591 • FAX: (919) 732-5196 • www.flexcellint.com

Appendix E

Additional Information

E.1 List of Presentations and Publications

E.1.1 Oral Presentations

1. TIPS For Building Rings With Spheres: A Regenerative Medicine Perspective. *Incontinence: The Engineering Challenge IX*; London, England; November, 2013.
2. High Content Imaging to Uncover Correlation Between Substrate Strain and Phenotypic Modulation. *9th Cell Based Assays and Screening Technologies*; Dublin, Ireland; October, 2014.
3. Exploiting Heterogeneity in Cell Stretching Experiment; *CoMPLEX Annual Conference*; London, England; May, 2015.
4. Development of New Methodology to Quantify Physical Strain and Cellular Response; *Research in Progress: UCL Division of Medicine*; London, England; April, 2016.

E.1.2 Poster Presentations

1. Cyclic Strain for In Vivo Smooth Muscle Regeneration: High Throughput Quantification for Initial Investigations; *CoMPLEX Annual Conference*; London, England; May, 2014.
2. Cyclic Strain for In Vivo Smooth Muscle Regeneration: High Throughput Quantification for Initial Investigations; *UCL Division of Medicine Research Retreat*; London, England; June, 2015.
3. Stretching Cardiovascular Cells: An Alternative Methodology to the FlexCell System.; *UCL Cardiovascular Science Symposium*; London, England; January, 2016.
4. Efficiency Optimisation of Stretch Induced Lipofectamine Transfection Using MagAct.; *UCL Division of Medicine Research Retreat*; London, England; June, 2016.

E.1.3 Publications

1. J. Puri and R. M. Day. *Magnetic Material as Trojans for Cell Therapy and Muscle Regeneration*, Proceedings of the Institution of Mechanical Engineers, Part H: Journal of Engineering in Medicine. *Under Review*